



Skolkovo Institute of Science and Technology

UNCONVENTIONAL RESERVOIR CHARACTERIZATION USING  
LOW-FIELD NUCLEAR MAGNETIC RESONANCE  
*Doctoral Thesis*

by

ALIYA MUKHAMETDINOVA

DOCTORAL PROGRAM IN PETROLEUM ENGINEERING

Supervisor  
Associate Professor Alexey Cheremisin

Moscow — 2021

© Aliya Mukhametdinova 2021

I hereby declare that the work presented in this thesis was carried out by myself at Skolkovo Institute of Science and Technology, Moscow, except where due acknowledgement is made, and has not been submitted for any other degree.

Candidate (Aliya Mukhametdinova)

Supervisor (Associate Professor Alexey  
Cheremisin)

## ABSTRACT

In recent years, the share of unconventional reserves in global oil production has been growing, while core analysis laboratories are looking for more effective methods for assessing unconventional resources. Conventional laboratory techniques for defining the reservoir properties and saturation of the rock are not applicable or not accurate for low-permeability, organic-rich, and carbonate rocks. Investigation of the reservoir properties of such formations requires a new approach due to low values of porosity and permeability, high content of organic components, including kerogen, and the presence of high-carbon bitumen or high-viscous oil. In turn, the permafrost study forms a different research direction, which indicates the importance of understanding the properties of the frozen soil.

Significant relevance in the study of unconventional reservoirs and, primarily, in the identification of saturating fluids was obtained by NMR-based core analysis workflows. NMR provides one of the most reliable assessments of hydrocarbon deposits at an early stage of exploration and provides an essential contribution to the evaluation of the petrophysical properties and efficiency of enhanced oil recovery methods.

In the current thesis, the methodologies and workflows for defining liquid saturation using NMR for unconventional rock samples are modified and developed. Enhanced workflows are used for accurate characterization of reservoir properties, including the porosity, oil and water saturation, wettability of a rock. The application of the proposed workflows is demonstrated on the example of the local organic-rich shale rocks, low-permeability, and highly-cavernous carbonates. Results of NMR are compared to results by other advanced experimental techniques, including PDP, MICP, and X-Ray CT. A new NMR  $T_1$ - $T_2$  maps interpretation approach was proposed for optimized fluid interpretation of shale rock samples. Thus, based on the accumulated experimental and analytical data on fluid identification,  $T_1$ - $T_2$  mapping schemes were developed.

A novel methodology for the evaluation of the unfrozen water content in permafrost was developed.  $T_2$  relaxation data was utilized for the calculation of the fluid volume in the core center at temperatures below 0°C. Novel experimental setups at formation conditions were

designed, and experiments were carried out in a high-pressure NMR cell. The results from the high-pressure, high-temperature (HPHT) experiments were used to analyze the process of the water and CO<sub>2</sub> diffusion in the oil-saturated core. The proposed concepts are of great interest in the fundamental study of the porous structure, saturation, and reservoir properties of unconventional reservoirs.

Developed techniques were implemented in applications of the NMR in thermal and gas enhanced oil recovery (EOR) research for evaluation of the oil displacement, saturation control during high-pressure air injection, *in-situ* combustion (ISC), and CO<sub>2</sub> injection for shale and heavy-oil carbonate formations.

## PUBLICATIONS DURING ENROLLMENT

### Journal Peer-Reviewed Papers:

1. **Aliya Mukhametdinova**, Andrey Kazak, Tagir Karamov, Natalia Bogdanovich, Maksim Serkin, Sergey Melekhin, Alexey Cheremisin, Reservoir Properties of Low-Permeable Carbonate Rocks: Experimental Features, *Energies* (Q1), DOI: 10.3390/en13092233.
2. Tatiana Bondarenko, **Aliya Mukhametdinova**, Evgeny Popov, Alexey Cheremisin, Anton Kalmykov, Igor Karpov, Analysis of Changes in Bazhenov Formation Rock Properties as a Result of High-Pressure Air Injection Based on Laboratory Modelling Data (Russian), *Oil Industry* (Q3), DOI: 10.24887/0028-2448-2017-3-40-44.
3. **Aliya Mukhametdinova**, Andrey Kazak, Tagir Karamov, Natalia Bogdanovich, Maksim Serkin, Ivan Putilov, Alexey Cheremisin, Experimental Workflow For Characterization of Storage and Transport Properties of Tight Domanic Reservoirs, *Oil Industry* (Q3), DOI: 10.24887/0028-2448-2020-11-2-87.
4. E.M. Chuvilin, N.S. Sokolova, B.A. Bukhanov, F.A. Shevchik, V.A. Istomin, **A.Z. Mukhametdinova**, A.G. Alekseev, E.S. Grechishcheva, Application of a Potentiometric Method for Determination of Unfrozen Water Content in Frozen Soils of Various Composition (Russian), *Earth's Cryosphere* (Q3), DOI: 10.21782/KZ1560-7496-2020-5(16-28).
5. Mehdi Razavifar, **Aliya Mukhametdinova**, Ehsan Nikooee, Alexander Burukhin, Amin Rezaei, Alexey Cheremisin, Masoud Riazi, Rock Porous Structure Characterization: A Critical Assessment of Various State-of-the-art Techniques, *Transport in Porous Media* (Q1), DOI: 10.1007/s11242-020-01518-6.
6. **Aliya Mukhametdinova**, Tagir Karamov, Natalia Bogdanovich, Sergey Borisenko, Svetlana Rudakovskaya, Alexey Cheremisin, Wettability of Organic-Rich Source Rocks: Case Study on Bazhenov Formation (Abalak-Bazhenov Group), *Advances in Geosciences* (Q2), DOI: 10.5194/adgeo-54-195-2020.
7. **Aliya Mukhametdinova**, Polina Mikhailova, Elena Kozlova, Tagir Karamov, Anatoly Baluev, and Alexey Cheremisin, Effect of Thermal Exposure on Oil Shale Saturation and Reservoir Properties, *Applied Sciences* (Q1), DOI: 10.3390/app10249065.
8. Evgeny Chuvilin, Natalia Sokolova, Boris Bukhanov, **Aliya Mukhametdinova**, Erika Grechishcheva, Andrey Alekseev, Vladimir Istomin, Freezing Point and Unfrozen Pore Water Contents of Permafrost Estimation by the Water Potential Method, *Geoderma* (Q1) (under review).
9. **Aliya Mukhametdinova**, Iwona Habina-Skrzyniarz, Andrey Kazak, Artur Krzyzak, NMR Relaxometry Interpretation of Source Rock Liquid Saturation — A Holistic Approach, *Marine and Petroleum Geology* (Q1) (under review).

### Conference Papers and Proceedings:

1. **Aliya Mukhametdinova**, Alexey Cheremisin, Vladimir Stukachev, Evgeny Popov, Dmitry Tyagusov, NMR Applications for Bazhenov Formation Reservoir Properties and Fluid Identification, AAPG ACE (2017), USA.
2. **Aliya Mukhametdinova**, Tatiana Bondarenko, Alexey Cheremisin, NMR as an Implicit Method for Oil Displacement Estimation in HPAI, ThEOR (proceedings) (2017), Kazan, Russia.
3. **Aliya Mukhametdinova**, Alexey Cheremisin, Evgeny Popov, NMR Applications for Unconventionals Core Analysis, Bazhenov Formation workshop, Moscow, Russia (2016).
4. **Aliya Mukhametdinova**, Alexey Cheremisin, Strahinja Markovic, NMR Applications for Unconventionals Core Analysis, PANIC, USA, (2018).
5. Evgeny Popov, Artem Myasnikov, Alexey Cheremisin, Ruslan Miftakov, Vladimir Stukachev, **Aliya Mukhametdinova**, Experimental and Computational Complex for Determination of the Effectiveness of Cyclic Carbon Dioxide Injection for Tight Oil Reservoirs, SPE Russian Petroleum Technology Conference and Exhibition held in Moscow, Russia, (2016).
6. **Aliya Mukhametdinova**, Tatiana Bondarenko, Evgeny Popov, Alexey Cheremisin, Victor Nachev, Philipp Denisenko, Aliaksandr Hancharou. Investigation of the Porous Structure of Unconventional Core During High-Pressure Air and Supercritical Water Injection, ThEOR (proceedings), Chengdu, China (2018).
7. Tagir Karamov, **Aliya Mukhametdinova**, Natalia Bogdanovich, Elena Kozlova, Zhanna Khakimova, Pore Structure Investigation Of Upper Devonian Organic-Rich Shales Within The Verkhnekamsk Depression, SGEM (2019).
8. **Aliya Mukhametdinova**, Tagir Karamov, Alexey Cheremisin, Natalia Bogdanovich, Vladimir Plotnikov, Complex Characterization Of Organic-Rich Carbonate Shales Saturation, SGEM (2019).
9. **Aliya Mukhametdinova**, Tagir Karamov, Natalia Bogdanovich, Alexey Cheremisin, Sergey Borisenko, Surface Wettability Evaluation of Bazhenov Formation Rocks by Different Methods, EAGE/SPE conference, Moscow (2019).
10. **Aliya Mukhametdinova**, Natalia Bogdanovich, Alexey Cheremisin, Svetlana Rudakovskaya, Experimental Determination of the Shale Wettability, EGU, online (2020).

# TABLE OF CONTENTS

ABSTRACT .....	iii
PUBLICATIONS DURING ENROLLMENT .....	v
LIST OF TABLES .....	x
ABBREVIATIONS .....	xii
UNITS CONVERSION TABLE.....	xiv
LIST OF FIGURES .....	xv
ACKNOWLEDGMENTS .....	xxi
INTRODUCTION.....	1
1.1 Defining Rock Saturation in Petrophysical Research.....	1
1.2 Review on NMR in Petrophysics .....	7
1.2.1 Physical Principles of NMR Relaxometry .....	7
1.2.2 NMR Applications in Shale and Tight Rock Analysis .....	12
1.2.3 Fluid Interpretation by NMR .....	15
1.3 Scope of Research and Research Objectives .....	22
1.4 Thesis Organization .....	25
MATERIALS AND METHODS .....	26
2.1 Samples Used in Study .....	26
2.1.1 Bazhenov Formation.....	26
2.1.2 Domanik Formation .....	28
2.1.3 Carbonate and Heavy-Oil Formations .....	31
2.1.4 Permafrost Soils .....	32
2.2 Methods .....	34
2.2.1 Core Selection.....	34
2.2.2 Nuclear Magnetic Resonance .....	36
2.2.3 Conventional Gas Porosity and Permeability of Plugs .....	37
2.2.4 Computed Tomography .....	38
2.2.5 Scanning Electron Microscopy .....	38
2.2.6 Rock-Eval Pyrolysis .....	38
2.2.7 Common Shared Methods.....	39
2.3 NMR Analysis .....	40
2.3.1 Calibration of NMR Unit .....	40
2.3.2 Precision, Accuracy, and Uncertainty of NMR Measurements .....	41
2.3.3 Hydrogen Index of Bulk Fluids .....	43
2.3.4 Experimental Procedure.....	44
2.4 Summary.....	46

CORE ANALYSIS BY NMR.....	48
3.1 Bazhenov Formation.....	48
3.1.1 Porosity by NMR.....	48
3.1.2 Fluid Interpretation by $T_1$ - $T_2$ map.....	52
3.1.3 Summary.....	53
3.2 Domanik Formation.....	54
3.2.1 Experimental Methodology.....	54
3.2.2 Porosity of Domanik Formation.....	54
3.2.3 Fluid interpretation by $T_1$ - $T_2$ .....	57
3.2.4 Summary.....	58
3.3 Comparison of NMR Results with Other Methods.....	59
3.3.1 Comparison with Neutron Porosity Logging Data.....	59
3.3.2 Comparison with Conventional Methods for Low-Permeability Rocks.....	61
3.3.3 Comparison with Conventional Methods for Organic-Rich Source Rocks.....	63
3.3.4 Comparison with Conventional Methods for Carbonate Rocks.....	64
3.3.5 Summary.....	66
3.4 Wettability by NMR Relaxometry.....	66
3.4.1 Experimental Methodology.....	68
3.4.2 Results.....	71
3.4.3 Influence of Rock Lithotype and OM Properties on Rock Wettability.....	74
3.4.4 Summary.....	78
3.5 Fluid Interpretation by NMR.....	79
3.5.1 Experimental Methodology.....	79
3.5.2 Digital Interpretation of the Fluid Saturation.....	80
3.5.3 Results.....	84
3.5.3 Summary.....	93
UNFROZEN WATER CONTENT IN PERMAFROST SOILS.....	95
4.1 Unfrozen Water in Ambient Conditions.....	95
4.1.1 Experimental Methodology.....	97
4.1.2 Results.....	100
4.2 Unfrozen Water under Gas Pressure.....	104
4.2.1 Experimental Methodology.....	104
4.2.2 Results.....	108
4.3 Summary.....	111
NMR APPLICATIONS IN DIFFUSION STUDIES.....	113
5.1 Introduction.....	113
5.2 Rock Samples.....	115
5.3 Experimental Methodology.....	115
5.3.1 Diffusion in Water-Water System.....	115

5.3.2 Diffusion in CO <sub>2</sub> –Oil System .....	116
5.4 Results .....	118
5.4.1 Dolerite Rock .....	118
5.4.2 Core Saturation .....	121
5.4.3 Organic-Rich Source Rock .....	123
5.4.4 Heavy-Oil Carbonate Rock.....	125
5.5 Summary.....	126
NMR APPLICATIONS IN THERMAL EOR STUDIES.....	128
6.1 Introduction .....	128
6.2 HPAI in the Shale Formation .....	130
6.2.1 Introduction.....	130
6.2.2 Experimental Methodology .....	131
6.2.3 Results.....	132
6.3 <i>In-Situ</i> Combustion in Heavy-Oil Carbonate Formation.....	144
6.3.1 Introduction.....	144
6.3.2 Experimental Methodology .....	144
6.3.3 Results.....	147
6.4 Summary.....	152
CONCLUSION .....	155
7.1 Summary.....	155
7.2 Conclusions .....	155
7.3 Recommendations .....	158
REFERENCES.....	160

## LIST OF TABLES

Table 1. Methods applied for reservoir properties laboratory assessment .....	3
Table 2. Comparison of different laboratory methods .....	5
Table 3. Published interpretation schemes .....	21
Table 4. List of rocks used for this study .....	26
Table 5. Characteristics of the studied soils .....	33
Table 6. Estimation of the systematic error of the NMR unit .....	43
Table 7. Estimation of the random error on example of Oilfield #6 samples .....	43
Table 8. Hydrogen indices of fluids .....	44
Table 9. Parameters of NMR testing .....	46
Table 10. List of target samples .....	49
Table 11. Porosity by NMR at different stages of saturation .....	55
Table 12. Determination of $T_2$ cut-off for samples of Oilfield #6 .....	57
Table 13. Comparison of porosity measurement results for Oilfield #6 .....	62
Table 14. Lithotypes of the studied collection .....	71
Table 15. Mineral composition of the target samples .....	80
Table 16. OM characteristics by Rock-Eval pyrolysis .....	85
Table 17. NMR modes for measuring the content of unfrozen water in frozen ground samples.	100
Table 18. NMR measurement modes for estimating the unfrozen water in frozen samples under pressure.....	109
Table 19. List of the investigated rock samples .....	115
Table 20. Results of NMR measurements .....	118
Table 21. List of the investigated samples .....	132
Table 22. Gas porosity and permeability before and after the combustion .....	134
Table 23. Results of NMR analysis of samples before and after CT .....	140

Table 24. Pyrolytic properties of samples before CT .....	140
Table 25. Pyrolytic properties of samples after CT .....	141
Table 26. List of rock samples .....	145
Table 27. Porosity change of oil-saturated samples .....	150

## ABBREVIATIONS

ABG	Abalak-Bazhenov Group
BF	Bazhenov Formation
BVI	Bound Volume Irreducible
CBW	Clay Bound Water
CPMG	Carr-Purcell-Meibum-Gill Sequence
CT	Combustion Tube
X-Ray CT	X-Ray Computed Tomography
EOR	Enhanced Oil Recovery
FFI	Free Fluid Index
FIB-SEM	Focused Ion Beam Scanning Electron Microscopy
FID	Free Induction Decay
GIT	Green Imaging Technologies
HC	Hydrocarbon(s)
HI	Hydrogen Index
HPI	High-Pressure Air Injection
HPHT	High-Pressure High-Temperature
ILT	Inverse Laplace Transform
IP	Inorganic Porosity
ISC	<i>In-situ</i> Combustion
LF-NMR	Low-field Nuclear Magnetic Resonance
LS	Liquid Saturation
MICP	Mercury Injection Capillary Pressure
MIP	Mercury Injection Porosimetry

MPCT	Medium Pressure Combustion Tube
MWW	Moderate Water-Wet
NSA	Number of Scans Acquired
NW	Neutral-Wet
OM	Organic Matter
PDP	Pulse-Decay Permeametry
PM	Potentiometric Method
RD	Recycle Delay
RF	Radiofrequency
SDR	Schlumberger-Doll Research
SEM	Scanning Electron Microscopy
SNR	Signal-to-Noise Ratio
SWW	Strong Water-Wet
$T_1$	Longitudinal Relaxation Time
$T_2$	Transverse Relaxation Time
TE	Time-Echo
TOC	Total Organic Carbon
USBM	U.S. Bureau of Mines Method
UV	Ultraviolet
WI	Wettability Index
$W_{uf}$	Unfrozen Water Content
WWW	Weak Water-Wet
XRD	X-Ray Diffraction
$\mu$ CT	Micro-Computed Tomography

## UNITS CONVERSION TABLE

Parameter	Utilized unit	SI unit
Pressure	1 psi	6894.76 Pa
Permeability	1 mD	0.9869 $\mu\text{m}^2$
Length	1 inch	25.4 mm
Temperature	0 C	273.15 K

## LIST OF FIGURES

Figure 1: Pore throat distribution according to <a href="#">Nelson (2009)</a> .....	3
Figure 2: Methods used for saturation evaluation in organic-rich shales ( <a href="#">Nikolaev and Kazak 2019</a> ).....	4
Figure 3: Hydrogen nuclei and magnetic fields in a fluid sample without application of an external magnetic field ( <a href="#">Coates et al. 1999</a> ).....	7
Figure 4: Polarization of hydrogen nuclei to the longitudinal direction under a static magnetic field ( <a href="#">Coates et al. 1999</a> ).....	9
Figure 5: Decay of secondary applied magnetic field to the initial magnetic field ( <a href="#">Coates et al. 1999</a> ).....	10
Figure 6: Schematic of the CPMG sequence ( <a href="#">Coates et al. 1999</a> ).....	11
Figure 7: Hydrogen nuclei and magnetic fields in a fluid sample without application of an external magnetic field ( <a href="#">Coates et al. 1999</a> ).....	11
Figure 8: Fluid detailing based on $T_2$ relaxation for organic-rich shales ( <a href="#">Jiang et al. 2013</a> ).....	14
Figure 9: $T_1$ and $T_2$ dynamics upon changing viscosity of the fluid ( <a href="#">Bloembergen et al. 1948</a> )... ..	17
Figure 10: Scheme for fluids mapping according to M. Fleury ( <a href="#">Fleury and Romero-Sarmiento 2015</a> ).....	18
Figure 11: 2D fluids mapping by ( <a href="#">Kausik et al. 2016</a> ).....	19
Figure 12: Separation of the fluids by (a) ( <a href="#">Rylander 2013</a> ); (b) ( <a href="#">Jiang et al. 2013</a> ).....	19
Figure 13: Different fluid interpretation schemes for $T_1$ - $T_2$ maps.....	21
Figure 14: Proposed directions of the research.....	24
Figure 15: The geographical location of the Bazhenov Formation.....	27
Figure 16: The thin-sections of Bazhenov Formation.....	28
Figure 17: The geographic location of the target Oilfield #6 (modified after ( <a href="#">Kadyrov et al. 2018</a> )).....	29
Figure 18: The identified lithotypes of Domanik deposits (A – micro-clotty limestones with bioclastic detritus; B – bioclastic limestones with detritus particles; C – close- to fine-crystalline limestones with biogenic detritus; D – bioclastic (tentaculitic) limestones, siliceous-carbonaceous; E – micro- to close-crystalline limestone with biogenic detritus; F – tentaculitic carbonaceous silicites). ( <a href="#">Mukhametdinova et al. 2019</a> ).....	30

Figure 19: 3D view photo of the whole core of Domanik Formation ( <a href="#">Mukhametdinova et al. 2020</a> ).....	30
Figure 20: The thin-sections of target heavy-oil carbonate formations.....	31
Figure 21: Location of the Oilfields #7 and #8. ....	32
Figure 22: Location of the samples probing. ....	32
Figure 23: Schematic diagram of the whole-core breakdown into subsamples. ( <a href="#">Mukhametdinova et al. 2020</a> ).....	34
Figure 24: Schematic diagram of the limited core investigation. ( <a href="#">Razavifar et al. 2021</a> ).....	35
Figure 25: Photograph of employed experimental setups. ....	36
Figure 26: Photograph of the NMR setup. ....	37
Figure 27: Identifying the operational fluid volume at LF-NMR.....	40
Figure 28: Workflow A – fast sequence for porosity determination. ....	44
Figure 29: Workflow B. ....	45
Figure 30: Workflow C. ....	45
Figure 31: Workflow D. ....	46
Figure 32: Porosity by NMR at different states of saturation.....	50
Figure 33: Porosity of samples before and after extraction.....	51
Figure 34: Comparison of kerosene and brine-saturated samples.....	51
Figure 35: Two-dimensional map $T_1$ - $T_2$ (from left to right: as-is saturation, saturated with kerosene before extraction, saturated with kerosene after extraction, saturated with brine model), Sample #95.....	53
Figure 36: Variation of $T_2$ relaxation for rock in a different state of saturation. ....	55
Figure 37: Variability of mean NMR porosity values for the Mendym, Domanik, and Sargay horizons of the Domanik oilfield with different fluid saturation (Stage I — samples are not cleaned; Stage II — non-cleaned samples are additionally saturated with decane; Stage III — samples are cleaned and saturated with decane; IV — samples are cleaned and saturated with brine). ( <a href="#">Mukhametdinova et al. 2019</a> ).....	56
Figure 38: $T_1$ - $T_2$ maps for Sample #702: 1) as-received 2) dried and saturated with decane, 3) cleaned and saturated with decane, 4) after repeated cleaning and saturated with brine. ( <a href="#">Mukhametdinova et al. 2019</a> ).....	58
Figure 39: Porosity by NMR for Well #7 (left) and Well #9 (right). ....	60

Figure 40: Comparison of porosity by NMR and GR neutron porosity logging for Well #7 (left) and Well #9 (right). .....	61
Figure 41: LS (left) and NMR porosity (right) crossplots for core plugs showing comparison with <i>a priori</i> data (Mukhametdinova et al. 2020).....	62
Figure 42: NMR vs. PIK-PP (left) and LS (right) comparison (Mukhametdinova et al. 2020)...	63
Figure 43: Comparison of gas (left) and LS (right) vs. NMR for Bazhenov rock samples.....	64
Figure 44: Comparison of LS (left) and gas porosity (PDP) (right) with NMR porosity for carbonate rock samples.....	64
Figure 45: Comparison of incremental (left) and cumulative pore (right) size distribution by NMR (red) and X-ray CT (blue) for carbonate rock sample. ....	65
Figure 46: Normalized (left) and cumulative (right) volume fractions obtained from various techniques (Razavifar et al. 2021). ....	65
Figure 47: Contact angle on the rock surface .....	70
Figure 48: Primary shapes of OM in rock samples by results of thin-section microscopy and SEM (arrows indicate the OM inclusions). (Mukhametdinova et al. 2020).....	72
Figure 49: Wettability determination by different methods (Mukhametdinova et al. 2020).....	73
Figure 50: Crossplots showing correlations of TOC vs. (a) WI adsorption; (b) WI NMR; (c) contact angle in as-received state; (d) contact angle for extracted rock with an indication of the lithotype (Mukhametdinova et al. 2020). ....	76
Figure 51: Combination of results by different methods over the target section (Mukhametdinova et al. 2020).....	77
Figure 52: Wettability determination by different methods (Mukhametdinova et al. 2020).....	78
Figure 53: Interpretation scheme by different NMR research groups. ....	81
Figure 54: Summary of all map layers. ....	82
Figure 55: Interpretation scheme by Li et al. (2020). Region 1 — bitumen & kerogen, Region 2 — adsorbed oil, Region 3 — free oil, Region 4 — structural & adsorbed water, Region 5 — free water. ....	83
Figure 56: The calculated total signal coverage for different schemes for native (left) and water-saturated (right) target rock samples. ....	84
Figure 57: Comparison of selected fluid categories with petrophysical references. Dashed horizontal lines indicate the corresponding (by color) petrophysical reference values.....	86
Figure 58: Comparison of total signal for Li et al. (2018) and Li et al. (2020) schemes. ....	87

Figure 59: Consecutive modifications of the Li, Jiang et al. (2020) interpretation scheme. Region 1 — bitumen & kerogen & OH, Region 2 — adsorbed oil, Region 3 — free oil, Region 4 — structural & adsorbed water, Region 5 — free water, Region 6 — free water in large pores.....	89
Figure 60: Determination of the cumulative intensity of the signals assigned to the regions of the modified scheme for CH1, B2, and S3, respectively.....	90
Figure 61: Example of zones allocation in $T_1$ - $T_2$ interpretation. ....	91
Figure 62: Fluid saturations of the target rock samples in a fully saturated state: CH1 (left), B2 (center), and S3 (right). ....	92
Figure 63: A fluoroplastic container (core holder) for NMR studies of permafrost samples.....	98
Figure 64: One-dimensional $T_2$ profile of the liquid phase distribution over the height of the soil sample in the thaw (left) and frozen (right) states. Red dashed lines indicate the sample direction; the red area corresponds to the central part of the sample.....	99
Figure 65: Change in the content of unfrozen water in medium-fine-grained sand with different salinity ( $D_{sal}$ , %). ....	101
Figure 66: Change in the content of unfrozen water in sandy loam ( $D_{sal}$ , 0.26%). ....	102
Figure 67: Change in the content of unfrozen water in polymineral clay. ....	102
Figure 68: Change in the content of unfrozen water in the loam sample — hysteresis loop for NMR results. ....	103
Figure 69: Change in the content of unfrozen water in complex polymineral clay (75% sand + 20% silt + 5% montmorillonite clay). ....	103
Figure 70: High-pressure cell (a) and schematic of sample location (b): 1—high-pressure NMR cell body; 2—power and data acquisition connectors; 3—handles; 4—confining pressure supply line; 5—pore pressure line (gas); 6—manometer and nipple for air purge; 7—upper flange; 8—core holder; 9—test sample; 10—confining fluid FC-40; 11—lower flange; 12—nipple for confining fluid. ....	105
Figure 71: Scheme of the core holder with a soil sample. 1—gas supply line; 2— a thermoshrinkable tube; 3—fluoroplastic insert; 4—soil sample; 6—gasket made of synthetic fabric; 7— mesh gasket (mesh size 0.2 mm); 8— O-rings. ....	106
Figure 72: High-pressure cell installed in the climate chamber, with a connected plunger for supplying confining pressure. 1—Isco 260D piston pump; 2—confining system; 3—Binder MK-240 climatic chamber; 4—a high-pressure NMR cell with a soil sample. ....	107
Figure 73: Manufactured high-pressure NMR cell for gas–pressure measurements.....	108
Figure 74: The effect of external pressure on the change of unfrozen water ( $\Delta W_{uf}$ , %) in frozen fine-grained quartz sand at $-5^\circ\text{C}$ . ....	110
Figure 75: The effect of external pressure on the change in the amount of unfrozen water ( $\Delta W_{uf}$ , %) in frozen polymineral clay at $-5^\circ\text{C}$ . ....	111

Figure 76: The sequence of the diffusion process: a) and b) sample preparation using a heat-shrink sleeve; c) saturation of samples with water; d) placing water-saturated samples in a container with heavy water.....	116
Figure 77: Schematic diagram of the core placement in the HPHT cell. ....	117
Figure 78: Hydraulic scheme of the experimental NMR HPHT setup.....	117
Figure 79: Change in the H <sub>2</sub> O saturation during diffusion.....	119
Figure 80: The saturation profile of Sample #430 after two weeks of diffusion.....	120
Figure 81: Pore size distribution before and after two weeks of the experiment, Sample #302.	120
Figure 82: Pore size distribution before and after two weeks of the experiment, Sample #420.	121
Figure 83: Pore size distribution before and after two weeks of the experiment, Sample #430.	121
Figure 84: Saturation profiles for Sample B1 recorded by NMR first 24 h with a 30 min leg (left); in 72 h period with 24 h leg (right).....	122
Figure 85: CO <sub>2</sub> phase diagram. ....	123
Figure 86: Change of NMR saturation profiles for Sample B1 (left) first 24 h of profiling; (right) first 3 h (normalized to initial saturation profile). ....	124
Figure 87: Normalized saturation profiles for Sample C2. ....	126
Figure 88: Location of the analyzed samples in the combustion tube (Modified after <a href="#">Bondarenko 2018</a> ). Zone numeration corresponds to the CT section numbers. ....	131
Figure 89: Photographs of cylindrical samples after the combustion tube experiment (upper left corner — sample id; lower right corner — tube section) (modified after <a href="#">Bondarenko 2018</a> )..	133
Figure 90: Change in gas porosity before and after the combustion ( <a href="#">Mukhametdinova et al. 2020</a> ). ....	134
Figure 91: $T_1$ - $T_2$ map studies, Sample n5 in (a) as-received state; (b) dried state; (c) decane-saturated state; (d) brine-resaturated state. ( <a href="#">Mukhametdinova et al. 2020</a> ).....	136
Figure 92: NMR analysis of Sample #16: (a) $T_2$ relaxation before (blue) and after CT (red); (b) $T_1$ - $T_2$ map for as-received sample; (c) saturation profiles before (blue) and after CT (red); (d) $T_1$ - $T_2$ map for the burnt sample. ( <a href="#">Mukhametdinova et al. 2020</a> ).....	137
Figure 93: Change in the fluid saturation by NMR before and after the combustion. ( <a href="#">Mukhametdinova et al. 2020</a> ) .....	138
Figure 94: Pore size distribution for Samples (a) #2 (b) #12. ( <a href="#">Mukhametdinova et al. 2020</a> )....	139
Figure 95: Crossplot of (a) porosity by gas; (b) residual saturation by NMR; and (c) residual TOC vs. temperature. Triangle-shaped symbols indicate the measured parameter before CT. ( <a href="#">Mukhametdinova et al. 2020</a> ) .....	143

Figure 96: Porosity (left) and permeability (right) of target collection. ....	145
Figure 97: Photograph of the MPCT setup ( <i>photo credentials: archive of Skoltech photo collection</i> ).....	146
Figure 98: Scheme of combustion tube packing. ....	146
Figure 99: Porosity (left) and permeability of samples (right) before and after CT.....	147
Figure 100: Photographs of the rock samples before and after CT. ....	148
Figure 101: 3D X-Ray CT visualization of the rock porous space before (left) and after the combustion test (right).....	149
Figure 102: Pore size distribution by NMR. ....	149
Figure 103: $T_2$ relaxation curves, Sample #7 (left); (b) Sample #14 (right). ....	151
Figure 104: Two-dimensional maps $T_1$ - $T_2$ (a) before and (b) after the experiment in the CT, Sample #7. The color scale for samples after CT is adjusted to detalize the fluid categories.....	152

## ACKNOWLEDGMENTS

I am grateful to the amazing team who guided and supported me throughout my study. First, I would like to express my great appreciation to my research supervisor, Associate Professor Alexey Cheremisin, for his patient guidance, advice, and useful critiques that he has provided throughout my MSc. and Ph.D. studies. Second, I would also like to thank my Ph.D. committee members – Professor Mikhail Spasennykh, Dr. Elena Kozlova for their advice and assistance, and support in doing the research. Third, I would like to thank my mentors and advisors – Dr. Boris Bukhanov, Dr. Natalia Bogdanovich, and Dr. Andrey Kazak, for their academic and personal guidance. Their help and contribution are much appreciated.

In addition to my supervisory team, I would like to thank Jury committee members — Professor Dimitri Pissarenko, Professor Yury Popov, Professor Sergey Stanchits, Professor Dmitry Koroteev, Professor Sudarshan Mehta, and Professor Reza Rezaee for their thoughtful comments and recommendations on how to improve my work.

My grateful thanks are also extended to Dr. Evgeny Popov, Dr. Evgeny Chuvilin, Mr. Vladimir Stukachev, and Mr. Pavel Grishin for their guidance and help in doing the experimental part of the thesis. I would also like to extend my thanks to the researchers, engineers, and technicians of the laboratory of the Center for Hydrocarbon Recovery department — Messrs. Alexander Borisov, Alexander Burukhin, Alexander Mishin, Sergey Grebenkin, and Philipp Denisenko for their help in conducting the experiments. I also thank the researchers and staff members of Arktik-Gers for help with XRD analysis, adsorption measurements, and thin-sections preparation.

I am thankful to my fellow colleagues and Skoltech friends who shared this experience with me — Dr. Lyudmila Khakimova, Mrs. Alina Sabitova, Mrs. Anastasia Gabova, Dr. Aysylu Askarova, Dr. Anastasia Ivanova, Mr. Evgeny Shilov, Mr. Strahinja Markovic, Ms. Aleksandra Scerbakova, Mr. Tagir Karamov, and many others. My thanks are shared with all my friends around the world who made this journey possible and always supported me in challenging moments.

I would also like to express my gratitude to the members of the Education and Admission Offices, Administration team of CHR at Skoltech for the help and support they provided me during the last six years.

I am grateful to my parents, sister, and family members for their support, love, and encouragement throughout my studies.

I express gratitude to our industrial partners and colleagues from Lukoil, Zarubezhneft, Rosneft, and Gazprom Neft companies for providing core material. I also thank the Russian Science Foundation for the support of the research (grant No. 18-77-10063) and the Ministry of Science and Higher Education of the Russian Federation (grants RFMEFI58114X0008 and No. 075-10-2020-119).

# CHAPTER 1

## INTRODUCTION

### **1.1 Defining Rock Saturation in Petrophysical Research**

Worldwide, oil reserves estimated in traditional reservoirs are in a consistent decline while triggering complications and enhancements of technologies of hydrocarbon (HC) exploration and characterization. One of the promising solutions to maintain production at current levels is the development of hard-to-recover reserves, including low-permeability (tight) organic-rich and heavy-oil carbonate reservoirs (Zhang et al. 2015, Sheng 2017). Unconventional reserves are of strategic importance to replenish the resource base in Russia and over the world. Their successful development can play a crucial role in increasing oil production and repeatedly compensate for the decline in production from depleted traditional reservoirs (Lopatin et al. 2003, EIA 2013, Ahmed and Nathan 2016).

The correct determination of reservoir properties remains challenging for oil and gas companies despite an increase in their interest in developing such formations and deposits (1985, Ahr 2008, Burchette 2012). Both porosity and permeability contribute significantly to resource assessment and reserves estimation of a target asset.

Tight organic-rich and carbonate rocks feature low porosity and permeability, the absence of structural and stratigraphic control of the distribution of oil-containing intervals, which does not allow distinguishing them from well-logging data. All mentioned factors lead to a low oil recovery factor (< 10–20%). Therefore, one critical task is the development of methods for estimating the reservoir properties of tight rocks with a higher degree of reliability.

Conventional methods for petrophysical core analysis were established during the 1970–1980s when the development of conventional reserves had reached its peak Roehl and Choquette (1985). Notably, the measured porosity varied in the range of 10–30% and permeability 10–200 mD.

The main obstacles to the proper determination of the reservoir properties (porosity and permeability) of tight reservoir rocks are their low porosity (< 3–5%), and low permeability (< 1 mD), as well as and a high degree of heterogeneity of void space structure. However, conventional laboratory methods were developed for the characterization of conventional highly porous and permeable reservoir rocks, such as well-sorted sandstones. Complex reservoirs reside at the edge of their operating envelope in terms of porosity and permeability [API \(1998\)](#). For example, conventional Dean-Stark extraction tends to overestimate water saturation in tight reservoirs, and reliable results require new approaches [\(Kazak and Kazak 2019\)](#). Indeed, conventional porosity techniques may overestimate and implicitly add uncertainty to the results of both geological and hydrodynamic modeling of field-scale processes [\(Goral et al. 2019\)](#).

At the current stage, laboratory petrophysical methods targeting unconventional reservoirs fall into two groups. The first group includes bulk methods, delivering a single integral property value (the result of determination) for a target rock sample. The second group improves the understanding of bulk values by direct (explicit) imaging of the void space structure, as well as mineral and organic matrix.

The petrophysical properties of the target rocks suggest a complicated inhomogeneous microstructure. The dimensions of voids fall below the micrometer scale. They require novel methods for evaluating the reservoir properties and high-resolution imaging, which obtains three-dimensional (3D) images of the void space structure with resolution up to 50 nm [\(Nelson 2009, Kazak et al. 2018\)](#) (Figure 1).

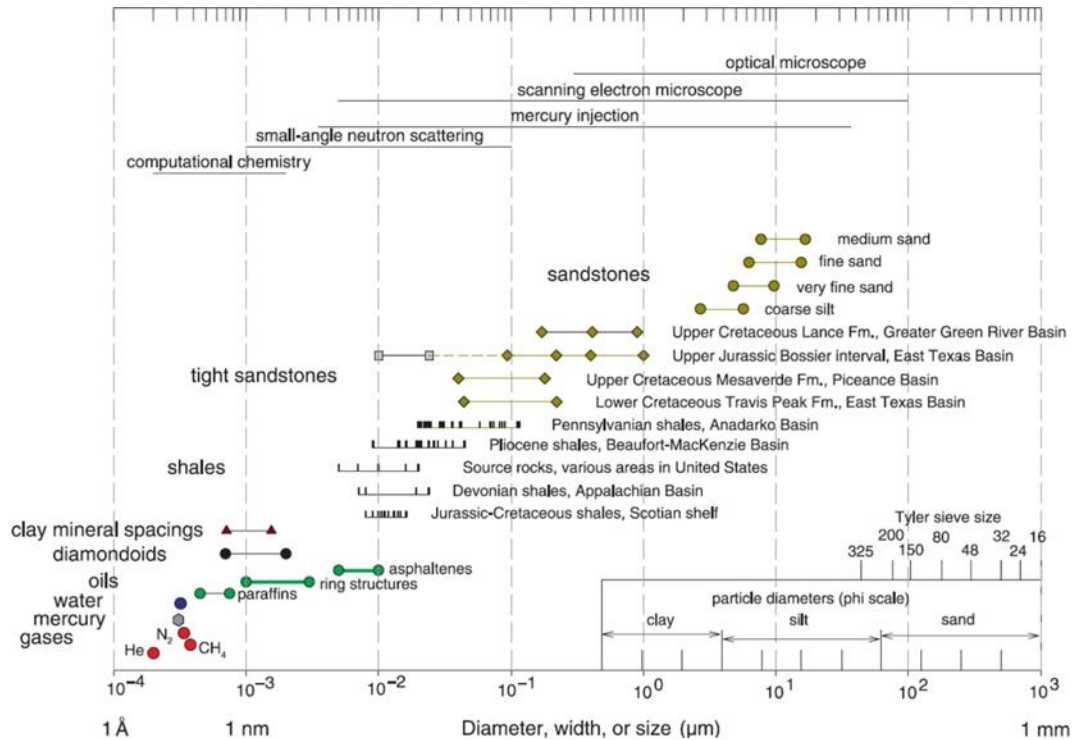


Figure 1: Pore throat distribution according to Nelson (2009).

Multiple publications characterize the porosity (Saidian et al. 2014, Labani and Rezaee 2015), the porous structure, and permeability of tight sands, shales, and carbonates (Moghadam and Chalaturnyk 2015, Profice et al. 2016, Sander et al. 2017). Based on published literature, we summarized conventional methods (basic core analysis) and advanced experimental methods (widely applied for tight rock characterization) (Table 1).

Table 1. Methods applied for reservoir properties laboratory assessment

Measured Parameter	Conventional Method	Advanced Method
Porosity	Gravimetric or Liquid	Nuclear Magnetic Resonance (NMR)
	Saturation (LS)	Mercury Injection Capillary Pressure (MICP)
	Pulse-Decay (PDP)	Gas adsorption
Permeability	Steady-State	Pulse-Decay Permeametry (PDP)
	Pulse-Decay (PDP)	Pseudo-Steady-State (PSS)
		Oscillating Pulse Technique (OPT)
		Gas Research Institute (GRI) method
Void Space Structure	Thin-sections	Mercury Injection Capillary Pressure (MICP)

Measured Parameter	Conventional Method	Advanced Method
		X-ray Computed Tomography (CT)
		Scanning Electron Microscopy (SEM)
		Low-Temperature Nitrogen Adsorption (LTNA)

The characterization of a liquid saturation in the organic-rich rocks is another important factor in assessing the resources and potential oil recovery. Similar to reservoir properties, standard laboratory methods are not able to characterize the saturation in tight shale rocks. In addition to low values of porosity and permeability, the high content of organic components, including a solid phase insoluble in organic solvents (kerogen), and pores of nano-size complicate the application of most experimental techniques. Liquid saturation in shales can be measured by a variety of methods, Figure 2:

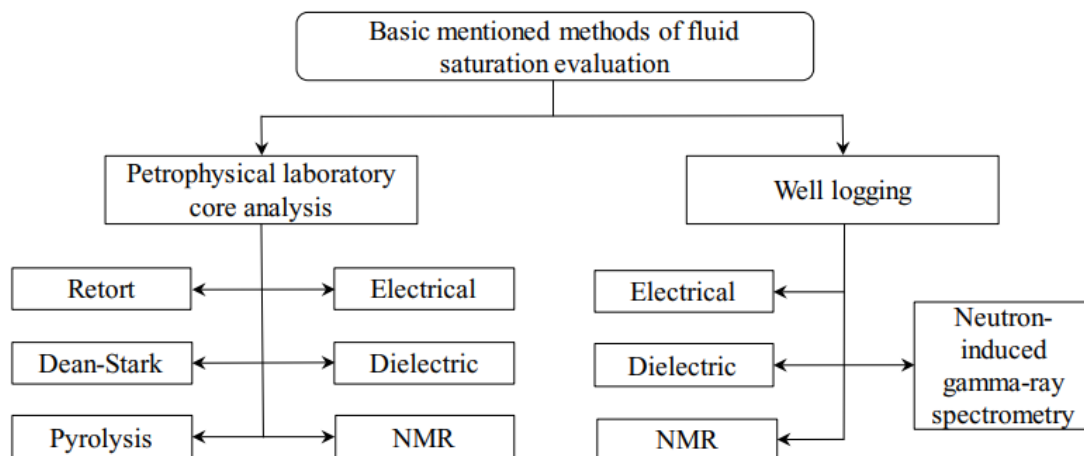


Figure 2: Methods used for saturation evaluation in organic-rich shales (Nikolaev and Kazak 2019).

For example, NMR logging and benchtop NMR has proven to be one of the most reliable methods for characterizing shale saturation (Liu et al. 2020). Routine and special core analysis workflows for shale rock samples employ NMR relaxometry at commonly used frequencies of 2–20 MHz (Yuan and Rezaee 2019). Short echo times allow registering components with short relaxation  $T_2$  times reaching nanopores and even rock matrix (Krzyżak et al. 2020).

Among the variety of methods, NMR has several advantages. NMR is one of the methods for non-invasive bulk fluid saturation measurement for organic-rich low-permeability reservoirs. A combination of the methods (NMR and centrifuge, pyrolysis) expands the characteristics of the core defined at laboratory scale. It can be compared with logging data and applied as input data in reservoir modeling and simulation or can be applied for studies under formation conditions. What is also of great importance, application of a low magnetic field reduces the impact of paramagnetic impurities on the measured/registered signal by reducing the effect of diffusion on measured  $T_2$  distributions and yields undistorted  $T_2$  distributions, reflecting accurate pore sizes (Washburn et al. 2008, Mitchell et al. 2013).

To summarize the discussion on methods used for characterization of reservoir properties, including the rock porosity, liquid saturation, and porous structure, a comparison of the available techniques is presented in Table 2. All advantages and disadvantages of the methods are derived from published papers and book chapters.

Table 2. Comparison of different laboratory methods

<b>Method</b>	<b>Advantages</b>	<b>Disadvantages</b>	<b>Summary</b>
Gas porosimetry	Speed and ease of use Non-invasive	The dependence of the results on sample preparation  The effect of cleaning on the results	Recommended for initial characterizing the core
NMR Relaxometry	Integral core characteristic  Advanced spatial tests  Non-invasiveness	Limited resolution  Test duration	Recommended for qualitative and quantitative characteristics of rocks
X-ray Computed Tomography	3D and 2D visualization  Quick testing	Limited resolution  Not applicable for shales	Recommended as a special tool
Low-Temperature Nitrogen Adsorption (LTNA)	Provides size of the pore and specific surface	Difficult sample preparation	Recommended as a special tool

Method	Advantages	Disadvantages	Summary
	Precise measurement		
Advanced gas permeameter (Darcypress, SMP)	A large number of samples in a series of measurements Ease of interpretation	Permeability and grain size are provided	Recommended for low-permeability rock studies
Centrifuging based methods	The standard method with a variety of provided data (RP, irreducible water saturation, etc.)	Not applicable for shale samples due to low permeability	Recommended in complex
Advanced microscopy (SEM, FIB-SEM)	Precise measurements and high resolution	Cost of the experiment, limited number of tests, sample preparation	Recommended as a special tool

This research covers the application of NMR in core analysis methods for the characterization of unconventional reservoirs. NMR studies allow us to describe the hydrocarbon (HC) deposits at an early stage of exploration and provide important input for further modeling. Defined parameters include but are not limited to reservoir properties, namely porosity and pore size distribution (PSD), rock wettability, fluid saturation, etc. Laboratory NMR core analysis can be an excellent replacement for many standard laboratory tests in cases of limited resources (time and core material) and provide a wide range of information on core analysis.

Currently, many industrial service companies offer special core analysis using NMR. Modern benchtop NMR core analyzers can measure geological core samples to determine critical pore and fluid properties and received data for NMR logging calibration using  $T_2$  relaxation cut-offs and permeability relationships for downhole logging calibration. Widely-spread is a low-field NMR relaxometry (LF-NMR) device that provides core-to-log calibration and can be used in a complex with a centrifuge to additionally determine the capillary pressure and relative permeability curves. The latest NMR analyzer is capable of measuring at the reservoir and ambient temperatures and reservoir pressure.

## 1.2 Review on NMR in Petrophysics

### 1.2.1 Physical Principles of NMR Relaxometry

NMR measurements can be performed on any nucleus that has an odd number of protons or neutrons, such as the nucleus of hydrogen ( $^1\text{H}$ ), carbon ( $^{13}\text{C}$ ), and sodium ( $^{23}\text{Na}$ ). Hydrogen, which has only one proton and not a single neutron, has been chosen as the unconditional object of NMR measurements in geophysical research.

The nucleus of a hydrogen atom is a positively charged proton with a kinetic moment or spin. A spinning proton is an ordinary electrical circuit that creates a magnetic field (or magnetic moment). Consequently, the hydrogen nucleus can be considered a kind of magnet, the axis of which is located along the spin axis of the nucleus (Figure 3).

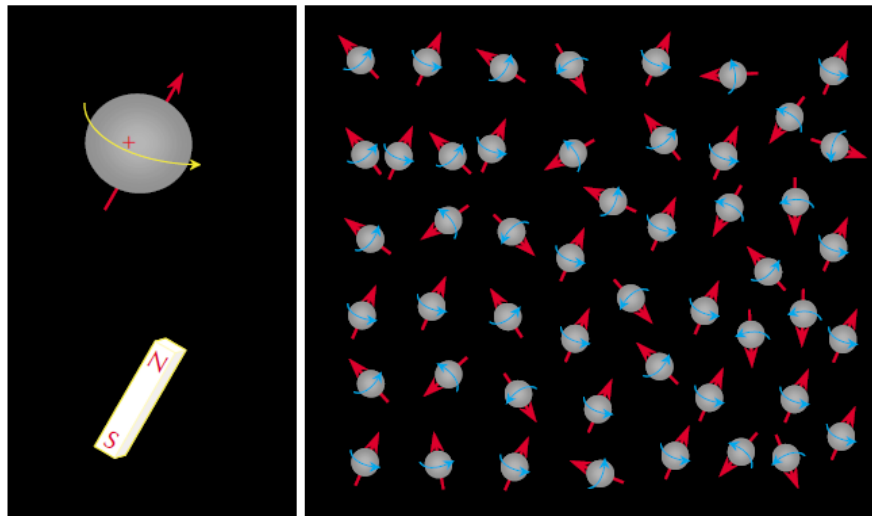


Figure 3: Hydrogen nuclei and magnetic fields in a fluid sample without application of an external magnetic field (Coates et al. 1999).

The permanent magnets of a nuclear magnetic relaxometer create a uniform magnetic field. This field, acting on the hydrogen nuclei, aligns the chaotically located magnetic moments of protons in the direction of the external magnetic field, which is expressed in the general nuclear magnetization of the formation fluids. The macroscopic magnetization of the studied system (porous media) is defined as the resulting magnetic moment of a particular volume. In other words, the nuclear magnetization of the system is primarily determined by the number of magnetized hydrogen nuclei, *i.e.* the amount of hydrogen-containing liquids

(water, oil, gas). The analytical form of the dependence of the nuclear magnetization, and, accordingly, of the resulting NMR signal is described by the Curie law for paramagnets:

$$M=N\frac{\mu^2B}{3k_B T}, \quad (1)$$

where  $N$  is the number of hydrogen atoms,  $\mu$  is the magnetic moment of the nucleus,  $B$  is the induction of the external magnetic field,  $k_B$  is the Boltzmann constant,  $T$  is the absolute temperature.

$$M(t)=M_0(1-e^{-t/T_1}), \quad (2)$$

where  $t$  is the time of the magnetic field  $B$  on protons,  $M(t)$  is the magnitude of the magnetization at time  $t$ ,  $M_0$  is the final and maximum magnitude of magnetization,  $T_1$  is the longitudinal relaxation time characteristic for each saturating liquid, as well as pores containing them (Figure 4).

$T_1$  time can be explained by the following mechanisms:

$$\frac{1}{T_1} = \frac{1}{T_{1\text{bulk}}} + \frac{1}{T_{1\text{surface}}}, \quad (3)$$

where  $T_1$  – is the recorded longitudinal time of relaxation,  $T_{1\text{bulk}}$  – relaxation of bulk fluid, and  $T_{1\text{surface}}$  – relaxation of the fluid in contact with the rock-fluid interface.

In practice, the longitudinal relaxation times are rarely measured; this is associated with significant time costs. On the contrary, measurements of the transverse  $T_2$  relaxation time are performed several times faster.

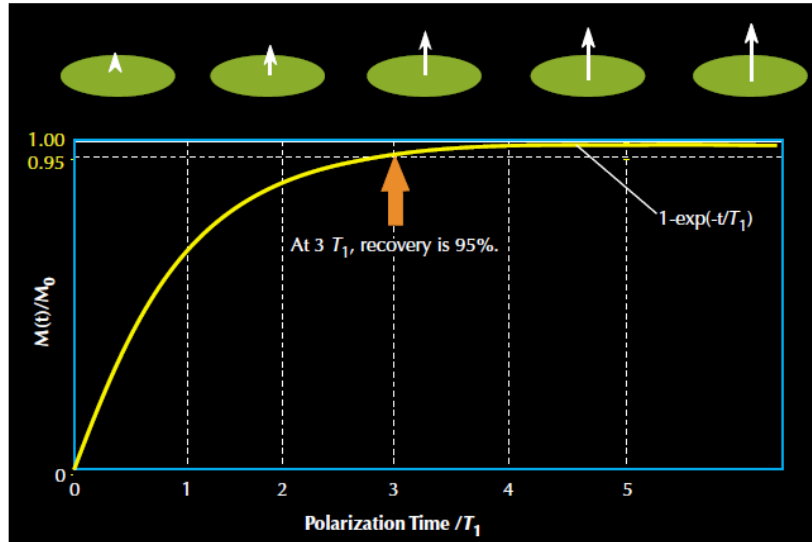


Figure 4: Polarization of hydrogen nuclei to the longitudinal direction under a static magnetic field (Coates et al. 1999).

Most petrophysical properties of the rock are defined by the results of the determination of transverse relaxation time ( $T_2$ ) of hydrogen nuclei in the sample.  $T_2$  relaxation and the pore size distribution are calculated from the results of  $T_2$  relaxation time. The secondary magnetic field ( $B_1$ ) is applied temporarily in the perpendicular ( $90^\circ$ ) or antiparallel ( $180^\circ$ ) direction of the initial static field. After the polarization to the static field direction, the hydrogen nuclei realign to a stronger field. The decay from this secondarily applied magnetic field to original polarization is reasoned by many fluid and fluid-pore interactions. By measuring the decay of this secondary applied magnetism to the initial static applied magnetic field, the  $T_2$  of the sample is determined, as demonstrated in Figure 5.

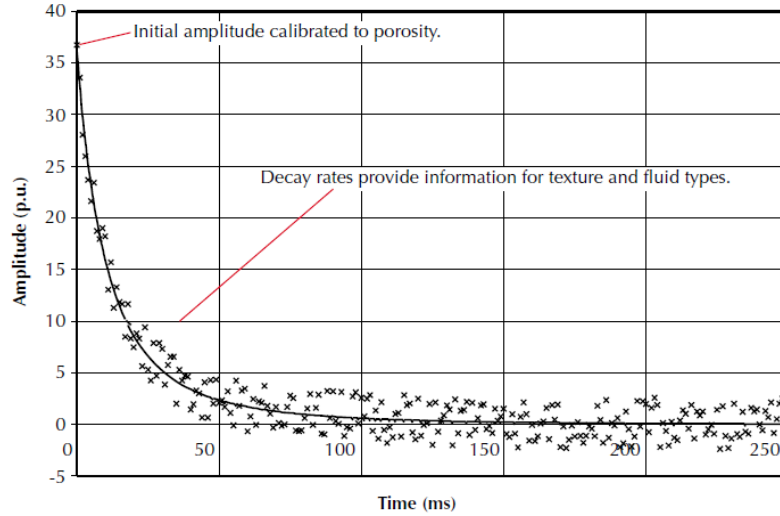


Figure 5: Decay of secondary applied magnetic field to the initial magnetic field (Coates et al. 1999).

The transverse relaxation is controlled by three different mechanisms. The  $T_2$  relaxation time is described by the following expressions:

$$\frac{1}{T_2} = \frac{1}{T_{2b}} + \frac{1}{T_{2s}} + \frac{1}{T_{2d}} \quad (4)$$

$$\frac{1}{T_{2s}} = \rho \left( \frac{S}{V} \right)_{\text{pore}} \quad (5)$$

where  $T_2$  is the transverse relaxation time of the pore fluid;  $T_{2b}$  is the relaxation time  $T_2$  of the pore fluid;  $T_{2s}$  — pore fluid relaxation time associated with surface relaxation;  $T_{2d}$  is the relaxation time  $T_2$  of the pore fluid caused by diffusion in a gradient magnetic field;  $\rho$  — relaxation activity of the rock or surface relaxivity ( $T_2$  relaxation force on grain surfaces);  $(S/V)_{\text{pore}}$  — the ratio of pore surface size to pore volume (specific surface).

Under conditions of significant inhomogeneity of the constant field, the  $T_2$  time can become so short that registration of the free precession signal will be difficult or impossible due to the very rapid signal decay. Under such conditions, the spin-echo method, or the modified and improved Carr-Purcell-Meiboom-Gill (CPMG) method, is used. The essence of the method consists in creating a sequence of high-frequency pulses of a certain duration, because of which a series of spin-echo signals are formed. The recorded relaxation curve, respectively, is the envelope of the amplitudes of the spin-echo signals (Figure 6).

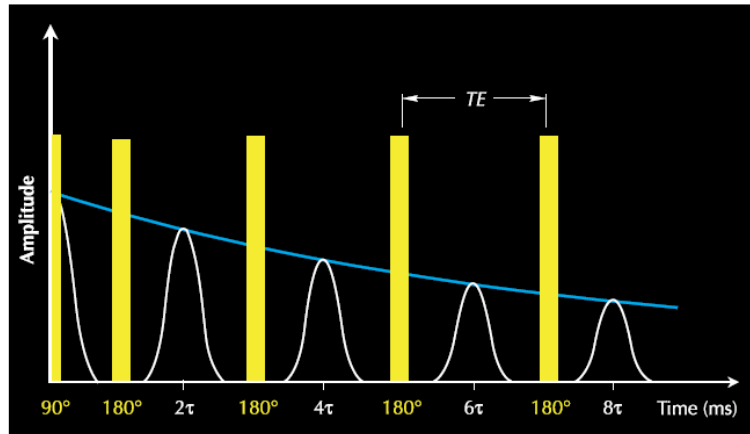


Figure 6: Schematic of the CPMG sequence (Coates et al. 1999).

As explained earlier, the NMR signal will depend on the pore size distribution in the region under study, as well as on its properties. Consequently, taking into account a certain model of the porous structure, one can go from the relaxation times directly to the pore sizes and, accordingly, calculate their size distribution. Unfortunately, the accuracy will depend on the chosen model, as well as on rock physicochemical properties. For instance, for sandstone rocks, the lithological composition is practically homogeneous for pores of different sizes, which doesn't apply to carbonate rocks. In summary, we can say that the relaxation rate will be greater the smaller the pore size (Figure 7).

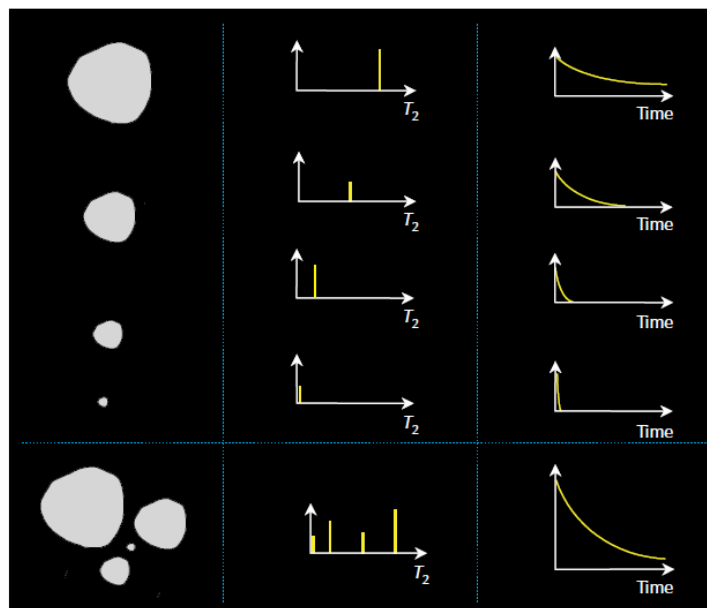


Figure 7: Hydrogen nuclei and magnetic fields in a fluid sample without application of an external magnetic field (Coates et al. 1999).

### 1.2.2 NMR Applications in Shale and Tight Rock Analysis

The NMR studies presented in this work are based on the basic interpretation principles used by NMR specialists in the petrophysical industry (Abragam 1961, Callaghan 1991, Kenyon 1997, Straley et al. 1997).

First of all, the use of NMR relaxometry in the study of low-porous sand and clay rocks should be singled out as a separate group. In the presence of clays or at low porosity, the most commonly used  $T_2$  cut-off values ultimately give inaccurate estimates of permeability due to reservoir heterogeneity. Musu and Widarsono (2007) present the results of NMR measurements on Tilrawarra sands from three wells located in the Cooper Basin, South Australia. The study reports the inappropriateness of using a  $T_2$  cut-off to determine the permeability and residual water in the samples. The Jian-Ping research team from China utilizes NMR relaxometry in constructing a void space model for low-porous and low-permeability sediments in the Dongying area (Jian-Ping et al. 2016). The authors of another work (Marschall et al. 1995) note the need for the integrated use of NMR and mercury porosimetry in order to assess the pore size distribution and capillary pressure and also offer an improved methodology for permeability recalculation.

Westphal et al. (2005) describe in detail the determination of bound and free fluids in source rocks using NMR analysis and computed tomography. The authors showed that the  $T_{2gr}$  cut-off values for mobile and residual fluids vary in carbonates. It has been proven that NMR analysis can be used to estimate the number of free/mobile fluids, as well as to provide information about pore connectivity in shale rocks. The authors argue that the results of NMR, CT, and gas porosimetry give similar estimates of the porosity of the rocks.

Singer (Singer 2013) investigated pore sizes, fluid saturation, wettability, and hydrocarbon content, combining NMR data and experimental studies of core in the lower Eagle Ford. This work is one of a series of works on NMR analysis of shale devoted to comparing the results of porosity obtained by NMR relaxometry with the values of standard laboratory tests and visualizing techniques (X-Ray tomography, Scanning Electron Microscopy, etc.).

A number of scientific works ([Mai and Kantzas 2002](#), [Westphal et al. 2005](#), [Jiang et al. 2013](#)) are devoted to the study of the relationship between permeability and the  $T_2$  relaxation time for various types of rocks. The absolute permeability calculation based on the model that relates the permeability to the results of NMR is complicated for organic-rich rocks. This is due to inhomogeneous petrophysical properties and the nonlinear dependence of permeability on pores in the samples. There are two main approaches to an approximate permeability assessment based on  $T_2$  relaxation time — the Schlumberger-Doll-Research (SDR) model and the Timur-Coates model:

Coates model:

$$K_{\text{coates}} = \left[ \left( \frac{\varphi}{C} \right) \frac{\text{FFI}}{\text{BVI}} \right]^2 \quad (6)$$

SDR model or mean  $T_{2gm}$  model:

$$K_{\text{sdr}} = C * T_{2gm}^2 * \varphi^4 \quad (7)$$

where  $\varphi$  is the effective NMR porosity,  $T_{2gm}$  is the geometric mean time  $T_2$ ,  $\text{FFI}$ ,  $\text{BVI}$  is the number of free (free fluid index or FFI) and bound fluids (BVI) in the sample,  $C$  is a numerical coefficient.

An important factor in the study of the shale porous structure by NMR is the  $T_2$  cut-off time determination, which allows one to estimate the amount of bound and free fluids in the sample. [Rylander \(2013\)](#) presents an intensive study of samples of the Eagle Ford field using a variety of laboratory methods — NMR, mercury porosimetry, and SEM. The obtained pore distribution data are compared to validate the  $T_2$  cut-off. A general scheme for classifying fluid types in oil shales was proposed by the [Jiang et al. \(2013\)](#) in Figure 8

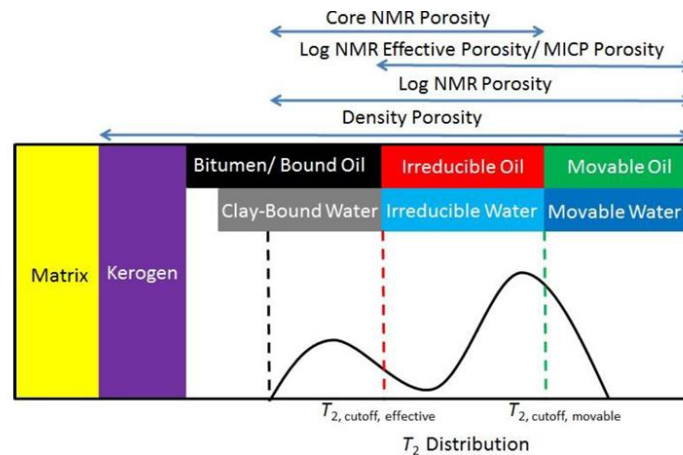


Figure 8: Fluid detailing based on  $T_2$  relaxation for organic-rich shales (Jiang et al. 2013).

There are multiple NMR applications in the field of petrophysics, geological and geochemical research. For example, Nes et al. (1993) presented NMR measurements on three different shales from the North Sea. They show that NMR is a fast, non-destructive analytical tool, which can measure the effective porosity of low-permeable shales. An NMR is an extensive tool in the study of shale wettability and effective surface relaxivity (Sulucarnain et al. 2012). Assuming the throats and bodies are equivalent, in this work, a scaling factor was used to match the NMR spectra and the MICP (Mercury injection capillary pressure) curves to estimate the shale wettability and effective surface relaxivity.

Bryan et al. (2005) describe a technique for using low-frequency NMR as a tool for measuring oil viscosity. The authors have developed a model that can estimate the viscosity by NMR results for a wide range of samples from different fields in Alberta. The model can be adapted for individual fields to build a correlation of viscosity values with temperature.

A study of shale wettability can be conducted using NMR to monitor the sequential imbibition of brine and oil (Oduşina et al. 2011). Authors indicate that fluids, brine, and oil are imbibed in shales so that NMR can be used to quantify the amount of imbibed fluids. Gravimetric measurements quantitatively support the NMR measurements. Observed relaxation times suggest both the brine and dodecane are having surface relaxation, *i.e.* they are wetting the shales.

[Borisenko et al. \(2017\)](#) used NMR to determine the residual water saturation in the deposits of the Timan-Pechora region in combination with other methods — the method of a semipermeable membrane and ultracentrifugation. Each of the three methods is based on different physical principles. Studies of hydrophobic carbonate deposits suggest that both residual water and residual oil may occupy the same porous system.

In continuation to the previous article, the authors of [\(Bogdanovich et al. 2017\)](#) describe a methodology for determining the wettability using a laboratory NMR device. The wettability is a crucial factor for shale oil and gas-bearing rocks since these rocks often have mixed wettability. A scientific group led by [Zhang et al. \(2014\)](#) was engaged in determining the nature of wettability for the Eagle Ford formation rock samples. Core samples from three different formations (Mancos, Eagle Ford, and Marcellus) were extracted and re-saturated with water and kerosene; at each stage of the experiment, NMR studies were carried out. Marcellus showed mixed wettability in small pores with a radius of less than 60 nm. The small pores of the Eagle Ford and Mancos samples have been shown to be hydrophilic, while the larger pores in the Eagle Ford and Mancos samples also show a mixed wettability that is close to hydrophilic.

Combined laboratory workflows are used to study capillary pressure, plot relative phase permeability, and estimate pore size ([Green et al. 2008](#), [Green 2009](#), [Green and Veselinovic 2010](#)). For low-permeability rocks, it is especially important due to high pressures in the formation. Also, the two-dimensional NMR maps for determining the fluid saturation of rock samples have become relevant in petrophysical studies of shales. The  $T_1$ - $T_2$  and  $D$ - $T_2$  time maps allow distinguishing between water, oil, and gas signals based on the contrast of  $T_1$  and  $T_2$  relaxation times or diffusion coefficient  $D$  and relaxation time  $T_2$ . A summary of the literature related to fluid interpretation by NMR is introduced in a section below.

### **1.2.3 Fluid Interpretation by NMR**

Bulk  $T_1$  or  $T_2$  NMR measurements, although offering a short turnaround time, do not deliver complete information of the tested sample ([Coates et al. 1999](#)). At the same time, proton populations with similar  $T_2$  relaxation times may originate from water or hydrocarbons. However, even at the same  $T_1$  or  $T_2$ , the  $T_1/T_2$  ratio depends on the binding of the proton

population to the hosting porous space (Bloembergen et al. 1948).  $T_1$ - $T_2$  measurements address these problems and provide much more comprehensive data on fluid saturation (Rylander 2013, Washburn and Birdwell 2013, Fleury 2014).

Previous NMR core research focused mainly on relatively porous and permeable reservoir rock, including sands, sandstones, and carbonates. However, the application of the well-developed NMR interpretation approaches to shale rocks delivers altered reservoir rock properties comparing to that obtained from advanced laboratory studies. Thus, valid interpretation requires adaptation of the traditional interpretation techniques to features of oil and gas shales. Complex reservoir rocks in general and organic rich mudstones in particular typically possess low porosity and permeability, high content of OM, including kerogen (insoluble in organic solvents), and high-carbon bitumen. Moreover, a complex spatial interrelation between the mineral skeleton and organic-matter matrix causes heterogeneity and variability of reservoir surface properties, such as cation exchange capacity (Kazak and Kazak 2020) and wettability (Odusina et al. 2011, Sheng 2018). Conventional approaches based on studying the distributions of the transverse relaxation times  $T_2$  in such objects either do not capitalize on the full potential of the NMR method.

NMR studies of low-permeability rock samples employ NMR  $T_1$ - $T_2$  relaxation time maps heavily. In turn, understanding of  $T_1$ - $T_2$  maps relies on the possible contrast in the spin-lattice relaxation mechanisms  $T_1$  of the structural zones of the rock sample, excellent surface properties, and the type of saturating fluid, attracted special attention in the field. In fundamental theoretical and experimental works of Bloembergen and Purcell, the difference between spin-spin and spin-lattice relaxation of fluids is illustrated in terms of the correlation time of Brownian motion for the first time (Bloembergen et al. 1948). According to the mentioned theory, it is possible to construct analytical dependencies of the longitudinal  $T_1$  and transverse  $T_2$  relaxation times on the fluid viscosity or the size of the molecules (Figure 9). An increase in fluid viscosity is accompanied not only by a change in the  $T_1$  and  $T_2$  relaxation times but also by the ratio of longitudinal relaxation to transverse relaxation times —  $T_1/T_2$ . In other words, the most crucial theoretical prerequisite in the joint interpretation of the longitudinal  $T_1$  time and transverse  $T_2$  time distributions for fluid identification is their ratio.

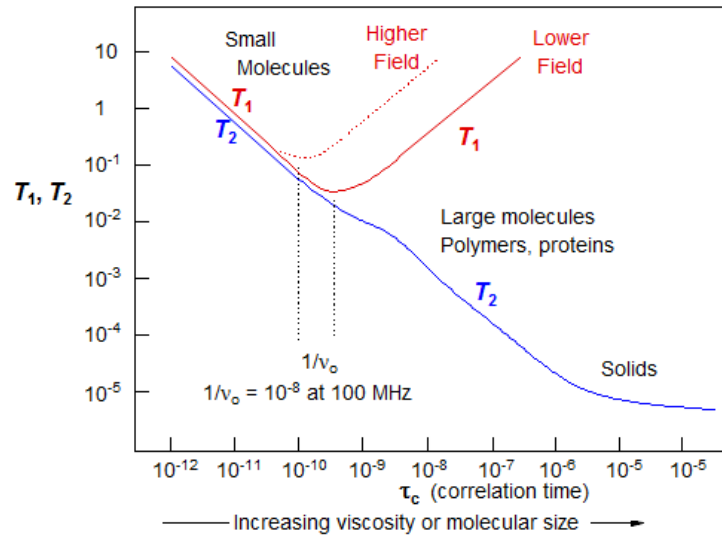


Figure 9:  $T_1$  and  $T_2$  dynamics upon changing viscosity of the fluid (Bloembergen et al. 1948).

Washburn and Birdwell (2013) took the “solid-echo” approach to register fast-relaxing components of hydrocarbon rock components. Rylander (2013) developed the algorithm for studying oil shales on NMR equipment at an operating radiofrequency (RF) of 2-MHz and presented important results Eagle-Ford rock samples. These and other NMR studies and the corresponding interpretation results assume that the  $T_1/T_2$  ratio varies for various structural fluid populations of oil shale rocks. Fleury (2014) was among the first who proposed the empirical basis for interpreting the  $T_1$ - $T_2$  maps recorded using a 20-MHz relaxometer for gas and oil shale samples. Applying a 2-MHz NMR scanner, Habina et al. (2017) characterized the rock components that are specific for oil and gas shales. The  $T_1$ - $T_2$  maps and the  $T_1/T_2$  ratios for smectite, illite, illite-smectite, kaolinite, chlorite, and kerogen samples were used to obtain the individual features.

A qualitative interpretation of the data of  $T_1$ - $T_2$  2D distributions was proposed by Fleury and Romero-Sarmiento (2015). The separation of fluids by the type of water-oil, as well as the degree of connection with a specific geometry of the pore space, are based on the apparent contrast of the  $T_1/T_2$  ratio for different groups of pores. Considering possible variations in the mineralogical composition of the rock skeleton, as well as surface adhesion, it is possible to develop a reliable scheme for isolating both the type of fluid and its commercial potential.

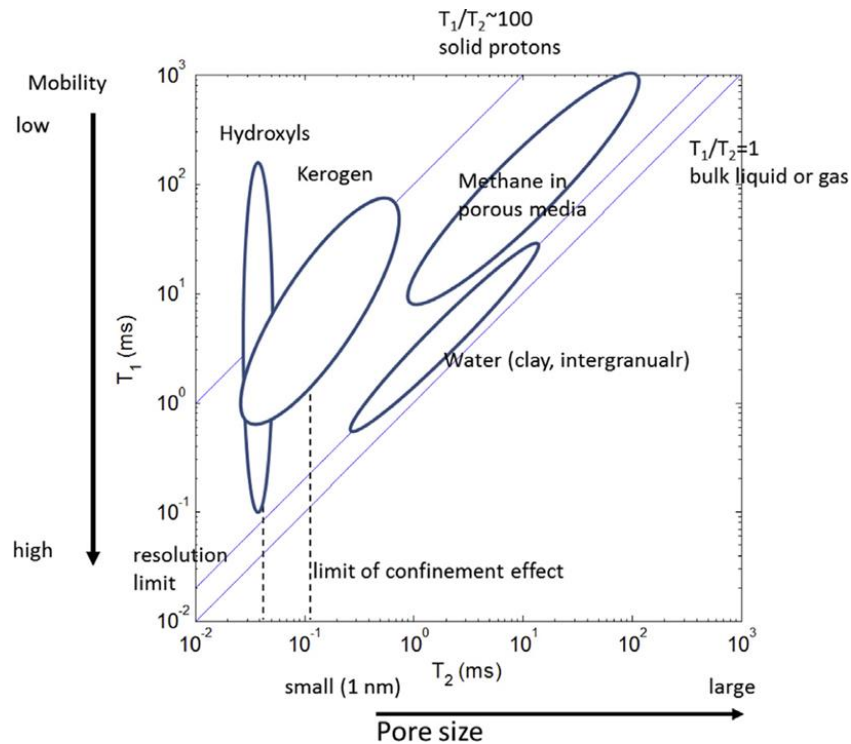


Figure 10: Scheme for fluids mapping according to M. Fleury (Fleury and Romero-Sarmiento 2015).

A continuation of the scheme proposed by M. Fleury for interpreting  $T_1$ - $T_2$  maps was made by Nicot et al. (2015). Their research presents the study of source-rock of the Vaca Muerta deposit, Argentina; moreover, the paper presents comparisons of NMR data obtained on relaxometers with different frequencies of Larmor proton precession — 2 MHz and 23 MHz. Another study of gas and oil low permeability rocks is described in the work of Kausik (2015). In the latter, the author published his version of the scheme for interpreting  $T_1$ - $T_2$  data depending on the type of saturating fluid and the degree of its connection/interaction with pore walls (Figure 11) (Kausik et al. 2016).

The possibilities of  $D$ - $T_2$  or  $D$ - $T_1$  two-dimensional distributions have not been widely used and reported in the literature at present due to the apparent limitations of the diffusion contrast of NMR in the pores of the nanometer and submicron ranges as well as highly viscous hydrocarbons. Therefore, a tool based on a comprehensive analysis of the distributions of  $T_1$  and  $T_2$ , or two-dimensional maps  $T_1$ - $T_2$ , is currently a priority in the study of shale gas and oil reservoir.

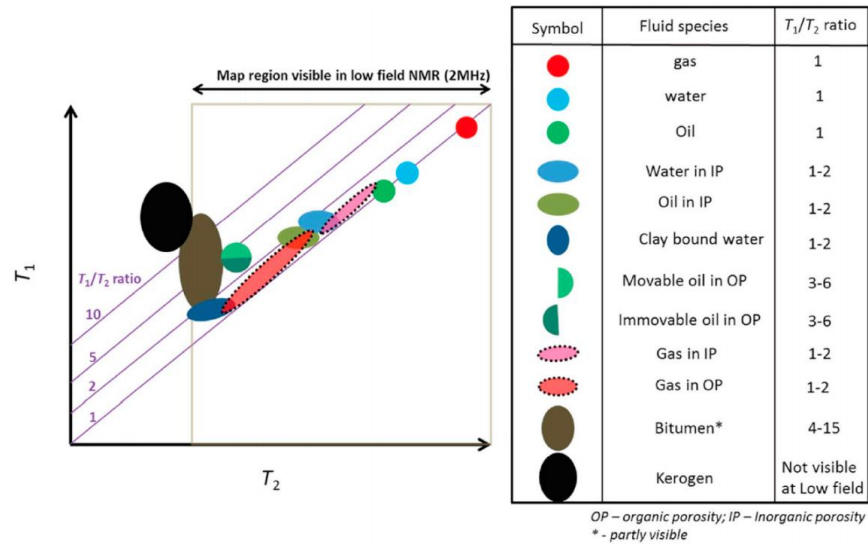


Figure 11: 2D fluids mapping by (Kausik et al. 2016).

The classification of pores by  $T_1$ - $T_2$  maps was also highlighted for samples of shale rocks, taking into account the lithological and petrophysical features of shale rocks. Similar schemes for interpreting  $T_1$ - $T_2$  maps were proposed in the earlier works of Jiang et al. (2013) and Rylander (2013) (Figure 12). In the construction of these diagrams, the results of experiments on samples of the Eagle Ford formation were used; verification and correction of NMR data of relaxometry were carried out using mercury porosimetry and retort tests.

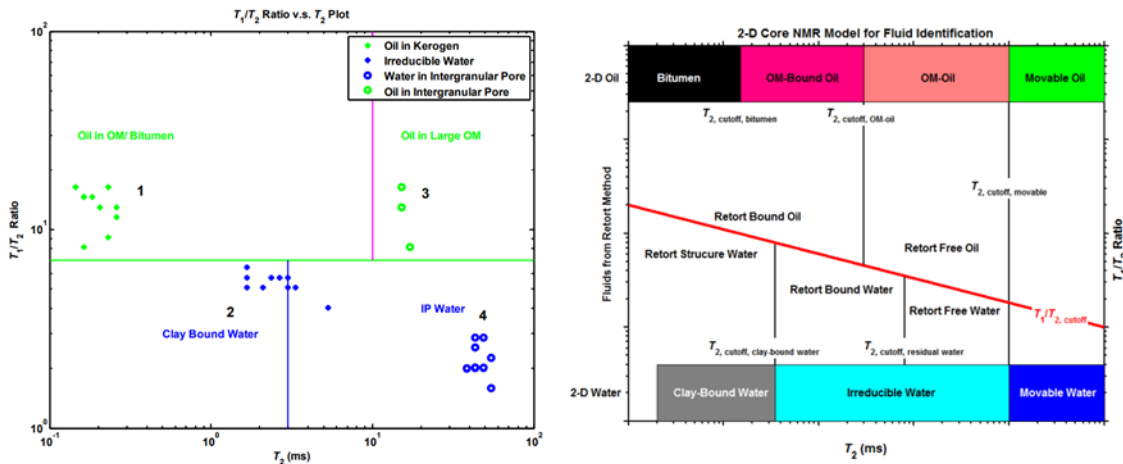


Figure 12: Separation of the fluids by (a) (Rylander 2013); (b) (Jiang et al. 2013).

Ali et al. (2016) presented the summarizing scheme for fluid interpretation. Li et al. (2018) and Li et al. (2020) established the updated version of  $T_1$ - $T_2$  for different hydrogen-bearing

components utilizing experimental features in the low NMR field and 20-MHz radiofrequency of the various fluids (kerogen, kerogen with adsorbed oil, clay minerals, shale, etc.). Comparison of received data with results by Fleury in terms of the map interpretation revealed higher contrast and sensitivity of Li's  $T_1$ - $T_2$  scheme; therefore, authors recommend using high-field NMR for better visualization of the fast relaxing hydrogen population such as kerogen and bitumen. [Khatibi et al. \(2018\)](#) and [Mehana and El-monier \(2016\)](#) analyzed the previously published papers on  $T_1$ - $T_2$  mapping. They summarized their generic version of the  $T_1$ - $T_2$  map, which employs all the traced zones for different fluid populations. Among recent publications, the work of [Zhang et al. \(2020\)](#) gains high interest. Detailed experimental work describes the NMR relaxation behaviors based on the NMR responses for shale rock and its extracted components (kerogen, clay, and five types of water in rock). The final  $T_1$ - $T_2$  interpretation map locates all the possible zones for shale rocks.

Qualitative interpretations of 2D NMR data of  $T_1$ - $T_2$  distributions have been proposed in several articles ([Fleury and Romero-Sarmiento 2015](#), [Ali et al. 2016](#), [Kausik et al. 2016](#), [Khatibi et al. 2018](#), [Li et al. 2018](#), [Zhang et al. 2020](#)). Another approach was proposed by the research team of [Li et al. \(2020\)](#). This scheme is a generalized version of typical circle-shaped zones and consists of trapezoid-based fluid identification. The current scheme is more applicable for different types of organic-rich rock analyses, including a variety of OM in the sample. Figure 13 demonstrates 6 out of 7 selected interpretation schemes.

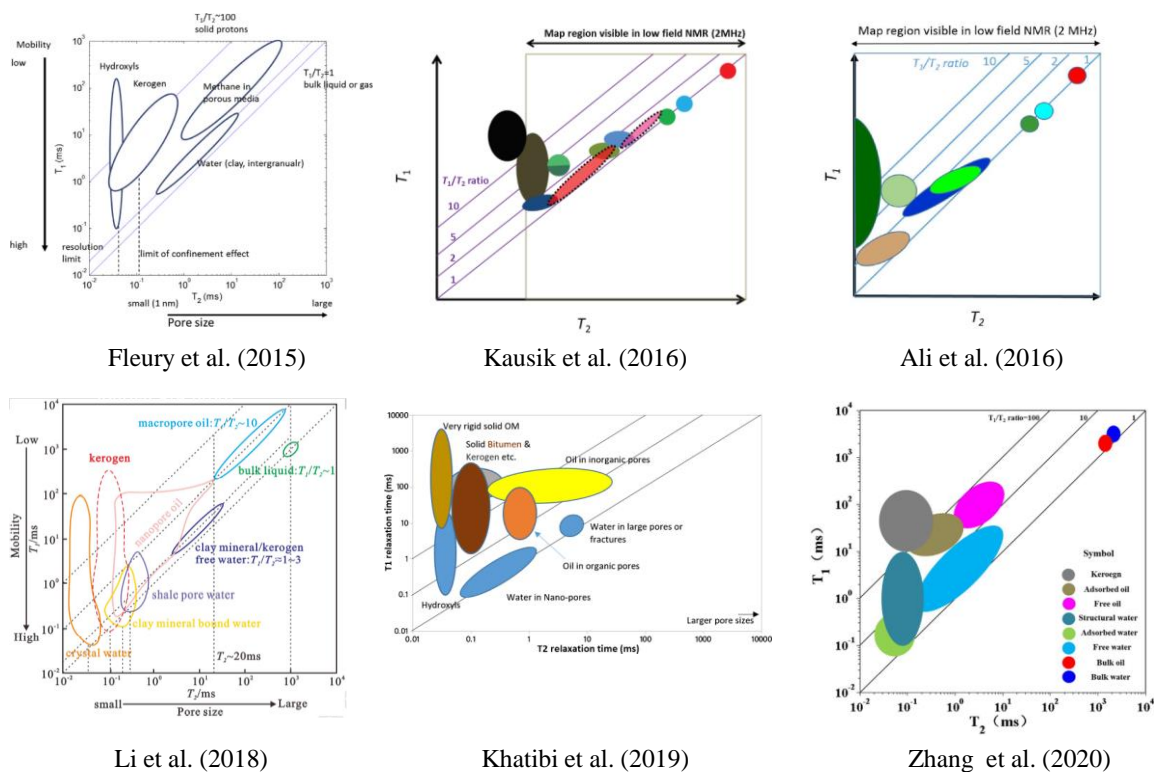


Figure 13: Different fluid interpretation schemes for  $T_1$ - $T_2$  maps.

Table 3 summarizes the main published  $T_1$ - $T_2$  interpretation schemes. A number of interpretation schemes were digitized into layered maps using specialized software. The analysis of  $T_1$ - $T_2$  maps was performed by utilizing all the available zones (fluid populations) in each of the mentioned interpretation schemes.

Table 3. Published interpretation schemes

#	Interpretation Scheme	NMR RF (MHz)	Formation	Number of Fluid Populations
1	Fleury and Romero-Sarmiento (2015)	23	Barnett	4
2	Ali et al. (2016)	2	Eagle Ford	8
3	Kausik et al. (2016)	2	Eagle Ford	12
4	Li et al. (2018)	21.36	Shahejie	8
5	Khatibi et al. (2018)	22	Bakken	8

#	Interpretation Scheme	NMR RF (MHz)	Formation	Number of Fluid Populations
6	Zhang et al. (2020)	21.36	Dongyinh Sag	8
7	Li et al. (2020)	21.36	Shahejie	5

Despite the fact that publications report a positive experience of NMR application, a quantitative interpretation of  $T_1$ - $T_2$  maps is still challenging. When it comes to  $T_1$ - $T_2$  fluid identification, this process turns to be very labor-intensive and subjective. Generally, the laboratory NMR studies utilizing benchtop low-field units require long-lasting experimental workflows (for example, involving kerogen isolation or an aggressive solvent cleaning in shales), unlimited human resources, and a certain level of expertise in the field. Within the framework of this publication, we presented the results of our first step towards automating the fluid interpretation based on the  $T_1$ - $T_2$  maps in shales. One of the tasks in NMR petrophysics is to provide a robust and efficient estimation of the shale saturation.

Similar questions were of interest to a few research groups in a recent couple of years. For instance, Venkataramanan et al. (2018) propose and modify an automated unsupervised learning algorithm called blind-source separation (BSS) for NMR  $T_1$ - $T_2$  map processing. Jiang et al. (2019) present the clustering approach for fluid characterization on  $T_1$ - $T_2$  maps by comparing six different algorithms: k-means, Gaussian mixture model, spectral clustering, and hierarchical methods. Indeed, NMR data interpretation using machine learning (ML) based methods is the trend in modern petrophysics.

### **1.3 Scope of Research and Research Objectives**

Concluding the review on unconventional reservoir characterization methods and the latest applications of NMR technique for liquid saturation evaluation in shales and carbonates, we have proposed a general workflow of the main research directions (Figure 14).

The first step consists of the application of the NMR method for the characterization of different rock types, including Domanik and Bazhenov shales, cavernous and low-permeability carbonates. In the thesis chapters, the accumulated data on reservoir properties (porosity, pore size, cut-off) and saturation defined by NMR will be collected, analyzed, and

compared with the results of other advanced methods (gas porosimetry, liquid saturation, computed tomography, MICP). Based on the results, the workflows of the NMR core analysis for each particular case will be developed.

The next direction will discuss an application of NMR studies on soils and permafrost in ambient and negative temperature zones, as well as NMR studies on the rock at formation conditions at high temperature and high pressure (HPHT). Performing investigation in HPHT conditions enables investigating the core petrophysical properties in models close to one in the reservoir. This direction will consist of diffusion studies and HPHT experiments. The set of characteristics modeled using formation pressure and the temperature is highly desirable and essential input data for commercial simulators and numerical hydrodynamic models.

Application of the adapted and newly developed NMR-based workflows will be demonstrated on the example of the EOR research. For instance, NMR fluid identification will be implemented into the oil displacement and saturation control during thermal EOR. The last direction will focus on a special core analysis, such as wettability determination, reserves evaluation by NMR fluid identification, and integrated workflow of several techniques, including NMR. All the above mentioned will be consequently applied within integrated research of core analysis of the shale formations (Bazhenov, Domanik), heavy-oil carbonate and cavernous carbonate fields, and permafrost samples.

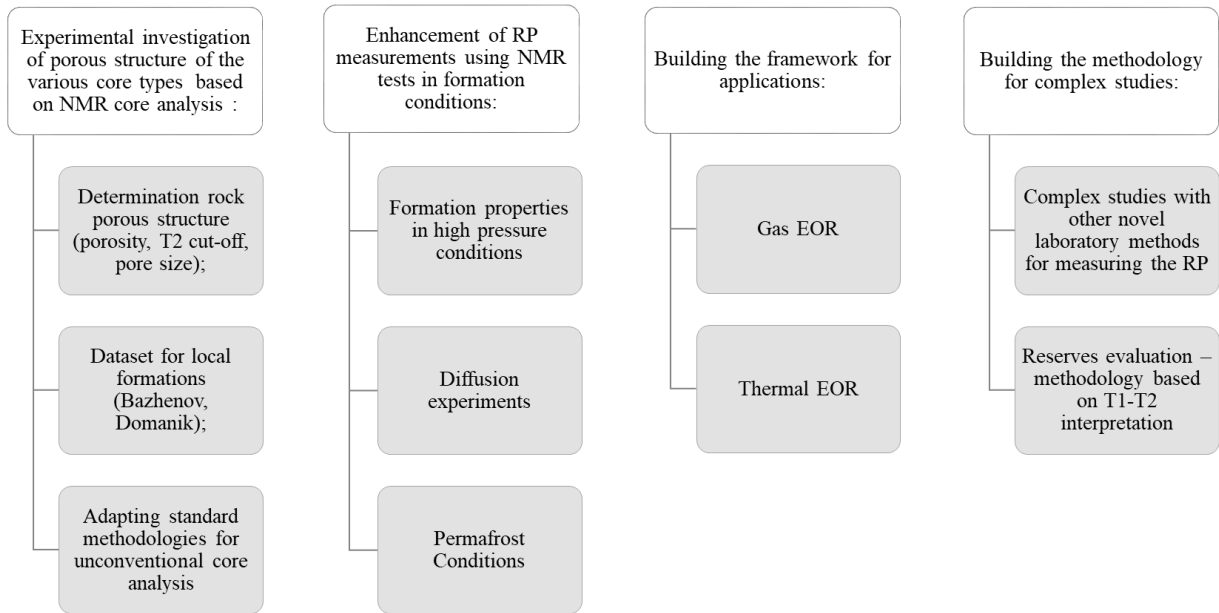


Figure 14: Proposed directions of the research.

In conclusion, the main thesis goals are summarized:

1. To develop new laboratory workflows using NMR for determining unconventional reservoir rock properties (saturation, porosity, pore size). To adapt existing techniques for core analysis of unconventional reservoirs;
2. To develop the methodology for defining the unfrozen water content in permafrost soils in ambient and high-pressure conditions based on NMR analysis.
3. To develop the methodology of the special core analysis using NMR  $T_1$ - $T_2$  maps for fluid interpretation in shale rock samples using experimental results and data analysis.
4. To develop an integrated workflow for defining the reservoir properties of the unconventional reservoir by NMR in conjunction with other experimental techniques such as gas porosimetry, Rock-Eval pyrolysis, thin-section analysis, X-Ray computed tomography, etc.

5. To prepare recommendations for possible applications of developed NMR-based workflows in thermal and gas EOR laboratory studies, including HPHT experiments.

#### **1.4 Thesis Organization**

This thesis is broken down into seven chapters. The first chapter introduces the motivation and outlines the main research objectives. The results of the literature review on NMR applications are also presented in the chapter. In Chapter 2, the targeted objects of the investigation and the main experimental methods, including the NMR experimental methodology, are presented. An overview of rock samples and their properties is summarized in Chapter 2 as well. Starting in Chapter 3, the results obtained within the course of research are presented. Chapter 3 is devoted to petrophysical core analysis of the unconventional reservoir, including the characterization of the porosity, porous structure, rock wettability, and fluid interpretation. Chapter 4 describes the novel methodology of determining unfrozen water content in permafrost under ambient and reservoir conditions. Chapter 5 outlines the results of experimental modeling of water and CO<sub>2</sub> diffusion in shale and carbonate rocks. Chapter 6 discusses the NMR applications in the study of thermal EOR efficiency and porous structure change for heavy-oil carbonates and shale formations. The main conclusion and the significant findings of this work are summarized in Chapter 7.

## CHAPTER 2

### MATERIALS AND METHODS

#### 2.1 Samples Used in Study

In the framework of the thesis, the number of local unconventional reservoirs and formations were investigated. The collection included organic-rich shale formation, low-permeability organic-rich carbonate formation, heavy-oil carbonate formation, bituminous sandstone, and numerous permafrost probing stations.

The major target objects of investigation are summarized in Table 4 below. Detailed characteristics of each subject will be provided in the current and following subchapters.

Table 4. List of rocks used for this study

#	Oilfield	Type of Formation	Formation	Chapter
1	Oilfield #1	Source-rock	Bazhenov	3.1; 3.3.3; 3.4; 3.5
2	Oilfield #2	Source-rock	Bazhenov	3.5; 6.2
3	Oilfield #3	Source-rock	Bazhenov	3.5; 5.4.2;6.2
4	Oilfield #4	Source-rock	Bazhenov	6.2
5	Oilfield #5	Source-rock	Bazhenov	6.2
6	Oilfield #6	Tight source rock	Domanik	3.2; 3.3.2
7	Oilfield #7	Heavy-oil carbonate	A2/A4 (Bashkirian Stage)	6.3
8	Oilfield #8	Heavy-oil carbonate	Vereysky Formation	5.4.3

Other investigated objects include bituminous sandstone samples (Section 3.3.1), cavernous carbonates rock (Section 3.3.4), outcrop carbonate rock samples (Section 3.3.4), and dolerite samples (Section 5.4.1).

#### **2.1.1 Bazhenov Formation**

The Bazhenov Formation (BF) — is the most prominent organic-rich source-rock formation in the West Siberian Basin (Russia), with an area >1 billion km<sup>2</sup> (Kontorovich et al. 1997,

Lopatin et al. 2003). Huge reserves of the formation are the main reason for the continuous investigation of its structure and physical properties; thereby, the BF is one of the best-studied and characterized Russian petroleum bearing formations (Prishchepa et al. 2014).

BF is Upper Jurassic-Lower Cretaceous marine-origin oil shales that occupy most of the West Siberian Petroleum Basin (Figure 15) with a thickness of 15–60 m and organic matter content up to 25% wt. (Ryzhkova et al. 2018). The main rock types are composed of silica, calcite, clay minerals, and organic matter with the domination of silica (Balushkina et al. 2014, Ryzhkova et al. 2018). In addition, BF is often characterized by high heterogeneity determined by interlaying of the silica and mudstone with kerogen-enriched laminas. Main clay minerals are kaolinite and illite; however, clays are also presented by illite/tobelite/smectite mixed-layered mineral compounds. Petrophysical properties complicate the rock study due to low permeability (< 1mD) and low open porosity (< 3%) (Khamidullin et al. 2012).



Figure 15: The geographical location of the Bazhenov Formation.

We have investigated core samples and accompanying core chips from five different oilfields of the Bazhenov Formation. As thin-sections illustrate, the main rock-forming component is

clay minerals ranging in 40–58% diapason with 51% on average; the second rock-forming mineral is quartz — 25–45% with an average value of 31%. Other components are carbonate minerals (< 5%) and pyrite (< 5%) (Figure 16).

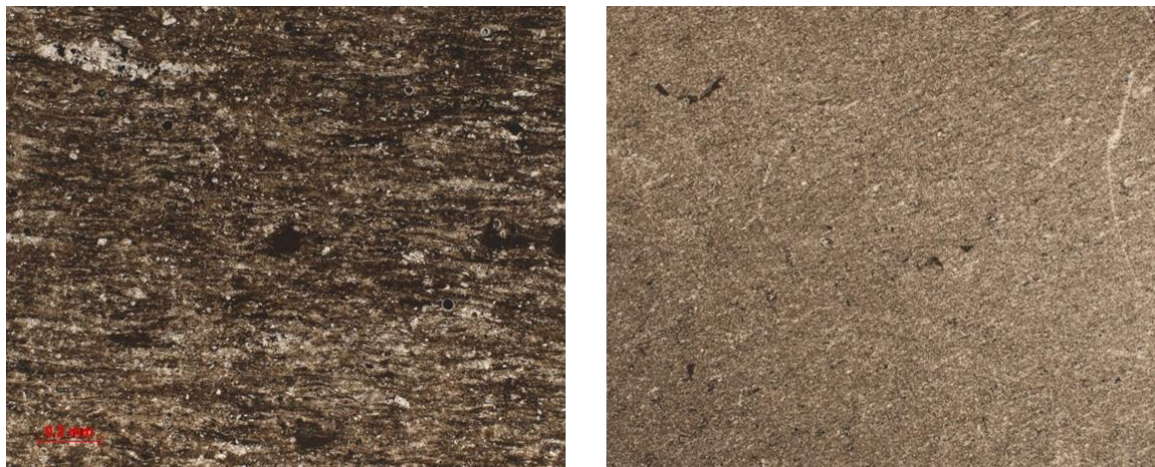


Figure 16: The thin-sections of Bazhenov Formation.

### 2.1.2 Domanik Formation

The study covers a representative collection of rock samples of an organic-rich carbonate Domanik (Tlyanchy-Tamakian) Formation of an Upper Devonian Frasnian age. The formation resides in the Volga-Ural and Timan-Pechora basins in the European part of Russia (Figure 17). Previous extensive studies characterized the formation in terms of geochemical properties, including oil generation potential (Bushnev and Burdel'naya 2013, Fadeeva et al. 2016, Gabnasyrov et al. 2016, Stupakova et al. 2017). The formation is one of the promising sources of oil in the basin (Requejo et al. 1995, Abrams et al. 1999). Assessments of oil resources in the formation vary from hundreds of millions to billions of tons (Prishchepa et al. 2014, Fadeeva et al. 2016, Stupakova et al. 2017). However, the highly heterogeneous rock texture and complex structure of voids essentially constrain the recovery of oil and gas.

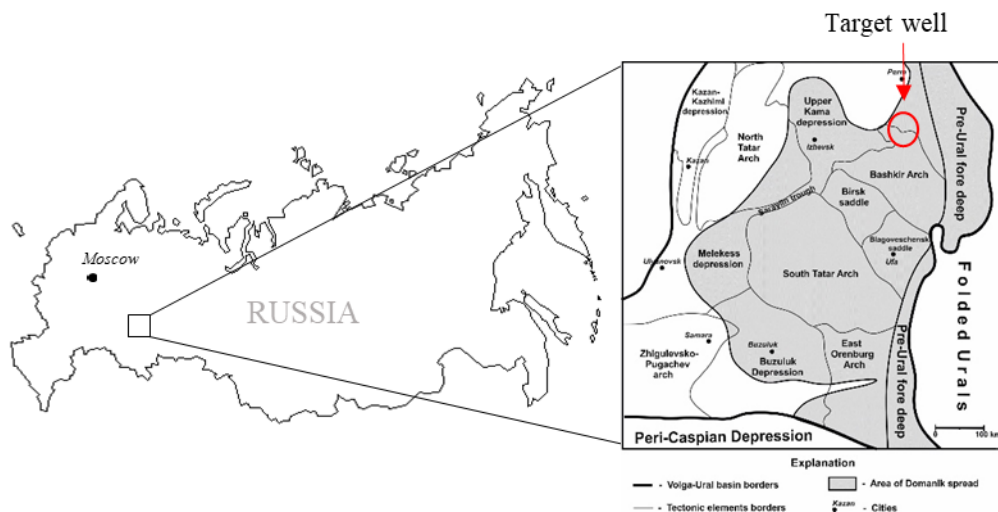


Figure 17: The geographic location of the target Oilfield #6 (modified after (Kadyrov et al. 2018)).

The target collection of rock samples relates to mostly carbonate, carbonate-siliceous thin-layered rocks with a moderate total organic carbon (TOC) content up to 10 wt.%. Carbonates are predominantly represented by organic-rich wackestones, in some cases, by packstones and crystalline limestones (Figure 18). Target rock samples came from a well located in the south of the Perm region of Volga-Ural province, Russian Federation, Oilfield #6. The entire collection of rock samples included 32 whole cores and more than 300 drilled core plugs corresponding to three main horizons — overlay Mendym / Trudolubian (D3tr), main Domanik / Tlyanchy-Tamakian (D3tch), and underlay Sargaevian (D3srg) unit. The reservoir properties ranged as follows: carbonate content 60–99%; clay content 0–10%; TOC content 0.5–10 wt.%.

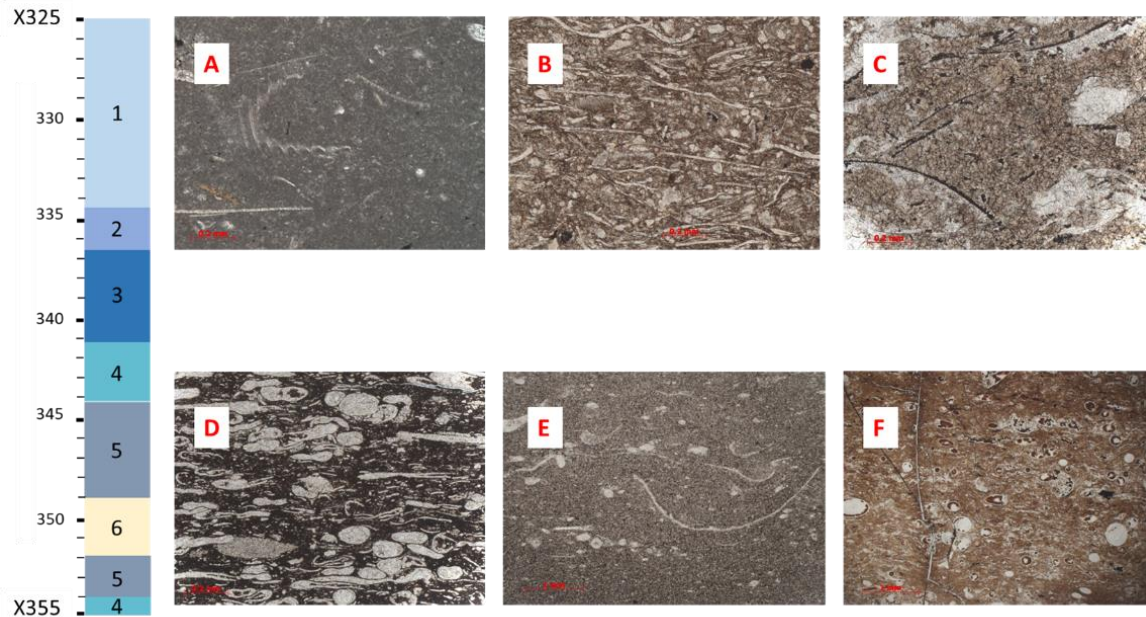


Figure 18: The identified lithotypes of Domanik deposits (A – micro-clotty limestones with bioclastic detritus; B – bioclastic limestones with detritus particles; C – close- to fine-crystalline limestones with biogenic detritus; D – bioclastic (tentaculitic) limestones, siliceous-carbonaceous; E – micro- to close-crystalline limestone with biogenic detritus; F – tentaculitic carbonaceous silicites). (Mukhametdinova et al. 2019)

Samples show high heterogeneity and anisotropy due to intense thin-bed layering (Figure 19). Various imprints of shells (presumably brachiopod) contribute to both rock heterogeneity and anisotropy.



Figure 19: 3D view photo of the whole core of Domanik Formation (Mukhametdinova et al. 2020).

### 2.1.3 Carbonate and Heavy-Oil Formations

The second group of oilfields (#7 and #8) belongs to Vereysky and Bashkirian stage formations located in the Volga-Ural Basin in Russia (Astarkin et al. 2016, Astarkin et al. 2017). The reservoir properties of Oilfield #7 range as follows: porosity ( $\phi$ ) 1.90–16.0%; permeability ( $k$ ) 0.01–1.5 mD; carbonate content 3–99%; clay content 0–10%; TOC content 0.5–4.69%. The Oilfield #7 samples are represented with crystalline calcite with dolomite (Figure 20). Calcite crystal size varies from 10 to 70  $\mu\text{m}$  with a dominant size of 30–40  $\mu\text{m}$ . Void space is represented by intercrystalline porosity.

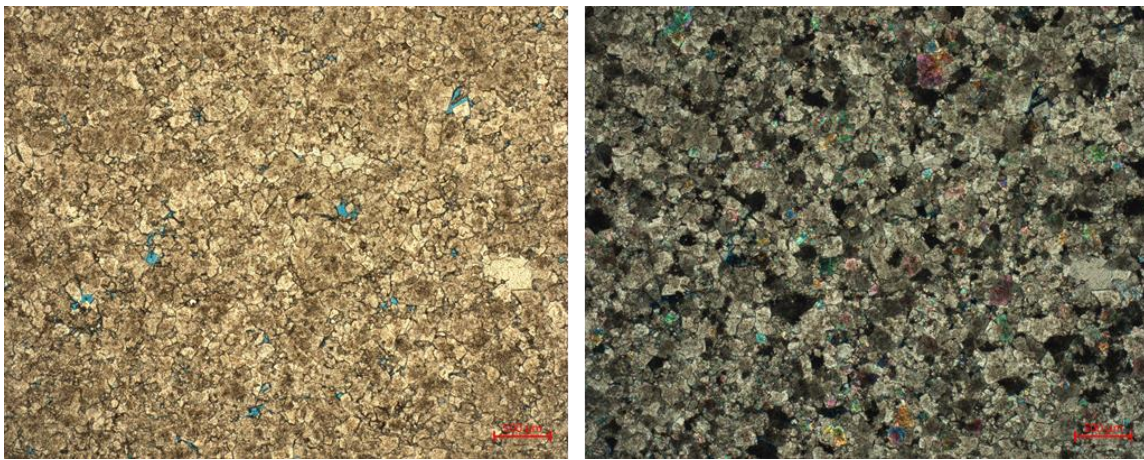


Figure 20: The thin-sections of target heavy-oil carbonate formations.

Oilfield #8 is mainly represented by limestones, clayey limestones, and terrigenous-carbonate rocks. The reservoir properties of Oilfield #8 range as follows: porosity ( $\phi$ ) 8–15.0%; permeability ( $k$ ) 0.1–200.0 mD; carbonate content 49–82%; clay content 0–10.49%. The locations of both target oilfields are illustrated in Figure 21. Cylindrical core plugs (25×40 mm and 30×30 mm) sampled from the target oilfields were used for research.



Figure 21: Location of the Oilfields #7 and #8.

#### 2.1.4 Permafrost Soils

Permafrost rocks (or frozen soils) are rocks that have a negative temperature and contain some amount of ice in pores or cracks. In determining the phase composition of water by the NMR method were soils of different dispersion and chemical-mineral composition (Table 5). The locations of sample probing stations are highlighted in Figure 22.



Figure 22: Location of the samples probing.

In the experiments, we used soils with both natural and artificial salinization (Table 5).

Table 5. Characteristics of the studied soils

Soil	Place of selection	Mineral composition, %	Salinity, %	
Montmorillonite clay	Dzhembel station, Turkmenistan	montmorillonite	93	1.99
		andesine	3	
		biotite	3	
Kaolinite clay	Novokaolinovy, (Chelyabinsk Region)	kaolinite	92	0.04
		quartz	6	
		muscovite	2	
Polymineral clay	Kudinovo (Moscow Region)	quartz	45	0.10
		microcline	9	
		illite	9	
		kaolinite	5	
		amorphous substance	28	
Loam-1	South Tambeyskoye gas condensate field (Yamal Peninsula) 59–71 m interval	quartz	46	0.34
		albite	25	
		chlorite	10	
		muscovite	7	
		kaolinite	5	
		orthoclase	7	
Loam-2	East Messoyakhskoye oil and gas condensate field (Gydan Peninsula)	quartz	38	0.06
		montmorillonite	20	
		albite oligoclase	15	
		orthoclase	11	
		muscovite	6	
		kaolinite	4	
Loam-3	East Messoyakhskoye oil and gas condensate field (Gydan Peninsula)	quartz	41	0.06
		montmorillonite	15	
		albite oligoclase	13	
		orthoclase	11	
		kaolinite	5	
		muscovite	4	
		amphibole	3	
		chlorite	2	
Loam-4	Yerkuta gas emission crater (Yamal Peninsula)	quartz	45	0.05
		albite	22	
		microcline	10	
		illite	9	
		chlorite	5	
		amphiboles	3	
		kaolinite	3	
Fine sand	Lyubertsy (Moscow Region)	quartz	> 90	0.01

## 2.2 Methods

### 2.2.1 Core Selection

Experiment planning typically involves the whole cores, which have a length of 200 mm and diameter of 100 mm (isolated from environmental exposure using layers of foil and paraffin (McPhee et al. 2015)). In other cases, core plugs come in an as-received state and are isolated by the layers of foil and paraffin.

In the case of whole cores, X-Ray CT is used to locate homogeneous areas with a certain amount of organic matter and separate the parts with artificial fractures and other inhomogeneities. To develop the multiscale characterization of the void space structure, in part of the study, we conducted the whole core separation into a set of subsamples (Figure 23). Different laboratory techniques have certain core preparation requirements. For instance, X-Ray CT (at macro and micro level), NMR, PIK-PP (unit for PDP measurements), LS (liquid saturation method) are performed on standard core plugs, whereas the Darcy test (variation of PDP) is conducted on the sample of 1 cm<sup>3</sup> volume. SEM, MICP (or MIP), XRD, and Rock-Eval pyrolysis employ crushed rock of specified mesh size.

In the case of the limited core material, the workflow is conducted at the best configuration for the existing core volume (Figure 24). For large collections of core plugs and chips, the visual inspection using day/UV light is conducted.

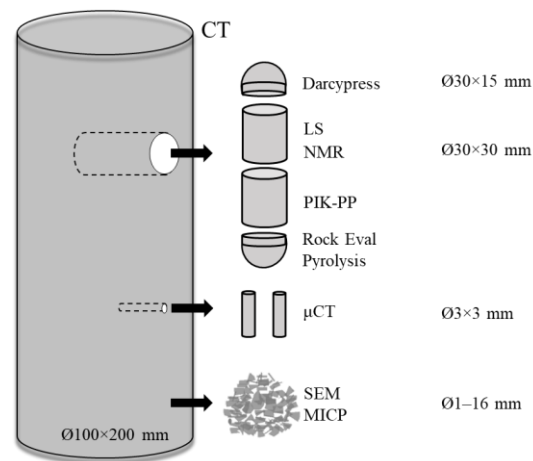


Figure 23: Schematic diagram of the whole-core breakdown into subsamples. (Mukhametdinova et al. 2020)

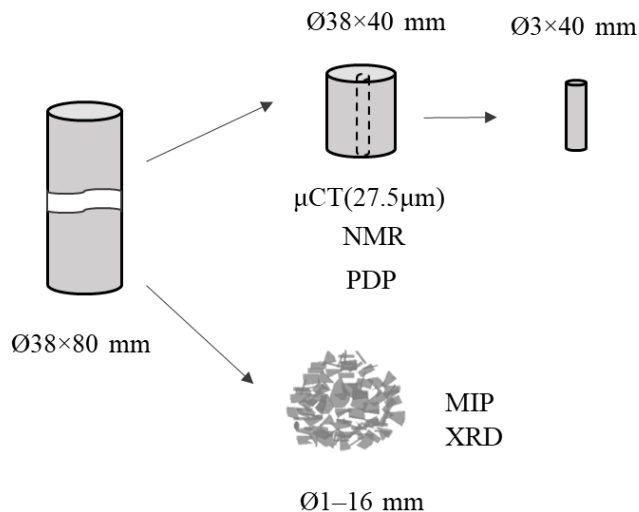


Figure 24: Schematic diagram of the limited core investigation. (Razavifar et al. 2021)

Multiscale characterization of the reservoir properties requires a suite of advanced laboratory methods and equipment for studying the porous structure and microstructure of the target rock. In current work, the main operational method was low-field NMR relaxometry. However, a number of other techniques for comparison, validation, and obtaining accompanying information were used (Figure 25). Bulk methods included gas porosimetry by PDP, NMR, and CT. Microstructural methods stand for visualizing techniques such as  $\mu\text{CT}$  and SEM. A separate method is MICP, which belongs to the transition group, *i.e.* provides porosity measurement and describes the void space structure as well. In addition, the Rock-Eval pyrolyzer was used for OM characterization, and equipment (automated saturator, automated extractor, and designed high-pressure systems) was employed in core preparation and conducting of HPHT experiments. Detailed information on each method is introduced in the latter sections.

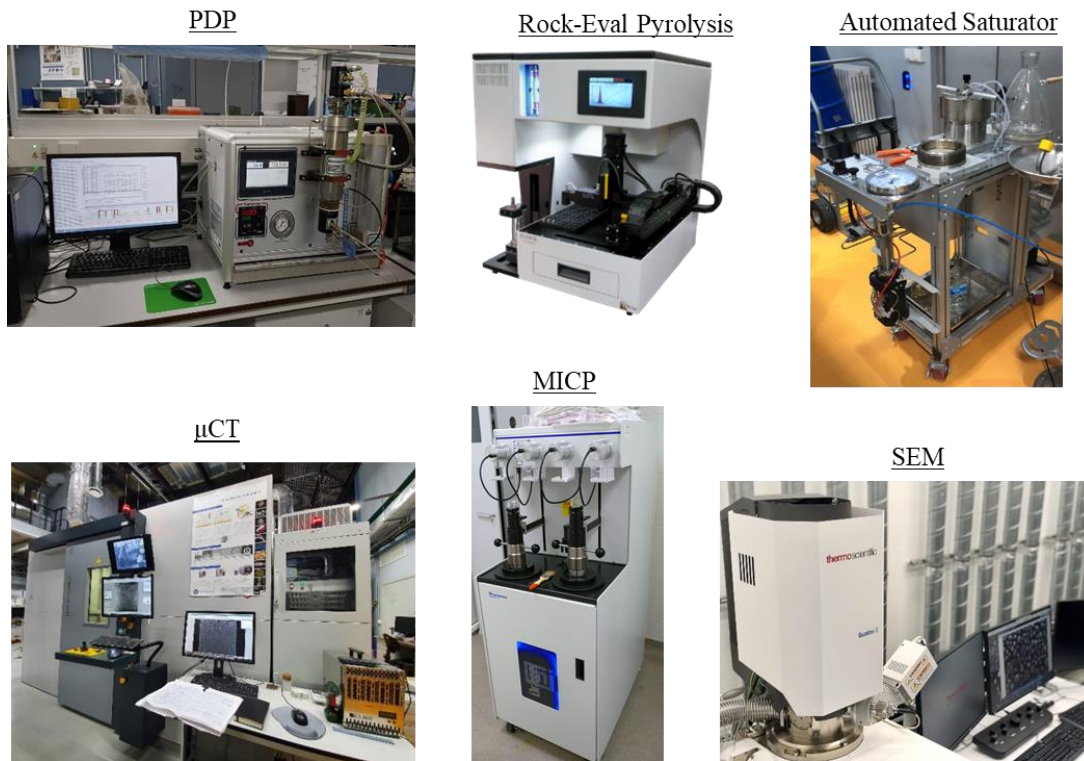


Figure 25: Photograph of employed experimental setups.

### 2.2.2 Nuclear Magnetic Resonance

NMR was employed to determine the porosity of the target rock samples. A low-field NMR unit, Oxford Instruments Geospec 2/53 (UK), estimated saturation and porosity at each step of the experimental workflow. NMR analysis is based on recording and measuring the polarization and relaxation of hydrogen atoms in a magnetic field of 0.05 T and radiofrequency (RF) of 2.28 MHz (Bloembergen et al. 1948, Abragam 1961, Callaghan 1991).



Figure 26: Photograph of the NMR setup.

The physical principles of the method are described in Section 1.2.1. Analysis and interpretation of results employed principles characteristic for NMR application in petrophysics (Straley et al. 1997). The instrument's calibration used reference samples supplied by the manufacturer with known parameters, including NMR liquid volume and length of the  $90^\circ$  and  $180^\circ$  pulse.  $T_2$ -relaxation curve measurements resulted from the Carr-Purcell-Meybum-Gill pulse sequence with the time-echo ( $TE = 2\tau$ ) set to 0.1 ms. Preliminary tests justified the number of trains (accumulations) of the pulse sequence ( $90^\circ$ - $\tau$ - $180^\circ$ - $2\tau$ - $180^\circ$ -...- $180^\circ$ ) and estimated the highest signal-to-noise ratio (SNR), as well as the minimum number of scans (NSA) — 128 unless otherwise specified. Data processing, analysis, and interpretation involved using a Green Imaging Technologies (GIT) Systems Advanced v.7.5.1 software (GIT 2014).

### 2.2.3 Conventional Gas Porosity and Permeability of Plugs

Porosity and permeability measurements employed an automated gas permeameter-porosimeter Geologika PIK-PP (Russia) (Geologika 2016). The tests used nitrogen as a probe gas, while permeability measurements resulted from the pulse-pressure decay (PDP) technique. The confining pressure was 3.4 MPa. The stabilization criteria for pressure decay was 0.1%/min. Data reliability required performing tests three times and calculating an average value. We calibrated the unit with supplied artificial samples with known parameters.

### 2.2.4 Computed Tomography

We imaged the microstructure of the target rock samples in 3D using both computed tomography (CT) and micro-CT (Remeysen and Swennen 2008, Cnudde and Boone 2013). For this purpose, we used GE phoenix v|tome|x L240 a versatile high-resolution microfocuss system for 2D and 3D computed tomography and 2D non-destructive X-ray inspection. We acquired raw data using GE datos|x acquisition 2.6.1-RTM software. Reconstruction of a set of 1,000–2,400 2D radiographic projections into 3D -ray density images involved the application of GE datos|x reconstruction 2.6.1-RTM software and processed the models using FEI PerGeos 1.5 software (PerGeos 2018).

### 2.2.5 Scanning Electron Microscopy

SEM was used for high-resolution 2D imaging and rock structure characterization. By means of the Thermo Fisher Scientific Quattro S electron microscope, we analyzed small rock probes (3–5 mm in size) split from main samples. The microscope allowed us to work with an electron beam current range from 1 pA to 200 nA with an accelerating voltage of 200 V to 30 kV. The highest spatial resolution was 5 nm (30 kV). Scanning included using secondary electrons (SE) and backscattered electrons (BSE), magnification range  $\times 500$ –35,000 k, acceleration voltage 10–15 kV, working distance 9–11 mm with approximately 5–6 nm maximum pixel size (Erdman and Drenzek 2013). The resulting images had dimensions of 1,536 $\times$ 1,094 px.

### 2.2.6 Rock-Eval Pyrolysis

Pyrolytic studies were carried out using a Wildcat Technology HAWK RW by the Rock-Eval method instrument and a standard program for source rock analysis and data interpretation (Peters 1986). The HAWK workstation (hydrocarbon analyzer with kinetics) is designed for express analysis of the distribution of organic matter in the rocks of core or cuttings along the well section or natural outcrops. The interpretation of results was based on the principles of pyrolytic data analysis for source rock (Espitalie and Bordenave 1993).

### 2.2.7 Common Shared Methods

Core analysis workflow employed main recommendations for rock analysis (API 1998).

We determined the open porosity of the target rock samples using the standard liquid saturation or gravimetric method. The technique consists of saturating a rock sample with a liquid (usually kerosene or water) and determining its volume by immersion in the saturating fluid utilizing precise laboratory scales A&D GH-202GH with AD1653 gravimetric console.

Rock typing was performed according to the classification proposed by Lazar (Lazar et al. 2015). Special ultra-thin sections (10  $\mu\text{m}$ ) were prepared for analysis, which employed ZEISS Axio 2m, Imager polarizing microscope. Mineralogy analysis on core powder was performed using the benchtop Rigaku Smartlab X-Ray diffractometer unit.

The core saturation procedure consisted of vacuuming the samples, capillary imbibition, and injection of a saturating fluid under a pressure of 15 MPa using an automatic saturating unit Geologika PIK-SK. In the case of fragile samples, the core saturation was carried out in a high-pressure vessel, with a consecutive vacuuming and step-by-step pressure increase.

Core crushing and probe preparation employed the crushing machine ASCS Scientific Jaw Crusher JC-300-ST-Q. We separated the core fractions by mesh size using the vibratory sieve shaker RETSCH AS 450 control.

Core cleaning (extraction) included cleaning the rock samples (core plugs and core chips) with a solvent. Core cleaning was of three types —mild (with kerosene), strong (with chloroform, and aggressive (with a CO<sub>2</sub>-toluene mixture under pressure). Kerosene and chloroform-based cleaning were conducted in the Soxhlet apparatus. We controlled the extraction quality by both visual inspections with a UV lamp and by measuring the TOC content on rock specimens every 24 h. The time of extraction averaged 150 h. CO<sub>2</sub>-toluene extraction was conducted in an automated core extractor under maintained pressure (up to 150 atm) and temperature (up to 100°C). The duration of controlled extraction averaged at 24-48 h.

After extraction, the rock samples were dried at a temperature of 70–100°C (depending on the removed fluid and rock type) in the laboratory-heating oven Memmert VO400 until the constant weight ( $\Delta 0.001$  g).

## 2.3 NMR Analysis

### 2.3.1 Calibration of NMR Unit

To define the limits and the measurement range by NMR, the two series of calibration samples (quality samples) were prepared:

1. Five isolated samples with different H<sub>2</sub>O: D<sub>2</sub>O ratios. Due to its magnetic moment, D<sub>2</sub>O (deuterium dioxide) is not registered by the low-field NMR. For this reason, D<sub>2</sub>O is often used as an invisible agent in different mixtures. Varying the ratio and concentration of the visible and invisible fluids in the probe, we can test the sensitivity of the NMR relaxometry. The correlation between the actual volume of the probe and the volume detected by NMR is shown in Figure 27 below. The slight deviation, an increase of the NMR signal can be related to the noise caused by the Teflon probe holders.

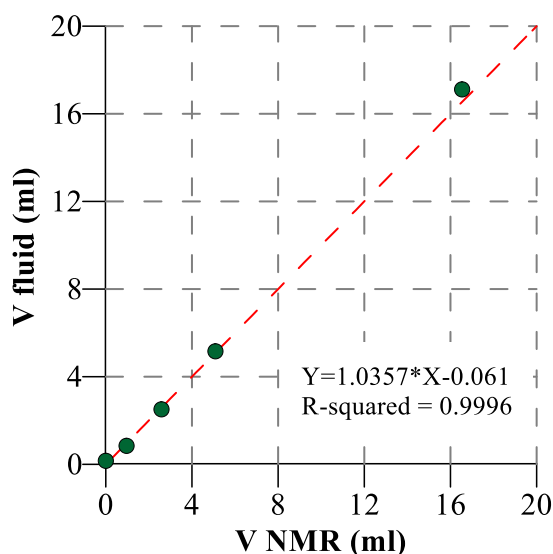


Figure 27: Identifying the operational fluid volume at LF-NMR.

2. To better analyze the operational limits by NMR, 20 probes with the different concentrations of the paramagnetic were prepared. The relaxation behavior ( $T_2$  logarithmic

mean values) was different in all the samples. Therefore, it enabled tracking the minimum relaxation time when the signal is not responding correctly. We established that for the current NMR unit, the minimal high-precision relaxation time equals 0.3 ms; therefore, the dead time of the unit is equal to 0.1 ms.

Before the start of NMR studies, core samples go through the preparation stage (weighing, measuring the geometry of the sample). Next, a series of NMR tests ( $T_2$  relaxation time) is carried out for samples in a state of as-is (as-received) saturation at atmospheric pressure.

To avoid evaporation of liquid during NMR measurements, the saturated samples in a saturated state are wrapped in a polyethylene film. To achieve uniform heating of all measuring units, especially the magnetic system, the device is kept in stable thermal conditions for 24 hours.

Calibration of the device is carried out using reference samples from the manufacturer of the device Green Imaging Technologies. The QC sample is a NaCl salt solution with a volume of 5 and 20 ml (depending on the porosity of the studied rock) with known parameters (liquid NMR volume). Calibration should be performed before each series of tests, at least once every five working days.

### **2.3.2 Precision, Accuracy, and Uncertainty of NMR Measurements**

Accuracy control includes control of intra-laboratory precision and control of the correctness of measurement results. The control of the intra-laboratory precision of the measurement results is carried out using reference samples as control samples (QC). The reference samples are sealed containers with different volumes of sodium chloride (NaCl) salt solution.

When performing this work, the volume of hydrogen-containing fluid was measured for each rock sample. To assess the accuracy of measurement results, it is important to know the SD, RMS, and total uncertainty of the measurement. The boundaries of the confidence interval are usually determined through the variance, which is a parameter of the normal distribution of random variables; for a small number, it can be found with low accuracy. Therefore, the boundaries of the confidence interval, in this case, are determined using the Student's

coefficient. The algorithm is identical for all measurements. Therefore, we present the example of a metrological study for two types of rocks with ultra-low initial saturation (Oilfield #6) and average saturation (Oilfield #1). To ensure the accuracy of the measurement results, measurements were taken at least three times. We calculate a square error for each measurement by the formula:

$$\Delta A_i^2 = \Delta V_i^2, \quad (1)$$

where  $\Delta A_i^2$  – measurement error square.

The estimation of the standard deviation (SD) of the measurement result is determined by the formula:

$$S(\bar{A}) = \sqrt{\frac{\sum_{i=1}^n ((x_i - \bar{A})^2)}{(n-1)}}, \quad (2)$$

where  $S(\bar{A})$  – assessment of the standard deviation (SD) of the measurement result.

The boundaries of the confidence interval of the random error are determined by the formula:

$$\varepsilon = t * S(\bar{A}) \quad (3)$$

where  $\varepsilon$  — confidence interval limits;  $t$  — Student's coefficient.

Accuracy control includes control of intra-laboratory precision and accuracy of measurement results. In accordance with the standards (GOST 8.207-78),  $t = f(n-1, p)$  and with a confidence level of  $P = 0.95$  we have  $t=3.2$ .

In turn, the accuracy is presented by a systematic error that provides data on the general quality of the measurement. Precision is estimated by the random error value. Uncertainty covers both the accuracy and precision of the measurement. In turn, accuracy and precision cannot be provided without the confidential level of the measurement.

The uncertainty  $U$  (total error) is determined by the formula:

$$U = \sqrt{A^2 + P^2} \quad (4)$$

To assess the systematic error, we perform measurements of the fluid volume on standard (QC) samples with a fixed fluid volume.

Table 6. Estimation of the systematic error of the NMR unit

$V_1$ (ml)	$V_2$ (ml)	$V_3$ (ml)	$V_{\text{calibration}}$ (ml)	$V_{\text{average}}$ (ml)	Systematic error ( $\lambda_{\text{sys}}$ )%
5.208	5.203	5.195	5.280	5.202	1.5
2.517	2.565	2.588	2.517	2.547	1.6

The calculation of the precision (random error) was conducted for each series of measurements.

Table 7. Estimation of the random error on an example of Oilfield #6 samples

Sample ID	Oilfield	$V_1$ (ml)	$V_2$ (ml)	$V_2$ (ml)	$V_{\text{av}}$ (ml)	RMS	Random Error $\lambda$ (%)	Total (%)
87	#1	2.058	2.048	2.010	2.049	0.009	1.10	1.80
95	#1	1.798	1.762	1.770	1.777	0.019	2.60	3.00
705	#6	0.229	0.235	0.235	0.233	0.004	3.70	4.00
723	#6	0.724	0.714	0.724	0.721	0.007	2.00	2.50
average							2.35	2.82

### 2.3.3 Hydrogen Index of Bulk Fluids

When working with fluids and indices other than the water index, a preliminary test is required to calculate the hydrogen volume of the fluid (Table 8). Working fluid of a certain volume undergoes NMR  $T_2$  test, and the Hydrogen Index (HI) is calculated.

Table 8. Hydrogen indices of fluids

№	Fluid	Volume (cc)	NMR volume (ml)	HI
1	Kerosene	5.00	4.54	0.90
2	Brine model	5.00	4.99	0.99
3	Hexane	5.00	4.56	0.92

### 2.3.4 Experimental Procedure

Depending on the tasks and research goals, the procedure of NMR studies may vary significantly. There is no unified order of the operation, including the core cleaning and saturation routine. The step sequence, as well as the details on core preparation, are directly affected by the following factors:

1. Rock mineral composition;
2. Rock mechanical fragility;
3. Rock's initial state of saturation.

In this section, we have tried to summarize some of the proposed and utilized workflows for NMR analysis of core samples. All the provided workflows are subject to modification and presented on an advisory basis. The first workflow (Figure 28) is a basic sequence for NMR analysis. It can be applied to rock with a low residual amount of mobile oil or shale samples. It doesn't include the core cleaning procedure but requires rock drying in order to remove the mobile water. Saturation fluid choice depends on the task and clay content of the rock.

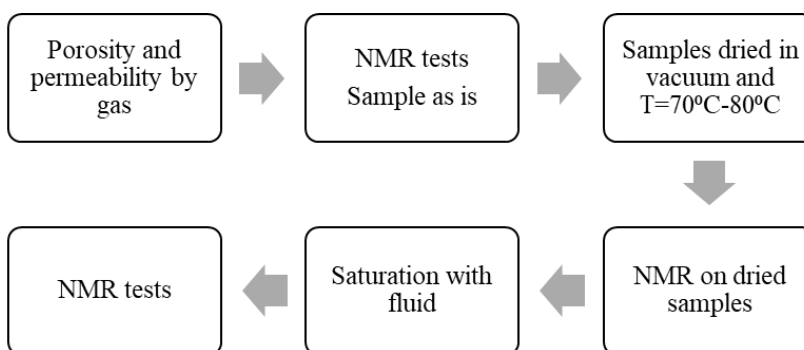


Figure 28: Workflow A – fast sequence for porosity determination.

The next workflow (B, Figure 29) is applicable for the characterization of the rock saturated with both fluids — oil (or modeling decane and kerosene) and water (brine model). It also does not include aggressive core cleaning and may be applied for shales.

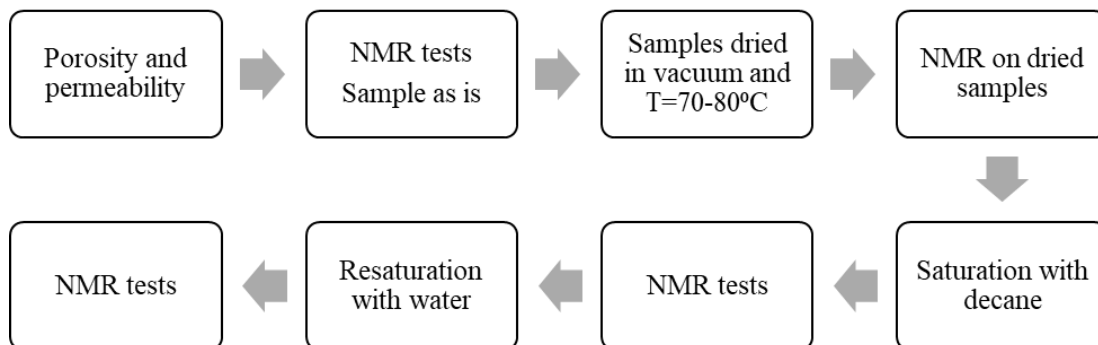


Figure 29: Workflow B.

The following workflow (Figure 30) is suitable for carbonate and sandstone samples. It consists of solvent cleaning, saturation, and centrifuging. Such sequence is utilized for detailed porosity study and defining the irreducible saturation,  $T_2$  cut-off, and permeability.

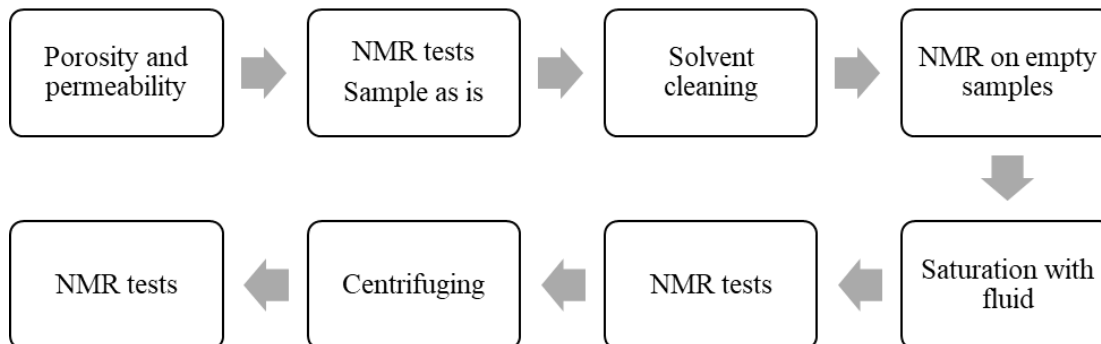


Figure 30: Workflow C.

The most expanded workflow (D, Figure 31) combines all possible manipulations and covers the range of tasks. It can be used for defining the porosity, wettability, and other computational parameters.

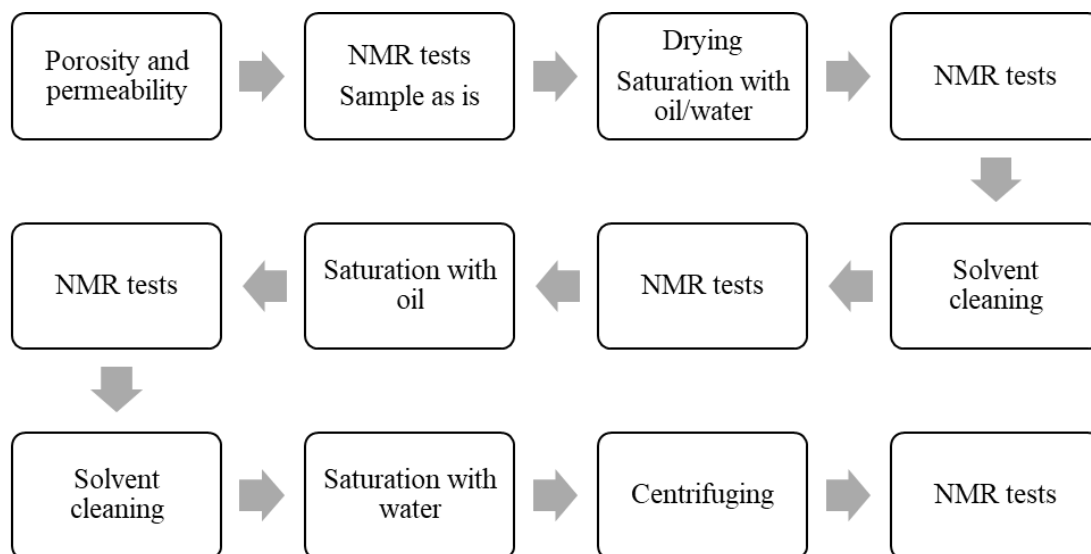


Figure 31: Workflow D.

The utilized parameters of NMR testing are summarized in Table 9 below. Similar to the core analysis workflow, the parameters of NMR testing vary depending on the investigated rock type and purpose of the study. In some cases, it is not possible to maintain the high resolution or the signal-to-noise ratio. For instance, such occurs in permafrost analysis, when the duration of the NMR test is crucial. Table 9 lists the recommended parameters which were obtained for tight rocks based on numerous laboratory studies.

Table 9. Parameters of NMR testing

№	NMR test	Testing parameter			Test duration, h
		NSA	RD	SNR (min)	
1	$T_2$	128	15000	100	0.5–1
2	Saturation profile	256–512	7500	100	0.5
3	$T_1$ - $T_2$ Map	16–32	7500	50	3–5

## **2.4 Summary**

In the current chapter, the following points are highlighted:

1. First of all, the main rocks and samples under investigation were introduced. They are divided into four main categories: organic-rich source-rock (shale), low-permeability rock, and heavy-oil carbonate rock and permafrost soils.
2. The primary information on targeted oilfields was provided, including data on location, petrophysical and geochemical properties, and references in the literature.
3. We identified the main experimental methods and techniques utilized in the study of rock properties. Based on our experience and numerous core sample studies, we developed certain NMR workflows that can be directly applied to target rock studies.
4. By using different calibration sets, we defined the limits of NMR applicability in terms of reliable fluid volume measurement and minimal relaxation time registered at high accuracy.

## CHAPTER 3

### CORE ANALYSIS BY NMR

Conventional core analysis is the primary task of low-field NMR relaxometry. Numerous papers and technical reports have been devoted to this topic. For years, researchers and NMR specialists have been establishing the existing methodologies and adapting them, given the specifics of the studied object. Nevertheless, every unconventional reservoir complicates the workflow due to several factors – specifics of the porous structure, mineralogy, and OM properties.

In the current chapter, the data obtained for local unconventional reservoirs by means of adapted experimental workflows are summarized. We demonstrate the results on porosity, PSD, fluid interpretation, and wettability of the samples. To confirm the applicability of the NMR technique, we perform a comparison with other conventional and state-of-the-art techniques.

The last section of this chapter is devoted to the most interesting and promising part of the research – fluid interpretation by NMR two-dimensional tests. Herein we attempt to find the reliable and best-fitting interpretation scheme for local shales and create one based on experimental results.

### **3.1 Bazhenov Formation**

#### **3.1.1 Porosity by NMR**

The collection of 13 cylindrical samples from Oilfield #1 was investigated (Table 10). The reservoir and geochemical properties of the target rock are introduced in Section 2.1.1. The extended workflow was selected for assessing not only rock saturation and porosity but wettability as well. The samples underwent saturation with kerosene, aggressive solvent cleaning, and consecutive saturation with kerosene and brine model.

Table 10. List of target samples

<b>Sample ID</b>	<b>Porosity by gas (%)</b>	<b>Permeability by gas (mD)</b>
87	2.75	0.068
88	3.42	0.018
89	2.85	0.058
90	0.71	0.013
91	3.17	0.014
92	-	-
93	2.42	0.01
94	0.57	0.059
95	1	0.011
96	1.15	0.005
97	0.74	0
98	5.44	0.024
99	6.8	0.651

It is worth noting that three sets of porosity values — in as-received (non-cleaned) oil-saturated, cleaned oil-saturated and water-saturated states were obtained (Figure 32). As-is samples are the ones examined after unpacking from the paraffin cover and exposed to air for the test duration. The next step consisted of the drying of non-extracted samples in order to remove light hydrocarbons and mobile water from the samples. Drying control was carried out at least once every 12 hours until the sample weight stabilized (change less than 0.01 g). It should be noted that the drying time to the specified accuracy was 11 working days.

The saturation technique is given in Section 2.2.7. At this stage, the porosity of samples by the NMR method and by the method of LS was determined. Extraction of samples was carried out in an automatic saturator by CO<sub>2</sub>-toluene mixture. The extracted core samples were dried in a vacuum drying oven and placed in a desiccator until further manipulations.

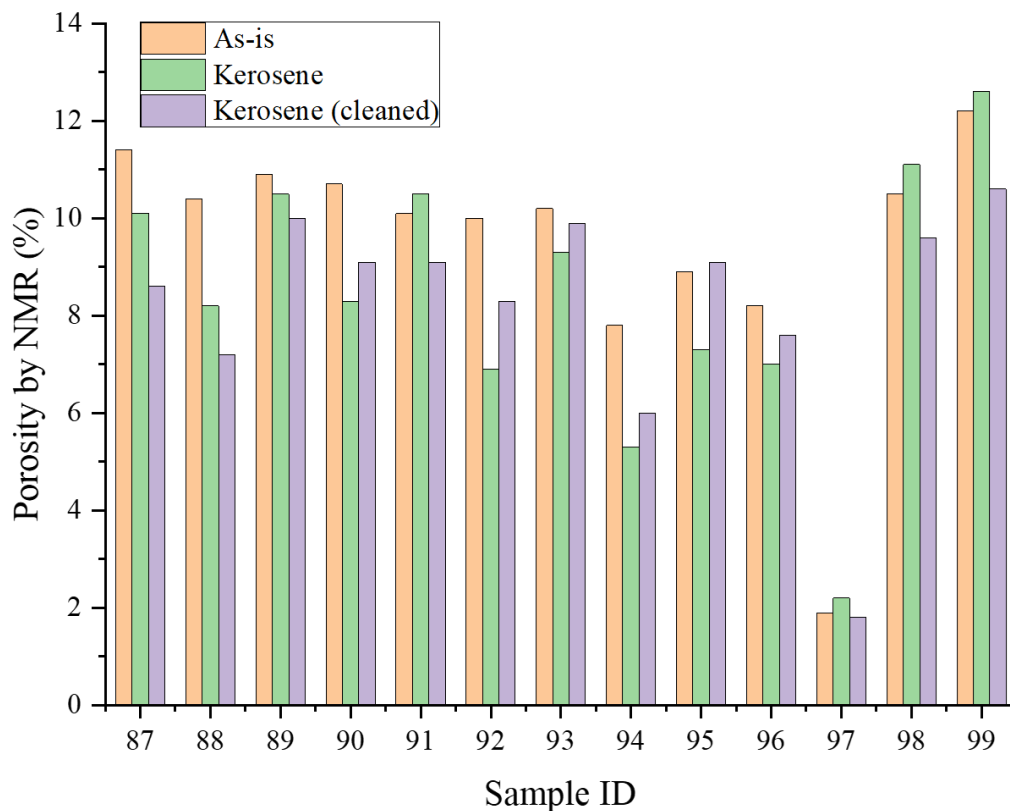


Figure 32: Porosity by NMR at different states of saturation.

The influence of solvent core cleaning for target samples was evaluated by comparing the porosity values for saturated samples before and after the aggressive cleaning with chloroform (Figure 33). The comparison illustrates that we do not observe a significant change in rock porosity after extraction, which is typical for conventional reservoir rock. It questions the importance of cleaning procedure within the main core analysis procedure for organic-rich shales. It should be noted that analysis of the change in porosity by NMR before and after extraction indicates reduced values of the total porosity after extraction. This is due to the removal of a significant part of the fluids (residual hydrocarbons) during the extraction process.

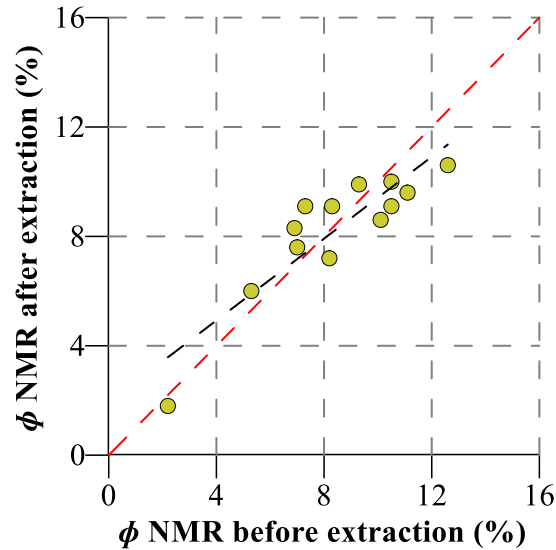


Figure 33: Porosity of samples before and after extraction.

Additional saturation of the samples with the brine model (20 g/L NaCl) is used to evaluate the reservoir properties of the rock, as well as to characterize the wettability of the samples at a qualitative level. The porosity of the samples saturated with the brine model varies from 11.7 to 16.6% for carbonate-siliceous-clay rocks (Figure 34). It is 1.8% for fine-grained limestones. Part of the collection (eight core plugs) were destroyed during the saturation process due to the high content of clay minerals which expanded and exploded when imbining the water.

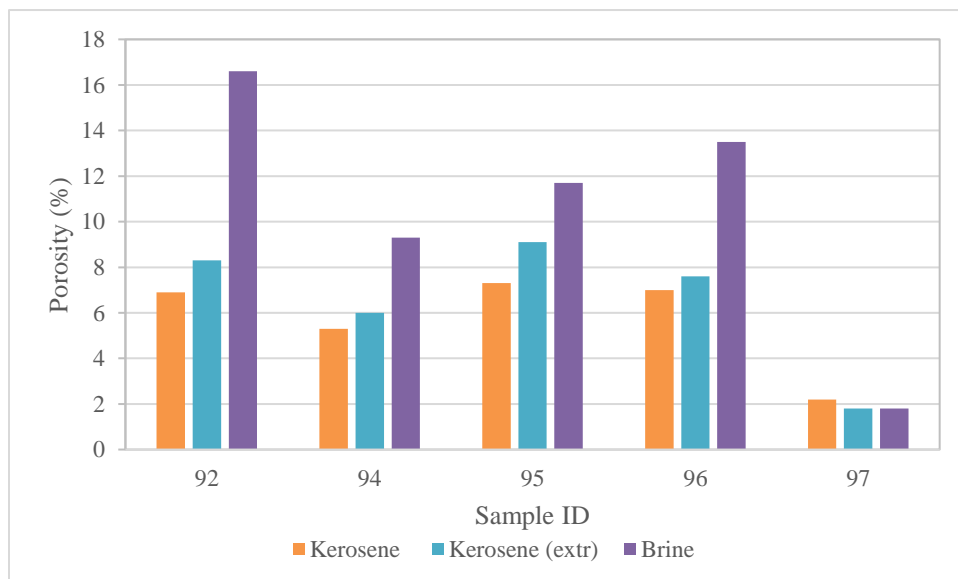


Figure 34: Comparison of kerosene and brine-saturated samples.

It is noteworthy that four out of five remaining samples are classified as siliceous-argillaceous rocks with a relatively low clay content (33–42%), whereas the fifth sample is characterized as fine-fine-grained limestone with minimal clay content (4.3%). In addition, the high porosity of brine-saturated samples can be explained by the occurrence of micro-crack and thin fractures in the matrix caused by clays extensively adsorbing water.

### 3.1.2 Fluid Interpretation by $T_1$ - $T_2$ map

For each sample,  $T_1$ - $T_2$  maps were constructed in all saturation states. Using GIT Advanced software, a qualitative and quantitative assessment of the fluid saturation of the sample was performed. A tool built into the software allows one to select a zone on the  $T_1$ - $T_2$  map and calculate the volume of fluid (in ml) corresponding to the zone, as well as estimate the percentage of the total volume of the fluid by NMR.

Thus, for samples in natural saturation, the residual (initial) oil and water saturation can be determined, and for samples saturated with water or kerosene — effective oil or water liquid saturation. By comparing the maps before and after extraction, the exact volume of the removed hydrocarbons, as well as the size of the occupied pores, are calculated. An example of  $T_1$ - $T_2$  maps is shown for Sample #95 in Figure 35.

Zones #1 and #2 correspond to the low-relaxation region, which typically corresponds to adsorbed oil and viscous HC. Those fluids are hosted by nano-sized or closed pores, as well as pores in an organic matrix. Zone #3 corresponds to large open pores filled with mobile fluids. Thus, all two-dimensional maps  $T_1$ - $T_2$  for the studied samples can be interpreted as follows:

1. Evaluation (qualitative and quantitative) of the removed volume of water and light hydrocarbons after drying of the rock (Zone #1). Identification of the adsorbed HC, including kerogen and bitumen signals.

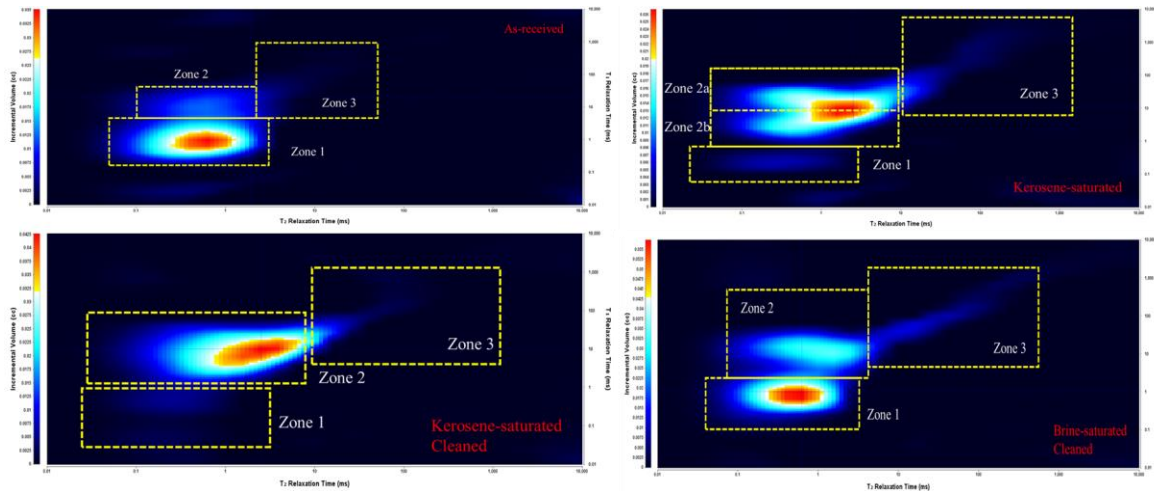


Figure 35: Two-dimensional map  $T_1$ - $T_2$  (from left to right: as-is saturation, saturated with kerosene before extraction, saturated with kerosene after extraction, saturated with brine model), Sample #95.

2. Determination of kerosene or mobile HC-hosting pores (maximum oil saturation, in %) for the stages before and after extraction. Identification of pore space (Zone #3) that is filled with kerosene during forced rock saturation by comparing the corresponding maps.
3. Comparison of kerosene saturation before and after cleaning to determine the volume occupied by viscous HC and dead oil (Zones #2a and #2b).
4. Additionally, a two-dimensional map  $T_1$ - $T_2$  for the brine-saturated sample can be used to define the pores occupied by the brine model (Zones #1 and #3). In the case of the absence of maps constructed after saturation with water), maps after drying can be used for evaluation of the adsorbed and mobile water.

### 3.1.3 Summary

NMR relaxometry was utilized for measurement of porosity, total and compositional fluid saturation on a collection of the Bazhenov Formation rock samples. The porosity of samples was defined at different stages of the saturation — as-received, kerosene-saturated, cleaned, and water-saturated. The conventional procedure of core analysis should be modified for the shale samples. The solvent cleaning step can be neglected for porosity estimation and may be removed from the core analysis workflow. The porosity of rock samples and fluid

saturation depends on the rock lithotype and mineral composition. The workflow of fluid identification by  $T_1$ - $T_2$  maps is demonstrated for rocks of the Bazhenov Formation.

## **3.2 Domanik Formation**

### **3.2.1 Experimental Methodology**

Integrated studies were conducted on a collection of 58 standard cylinders of  $30 \times 30$  mm size and irregularly shaped samples (paired with cylinders) of Oilfield #6, Domanik deposits. Rock reservoir and geochemical properties are described in Section 2.1.2.

Studies included different directions — evaluation of the cleaning (extraction) quality, wettability, the porosity of samples at different states of saturation, fluid identification by  $T_1$ - $T_2$  maps, determination of residual water saturation, and  $T_2$  cut-off. Therefore, the principal investigation scheme consisted of several workflows (workflows A–D, Section 2.3.4). All samples were saturated with the decane (reagent grade) and brine model using the capillary imbibition method and additionally resaturated under pressure. The duration of sample saturation was accepted as 72 hours and saturation pressure — 150 atm (limited by equipment). In contrast, variations in reservoir properties and non-uniformity of natural saturation of samples were not taken into consideration. Core cleaning was of two types: strong solvent cleaning (with chloroform) and aggressive cleaning ( $\text{CO}_2$  and toluene-based).

### **3.2.2 Porosity of Domanik Formation**

As a result of NMR studies,  $T_2$  relaxation spectra and 2D  $T_1$ - $T_2$  maps were obtained; detailed analysis made it possible to calculate saturation and evaluate the porosity of samples. Porosity variations at different stages of experimental operations for one of the samples are shown in Figure 36.

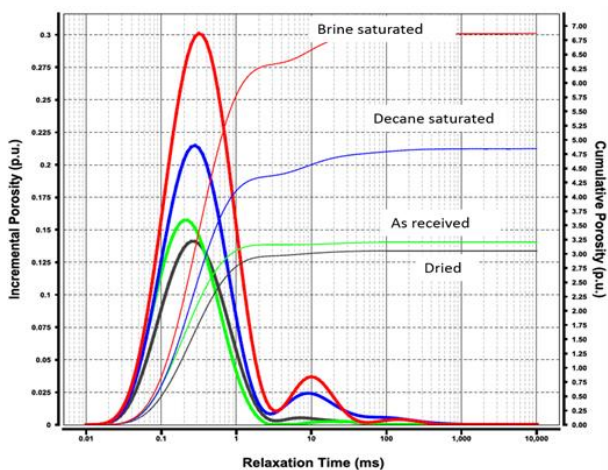


Figure 36: Variation of  $T_2$  relaxation for rock in a different state of saturation.

NMR measurements were conducted at four stages: NMR of non-cleaned samples; NMR of non-cleaned and decane-saturated samples; NMR of cleaned and decane-saturated samples; NMR of cleaned and brine-saturated samples (Table 11).

Table 11. Porosity by NMR at different stages of saturation

Sample ID	Porosity (as-is)	Porosity (decane)	Porosity (cleaned)	Porosity (cleaned, decane)	Porosity (brine)	Porosity (cleaned, brine)
	%	%	%	%	%	%
583	1.8	2.0	9.8E-1	2.8	2.0	2.0
686	1.0	1.0	3.2E-1	2.5	1.3	1.7
694	1.9	2.6	7.4E-1	3.2	4.7	3.1
703	1.5	1.8	5.9E-1	1.3	2.2	1.5
711	9.4E-1	1.4	1.3E-5	2.4	1.4	1.8
721	1.4	2.4	6.1E-1	2.0	3.1	1.4
740	1.4	1.6	6.7E-1	1.3	1.2	1.2
748	1.5	2.9	6.4E-1	3.5	3.5	1.5
800	1.4	3.1	7.5E-1	2.6	2.2	2.4
817	1.5	6.3	3.7E-6	8.4	10.8	-

It is noted that for most of the collection maximum NMR porosity values are characteristic for stage three, at which analyzed samples saturated with decane. After saturating the samples with the brine model, porosity reduction for some samples was observed; this might be

indirectly indicative of the dominantly hydrophobic character of the sample's wettability. Figure 37 illustrates changes in porosity according to NMR data of mean porosity for rocks of three different horizons within Domanik deposits of the Oilfield #6.

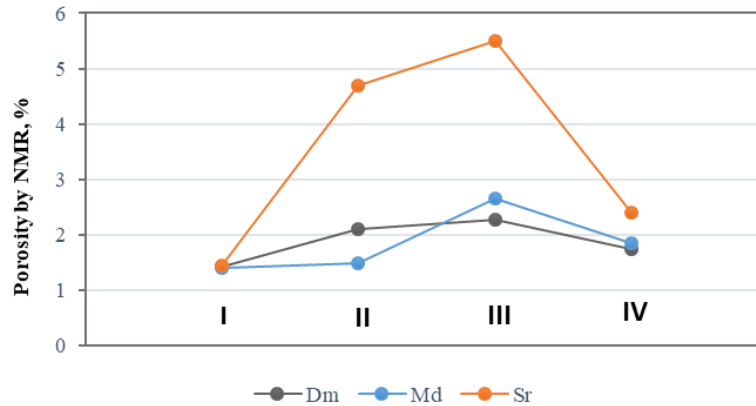


Figure 37: Variability of mean NMR porosity values for the Mendym, Domanik, and Sargay horizons of the Domanik oilfield with different fluid saturation (Stage I — samples are not cleaned; Stage II — non-cleaned samples are additionally saturated with decane; Stage III — samples are cleaned and saturated with decane; IV — samples are cleaned and saturated with brine). (Mukhametdinova et al. 2019)

In addition, we attempted to demonstrate the determination of the  $T_2$  cut-off for the residual water saturation of the samples in several ways. The calculation of the  $T_2$  cut-off from the relaxation spectrum is performed by comparing the  $T_2$  for the sample in the saturated state and at the residual water saturation. There are several ways to achieve residual water saturation for a 100% water-saturated sample:

1. Centrifugation of samples at the maximum speed (4500 rpm) with a constant volume change control;
2. Stage-by-stage drying of core samples in a drying oven at  $T= 60\text{--}80^\circ\text{C}$  with a sample weight control every 1 h;
3. Displacement of fluid with nitrogen using a semipermeable membrane method at a pressure in the range of 7–14 atm.

As a reference value, the data obtained on average residual water saturation of Domanik formation by the evaporation method was used. Comparison of the  $T_2$  curves allows one to

determine the  $T_2$  cut-off. All samples after drying, centrifugation, and capillarimetry were analyzed on an NMR unit. For seven samples, the standard  $T_2$  cut-off was determined using the built-in mathematical tools in the NMR software. The results of determining the  $T_2$  cut-off (mobile and residual fluids) are shown in Table 12. Cut-off values varied in the range of 0.4–31 ms with an average time equal to 9.4 ms.

Table 12. Determination of  $T_2$  cut-off for samples of Oilfield #6

Sample ID	Displacement method	$T_2$ cut-off (ms)
701	Centrifuge	7.8
707	Centrifuge	0.4
709	Centrifuge	3.9
717	Membrane method	31
723	Drying	16.5
766	Centrifuge	2.9
772	Drying	3.4
Avg.		9.4

Experimental determination of the  $T_2$  cut-off is used for a detailed analysis of the  $T_2$  relaxation spectra and highlighting the total and effective porosity. For example, for sample #723 with a  $T_2$  cut-off of 16.5 ms, the detailed fluid volume (and porosity) can be shown as below:

- Total NMR volume: 0.724 ml; Clay Bound Water (CBW): 0.010 ml;
- Effective Volume: 0.714 ml; BVI: 0.170 ml; FFI: 0.544 ml.

### 3.2.3 Fluid interpretation by $T_1$ - $T_2$

The important part of the studies of the Domanik Formation rocks is devoted to an analysis of 2D  $T_1$ - $T_2$  maps. Interpretation of maps is used to evaluate the void space filled with hydrocarbon fluids and dimensions of pores saturated in low-permeability rocks.

These 2D maps are used to calculate residual and effective oil saturation and water saturation of samples under investigation. Figure 38 presents the results of  $T_1$ - $T_2$  maps construction for

a representative sample of Lithotype 3 (Section 2.1.2), highlighting the changes in saturation and porosity at each experimental stage. Based on the comparison of  $T_1$ - $T_2$  maps before and after drying (Map 1, zone A), the initial oil and water saturation of the sample is determined. After saturating a sample with decane, effective oil saturation can be calculated (Map 2, zones A and B), and after extraction — the amount of non-removable HC and kerogen. A map for brine-saturated sample (Map 3 for mixed saturation and Map 4 for brine-only after core cleaning) allows evaluation of the water saturation and maximum water saturation of the rock.

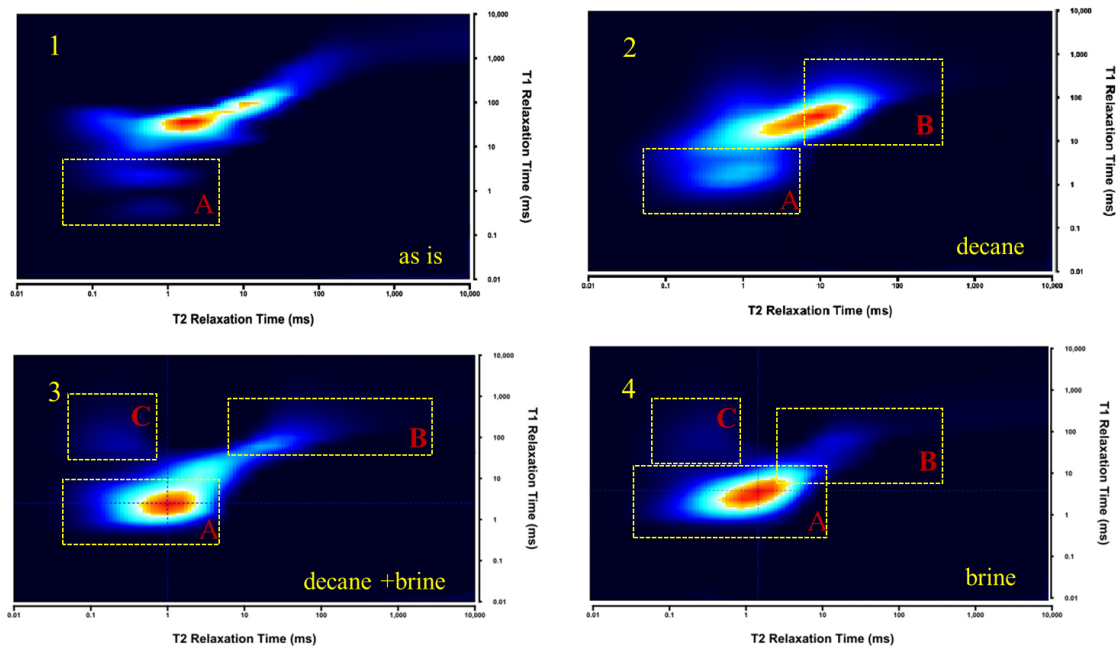


Figure 38:  $T_1$ - $T_2$  maps for Sample #702: 1) as-received 2) dried and saturated with decane, 3) cleaned and saturated with decane, 4) after repeated cleaning and saturated with brine. (Mukhametdinova et al. 2019)

### 3.2.4 Summary

Results of the Domanik Formation rocks investigation by NMR are presented in this section. The described methodology of NMR for applied collection allowed the proper characterization of core saturation at different stages of research. Results of  $T_2$  relaxation time distribution for the collection of samples from the Mendym, Domanik, and Sargay horizons showed that the porosity of samples varies from 0.94% to 10.8%. An increase in porosity values after extraction confirms the presence of a significant amount of high-

viscosity components in the samples before extraction. Maximum porosity was reached after solvent cleaning and saturation with decane. The utilized set of techniques for modeling residual water saturation was employed to determine the  $T_2$  cut-off value.  $T_1$ - $T_2$  map interpretation approach was demonstrated for a representative sample of the collection.

### **3.3 Comparison of NMR Results with Other Methods**

To define the reliability and applicability of the NMR technique for measuring rock saturation and porosity, it is crucial to correlate the experimental results by various methods obtained for the same samples. In this section, the comparison of NMR with other techniques is demonstrated.

#### **3.3.1 Comparison with Neutron Porosity Logging Data**

2-MHz laboratory NMR setups are often used for calibration of the well-logging tools working at the same Larmor frequency. Therefore, it is crucial to understand the reliability of laboratory measurements with the ones obtained by conventional logging tools. It is important to note that NMR logging is not widely used within a standard logging complex due to its high operation price and availability. For this reason, we compare laboratory NMR porosity results with the ones by gamma-ray neutron porosity logging tool. Neutron porosity logging is one of the classical porosity logging tools. It employs a neutron source to measure the hydrogen index in a reservoir, which is directly related to porosity. So, the obtained porosity also relates to the liquid-filled porosity of the rock.

For assessment of NMR comparison with porosity logging techniques, a significant number of samples is required. Therefore, we have selected a collection of bituminous sandstone samples which came with accompanying logging data and a significant number of core plugs available. The goal was to compare the results of laboratory NMR testing with well logging (gamma ray-neutron logging) data; more than 200 core plugs were tested and analyzed. NMR results for samples of Wells #7 and #9 are displayed in Figure 39. Porosity by NMR varies from 2.4 to 35%, with an average value of 22% (for Well #7) and 24% (for Well #9).

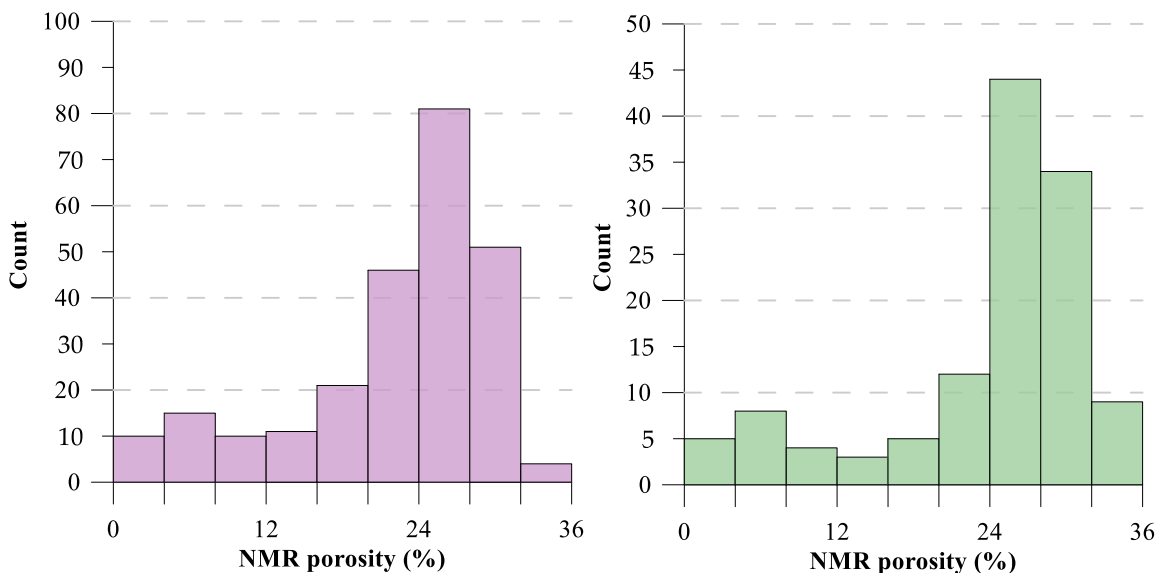


Figure 39: Porosity by NMR for Well #7 (left) and Well #9 (right).

Additional saturation of samples with kerosene led to an increase in porosity by 15–20% (relative). However, it should be noted that the use of kerosene led to partial removal of the original oil from the rock, which could distort the results obtained for saturated samples. Therefore, it is recommended to use NMR primary results for as-received samples. Thus, the data obtained by NMR most closely reflect the state of the rock in natural saturation in the reservoir. A comparison of NMR and logging data is shown in Figure 40. As can be seen from the graphs, the NMR shows good convergence with the data of Gamma-ray neutron porosity (GRNP) logging for most of the collection in the range from 20–30%, which are probed from the same depth interval. Slight deviations in porosity in the interlayers above and below the indicated interval can be explained by partial drying of core samples during transportation and preparation of the core material.

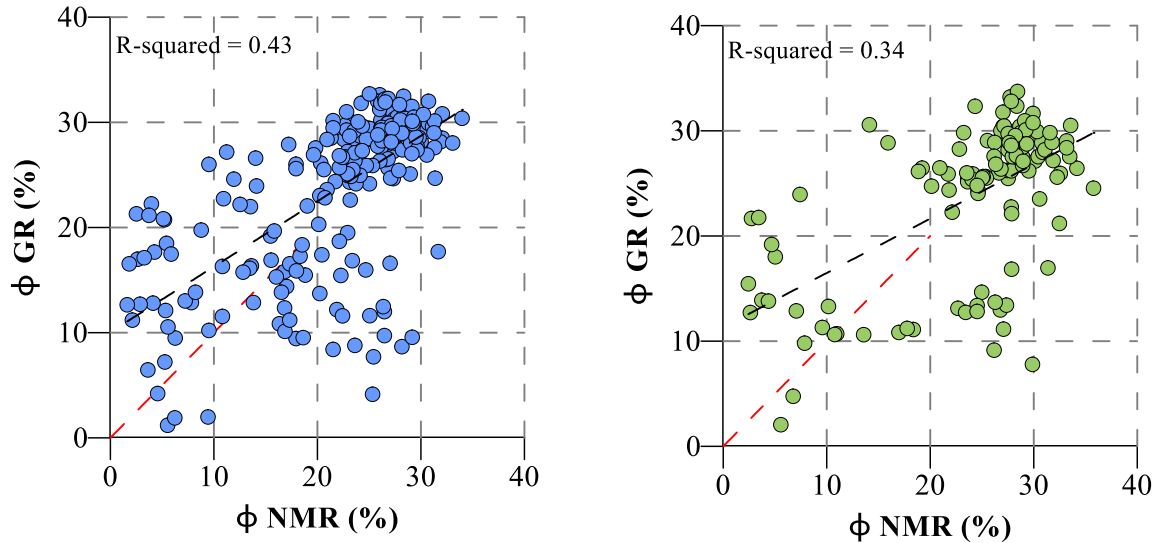


Figure 40: Comparison of porosity by NMR and GR neutron porosity logging for Well #7 (left) and Well #9 (right).

### 3.3.2 Comparison with Conventional Methods for Low-Permeability Rocks

For advanced petrophysical research of tight source-rock samples (Oilfield #6), we have a number of methods such as NMR (and LS method), MICP, and PDP for measuring porosity on core plugs. The full dataset is published in [Mukhametdinova et al. \(2020\)](#). Crossplots between NMR, LS, and PDP gas porosity demonstrated several features (Figure 41).

Firstly, we consider LS porosity and PDP gas porosity to be the same within the uncertainty of the method. It is known that LS, also often referred to as the gravimetric method, provides excellent results for rock with a distinct amount of open pores. In our case, the major shares are the tiny pores filled after saturation and liquid remaining on the surface when the sample is weighed.

Secondly, a comparison of NMR vs. PDP showed no clear correlation between NMR and *a priori* PDP data (gas porosity). *A priori* data is porosity and permeability data provided by an industrial operator. We explain the behavior by the low reliability of the PDP gas porosity.

In summary, we consider that PIK-PP (and its analogs based on PDP) provides uncertain gas porosity. The highest porosity values are obtained by the NMR method.

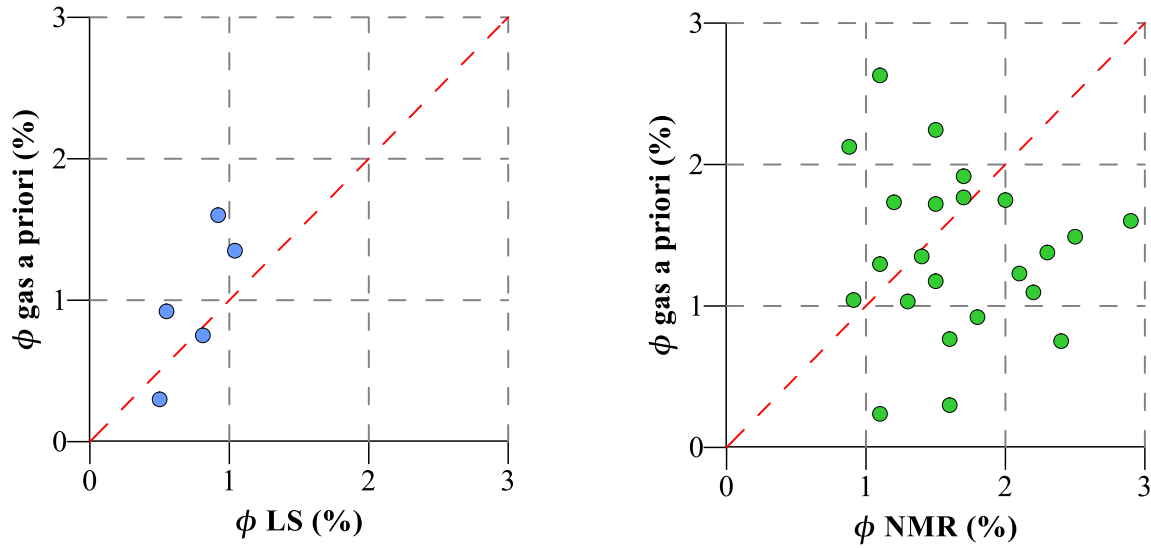


Figure 41: LS (left) and NMR porosity (right) crossplots for core plugs showing comparison with *a priori* data (Mukhametdinova et al. 2020).

Fourthly, LS provides values similar to the ones by gas porosity. The reason is initially low open porosity, which both of these methods at the same category in describing target samples. In addition, more methods were probed on whole core samples according to the scheme in Figure 23. Table 13 summarizes the results for two samples.

Table 13. Comparison of porosity measurement results for Oilfield #6

Fluid, technique, sample form-Factor & property	Whole core	
	#545	#551
Gas whole-core porosity ( <i>a priori</i> ) (%)	0.74	1.31
Kerosene NMR core-plug porosity (%)	1.20	2.30
MICP crushed-rock porosity (%)	1.60	1.80
Gas volumetric core-plug porosity (%)	0.62	0.84
Kerosene liquid-saturation core-plug porosity (%)	1.08	1.22

Thirdly, NMR tends to provide the highest porosity value (Figure 42, Table 13). We explain this observation by the technical capability of NMR to detect the full range of pores — from nano-sized pores filled with high-viscous components to large voids occupied by mobile

fluids. Pore size radii captured by low-field NMR typically is in the range of 10 nm–10  $\mu\text{m}$  (Yao and Liu 2012, Lyu et al. 2018).

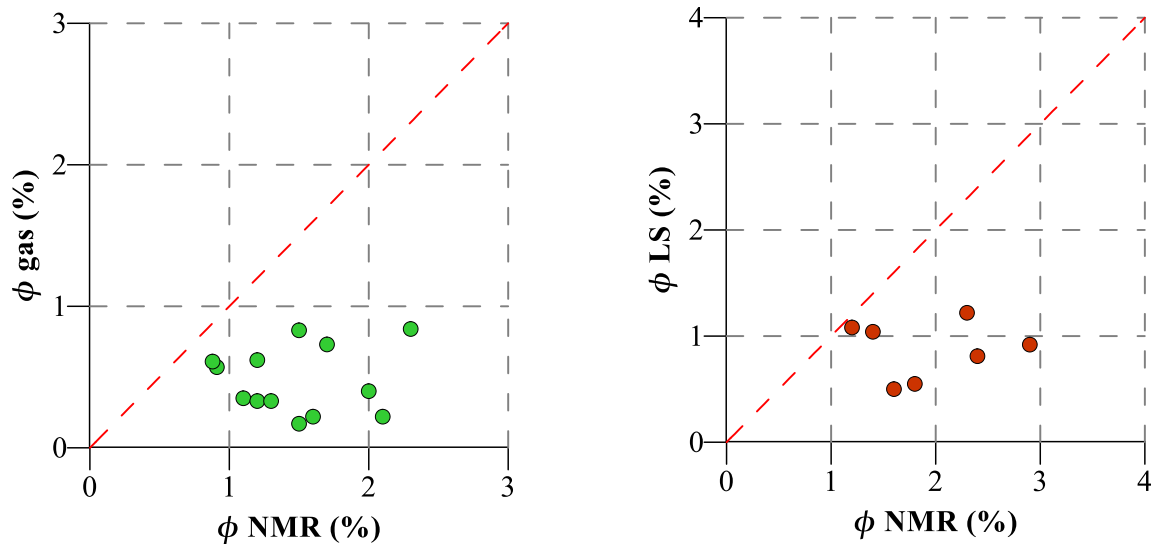


Figure 42: NMR vs. PIK-PP (left) and LS (right) comparison (Mukhametdinova et al. 2020).

### 3.3.3 Comparison with Conventional Methods for Organic-Rich Source Rocks

Collection of 13 samples of Oilfield #1 were analyzed in the extracted (by aggressive cleaning) for g and kerosene-saturated states. It can be seen from the graph that the most considerable convergence is expected to be shown by NMR and liquid saturation methods. The gas porosity values repeat the general trends but are lower than the NMR porosity by 25-40% (Figure 43). This may be due to the presence of closed pores and pores in the organic matter not removed during extraction. For extracted samples, the LS and NMR show good conformity in porosity results.

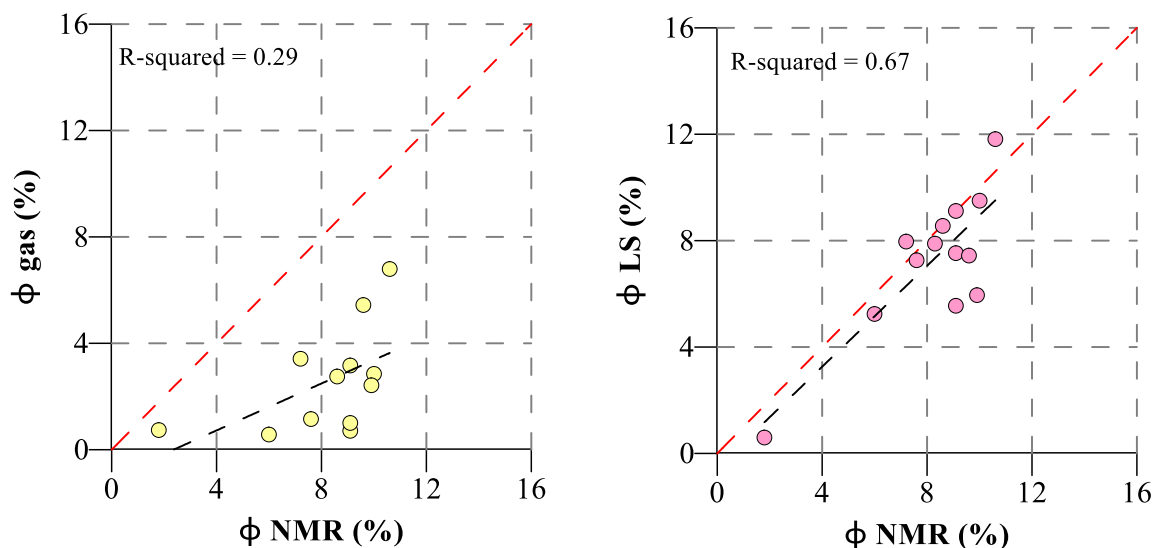


Figure 43: Comparison of gas (left) and LS (right) vs. NMR for Bazhenov rock samples.

### 3.3.4 Comparison with Conventional Methods for Carbonate Rocks

We have investigated 33 high-cavernous carbonate core plugs. The porosity by NMR varied in the range of 4.68–19.41%, with an average value of 11.24%. The porosity by NMR shows good convergence with other laboratory methods — liquid saturation and PDP using helium (Figure 44).

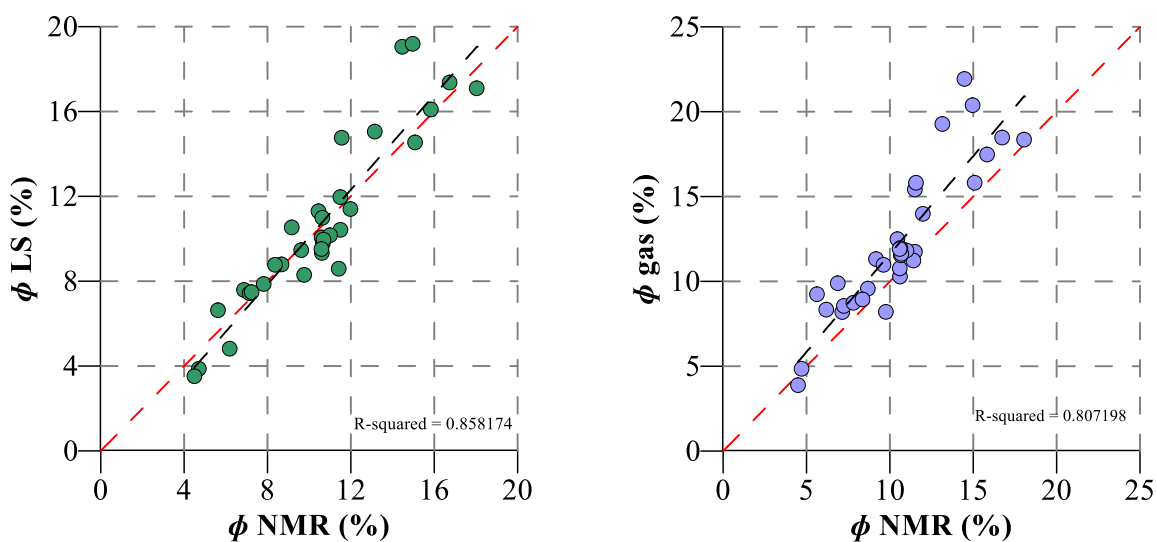


Figure 44: Comparison of LS (left) and gas porosity (PDP) (right) with NMR porosity for carbonate rock samples.

Recalculation of  $T_2$  relaxation time to pore size was carried out, taking into account the surface relaxivity coefficient ( $\rho = 0.01 \mu\text{m}/\mu\text{s}$ ) according to published data for carbonate rocks. Calculation of pore size distribution based on NMR and capillarimetric studies showed comparability of the results. The resolution of the NMR method is significantly higher than the resolution of X-Ray tomography on standard-sized core plugs (Figure 45).

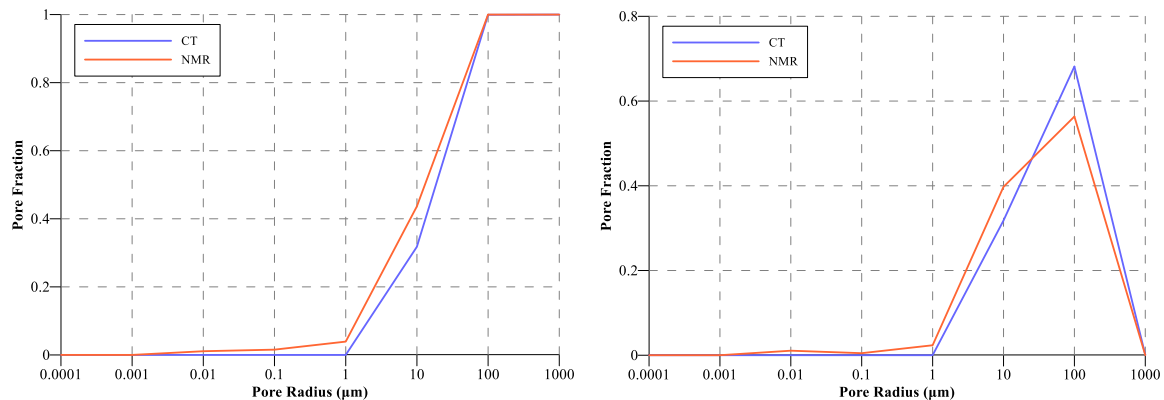


Figure 45: Comparison of incremental (left) and cumulative pore (right) size distribution by NMR (red) and X-ray CT (blue) for carbonate rock sample.

In a different study on rock porous structure assessment for outcrop carbonate rocks, we have compared a number of the most-advanced laboratory methods (Razavifar et al. 2021). We utilized NMR, gas porosimetry, MIP, and micro-CT. Based on the experimental results, we compared the pore size distributions for a single core (Figure 46).

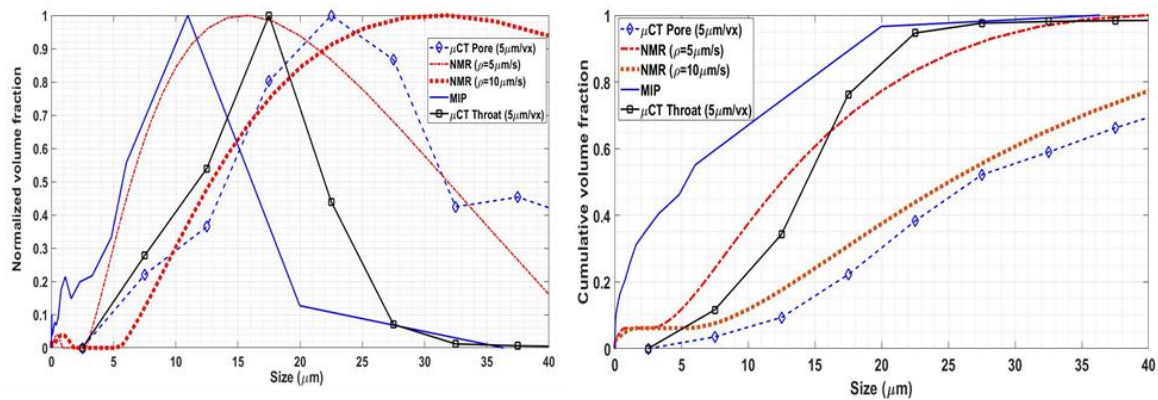


Figure 46: Normalized (left) and cumulative (right) volume fractions obtained from various techniques (Razavifar et al. 2021).

We revealed that the pore size distribution obtained from other methods such as NMR and MIP (MICP) is considerably different from real pore size distribution. The results of NMR

and MIP would rather provide an estimation of the throat size distribution, which without pore size distribution, fails to give a complete characterization of the porous skeleton. Therefore, either the bundle of capillary conceptualization used to interpret MIP and NMR techniques has to be modified to result in both pore and throat size distributions, or imaging has to be considered as an inevitable part of any porous media characterization process.

### **3.3.5 Summary**

In this section, we discussed the difference between NMR and other laboratory techniques for analysis of the porosity and pore size in a variety of rock types – organic-rich source rocks, tight and cavernous carbonates. NMR results were first compared to neutron porosity logging data and showed good convergence. For source-rocks, in comparison with LS, conventional gas porosimetry and MICP, and NMR tends to provide higher values. In the case of shale samples, it can be explained by NMR registering the closed and disconnected pores or fluids of high viscosity. For carbonates, the same tendency is caused by a wider range of detected pores in the rock. NMR pore size distributions for carbonates can be tuned by data from micro-CT and MICP. However, a more detailed comparison showed that the MICP is a more reliable method for tuning the surface relaxivity coefficient in NMR studies.

### **3.4 Wettability by NMR Relaxometry**

The wettability of the reservoir rock is one of the most critical factors affecting the residual saturation and flow properties in the formation. However, as multiple petrophysical studies showed, traditional laboratory methods for characterizing wettability are not applicable for low-permeability source rocks.

Wettability is an ability of a rock surface to interact with a reservoir fluid molecularly, and it is one of the essential characteristics associated with the development of oil and gas fields and reserves estimation (Morrow 1990, Ogunberu and Ayub 2005). The nature of the rock surface wettability in the reservoir significantly affects the residual saturation, total recovery factor, etc. The preliminary recovery of fully or partially hydrophobic reservoirs leads to an artificial overestimation of the residual water saturation when estimated by indirect methods.

According to the literature data, wettability in shales is characterized by mixed wet properties, controlled by numerous factors such as total organic carbon content, organic matter maturity, mineralogical composition, porosity, pressure, temperature, and brine salinity. Rui Yang (Yang et al. 2018) reports that samples of marine Longmaxi shales with higher TOC and quartz content are characterized as predominantly oil-wet. Xuan Liu (Liu et al. 2018) emphasizes that the main factors controlling the wettability of Longmaxi shales are migrating organic matter and clay minerals: increasing migrating organic matter leads to oil-wet behavior of the rock; the same is true for illite and smectite components. Moreover, they mentioned that if TOC content is less than 1.5%, then the main controlling factor is clay mineral content, and if TOC content is higher 1.5% TOC and organic matter uniformly developed and distributed — content TOC plays key role in wettability behavior. At the same time Eric J. Guiltinan (Guiltinan et al. 2017) showed that TOC and OM thermal maturity have no significant effect on Barnett Formation shale samples wettability, which may be a demonstration of mineral heterogeneity. Archana Jagadisan and Zoya Heidari (Jagadisan and Heidari 2019) experimentally found that the wettability of the kerogen is a function of OM maturity: at high thermal maturities, kerogen is strongly oil-wet when at low thermal maturity, kerogen is predominantly water-wet. Bin Pan (Pan et al. 2020) with coauthors are quite categorically state that with increasing TOC behavior of shale samples are more oil-wet when increasing temperature leads to water-wet, but increasing of TOC reduces the influence of temperature on shales. Salinity is a different factor that influences the wettability behavior of shales; it is shown in (Safari et al. 2020) and (Liu et al. 2020): with decreasing brine salinity with NaCl contact angle decreases, when decreasing of concentration of MgCl<sub>2</sub> leads to the opposite effect.

There are multiple conventional methods for assessing the wetting properties of shale rocks in laboratory conditions, but obtained results are often contradictory and difficult to reproduce. Mainly they are based on the phenomenon of the capillary imbibition (Amott, (Amott 1959)), capillary displacement (USBM, (Donaldson et al. 1969)), microscopic techniques, and a combination of few methods (Abdallah et al. 2007). The abovementioned experimental methods are widely known for characterizing the wettability for sandstone and carbonate formations (Thyne 2015, Ivanova et al. 2019).

Determination of wettability for shale rocks is complicated due to the low rock permeability (< 1 mD), low porosity (< 3–5 %), and a high content of clay and highly viscous components. To increase the accuracy of wettability evaluation, shale rock assessment requires an integrated approach composed of different laboratory methods. Nuclear magnetic relaxometry has gained high interest in the last 20-30 years due to the non-invasiveness and prompt testing and characterizing the primary reservoir properties, including the wettability of the source rocks (Odusina et al. 2011, Valori and Nicot 2019).

In the framework of this work, the fluid saturation and wettability of Abalak and Bazhenov rocks were analyzed employing the adsorption method, NMR, as well as by determining the wetting contact angle of the rock surface. Microlithological and microstructural study of rocks was carried out using thin (less than 7 microns) petrographic sections.

### 3.4.1 Experimental Methodology

Abalak-Bazhenov group is represented by the Abalak Formation (AF) and Bazhenov Formation (BF). Detailed information on the target oilfield (Oilfield #1) is provided in the Materials chapter, Section 2.1.

To study the wettability of the Abalak-Bazhenov group (ABG) rocks, we have proposed a combination of three laboratory methods: water vapor adsorption, contact angle measurement, and NMR. Details on experimental techniques are provided in Section 2.2.

Wettability characterization by NMR was based on the calculation of the logarithm of the ratio of the average logarithmic times  $T_2$  for water- and kerosene-saturated samples after extraction (Borisenko et al. 2017):

$$W_{nmr} = \log \frac{T_{2lm\ oil}}{T_{2lm\ water}}, \quad (1)$$

Values of  $W_{nmr}$  index vary from -1 to +1; negative values indicate the oil-wet, near-zero, and positive values correspond to a neutral and water-wet character. For the convenience of comparison with the WI by the adsorption method,  $W_{NMR}$  can be recalculated in the range from 0 to 1 so that zero value corresponds to water-wet, 0.5 to neutral wettability, and values about 1 to oil-wet.

$$WI = 1 - \frac{W+1}{2} \quad (2)$$

Where  $W_{nmr}$  and  $WI$  are wettability indexes and  $T_{2lm \text{ oil}}$  and  $T_{2lm \text{ water}}$  – logarithmic mean  $T_2$  times for oil and water-saturated samples, accordingly. The current approach is based on the alteration of the  $T_2$  relaxation time spectra under the influence of saturation fluid (Foley et al. 1996).

A measure of wettability is considered to be the wetting angle, depending on the size of which the surfaces are divided into hydrophilic and hydrophobic.

For water-oil shown in the figure below, surface energies are distributed according to the Dupre-Young equation extensions:

$$E_o - E_w = E_{ow} \cdot \cos \theta \quad (3)$$

where:  $E_o$  — surface binding energy between oil and rock surface (dyne/cm);  $E_w$  — binding energy between water and a solid surface (dyne/cm);  $E_{ow}$  is the binding energy between water and oil, (dyne/cm);  $\theta$  — contact angle at the oil-water-solid surfaces, measured from the waterside (deg). There are no methods for the direct determination of  $E_o$  and  $E_w$ . Still, the equivalent value of  $E_o - E_w$ , i.e.,  $E_{ow} \cdot \cos \theta$  can be obtained by independent measurement of  $E_o$  and, thus, characterize the rock wettability. Contact angles of less than  $90^\circ$  determine the predominant water-wet surface, whereas the limiting case ( $\theta = 0^\circ$ ) shows that the movement of oil by water from the surface will be spontaneous and will not require external forces. On the contrary, the condition  $E_o < E_w$  leads to variation of  $\theta$  angle from  $90^\circ$  to  $180^\circ$ . Therefore, contact angles greater than  $90^\circ$  determine the predominant wettability of the surface with oil; otherwise, it indicates hydrophobicity of the surface.

For the contact angle measurement, core plugs were probed, and fresh-cut plug faces were polished for a smooth surface. The contact angle was defined in an air-water-flat surface system for dry core samples. Measurements were conducted in ‘native’ state of the rock saturation and after cleaning with chloroform in the Soxhlet unit. A drop of distilled water is dripped from a pipette onto a flat surface of the cylindrical core sample (flat and homogeneous) (Figure 47).

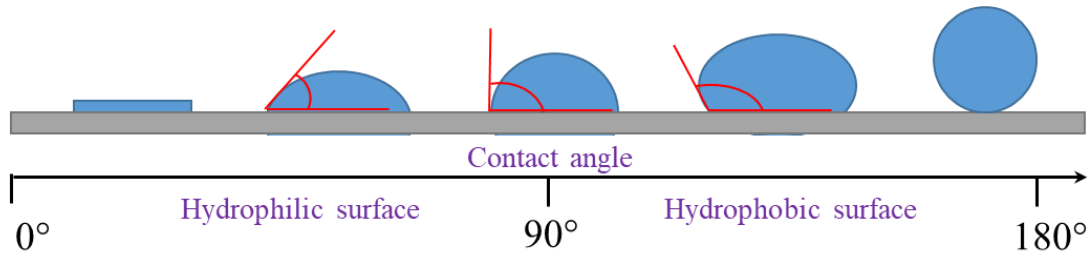


Figure 47: Contact angle on the rock surface

The photo recording of the droplet shape on the cylinder face is performed 10 seconds after application. Using the ImageJ software package, the diameter and length of the drop are determined, and the wetting contact angle is calculated by the following equation for the idealized rock surface:

$$\alpha = \arcsin\left(\frac{L}{D}\right), \quad (4)$$

where  $\alpha$  – wetting angle,  $L$  – drop width, and  $D$  – diameter of the drop.

The vapor adsorption method is convenient for the simultaneous study of a large number of crushed core samples of rock. The sample of 20-30 g is crushed to pieces with a 3–5 mm mesh size and divided into two equal probes (Gudok and Bogdanovich 2007a). Samples are dried to constant weight at 75°C in the vacuum; the first probe is extracted in a Soxhlet apparatus with the chloroform, while the second probe remains in the same state. For vapor adsorption, both probes are located into desiccators containing salty brines that maintain a precise relative humidity at a constant temperature of 25.0°C±0.2. Monitoring in changing the mass of samples during the experiment is conducted 1–2 times a week until the weight of the sample is stabilized; recalculation of the adsorbed vapor is carried out according to the formula:

$$\alpha = \frac{(m_{ad}-m_d)}{18*m_c} * 10^3 \quad (5)$$

where  $m_d$  — the weight of dry rock sample;  $m_{ad}$  — the weight of the sample with adsorbed water at a given value of relative humidity. Based on the obtained values, adsorption isotherms are constructed for each sample. The wettability coefficient of the rock surface is determined by the ratio:

$$WI = \frac{(a_{ex} - a_{nex})}{a_{ex}}, \quad (6)$$

where  $a_{ex}$  and  $a_{nex}$  — adsorption values on extracted and non-extracted surfaces, respectively.

### 3.4.2 Results

By standard gas porosity and permeability measurement, we observe that the open porosity of target collection falls into 0.5–7.1% range, and permeability varies from 0.01 to 0.7 mD. Petrographical characterization of thin sections and XRD showed that according to the classification proposed by Lazar ([Lazar et al. 2015](#)), the target collection of ABG rock samples are composed of different types of siliceous mudstones which are enriched with OM (Figure 48). Samples are mostly homogenous in mineral composition; therefore, lithotyping was performed based on specific peculiarities such as TOC, texture, pyrite fraction, bioturbation, and presence of carbonates. The main component of the rock is clay minerals ranging in the 40–58% range with 51% on average; the second rock-forming mineral is quartz — 25–45% with an average value of 31%. Other components are carbonate minerals (< 5%) and pyrite (< 5%). We have differentiated eight main lithotypes in the collection (Table 14). Rock-Eval analysis has shown that the content of TOC is moderately high and varies between 1.4–11% wt, with an average of 5.75% wt. in organic-rich layers.

Table 14. Lithotypes of the studied collection

Code	Lithotype
L1	argillaceous-siliceous mudstone with siltstone
L2	calcareous-argillaceous mudstone with bioturbation and organic detritus
L3	siliceous carbonaceous mudstone with single radiolarians
L4	microcrystalline limestone
L5	calcareous-siliceous carbonaceous mudstone
L6	siliceous carbonaceous mudstone with pyrite
L7	siliceous carbonaceous mudstone with lenticular structure

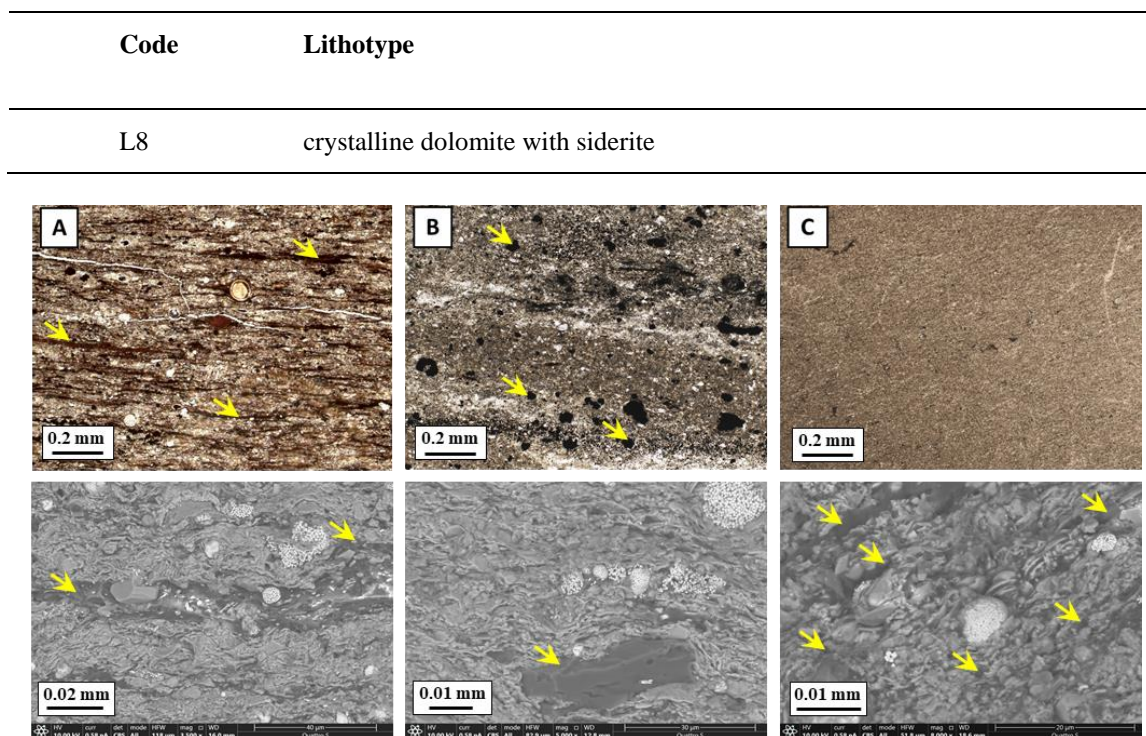


Figure 48: Primary shapes of OM in rock samples by results of thin-section microscopy and SEM (arrows indicate the OM inclusions). (Mukhametdinova et al. 2020)

The dominant difference along the section is the texture of the organic matter in the rock. We have identified three primary morphologies of OM present in the investigated set: dispersed, laminated, or in the form of inclusions. To illustrate the microtextural details of OM in the rock, we have selected three thin sections and SEM images corresponding to the same category of OM appearance (Figure 48). Category A is characterized by OM distributed by layers in the form of frequent extended thin veins and lenses (Figure 48A); their size reaches a width of up to 0.05 mm, a length of up to 1–2 mm. Type B corresponds to samples in which the OM is distributed unevenly in the form of inclusions of 0.05–0.1 mm in size (Figure 48B) and less often in the form of single veins. Finally, type C is a group of samples with a uniform finely dispersed OM distributed over the rock (Figure 48C). It is essential that OM may be present in all distinct forms in one sample, but we have observed that almost in all cases, one of the textures significantly dominates.

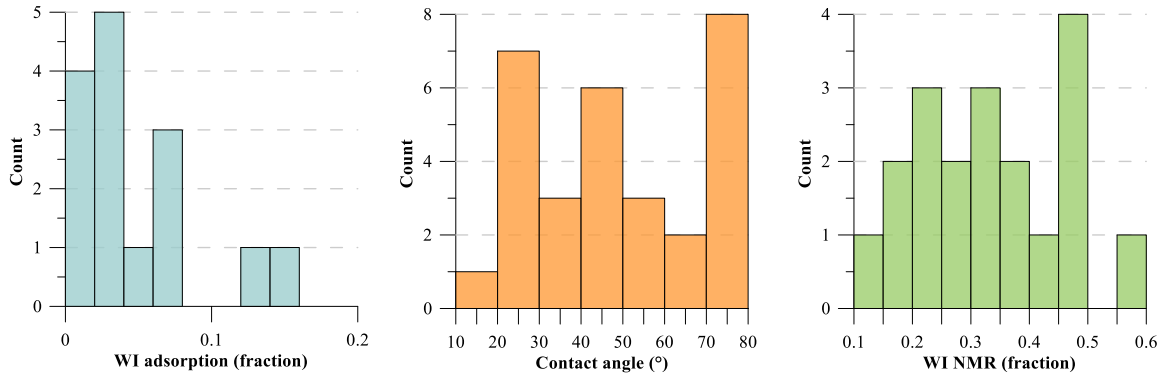


Figure 49: Wettability determination by different methods (Mukhametdinova et al. 2020).

In this experiment, 20 samples of ABG rocks (Oilfield #1) before and after extraction were examined by vapor adsorption isotherms. The wettability index was estimated according to the introduced methodology and illustrated the predominantly hydrophilic surface of the rock (Figure 49a) with a *WI* ranging from 0.003 to 0.144. Results of wettability estimation by vapor adsorption significantly depend on the cleaning of the rock: duration, solvent, and overall quality of OM extraction. Therefore, the indecent extraction of core samples may lead to the similarity of the adsorption isotherms for cleaned probes, *i.e.* result in low values of wettability index and cause uncertainty in wettability estimation.

The wetting contact angle was estimated for the set of 30 core plugs (Figure 49b). Measurements were conducted before and after the core extraction. Results show that the wettability angle of the core in the as-received state varies in the range of 19–79 degrees, which indicates the hydrophilic rock surface. The angle cut-offs of 0° and 90° were established for idealized rock surface; therefore, new criteria were set to describe the hydrophilicity of the rock surface (Fanchi 2002). We implement the differentiation for strong water-wet (SWW if  $0 < \alpha < 30^\circ$ ), moderate water-wet (MWW if  $30^\circ < \alpha < 60^\circ$ ), and weak water-wet or neutral-wet (NW if  $60^\circ < \alpha$ ) characterization of the surface.

In the framework of NMR analysis, the  $T_2$  relaxation curve was derived for 25 measured core plugs. Due to high-pressure manipulations, few samples (6 plugs) disintegrated during extraction and the following saturation. Thus, NMR wettability was estimated for 19 core plugs in total (Figure 49c). Wettability index (*WI*) is estimated according to Eq. (2) varied from 0.15 to 0.58, with an average of 0.33, indicating the prevailing water-wet rock behavior.

Comparable to contact angle interpretation, we have subcategorized the SWW (0–0.25), MWW (0.25–0.5), and WWW or neutral-wet (NW > 0.5) groups.

### 3.4.3 Influence of Rock Lithotype and OM Properties on Rock Wettability

All utilized methods characterized the target core collection as dominantly water-wet rock, varying from SWW to NW for various samples. Published works on Bazhenov Formation noticed mixed or mosaic behavior of the rock wettability (Bogdanovich et al. 2017). It occurs because of the complicated lithological structure and geochemical properties of the OM, mainly due to the high amount of kerogen. For high-porous media, it can be related to the minerals that make up the rock, for instance, quartz, clay, and carbonate minerals (Song et al. 2018). For shale rock, the wettability depends on both the rock matrix and OM properties, including the lithotype characteristics (mineral composition, structure, and texture) and amount of kerogen, its maturity, and type of OM. Target shale samples are characterized with low-to-moderate maturity OM with  $T_{\max}$  values from 429 to 442°C with an average of 437°C, which corresponds to 0.5–0.85%  $R_o$ .

Within the scope of the current communication, we research the correlations between the experimental results and OM content, TOC, rock type, and OM morphology. The main rock-forming components of the investigated samples are clay minerals, quartz, and OM. In our case, the amount of clay minerals and quartz is quite stable from sample to sample. Relative homogeneity in mineral composition means that clays and quartz should not significantly influence wettability. In most cases, OM is characterized as hydrophobic, which means that its variations may cause significant differences in the wettability coefficient (Iglauer 2017). OM has variable morphologies in different samples, which leads to serious inconsistency between measurement techniques. For example, the horizontal lenticular texture of the OM is the reason for anisotropy of shales (Sayers 2013, Yan and Han 2013), which appears in many petrophysical properties (permeability, acoustic properties, etc.), and wettability is not an exception.

Firstly, we have examined the influence of TOC and rock lithotype on obtained wettability indices. Results of water vapor adsorption on the target rock samples showed a robust water-wet surface. The cross-plots illustrate no clear correlation between the adsorption wettability

index and TOC (Figure 50a). It may be reasoned by a moderate amount of OM (including insoluble kerogen), which does not allow the full removal of OM during solvent extraction. Nevertheless, Figure 50a demonstrates that sample lithotype is a significant factor in the current discussion. For instance, increasing the wettability index with growing value for TOC is clearly shown for L2 lithotype — calcareous-argillaceous mudstone with bioturbation and organic detritus. Other lithotypes, namely L6, L1, and L3–L5, show similar (for a certain lithotype) behavior, but the number of measured points is not enough to highlight and confirm the trend. In summary, only microcrystalline limestone (L4) has relatively high WI, which may be explained by the influence of its calcareous composition. It is important to note that the most kerogen-enriched lithotypes L6 and L3 show the opposite trend that is reasoned by the presence of non-removed solid OM in the rock (kerogen), which remains after solvent cleaning.

Results of contact angle measurements (Figure 50c, d) show that in the majority of cases, increasing TOC leads to a higher wettability angle for the target collection. Based on the lithotypes of the rock samples, we can differentiate the groups with similar behavior — distinct clusters for L1, L2, L5, and L6. After extraction (Figure 50d), we observe the visible effect of OM removal on L1, L3, L5, and L6 samples, which initially contained a moderate amount of OM. Hence, the general linear trend after extraction does not change significantly and is characteristic mainly for L5 and L6 — both carbonaceous mudstone — the slope sharpens after the extraction. It, therefore, confirms the importance of mineral composition as one of the wettability forming factors. L1, L2, and L3 clusters show low sensitivity for TOC values with the values of contact angle in the range of 10–80 deg.

We attempted to highlight the clusters for NMR measurements (Figure 50b) by the same lithotyping classification. Similar to the contact angle results, L5 and L6 show a linear dependence of TOC and WI. The distinct groups are formed by L1, L2, and L4; L4 (limestone) again tends to have the most hydrophobic character. The strongest hydrophilicity or strong water-wet rocks include L2 and L7 — argillaceous and siliceous mudstones.

Secondly, in addition to the rock type and mineral composition, we have distinguished three distinct categories of OM occurrence by means of optical and electron microscopy (A, B, C

in Figure 48). The samples where two categories prevail uniformly were marked as a category D. To analyze the possible impact of OM morphology on wettability results, we have plotted the TOC vs. WI adsorption/ WI NMR/ Contact angle correlations indicating the predominant type of OM occurrence for each measured point (Figure 51). For adsorption (Figure 51a) and NMR results (Figure 51b), we observe the poor differentiation for all three categories; the most distinct ones are samples, which belong to A cluster (layered distribution) — with an inherently high value of TOC and low sensitivity of the WI to the TOC value. The mixed occurrence of categories B (large inclusions) and C (dispersed distribution) may be reasoned by the technique specifics. In the case of water adsorption, we deal with the core matrix in the form of the crushed core, where the influence of OM texture is minimized. For NMR analysis, we utilize the standard core plugs and provide an estimation of the wettability index as an integral characteristic.

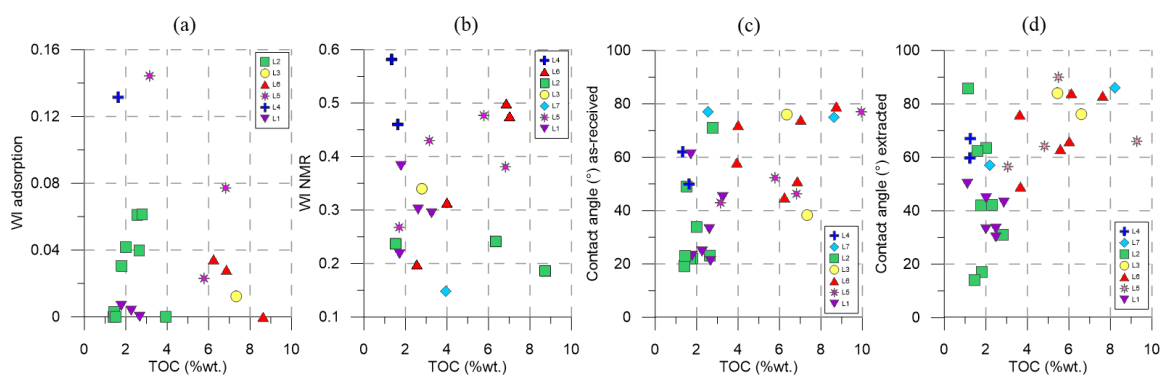


Figure 50: Crossplots showing correlations of TOC vs. (a) WI adsorption; (b) WI NMR; (c) contact angle in as-received state; (d) contact angle for extracted rock with an indication of the lithotype (Mukhametdinova et al. 2020).

The influence of the OM distribution form is demonstrated on measured contact angles. For the rock in the as-received state, we can distinguish the separate clusters for A, B, and C categories with a slight overlapping of the OM forms in the zone of high TOC values (Figure 51c). After the solvent cleaning, a certain amount of OM is removed, and it results in a more homogeneous distribution of point (Figure 51d). Primarily, the OM is extracted out of the thick layers (A) and relatedly large inclusions (B), which affect the previous correlation and remove the focus to rock matrix as a rock wettability forming factor. The sensitivity of results to the core extraction may also be caused by the physical principles of

the technique, which is based on the surface wettability measurement. Despite the routine procedure of solvent extraction, core plug faces are most exposed to the solvent.

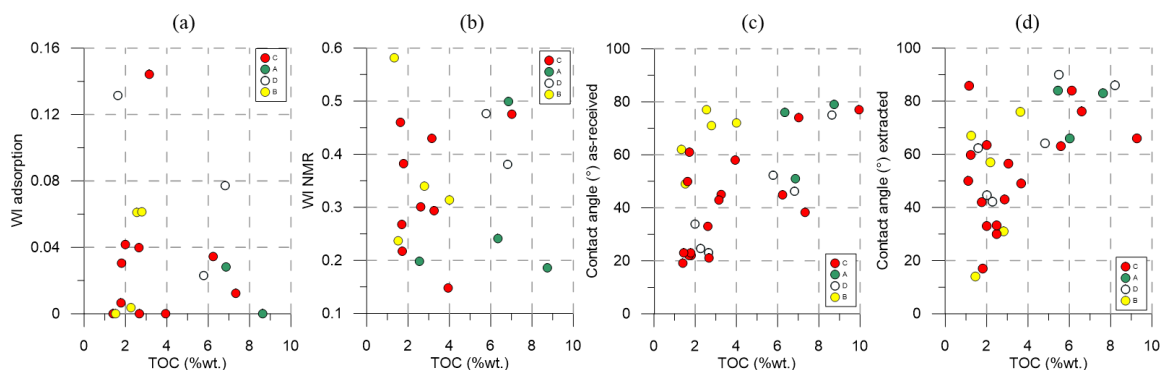


Figure 51: Combination of results by different methods over the target section (Mukhametdinova et al. 2020).

The results of evaluating the ABG rocks' wettability by the combination of laboratory techniques are illustrated in Figure 52. The wettability indices obtained by the water adsorption method correspond to a strongly water-wet surface over the entire section, which does not contradict previous studies (Bogdanovich et al. 2017, Borisenko et al. 2017). Hence, the adsorption isotherms and close-to-zero values of the wettability index confirm that the application of this technique is limited due to the remaining kerogen in rock.

Contact angle and NMR wettability techniques exhibit the same water-wet characteristic, but their results (wettability indices) describe the rock surface in a broader range of wetting behavior. Due to the complexity of the rock matrix, OM properties, and high anisotropy of shales, labeling the rock as fully water-wet or hydrophilic leads to high inaccuracy in rock characterization. This classification is used to detail the wettability of the rock surface by results of contact angle measurement and NMR. In wettability determination, the contact angle may vary on the different core planes with respect to the bedding of OM.

In our case, the contact angle was measured on the plane parallel to the bedding. OM inclusion on that plane occupies more area in comparison to the plane perpendicular to bedding. As a result, rock wettability is biased toward hydrophobic behavior. We suggest that this effect is illustrated for the rocks with lenticular OM and characterized with the

highest contact angle. In contrast, according to the NMR technique (the result does not depend on the sample orientation), these samples are characterized by the lowest *WI*.

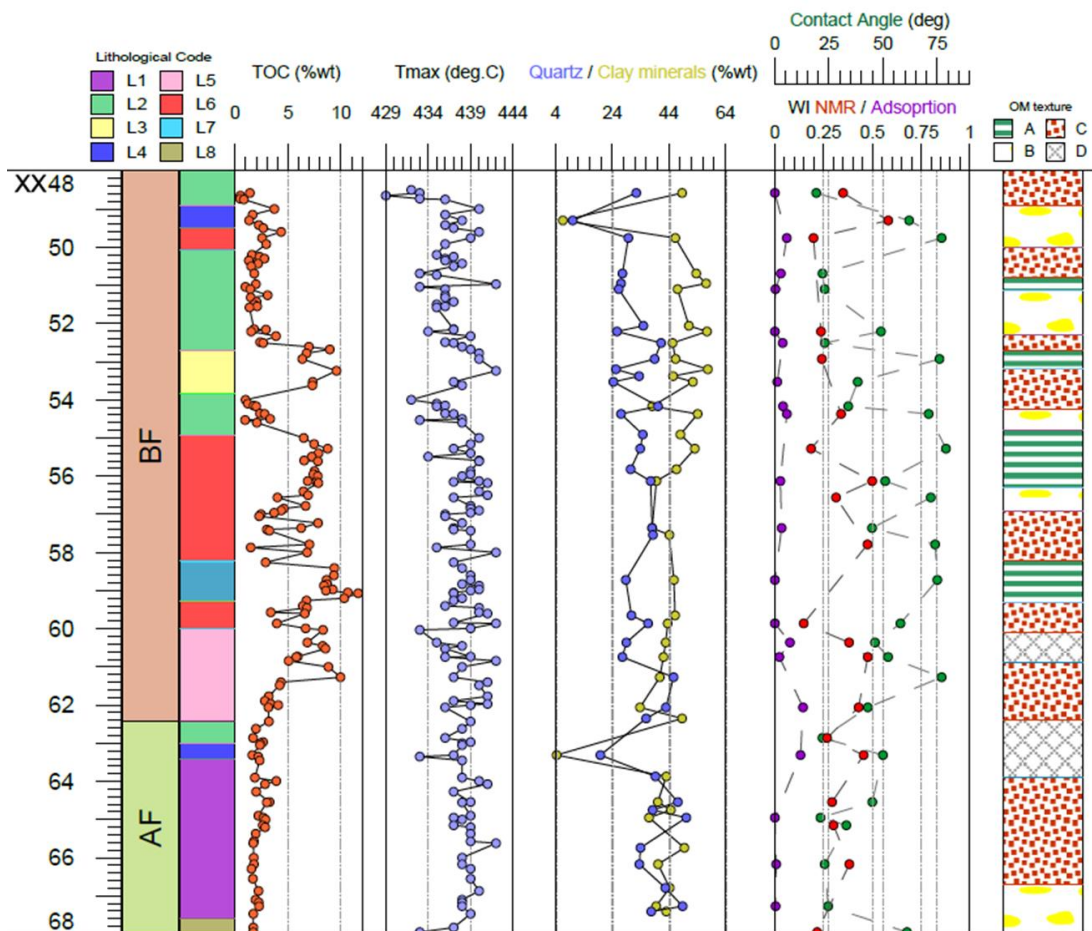


Figure 52: Wettability determination by different methods (Mukhametdinova et al. 2020).

### 3.4.4 Summary

In this section, the experimental results of the Abalak-Bazhenov rocks wettability characterization by a number of techniques (contact angle, adsorption, and NMR) are presented. In summary, we can highlight the main findings of the conducted research:

1. All methods provided an initial assessment of the shale rock wettability. The results showed mainly a water-wet and neutral wettability of the section. For target rock samples, the surface wettability turned out to be significantly sensitive to the rock lithology and OM morphology in the rock.

2. The vapor adsorption technique involves core extraction and depends on the quality of OM removal. Standard protocols of solvent cleaning on the crushed core do not allow removal of the kerogen and result in distorted data on measured points for organic-rich rocks. Therefore, the application of this technique for shales is limited given the current cleaning procedure and requires acidation-based kerogen isolation from the shale sample.
3. The calculation of the wetting angle enabled the detailed characterization of the rock wettability before and after the extraction. We observed the near-linear correlations between the wetting angle and the content of TOC, which is relevant for Abalak-Bazhenov Formation rocks of certain lithotypes (L5 and L6 — calcareous-siliceous carbonaceous mudstone and siliceous, carbonaceous mudstone with pyrite). The lithological description of thin sections and OM morphological categories were applied to highlight the clusters with similar behavior.
4. NMR obtained index provides the integral wettability characteristic for the entire core plug. This technique showed low sensitivity for clusters of rock lithotypes and OM categories and mostly characterized the rock as a medium to strong water-wet.
5. OM morphology mostly influences the results obtained by contact angle technique: the dominance of lenticular OM in the sample may be a reason for hydrophobicity overestimation due to rock anisotropy. In the case of inclusions and dispersed OM, good conformity was observed for results obtained with different methods.

### **3.5 Fluid Interpretation by NMR**

#### **3.5.1 Experimental Methodology**

Qualitative interpretations of 2D NMR data of  $T_1$ - $T_2$  distributions have been proposed in many published works. Within the framework of this section, the fluid saturation of the rocks of the Bazhenov deposits was studied using both existing methods and those modified by the method of interpretation of  $T_1$ - $T_2$  maps. The advantages and disadvantages of using unified data interpretation schemes were discussed, and the features of the identification of various fluids in relation to the studied collection were discussed.

For analysis, we have chosen three standard core samples of the Bazhenov Formation with a different stage of kerogen maturation. According to the mineral composition, Samples CH1 and S3 — are silica-rich argillaceous mudstone, and B2 — silica-dominated rock type.

Table 15. Mineral composition of the target samples

Sample ID	Oilfield	Quartz	Clays Total	Albite	Calcite	Dolomite	Anhydrite	Pyrite
CH1 (wt.%)	#3	28.7	54.3	12.5	0	3.3	0	1.2
B2 (wt.%)	#2	82.9	3.8	10.1	1.3	0	1.2	0.7
S3 (wt.%)	#1	27.7	61.2	8.9	1.6	0	0	0.6

The porosity measurements (gas, mass-volume, and NMR) are performed on plugs; X-ray diffraction (XRD) analysis and Rock-Eval pyrolysis employed crushed fragments. NMR measurements and experimental interpretation was performed by specialists at LaTiS NMR Tomography and Spectroscopy Laboratory of AGH University of Science and Technology (Krakow, Poland).

Samples were measured at as received state (native), then exposed to ambient conditions (for two months, mean temperature of 22°C and relative humidity of 30%, native repeated), in the next steps saturated with demineralized water and dried at 110°C. Saturation and drying procedures were conducted at vacuum conditions (0.07 atm) for 12 h. The porosity of samples by LS and NMR was defined at each stage of the analysis.

### 3.5.2 Digital Interpretation of the Fluid Saturation

While analyzing fluid saturation, we followed the holistic approach. Firstly, we describe T<sub>1</sub>-T<sub>2</sub> maps resulted from NMR studies of the samples in different saturation states. Secondly, we investigate the applicability of different map interpretation schemes to derive fluid saturation. Eventually, we proposed a modified map interpretation scheme and showed its features. A set of 6 most cited and published interpretation schemes was digitized into layered maps using the Surfer software package (Golden Software Inc.) (Figure 53). It was digitized by the separation of the whole map to a set of different fluid regions.

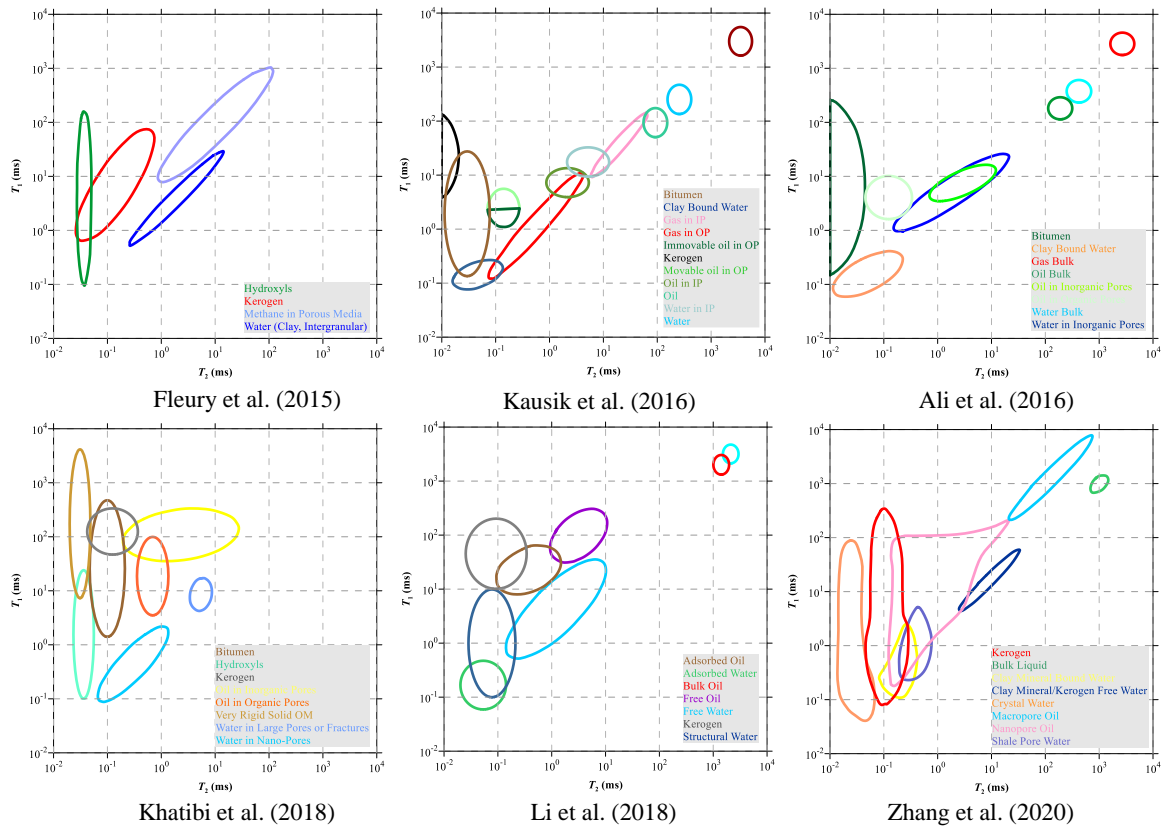


Figure 53: Interpretation scheme by different NMR research groups.

The analysis of  $T_1$ - $T_2$  maps was performed by utilizing all the available zones of irregular shapes in each of the mentioned interpretation schemes (Figure 54). We have applied the schemes to the target 12 maps (3 samples in 4 saturation states) and calculated the total NMR signal intensity as a sum of values for each allocated region. The schemes consider different fluid types as relatively simple shapes of regular (such as circles, ovals, and smooth blobs) and irregular sizes.

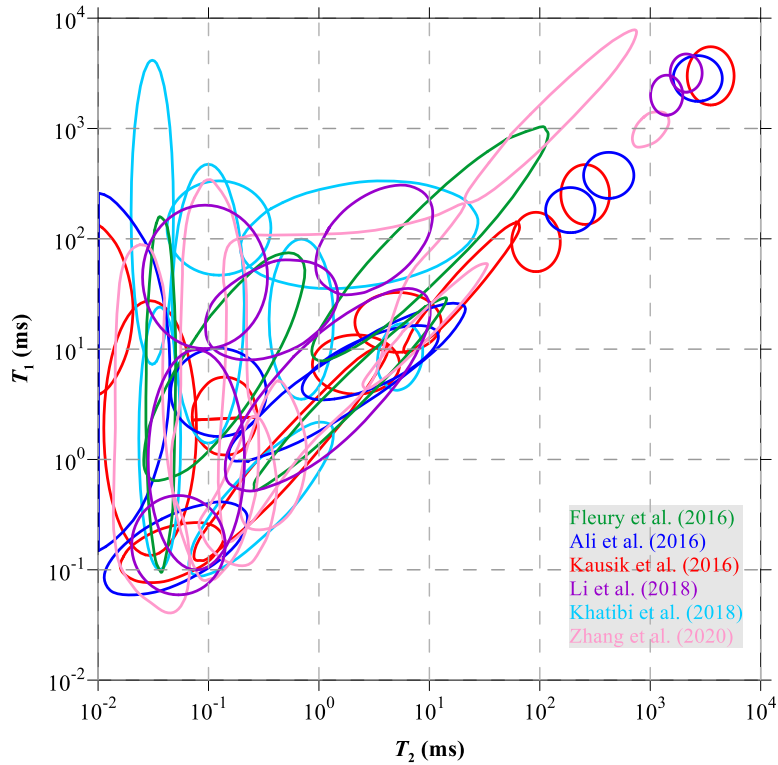


Figure 54: Summary of all map layers.

At the second stage, we treated a more sophisticated scheme proposed by (Li et al. 2020), which is an improved version of the scheme proposed by (Li et al. 2018). The scheme was proposed for shale rock analysis based on the set of experimental data, including NMR results, Rock-Eval, and nitrogen adsorption. Notably, the NMR unit used in (Li et al. 2020) operated at a frequency of 22-MHz, which formally falls into the category of low-frequency devices but certainly is much more sensitive and precise in the field of low relaxation times than a 2-MHz setup. The low-frequency domain is of great importance in shale rock analysis since it describes the high-viscous components (bitumen) and solid OM. By means of NMR relaxometry at 22-MHz, it is possible to resolve the  $T_1$ - $T_2$  maps for heavy components and calibrate data coming from 2 MHz bench-top and well logging tools (Kausik et al. 2016).

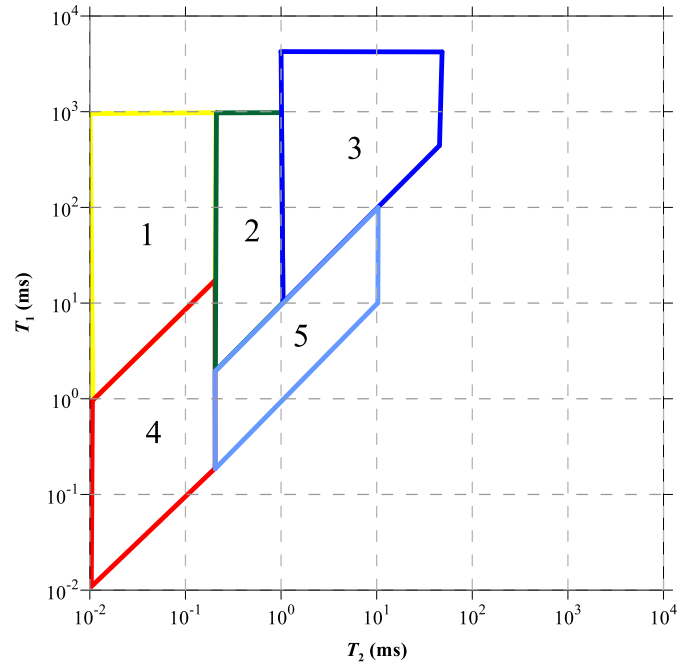


Figure 55: Interpretation scheme by [Li et al. \(2020\)](#). Region 1 — bitumen & kerogen, Region 2 — adsorbed oil, Region 3 — free oil, Region 4 — structural & adsorbed water, Region 5 — free water.

To choose the schemes that are compatible with the maps for the target rock sample, we analyzed the results in terms of a visual match, total signal coverage, correlation with petrophysical data.

A visual match is one of the quality control criteria. Based on the visual inspection of primary experimental data ( $T_1$ - $T_2$  maps) and differential maps, we have selected the four schemes with satisfactory fitting ([Khatibi et al. 2018](#)), ([Li et al. 2018](#)), ([Li et al. 2020](#), [Zhang et al. 2020](#)). The total signal coverage is a parameter showing the maximum signal area covered by the applied scheme. Signal coverage is understood as the percentage of the signal from our maps within the zones of a given model (for native and saturated samples). After analyzing the set of data, the schemes with maximum signal coverage were chosen. Eventually, we correlated the interpreted fluid contents to those resulted from independent petrophysical studies performed on the accompanying chips.

### 3.5.3 Results

Figure 56 demonstrates the total signal coverage for native and saturated rock samples since these two states demonstrate the maximum variety of registered fluid types. For further analysis, we selected the top three schemes with the highest total signal coverage — (Li et al. 2018), (Khatibi et al. 2018), (Zhang et al. 2020), (Li et al. 2020). It is worth noting that the scheme by Zhang et al. 2020 has overlapping regions (Figure 56), which leads to intensity overestimation (more than 100% of coverage). Schemes by (Li et al. 2018) and (Li et al. 2018) possess the highest total signal coverage.

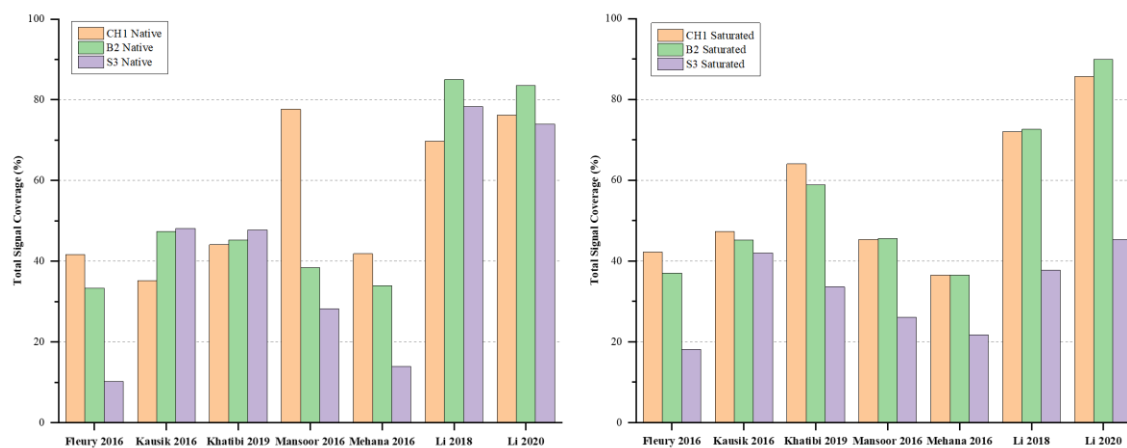


Figure 56: The calculated total signal coverage for different schemes for native (left) and water-saturated (right) target rock samples.

At this stage, we further proceed with comparing the NMR signal corresponding to certain regions by different interpretation schemes. For this reason, we select four categories of fluid that can be verified by independent petrophysical tests such as Rock-Eval pyrolysis, mass-volume measurements (gravimetric method), and NMR  $T_2$  test results. Based on these values, we identify the following groups: bitumen & kerogen (S2 by Rock-Eval), free oil (S0+S1 by Rock-Eval), free water (mass and  $T_2$  volume change for dried and saturated samples), adsorbed water (mass and  $T_2$  volume change for dried and native samples). Rock-Eval results show heterogeneity in all the parameters (Table 16). All values were recalculated to volumetric units using the average (from previous experimental research) density values — 1.1 g/ml for bitumen & kerogen and 0.87 g/ml for free oil. Thus, these values were directly related to NMR signal intensities also converted to the fluid volume occupied by specific

fluid type (Figure 57). We used a digitized dataset, which includes the calculations for each region by each of the interpretation schemes. We derived the analogous fluid types wherein we regrouped some regions or combined identical or similar ones, in particular for kerogen & bitumen and free water. For NMR data, we utilized results for saturated samples since we assumed insignificant displacement of heavy components during non-aggressive rock saturation.

Table 16. OM characteristics by Rock-Eval pyrolysis

Sample ID	S0	S1	S2	S3	TOC	T <sub>max</sub>	Carbonate Carbon
	mg HC/g rocks	mg HC/g rocks	mg HC/g rocks	mg CO <sub>2</sub> /g rocks	wt.%	°C	wt.%
CH1	1.13	5.11	25.87	0.77	7.93	445	0.43
B2	0.65	1.72	50.47	0.9	10.26	420	0.38
S3	0.02	0.38	1.28	0.69	2.2	443	0.59

The comparison demonstrates that we cannot achieve accurate interpretation results by directly applying the proposed scheme to raw  $T_1$ - $T_2$  data without combining the zones and their modification (Figure 57). Based on the preliminary comparison, we highlight the schemes which provide the closest values to reference ones for the target rock type: [Fleury and Romero-Sarmiento \(2015\)](#), [Li et al. \(2018\)](#), [Khatibi et al. \(2018\)](#), [Zhang et al. \(2020\)](#), [Li et al. \(2020\)](#).

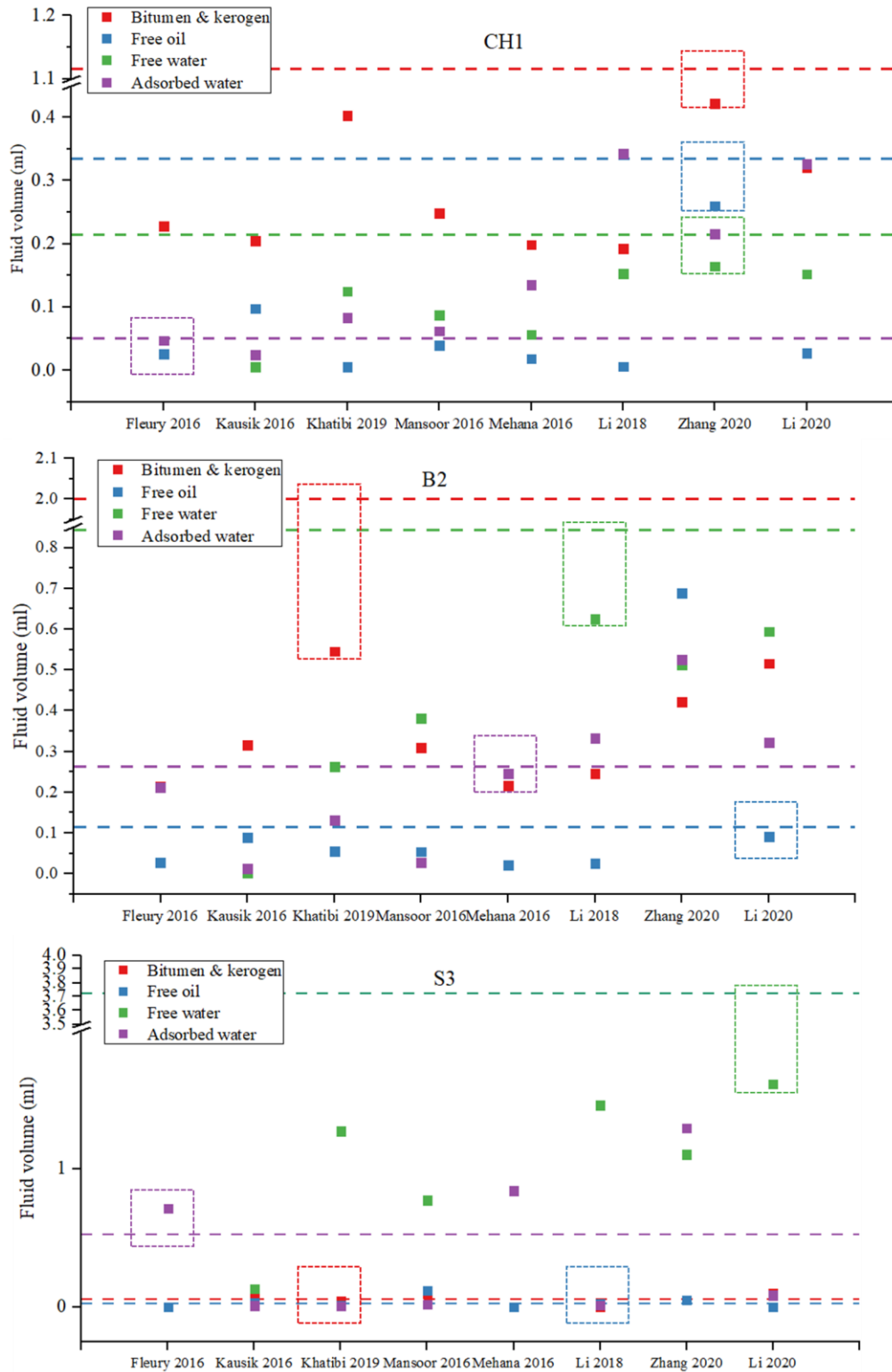


Figure 57: Comparison of selected fluid categories with petrophysical references. Dashed horizontal lines indicate the corresponding (by color) petrophysical reference values.

For the next iteration, we compared the schemes by Li et al. (2018) and (Li et al. 2020). Both schemes showed good signal coverage and also provided a satisfactory match with petrophysical values. The trapezoid-based scheme by Li et al. (2020) showed higher reliability and higher coverage for saturated samples (Figure 58). We explain this by simplified geometry of interpretation, reduced number (delumping) of fluid types, and easy applicability for less-sensitive results obtained by 2 MHz NMR setups. We conduct analysis on water-saturated samples to obtain the maximum signal intensity and fluid variety (including free fluids). However, worth noting that a certain amount of specific fluid types can be missed due to such a scheme of interpretation.

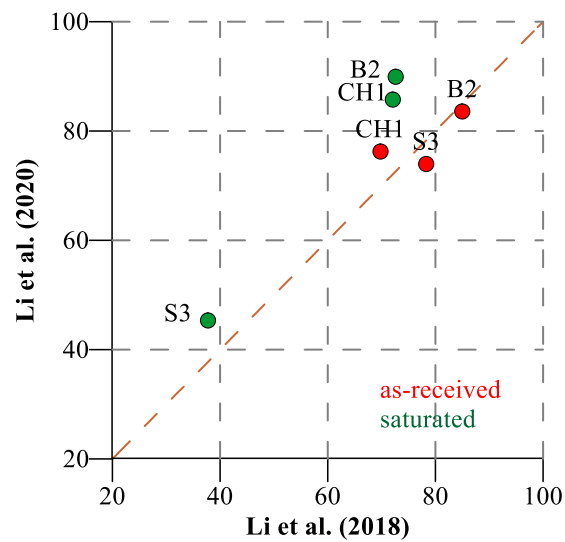


Figure 58: Comparison of total signal for Li et al. (2018) and Li et al. (2020) schemes.

In summary, we couldn't reveal a single interpretation scheme, which can be applied without modification to determine the target petrophysical properties. However, Figure 57 demonstrates that we can use the interpretation framework consisting of the certain scheme components.' Modification of such a composed scheme can provide a higher accuracy by fitting the NMR signal from different fluids and interpretation patterns. In this work, we have proceeded with the Li et al. (2020) scheme as an example base for further investigation and modification.

To achieve a better separation of fluids, we have attempted to develop a universal scheme (for target shale samples) based on that by [Li et al. \(2020\)](#). The modification process included several steps (Figure 59) described below:

- a) We take the regions proposed by [Li et al. \(2020\)](#) and put them on a  $T_1$ - $T_2$  graph.
- b) Based on the obtained  $T_1$ - $T_2$  maps (including differential maps), we first lower the  $T_1/T_2$  ratio line corresponding to the water signal (water line) from 1 to 0.1. Thus, Zones 4 and 5 extended to include the full areas of the Inverse Laplace Transform (ILT) spots.
- c) We detected a non-zero NMR signal indicating the presence of water in medium and large-sized pores in the zone corresponding to the  $T_2$  of 10–100 ms. To capture the feature, we added a new zone for mobile fluid (in our particular case, water) in large pores — Region 6.
- d)  $T_2$  cut-off value is one of the crucial parameters in reserve estimation. Similar to the basic  $T_2$  relaxation curves estimation, the accurate cut-off value is of great help in the interpretation of fluid populations and defining the borderline between immobile and mobile fluids. To handle this, we shifted  $T_2$  cut-off value to the zone of shorter  $T_2$  relaxation times. To determine the new cut-off value, we have investigated the  $T_2$  relaxation spectra change in neighboring zones on the map and signal change in differential maps. We derived the  $T_2$  cut-off values individually for each sample based on the NMR responses in water-saturated and dried states. We compared saturated and dried  $T_2$  spectra, assuming the removal of light oil fractions and water during the drying procedure. We set the new value to 0.1 ms. Figure 59d shows the improved version of [Li et al. \(2020\)](#) scheme.

The variability of  $T_2$  cut-off values falls into the range of 0.07–0.15 ms. To increase accuracy, it is crucial to select the best fitting cut-off value, which will precisely separate the immobile and mobile fluid for a particular measurement. However, in the case of batch data processing for a large number of samples, an individual account is laborious. Therefore it is worth using an averaged  $T_2$  cut-off value for data in data interpretation. The latter approach inevitably introduces an unknown error in fluid separation in a short  $T_2$  time region. We plan to study mitigation strategies within the upcoming research on an extensive set of rock samples.

Besides the listed changes and differential map analysis, we discovered that differential maps indicate the presence of OH groups in Regions 1 and 4. Therefore, the working set of fluid types in the improved scheme is the following: Region 1 — bitumen & kerogen & OH; Region 2 — adsorbed oil; region 3 — free oil; Region 4 — structural & adsorbed water; Region 5 — free water; Region 6 — mobile fluid in large pores.

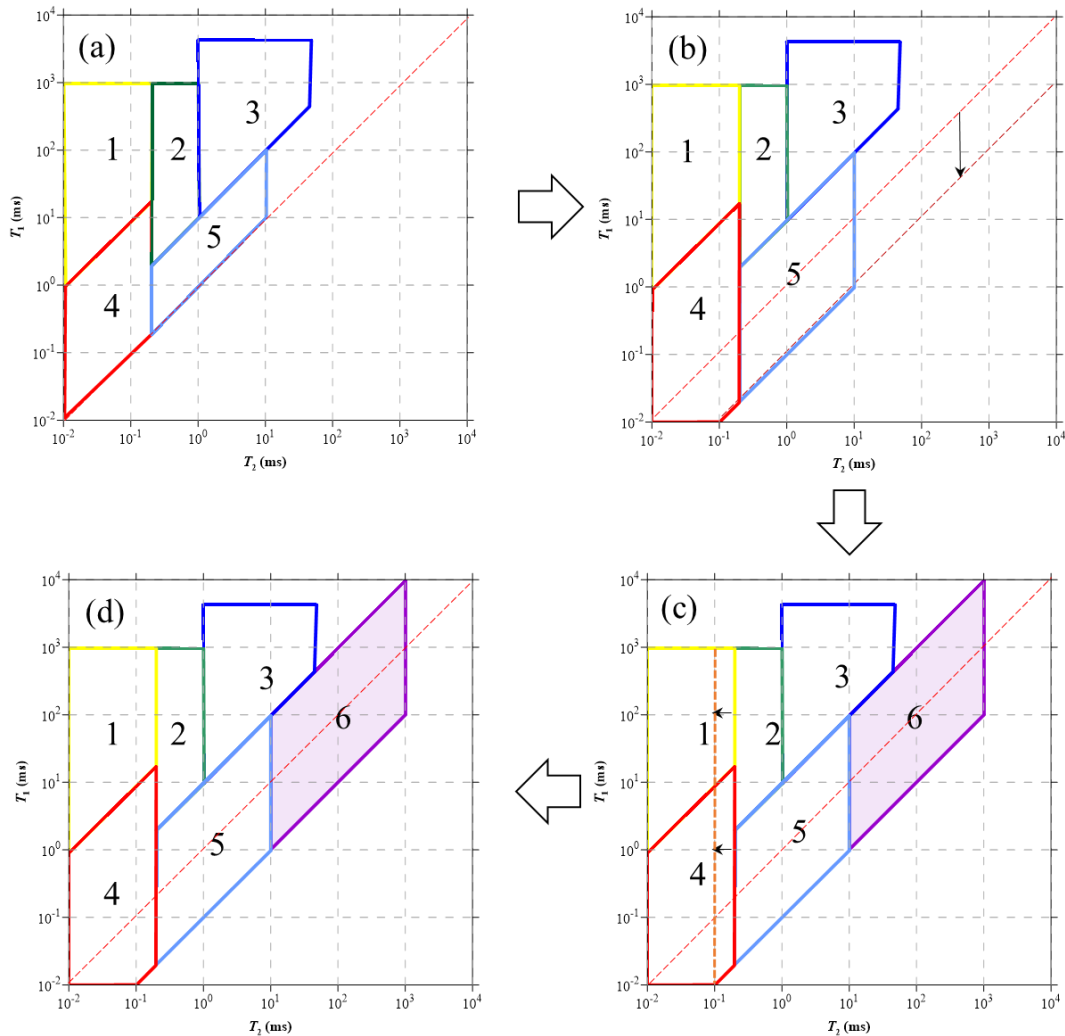


Figure 59: Consecutive modifications of the Li, Jiang et al. (2020) interpretation scheme. Region 1 — bitumen & kerogen & OH, Region 2 — adsorbed oil, Region 3 — free oil, Region 4 — structural & adsorbed water, Region 5 — free water, Region 6 — free water in large pores.

We applied the proposed scheme to the gathered NMR data for the target rock samples. For this purpose, we calculated the sum of data samples within each region for  $T_1$ - $T_2$  maps from four different saturation states (Figure 60).

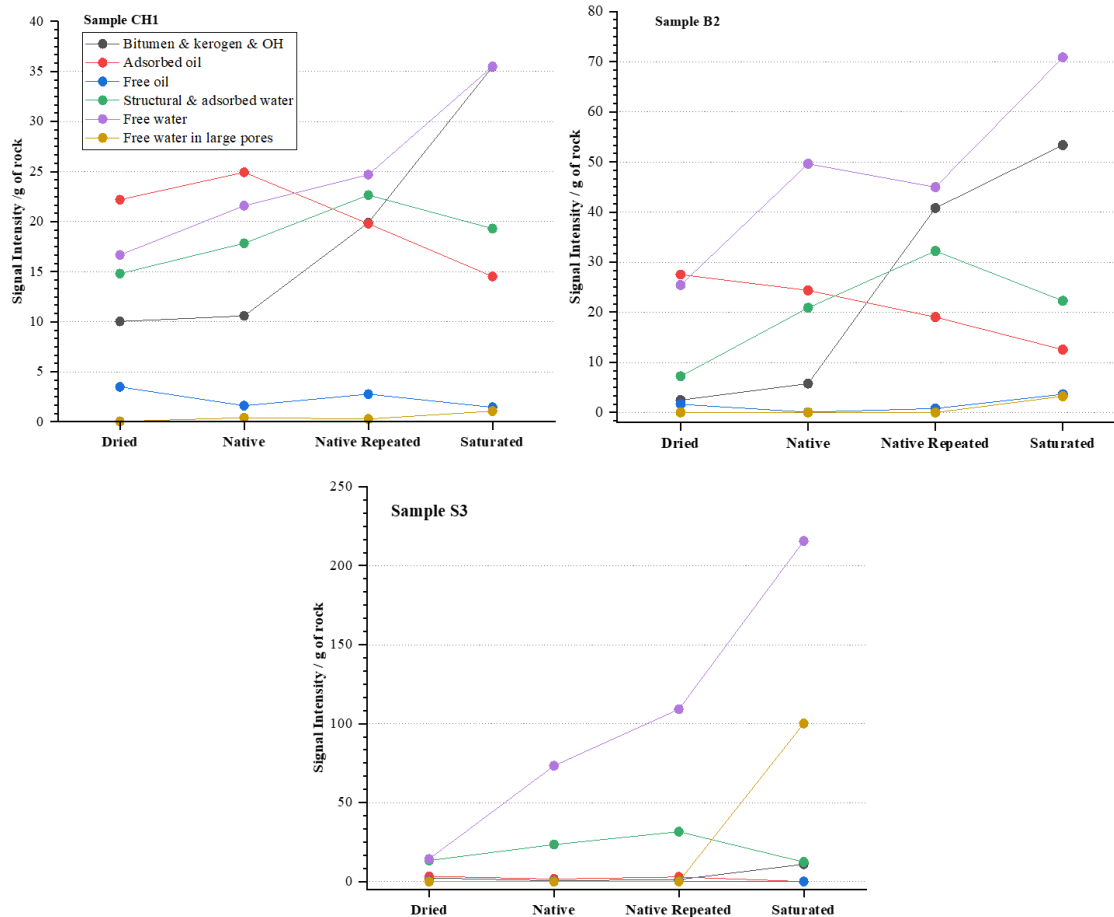


Figure 60: Determination of the cumulative intensity of the signals assigned to the regions of the modified scheme for CH1, B2, and S3, respectively.

For sample CH1, Regions 1 (bitumen and kerogen) and 6 (free water) show the maximum values in a saturated state, which means that the saturating fluid partially occupies the pores in the low  $T_2$  relaxation area. Sample B2 behaves similarly. Regions 3 (free oil) and 6 (free water in large pores) remain flat at different saturation states for Samples CH1 and B2. In contrast, Sample S3 demonstrates different behavior: the contribution of Region 5 (free water) and 6 (free water in large pores) increases in the results of sample saturation. We explain the growth by a significant amount of water-hosting medium-sized and large pores in the rock. Other fluid types (bitumen, adsorbed oil, free oil, and structural water) vary slightly. Notably, the signal corresponding to region 4 (structural and adsorbed water) for all the samples is maximal in a native-repeated state proving the high adsorption potential of rock when exposed to air humidity.

The presented approach has several key advantages over the existing solutions. We consider that the presented approach is a brick in the solid foundation of robust and accurate  $T_1$ - $T_2$  map interpretation. Our long-term goal is to develop a database of interpretation patterns that can be applied to various shale rock types.

To date, the experimentally obtained NMR data are considered as a set of various regions where each region corresponds to a certain HC population (type). In contrast, we propose to interpret a  $T_1$ - $T_2$  map using a composite interpretation scheme (for example, the one suggested here). The custom interpretation scheme is a Lego system consisting of multiple bricks (regions). However, instead of crafting the custom bricks fitted to target NMR data, we collect the bricks from different Lego sets (published schemes) and leave the ones sustaining the greatest match between NMR interpretation results and data from independent petrophysical laboratory studies. The custom scheme will include regions from various previous schemes (Figure 61). Moreover, we leave an opportunity to modify (reshape and/or relocate) the input regions to achieve a better fit to petrophysical data in terms of NMR-to-core relationships.

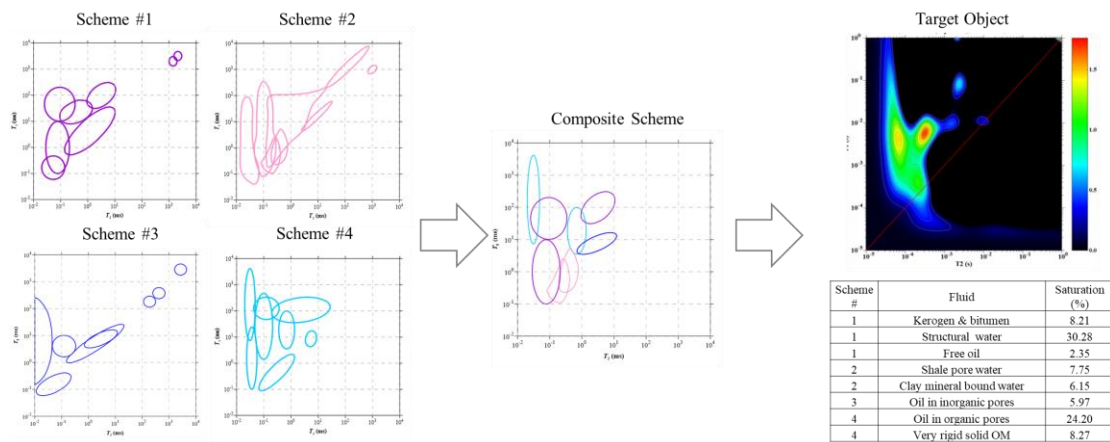


Figure 61: Example of zones allocation in  $T_1$ - $T_2$  interpretation.

In turn, each custom interpretation scheme comes along with the NMR and petrophysical dataset supporting it. A set of custom interpretation schemes and supporting data, along with existing (previously published) interpretation schemes, and modified regions, form an NMR interpretation database. The presented research makes the step in this direction.

The application of the presented approach revealed several features in the target NMR data. The majority of laboratory NMR data comes from 1 H low-field 2-MHz NMR relaxometers since they are highly available commercially and compatible with NMR well logging tools. However, due to physical reasons, 2-MHz units don't capture many HC populations registered by 20 MHz units. The low resolution of 2-MHz  $T_1$ - $T_2$  maps makes it hard to separate the fluids with similar  $T_1/T_2$  ratios. Thus we consider that interpretation schemes for 2-MHz data should focus on separation quality by lumping particular regions into composite ones. In other words, a high number of regions derived from 20-MHz data don't make sense on 2-MHz maps. For example, the 2-MHz setup only partially registers signal from kerogen (Kausik et al. 2016), and thus following the published research and our experimental data, we combine regions corresponding to kerogen and bitumen to a single region.

In the current paper, we first demonstrated the interpretation process modification process on the basis of the Li et al. (2020) interpretation pattern since its simplified geometry of interpretation, reduced number (delumping) of fluid types showed easy applicability for less-sensitive results obtained by 2 MHz NMR setups. The scheme proposed here reliably described different fluid contents for the target rock samples. Notably, Samples CH1 and B2 showed good repeatability and sensitivity in terms of fluid saturations, including adsorbed oil, bitumen, and free water (Figure 62). In turn, S3 differs significantly from both CH1 and B2. The target samples came from far-located oilfields and likely differ in rock type (mineral composition) and petrophysical background (porosity and fluid saturation). Despite this, the scheme captured rock heterogeneity in terms of fluid contents.

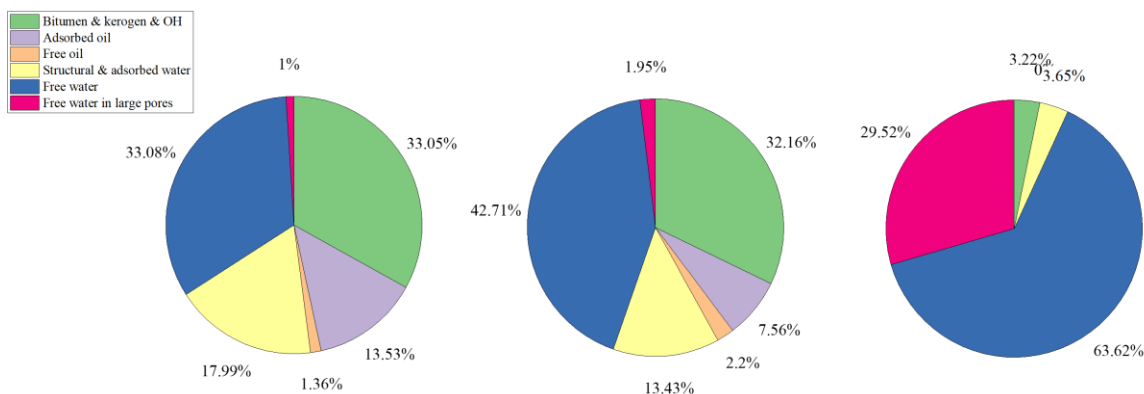


Figure 62: Fluid saturations of the target rock samples in a fully saturated state: CH1 (left), B2 (center), and S3 (right).

At the same time, the approach has several limitations. Fortunately, in the presented case, we successfully applied a single scheme to the maps of three rock samples with different fluid contents. However, it is likely that such a robust application to a greater number of NMR datasets may not work well since some of the maps require manual region adjustment to sustain the accuracy of interpretation results. We see a viable direction to handle the issue by automated dynamic modification (adaptation) of the affected regions until they fully capture the target map anomalies. We consider modern ML-based tools, including deep learning, as a promising framework for creating such an interpretation environment.

Besides, we developed the presented approach for a limited rock sample collection. Its application to a larger set of samples may reveal currently unexpected negative features adversely affecting interpretation results' accuracy. Those include variations in the cut-off value resulting in inaccurate estimation of mobile fluids, and in a number of registered fluids and range and presence of different pore sizes.

Our experience suggests that the search, selection, and modification of NMR data interpretation schemes is rather creative and non-straightforward processes than a formalized workflow, especially for petrophysicists interpreting NMR data for complex reservoirs, such as shales. We consider that the presented research is another brick in the solid foundation of objective (person-independent) interpretation of NMR data to deliver quality and reliable results.

### **3.5.3 Summary**

1. We compared interpretation results for 6 existing schemes on organic-rich rock samples and noticed significant variations in final fluid typing results. The review shows that no single published interpretation scheme may be applied to fluid identification in target rock without modification and adaptation. We selected the most accurate scheme (by Li et al, 2020) and proposed the original, sophisticated way to modify it for target samples based on our experimental results and petrophysical data.
2. Using the proposed interpretation schemes, we qualitatively analyzed the fluid saturation of target rock samples and established the dominating fluid types in the reservoir

(Figure 62). The dominating part of pores was expectedly occupied by saturating brine for all three reservoir types. However, we captured rock heterogeneity in terms of fluid contents in terms of the presence of bitumen & kerogen, structural & adsorbed oil, and water. It is important to note that the rock contains a significant amount of adsorbed water (3.65–17.99%), which confirms the previous results and proves that Bazhenov deposits contain the bound water.

3. We proposed and described a generic framework for finding, adapting, and developing the  $T_1$ - $T_2$  interpretation scheme, which would not require laborious core analysis. In the paradigm, we find the best regions from multiple interpretation schemes for the target collection of rock samples and use them to get the best quality interpretation results. In case of insufficient quality (poor match with laboratory petrophysical data), we consider modification (adaptation) of the original regions to improve results. Involving ML-based algorithms, we plan to develop an automated platform for robust NMR interpretation enabling semi- or fully-automated processing of numerous  $T_1$ - $T_2$  maps in batch mode.

## CHAPTER 4

### UNFROZEN WATER CONTENT IN PERMAFROST SOILS

#### 4.1 Unfrozen Water in Ambient Conditions

In Russia, some new large oil and gas fields are located in the Arctic, *i.e.* in the area of permafrost distribution (continent or Arctic shelf); therefore, for the safe development of these deposits, an understanding of the specifics of permafrost is crucial. These specifics are especially important while drilling and operation of production wells (facing thawing areolas around the wells and affecting the stability of the wellbore). The risks include a decrease in reservoir temperatures (up to negative ones) in the bottomhole zone of the wells due to the Joule-Thomson effect (throttling). In addition, there is an evident presence of large gas accumulations within the permafrost (intrapermafrost gas and gas hydrates), which at the testing stage of field development can be considered as promising for production.

This thesis is aimed at the application of NMR in various scientific and applied areas, the purpose of which is to help in the development of cost-effective and safe (accident-free) technologies for the development of new unconventional fields in Russia, both on the continent and on the shelf. Therefore, the study of the phase composition of the gas-containing permafrost horizons is of great importance as well ([Andersland and Ladanyi 1994](#)). In recent days, in many countries (China, USA, Japan, Canada), NMR technologies are actively used to study permafrost and intrapermafrost gas accumulations (including gas hydrates). This chapter covers the application of low-field NMR relaxometry in defining the saturation in permafrost under different conditions.

The first experimental data on incomplete freezing of pore water in permafrost were obtained at the beginning of the 20<sup>th</sup> century ([Andrianov 1936](#)). The idea that the permafrost of natural composition (simultaneously with ice) can contain a certain amount of water in the liquid phase was reflected in the fundamental work on the permafrost ([Sumgin et al. 1940](#)).

Based on experimental research, the principle of phase equilibrium of pore water in permafrost ([Are 2014](#)) states that at any, even at very low negative temperatures, the soils

contain a certain amount of unfrozen water, which is determined by temperature and pressure. Later, in the 1950s and 1970s, with the development of advanced instrumental methods for determining unfrozen water in frozen rocks, researchers obtained numerous experimental data on the effect of dispersion, mineral composition of the solid component, as well as the degree of salinity on the phase composition of pore water (Anderson and Tice 1972, Watanabe and Mizoguchi 2002, Kozłowski and Nartowska 2013). It has been confirmed that unfrozen water in permafrost-dispersed rocks can be represented by various categories of pore water: capillary-bound, thin-layered, and adsorbed. In the course of the research, it was also found that the content of unfrozen water has a significant effect on various physical, thermal, mechanical, and geophysical properties of permafrost, as well as on the development of various physicochemical processes.

To date, several experimental methods have been developed to determine the phase composition of water in frozen soils, namely: cryoscopic, contact, and adsorption methods, isothermal and differential scanning calorimetry, NMR, electric, dielectric, and ultrasonic methods (Anderson and Tice 1972, Patterson and Smith 1981, Handa et al. 1992, Ishizaki et al. 1996, Watanabe and Mizoguchi 2002). Each technique has its own field of applicability, which depends on the type of soil and temperature ranges, and is characterized by different complexity of hardware implementation and time costs. It is important to emphasize that most of the methods are very labor-intensive. Therefore, the improvement of existing techniques, as well as the development of express methods for determining the amount of unfrozen water, is currently an urgent task.

One of the modern methods for determining the phase composition of water in permafrost samples is low-field NMR relaxometry (Tice et al. 1982, Tice et al. 1988). The data obtained from the amplitude of the spin-echo signal are used to determine the  $T_1$  and  $T_2$  relaxation times, which can be used to determine the number of integral characteristics of the sample, including the amount of free (mobile) and bound pore fluids (unfrozen water).

The first attempts to use this method to study the liquid phase content in frozen rocks were made quite a long time ago (about 40 years ago) (Tice et al. 1982), but only recently, with the advent of more advanced NMR devices, it became possible to use them successfully for

rocks and porous media at low temperatures (Watanabe and Mizoguchi 2002, Kleinberg and Griffin 2005, Watanabe and Wake 2009, Vugmeyster et al. 2017).

The main advantages of this method are related to the possibility of measuring unfrozen water on one sample (*i.e.* constructing a curve of changes in the unfrozen water content in a wide range of negative temperatures), the speed of measurement (several minutes per measurement), and high accuracy. The main drawback is the problem associated with heat from the magnet (the temperature of which in the operating mode is maintained at 35°C). Thus, with long-term (up to 8-10 minutes) measurements, the magnet heat can lead to an increase in temperature (thawing) of the frozen sample and, as a result, to overestimated values of the content of non-freezing water. However, these difficulties can be overcome using some methodological techniques, such as the choice of optimal scanning modes and the introduction of additional amendments. Thus, in many studies, the influence of this factor was evaluated by comparing the NMR results (mainly based on FID tests) with other methods (Watanabe and Mizoguchi 2002, Yoshikawa and Overduin 2005, Watanabe and Wake 2009). In general, the authors were able to obtain reasonable convergence of the results, which indicates the prospects of using the NMR method for studying unfrozen water in frozen soils.

The task comprised developing the NMR methodology based on CPMG testing for the investigation of permafrost samples and adapting the techniques for reliable and high-quality determination of saturation.

#### **4.1.1 Experimental Methodology**

In the framework of this work, the methodology for assessing the phase composition of water in permafrost using NMR was further developed and improved. To ensure the best accuracy in measuring the liquid phase in the studied soils, a series of calibration measurements were carried out on 5 ml and 10 ml NaCl-brine calibration samples of a specific volume.

Samples were soil samples of the various particle size distribution and chemical-mineral composition (quartz sand, sandy loam, polymineral clay), some of which were selected from a cryolithozone (Section 2.1.4). In the experiments, soils with both natural and artificial

salinization were used. Modeling of soil salinization was carried out using aqueous solutions of sodium and calcium chlorides with the following concentrations: 0.2n, 0.5n, and 1n. The solutions were prepared by dissolving the pure crystals of NaCl and CaCl<sub>2</sub> salts (reagent grade) in distilled water. Samples with artificial salinization were prepared by adding a ready-made brine solution (NaCl and CaCl<sub>2</sub>) of a known concentration to a sample of dried soil using a micro-dispenser and thorough mixing in a glass cup.

To determine the phase composition of water content in the studied media, fluoroplastic cylindrical containers (core holders) with an inner diameter of 25 mm and a height of 40 mm were designed (Figure 63). Their main task was to protect the investigated frozen samples from temperature increase during measurements in the NMR device. Soil samples with given moisture content in fluoroplastic containers were prepared by the method of layer-by-layer compaction. The volume of samples was calculated from geometric data, and they were weighed on analytical scales with an accuracy of 0.001 g.

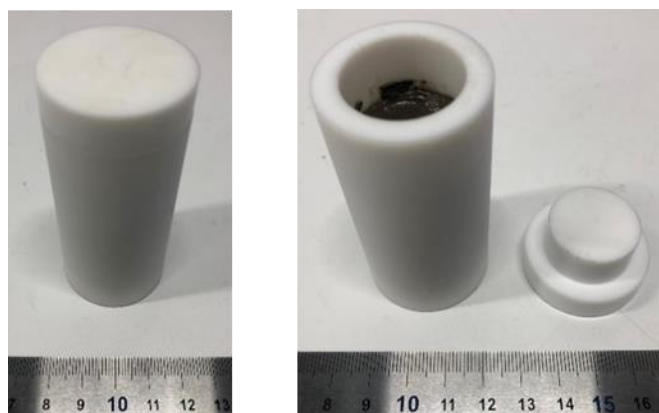


Figure 63: A fluoroplastic container (core holder) for NMR studies of permafrost samples.

As a result, for each studied soil sample placed in a container, the weight and volume humidity, density, and density were determined. Then the samples were placed in a Binder climatic chamber (MK-240 model), where a constant negative temperature was set (with an accuracy of 0.1°C) in the temperature range from -3.0 to -6.0°C. Frozen samples prepared for research were stored in containers for at least 24 hours at a given negative temperature and then placed in the measurement cell of an NMR relaxometer.

During the NMR measurement, the total volume of the liquid phase (bound and mobile water) was determined from the transverse  $T_2$  relaxation data (in  $\text{cm}^3$ ), as well as the one-dimensional profile of the spatial  $T_2$  distribution of the liquid phase along the axis of the sample. The  $T_2$  relaxation curve obtained during the measurement allows one to determine the total fluid content in the pore space, as well as to estimate the proportion of different categories of pore water in the frozen sample. Additionally, one-dimensional tests were carried out to assess the distribution of the liquid phase along the axis of the frozen sample.

Upon completion of the measurement, the middle part of the sample (the central part is 1 cm high) was extracted from the one-dimensional profile. The content of unfrozen water was determined for this part, which was compared with the result of the  $T_2$  test by the total volume of the liquid phase for the entire sample (Figure 64).

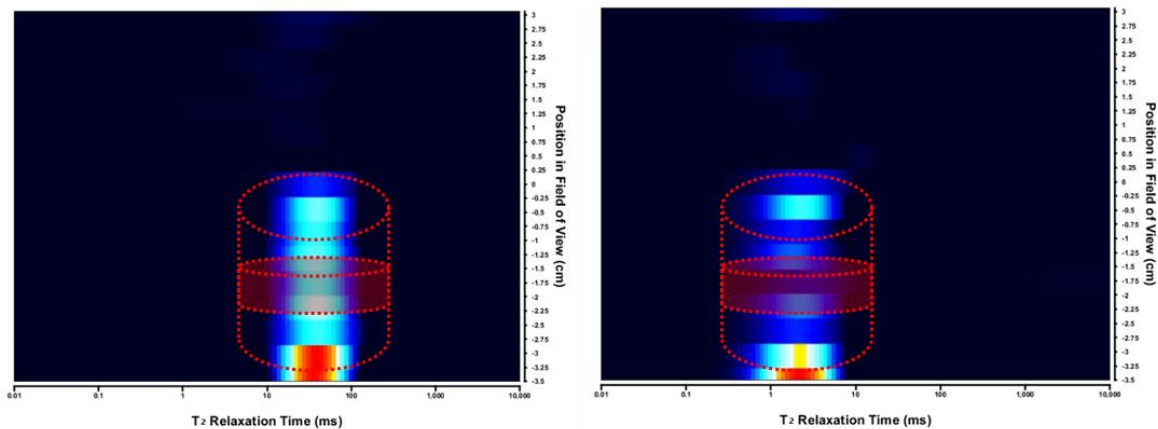


Figure 64: One-dimensional  $T_2$  profile of the liquid phase distribution over the height of the soil sample in the thaw (left) and frozen (right) states. Red dashed lines indicate the sample direction; the red area corresponds to the central part of the sample.

As a result, the use of various indicators (the integral content of the liquid phase, the distribution of unfrozen water along with the height of the sample and its content in the center of the sample) enabled to register the presence of a thawed liquid in the samples, as well as to reveal the technical limitations during NMR measurements. The optimum NMR measurement modes were experimentally selected for permafrost investigation, which guaranteed the absence of sample thawing and provided the necessary accuracy in determining the freezing water content (Table 17).

Table 17. NMR modes for measuring the content of unfrozen water in frozen ground samples.

№	Test	Parameters		Duration, sec
		NSA	SNR	
1	Integral moisture content (according to $T_2$ )	32	Not less than 50	60
2	One-dimensional moisture content profile along with the height of the sample (according to $T_2$ )	16	Not less than 20	90

In general, it was experimentally established that for the studied frozen media (placed in fluoroplastic containers), the total NMR measurement time should not exceed 3 minutes. For this reason, the scanning modes (number of scanning cycles, signal-to-noise level) were chosen so that the total volume of the liquid phase (unfrozen water) in the sample was determined to be about 60 seconds. The profiling of the distribution of unfrozen water along the height of the sample should not exceed 90 seconds.

#### 4.1.2 Results

The obtained methodological developments allowed us to determine the content of unfrozen water ( $W_{uf}$ , %) in frozen soils, as well as to compare the results with other methods. First, the method was probated on sand samples that do not contain the unfrozen water at negative temperatures (Figure 65).

So, for non-saline quartz sand, characterized by a low content of unfrozen water (less than 0.2%), good convergence of the results was obtained in the temperature range from -3 to -6°C (Figure 65). For saline sand ( $D_{sal}=0.03\%$ ), the difference in the values of the content of non-freezing water at a temperature of -5°C was only 0.1% when comparing the NMR data ( $W_{uf}=2.0\%$ ) with the calculation results from the experimental data on the activity of pore moisture ( $W_{uf}=1.9\%$ ).

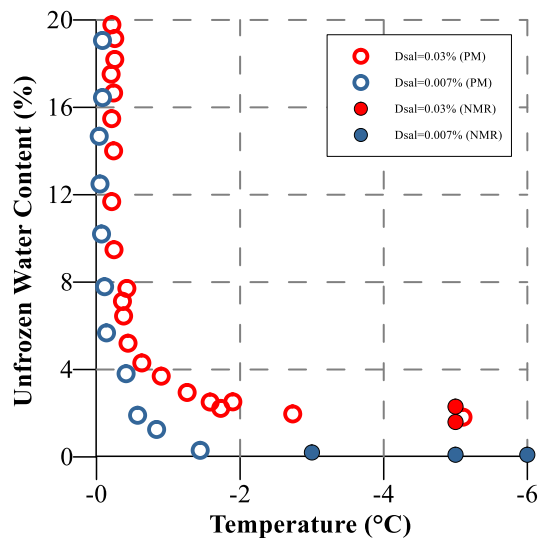


Figure 65: Change in the content of unfrozen water in medium-fine-grained sand with different salinity ( $D_{sal},\%$ ).

The figure illustrates the comparison of calculated data by the water potential method (PM) in the sand with a salinity of 0.007% and 0.03%, respectively. Results of the NMR method for sand with a salinity of 0.007% and 0.03% are presented. NMR registers near-zero values for low-salinity samples and an increased amount of remaining fluid for sand with 0.03% salinity.

For a soil sample of sandy loam ( $D_{sal}=0.26\%$ ) probed from the cryolithozone of the Laptev Sea shelf, the difference between the content of non-freezing water (at  $-5^{\circ}\text{C}$ ) according to NMR ( $W_{uf}=5.0\%$ ) and water activity calculations ( $W_{uf}=5.4\%$ ) was 0.4% (Figure 66).

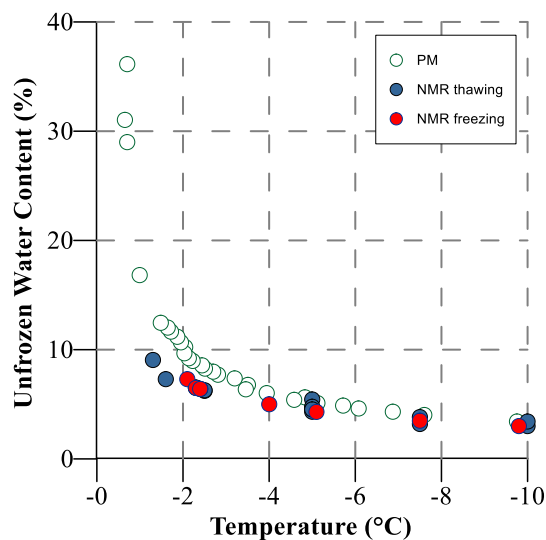


Figure 66: Change in the content of unfrozen water in sandy loam ( $D_{sal}$ , 0.26%).

Good consistency of results was obtained for polymineral clay at 0.19%  $D_{sal}$  (at  $-5^{\circ}\text{C}$ ), where the difference between the NMR values of  $W_{uf}$  and other methods (Istomin et al. 2017, Istomin et al. 2017, Istomin et al. 2017) did not exceed 0.3% (Figure 67). Besides standard sample freezing, the effect of hysteresis on sample freezing and thawing for a set of soils was also examined (Figure 68).

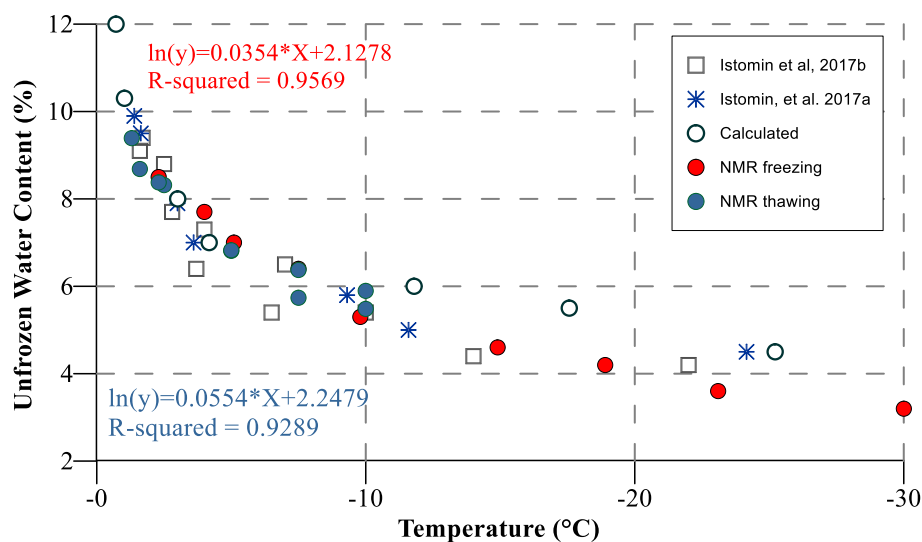


Figure 67: Change in the content of unfrozen water in polymineral clay.

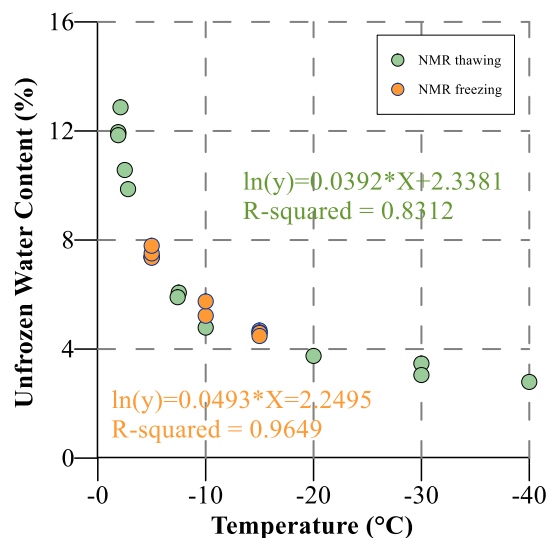


Figure 68: Change in the content of unfrozen water in the loam sample — hysteresis loop for NMR results.

In general, a developed NMR workflow allows one to determine the phase composition of water content in frozen soils of various compositions and to obtain results showing good agreement with other methods. For some complex soils containing multi-layers of water inside, the NMR reported higher values of saturation (Figure 69).

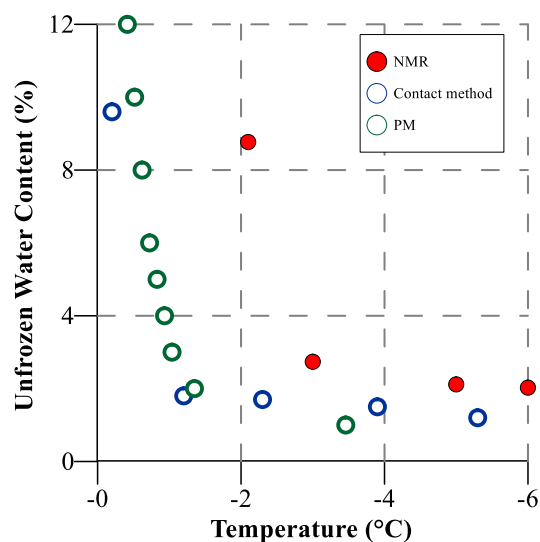


Figure 69: Change in the content of unfrozen water in complex polymineral clay (75% sand + 20% silt + 5% montmorillonite clay).

In the framework of this research direction, the methodology for determining the phase composition of pore water in frozen sediments in ambient pressure was developed using low-

field NMR-relaxometry and basic data processing. As a result of methodological tests, optimal NMR scanning modes (total scanning time, number of scans acquired, signal-to-noise ratio) were established. This workflow can be used for studying the sediment samples in the temperature range of  $-3...-6^{\circ}\text{C}$  to obtain the right consistency of the NMR data with the results of other methods for determining the water phase composition of frozen soils. Therefore, the difference of unfrozen water values obtained by NMR and results of calculation by the activity of pore water or the contact method was averaged 0.2%, which is comparable with the accuracy of the methods used.

## **4.2 Unfrozen Water under Gas Pressure**

### **4.2.1 Experimental Methodology**

In addition to previous studies, the existing NMR relaxometer unit was upgraded to be used to study the unfrozen water content in frozen gas-saturated sediments under gas pressure. A new NMR measurement cell was modified, which allows scanning target samples under certain gas pressure. This is accomplished by setting the pore pressure by gas injection into the soil sample and maintaining the external confining pressure (through the membrane) by a fluorinated electronic liquid, which does not contain hydrogen atoms and, thus, is “transparent” for NMR.

At the first stage, the existing NMR high-pressure cell (P5, Oxford Instruments Inc.) was modernized. For this reason, we have designed and fabricated Teflon-made core holders and used a set of O-rings (Figure 70, Figure 71).

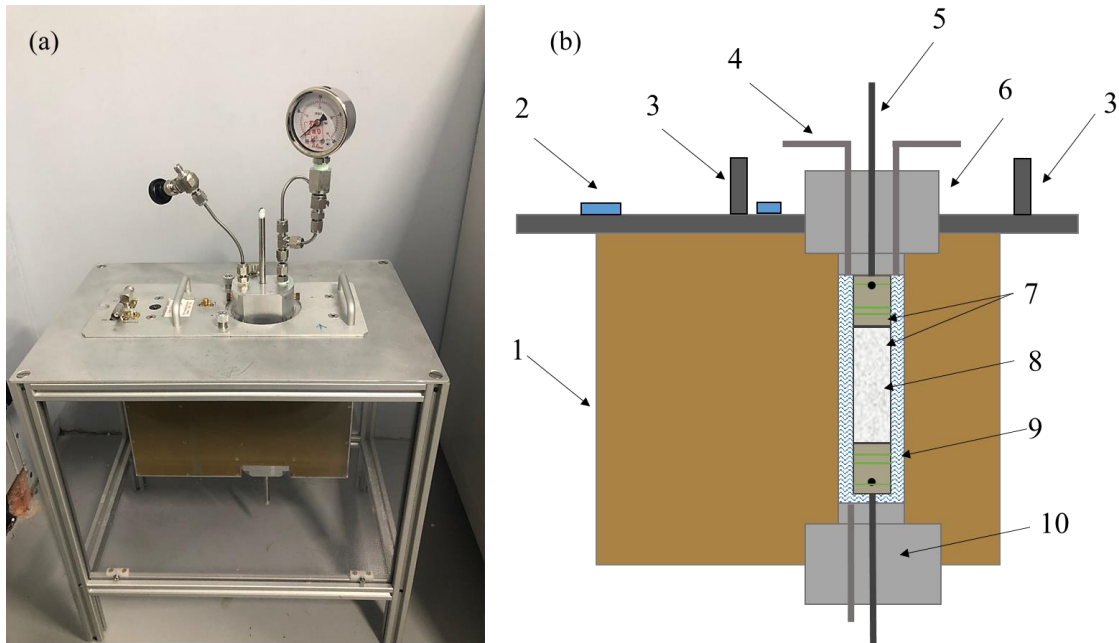


Figure 70: High-pressure cell (a) and schematic of sample location (b): 1—high-pressure NMR cell body; 2—power and data acquisition connectors; 3—handles; 4—confining pressure supply line; 5—pore pressure line (gas); 6—manometer and nipple for air purge; 7—upper flange; 8—core holder; 9—test sample; 10—confining fluid FC-40; 11—lower flange; 12—nipple for confining fluid.

The high-pressure cell for NMR studies resembles a vertically mounted core holder, in which the soil sample is clamped at the ends between two perforated ceramic parts ( $\text{\O}2.5$  cm), to which the gas supply lines are connected, and where the sample is sealed in a transparent heat shrink tube (Figure 70).

During the methodological tests, the core holder design was finalized to prevent the FC-40 confining fluid from leaking into the frozen sample during investigation. The revision, first of all, included the installation on each ceramic stamp of several O-rings (made of Viton material) of various thicknesses. Test experiments have shown that the installation of three O-rings (two of which have a thickness of 1 mm and one with a thickness of 1.9 mm) can be considered the optimal solution.

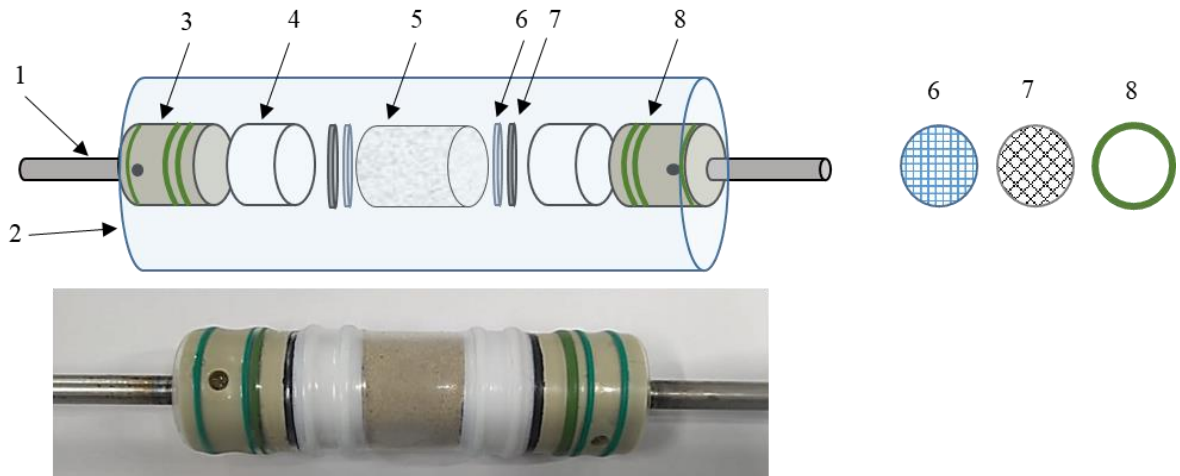


Figure 71: Scheme of the core holder with a soil sample. 1—gas supply line; 2— a thermoshrinkable tube; 3—fluoroplastic insert; 4—soil sample; 6—gasket made of synthetic fabric; 7— mesh gasket (mesh size 0.2 mm); 8— O-rings.

In addition, between PEEK pistons and a frozen ground sample, it was decided to install cylindrical fluoroplastic inserts 1.4 cm high (to prevent the frozen sample from thawing during measurement), as well as synthetic filter gaskets. To ensure the possibility of supplying gas to the studied soil sample, a through-hole was drilled in the upper fluoroplastic insert, which is connected to the gas supply line in the upper part of the core holder. The lower fluoroplastic insert does not have through holes to prevent overflow (squeezing) of the pore fluid from the test sample into the lower piston when increasing the pressure in the sample. As a result, taking into account the modernization of the core holder, the volume of the test sample was about  $10 \text{ cm}^3$  (2.5 cm in diameter, 1.8–2.2 cm of height).

The sample under study was fine-grained quartz sand. As previous studies have shown, this soil is characterized by a shallow content of unfrozen water ( $W_{uf}=0.1\%$  at  $-5^\circ\text{C}$ ) at atmospheric pressure. The prepared sample with given moisture content (10–14%) was placed by a layer-compaction method inside a plastic container with an inner diameter of 2.5 cm and then frozen for 3–4 hours at a temperature of  $-10^\circ\text{C}$ . After that, the frozen sample was removed from the container, and then measurements were made in the freezer room (at  $-7^\circ\text{C}$ ) to prevent thawing, and its weight was determined on an analytical balance with an accuracy of 0.001 g.

As a result, the weight and moisture volume, density were determined for the investigated frozen soil sample. After measurements, the frozen sample was placed between two PEEK pistons with fluoroplastic inserts, on which a heat-shrink tube was put on with a technical dryer (Figure 71b). Then, at room temperature, the sample was thawed, the quality of compression of the sample with holders by a heat shrink tube was visually checked, the assembled system (holder-sample-holder) was placed in a high-pressure cell, which was then sealed using the upper flange. The cell with the sample was installed in the Binder climatic chamber (model MK-240), where the required temperature conditions were set with an accuracy of  $0.1^{\circ}\text{C}$  (Figure 72)

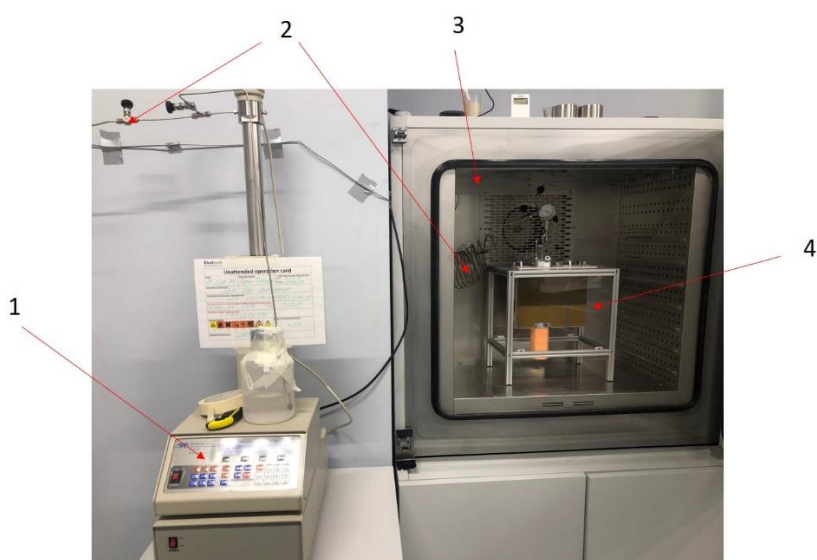


Figure 72: High-pressure cell installed in the climate chamber, with a connected plunger for supplying confining pressure. 1—Isco 260D piston pump; 2—confining system; 3—Binder MK-240 climatic chamber; 4—a high-pressure NMR cell with a soil sample.

After applying the necessary confining pressure, the cell with the soil was kept for several hours to check the tightness of the system and confirm that there was no leakage of the confining liquid into the sample. Then the cell with soil under pressure was cooled to  $-5^{\circ}\text{C}$  (using a climate chamber) and maintained at this temperature for 24 hours. The pressure in the system during cooling was maintained by a constant injection of confining fluid.

Before the NMR measurement, the cell was disconnected from the supply lines placed in the NMR device, and a scanning sequence was run. The procedure for installing a cell inside the

NMR device, on average, took about 30–40 seconds. During the NMR measurement, the total volume of the liquid phase (bound and mobile water) was determined from the  $T_2$  relaxation data (in  $\text{cm}^3$ ), as well as the one-dimensional ( $T_2$ ) distribution profile (Figure 64). In addition to the modified NMR cell, a new coreholder made of PEEK material was manufactured from scratch (Figure 73). This cell was used for conducting measurements at gas pressure up to 80 atm.



Figure 73: Manufactured high-pressure NMR cell for gas–pressure measurements.

#### 4.2.2 Results

As a result, the optimal NMR scans were additionally refined for pressure measurements, which guaranteed the absence of thawing of the sample during the measurement and provided the necessary accuracy ( $\pm 0.05\%$ ) in determining the unfrozen water content (Table 18).

Table 18. NMR measurement modes for estimating the unfrozen water in frozen samples under pressure.

№	Test	Parameter		Test duration (s)
		NSA	SNR	
1	Integral saturation ( $T_2$ )	32	> 45	63
2	1D saturation profile ( $T_2$ )	4/16	-	120/154

So it was experimentally established that for the frozen sand, which is in the cell under pressure, the total time of NMR measurements should not exceed 4 minutes. Therefore, the scanning modes (number of scanning cycles, signal-to-noise level) were chosen so that the total volume of the liquid phase (non-freezing water) in the frozen sample was defined in about 60 seconds. The distribution profile of unfrozen water was recorded. The duration of the second test did not exceed 160 seconds.

As a result, the obtained methodological developments allowed the NMR method to determine the content of unfrozen water ( $W_{uf}$ , %) in frozen sand under pressure at a temperature of  $-5^{\circ}\text{C}$  (Figure 74). The  $\Delta W_{uf}$  is the difference between the initial content of unfrozen water at atmospheric pressure (for this soil 0.1% at  $-5^{\circ}\text{C}$ ) and the final content of the liquid phase in the frozen sample under pressure.

Two series of experiments were conducted with the saturation of frozen soil with various gases. In the first series of tests, the pore space was saturated with air (pore pressure 0.1 MPa), and pressure on the frozen sand ( $W=14\%$ ) was created by a confining liquid (from 0.1 to 7 MPa).

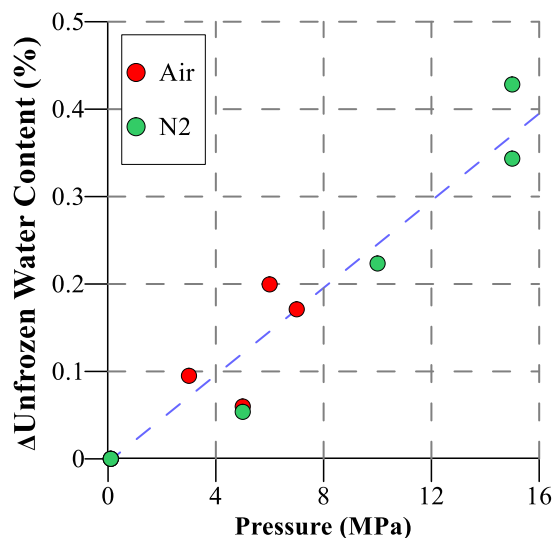


Figure 74: The effect of external pressure on the change of unfrozen water ( $\Delta W_{uf}$ , %) in frozen fine-grained quartz sand at  $-5^{\circ}\text{C}$ .

In the second series, the gas component of frozen sand ( $W=10\%$ ) was represented by pure nitrogen (N3.0) (pore pressure 0.1–0.15 MPa), and the external pressure was set to 15 MPa. As a result, in both cases, an almost linear increase in the content of unfrozen water in frozen sand is observed with an increase in external pressure. So, for a sample (at  $-5^{\circ}\text{C}$ ) containing air, with an increase in pressure from 0.1 MPa to 7 MPa, an increase in the amount of unfrozen water was about 0.2%, which is three times higher than the initial content of unfrozen water at atmospheric pressure. For a sample saturated with nitrogen, an increase in pressure to 15 MPa was accompanied by a regular increase in the liquid phase to  $\Delta W_{uf}=0.43\%$ , which ultimately turned out to be almost five times higher than the initial content of unfrozen water in sandy soil at atmospheric pressure ( $W_{uf}=0.1\%$ ). The second experiment under pressure was performed for the sample of polymineral clay (Figure 75).

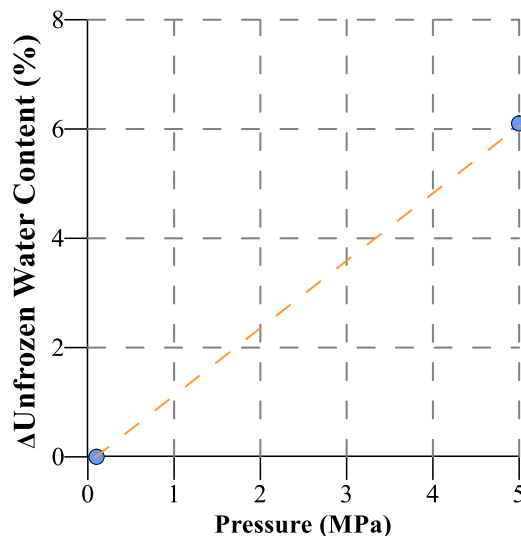


Figure 75: The effect of external pressure on the change in the amount of unfrozen water ( $\Delta W_{uf}$ , %) in frozen polymineral clay at  $-5^{\circ}\text{C}$ .

For the studied gas-containing soil, an increase in pressure of 1 MPa will cause an increase in the content of unfrozen water by about 0.03%. The obtained experimental result confirms the increase in the content of unfrozen water under pressure, previously obtained by other researchers for frozen clay soils. At the same time, our research extends this pattern to frozen sandy rocks. Separate experiments that were carried out by [Kondakov et al. \(1989\)](#) on frozen sand and sandy loam samples did not reveal the effect of pressure increase (from 0.1 to 1 MPa) on the liquid phase content, which is most likely associated with a relatively small change in the pressure range under consideration, and for this reason comparable with the accuracy of the research. Therefore, the developed experimental NMR research technique allowed for the first time to quantitatively assess the effect of pressure (up to 15 MPa) on the phase composition of frozen sand, which creates the prerequisites for the successful use of this technique in determining the content of unfrozen water under pressure for the varied composition of permafrost. This opens up excellent prospects for the quantitative determination of the liquid phase in gas-saturated dispersed rocks at low positive and negative temperatures.

### **4.3 Summary**

In this work, the content of unfrozen water in frozen soils by the NMR method was determined. The approach was based on measuring the values of fluid saturation by means

of the NMR technique. The methodology for conducting measurements on permafrost samples under negative temperature and gas pressure was developed. The proposed method is characterized by high accuracy and comparable to the existing methods. All concluding remarks can be summarized into the following points:

- The methodology based on the NMR CPMG sequence was developed and refined for testing and measuring the unfrozen water content in soils and permafrost samples. CPMG  $T_2$  test was proved as an efficient and fast tool in comparison with the standard method based on FID;
- The set of soils and permafrost samples was tested in the range of negative temperatures in ambient NMR cell. Results showed good convergence with other conventional methods (less than 0.3% of divergence) and created a framework for further tests under pressure;
- The equipment modification and developed methodology allowed us to note a linear increase in the unfrozen water content for studied soils with an increase in pressure to 15 MPa. So, for frozen sand at  $-5^{\circ}\text{C}$ , an increase in pressure by 1 MPa will cause an increase in the content of the liquid phase by about 0.03%. The obtained result confirms the increase in the content of the liquid phase in frozen rocks under pressure, previously noted by other researchers using the example of frozen clay soils. However, our research extends this pattern to frozen sandy rocks;
- The developed experimental technique of NMR studies made it possible for the first time to quantitatively assess the effect of pressure (up to 15 MPa) on the phase composition of frozen sandy rocks, which creates the prerequisites for the successful use of this technique to determine the content of unfrozen water under pressure for frozen rocks of different composition.

## CHAPTER 5

### NMR APPLICATIONS IN DIFFUSION STUDIES

#### **5.1 Introduction**

In recent years interest in methods for enhancing oil recovery is growing and leads to the development of works aimed at choosing the most effective field development technologies with the highest recovery rate and lowest economic costs (Alvarado and Manrique 2010, Ahmed and Nathan 2016). One of the effective methods for increasing the recovery factor can be the application of gas EOR, specifically the injection of CO<sub>2</sub> into the reservoir.

The technology for injecting carbon dioxide into the reservoir became known more than fifty years ago and during this period received significant development. When it is used as a displacing agent, a significant increase in the oil recovery coefficient can be achieved — by 6–10% according to some estimates. The partial or complete dissolution of carbon dioxide in oil can lead to rheological properties change, which, in turn, contributes to the extraction of viscous oil. Besides shales, carbonate and terrigenous reservoirs containing highly viscous oils are also promising for the application of CO<sub>2</sub> injection-based recovery methods. The effectiveness of the methods of displacement and oil production by carbon dioxide injection into the reservoir is confirmed by a large number of experimental and theoretical studies, pilot projects, and industrial development of low-permeability deposits in various countries (Du and Nojabaei 2019, Burrows et al. 2020).

The effectiveness of CO<sub>2</sub> injection is primarily influenced by the mixing of the phases, CO<sub>2</sub> diffusion, and transport of carbon dioxide in a porous medium. Therefore, all the parameters of CO<sub>2</sub>-based EOR should be defined by experimental studies on actual-field rock and oil samples. The diffusion coefficients obtained in the experiment can be used in the numerical simulation of field development using commercial simulators.

However, conventional laboratory and numerical methods for estimating the diffusion coefficient of CO<sub>2</sub> are not able to describe the processes occurring in low-permeability porous media due to the low diffusion rate and filtration. The main issue is defining the

saturation of such rock in the course of the experiment. The literature review revealed a relatively small number of proposed experimental methods for determining the diffusion coefficient of CO<sub>2</sub>, which can be used to analyze the diffusion of carbon dioxide in the complex reservoir.

In one of the works (Fernø et al. 2015), positron-emission tomography (PET) and CO<sub>2</sub> injection with a radioactive C11 isotope on the 1.5 inches core are used to determine the diffusion coefficient. Chen et al. (2018) propose the following workflow for CO<sub>2</sub> diffusion measurements: first, NMR is used to analyze the concentration of oil in the sample during the CO<sub>2</sub> injection process. Based on oil concentration and the concentration of CO<sub>2</sub> at the inlet and outlet of the cell, nonlinear dependence of diffusion at applied pressure is constructed. NMR is used for estimating the pore size change after the bituminous coal treatment by supercritical CO<sub>2</sub> (Wen et al. 2005).

Scientists from the University of Calgary shared another promising method for defining the diffusivity of CO<sub>2</sub> in heavy oils — they utilized X-Ray tomography at reservoir conditions (Wen et al. 2005). The X-Ray CT method was also proposed in other research works (Eide et al. 2013, Trevisan et al. 2013, Eide et al. 2016), where authors used this method for determining the effective diffusion coefficient of CO<sub>2</sub> using visualization of the process by CT imaging.

The goal of this research was an experimental determination of the CO<sub>2</sub> diffusion coefficient in oil-saturated porous media at reservoir conditions under the control of NMR. Previous studies on experimental modeling of supercritical CO<sub>2</sub> injections were conducted and showed the importance of CO<sub>2</sub> diffusion in terms of numerical modeling (Popov et al. 2016).

In the current chapter, the methodology of CO<sub>2</sub> diffusion characterization by means of online NMR profiling at formation conditions was developed. The proposed experimental procedure was composed of the injection of CO<sub>2</sub> into oil-saturated samples of local carbonate and shale formations in a high-pressure NMR cell with constant process control using NMR 1D profiling. The methodology was tested on two different types of formation — heavy oil carbonate and organic-rich core samples. The chapter also includes the diffusion studies on

low-permeable rock samples of dolerite, where the NMR saturation profiling testing was approbated.

## **5.2 Rock Samples**

In this study, we have investigated the CO<sub>2</sub> diffusion on two rock types — shale and carbonate (Table 19). Both cores are actual-field rock samples (cylinder plugs) cored from two different oilfields. Each core cylinder came with a 25 mm diameter size in the preserved state. Reservoir properties of both oilfields are introduced in the Materials section. Diffusion of the water-water system was performed on dolerite (diabase) rock samples. This rock type is represented by ultra-low permeable porous media of high strength and rigidity.

Table 19. List of the investigated rock samples

<b>Sample ID</b>	<b>Oilfield</b>	<b>Diameter (mm)</b>	<b>Length (mm)</b>	<b>Porosity (%)</b>	<b>Permeability (mD)</b>	<b>Rock type</b>
B1	#3	24.53	48.29	2.78	0.005	Organic-rich shale
C1	#8	24.90	43.29	15.60	138	Heavy-oil carbonate
302	n/a	30	30	0.92	n/a	Dolerite
420	n/a	30	30	3.84	n/a	Dolerite
430	n/a	30	30	4.33	n/a	Dolerite

## **5.3 Experimental Methodology**

### **5.3.1 Diffusion in Water-Water System**

The proposed experimental technique assumes immersing a water-saturated sample into a container with heavy water (deuterium oxide) and monitoring the change in rock saturation in the NMR cell during diffusion and displacement for the water–water (distilled water–deuterium oxide) system. As shown in Figure 76, the sample is confined with a heat-shrink sleeve (a, b), after which it is saturated with distilled water (c) and placed in a container with

heavy water (deuterium oxide  $D_2O$ ) (d). Thus, the diffusion process occurs from two ends of the sample. With an interval of 24–48 h, the  $T_2$  relaxation curve is recorded, according to the results of which the volume of the displaced liquid is subsequently calculated, and the propagation of water is defined.

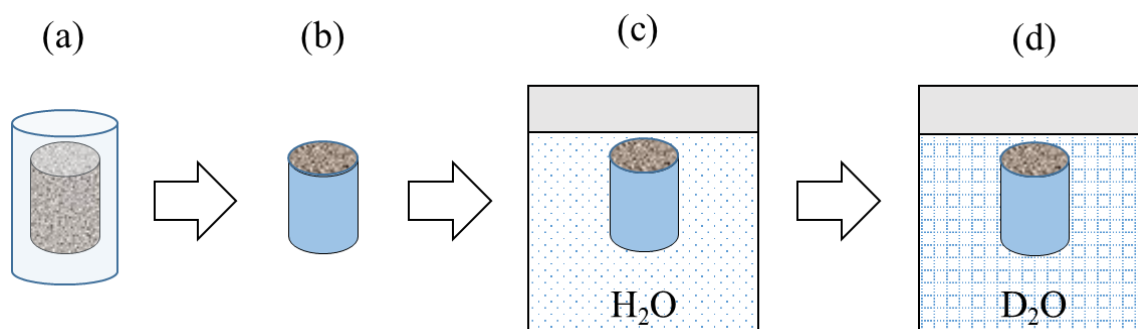


Figure 76: The sequence of the diffusion process: a) and b) sample preparation using a heat-shrink sleeve; c) saturation of samples with water; d) placing water-saturated samples in a container with heavy water.

### 5.3.2 Diffusion in $CO_2$ –Oil System

Cylindrical core plugs (25×40 mm) sampled from the target oilfields were used for research. Prior to the main NMR experiment, core samples underwent a preparation stage (weighing, measuring the sample geometry). Next, a series of NMR tests ( $T_2$  test and saturation profile) is carried out for the samples (before solvent cleaning) at atmospheric pressure in the HPHT cell.

Figure 77 describes the scheme of conducting NMR experiments in HPHT cell for  $CO_2$  injection at reservoir conditions (reservoir pressure and temperature). The saturated sample is placed in a heat-shrinkable sleeve (TFPE) and placed in a cell with two PEEK core holders (Figure 77). The sample in the cell is positioned vertically, and a confining pressure is obtained using a fluorinated liquid that does not contain hydrogen atoms.  $CO_2$  is supplied from the upper end of the sample, whereas oil from the lower end is maintained consequently.

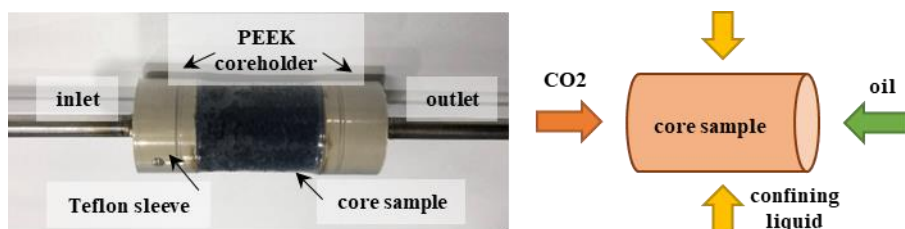


Figure 77: Schematic diagram of the core placement in the HPHT cell.

Experimental NMR setup consisted of an HPHT NMR cell (P5) and supporting infrastructure. The maximum pressure for the P5 cell is 340 atm, and the temperature is 100°C. In order to model reservoir conditions, double plunger pumps (Quizix) and a plunger pump (Isco 260D) were used. As a saturating liquid, the sample of oil was used (probed from both oilfields) and CO<sub>2</sub> (99.9999%). The cell was confined using FC-40 (product of 3M company) fluorinated liquid heated in a thermostat at reservoir temperature. Supply of CO<sub>2</sub> and oil at a pressure of up to 250 atm is carried out by one of the pump plungers. The experimental scheme is presented in Figure 78:

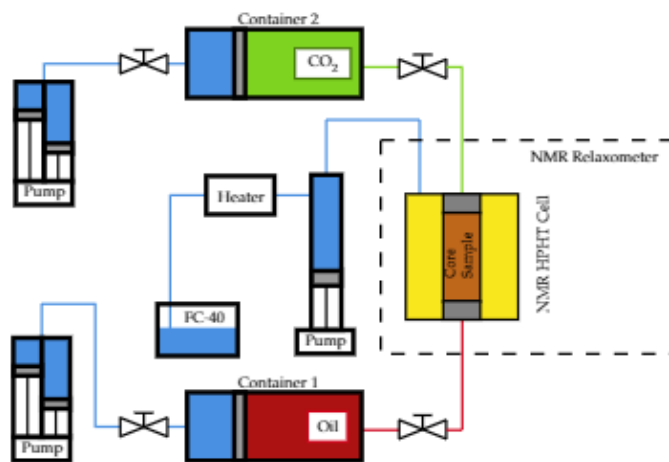


Figure 78: Hydraulic scheme of the experimental NMR HPHT setup.

After preliminary tests at atmospheric pressure, a confining pressure of 60 atm is created. The next step is the injection of CO<sub>2</sub> into the oil-saturated core sample at the pressure of  $P_{\text{conf}}=200$  atm and  $P_{\text{CO}_2}=150$  atm and  $P_{\text{oil}}=150$  atm. The NMR measurements (saturation profile) are repeated for the sample with an interval of 10–30 minutes. One porous line towards the sample is filled with CO<sub>2</sub>, while the pump plunger maintains pressure. The second porous line is filled with oil; another plunger pump maintains the pressure. The

system is held at these pressures to achieve diffusion stability, *i.e.* no change in saturation profile (and  $T_2$ ) controlled by NMR. Based on the data obtained, an analysis of changes in the saturation profile is carried out, and the diffusion coefficient of  $\text{CO}_2$  is calculated.

## **5.4 Results**

### **5.4.1 Dolerite Rock**

For a set of three samples, a specified list of studies was performed. The results of preliminary studies for the dry and water-saturated state of the samples are shown in Table 20.

Table 20. Results of NMR measurements

<b>Sample ID</b>	<b>Initial volume H<sub>2</sub>O (ml)</b>	<b>Final volume H<sub>2</sub>O after 14 days (ml)</b>	<b>Final volume D<sub>2</sub>O after 14 days (ml)</b>	<b>Depth of diffusion (mm)</b>
302	0.154	0.061	0.093	15
420	0.482	0.372	0.110	-
430	0.785	0.681	0.104	15

Two cylindrical plugs (#302 and #430) were placed in a heat-shrink sleeve prior to saturation. Thus, the process of diffusion and replacement of distilled water with deuterium oxide occurred from the ends of the sample. Sample #420 was placed in a container with deuterium oxide without a sleeve, so the contact of the two fluids flowed over the entire surface of the cylinder. Figure 79 shows the change in water saturation (in %) during the diffusion process. Various speeds of diffusion and displacement can be explained by initially different porosity values of each sample (Table 19).

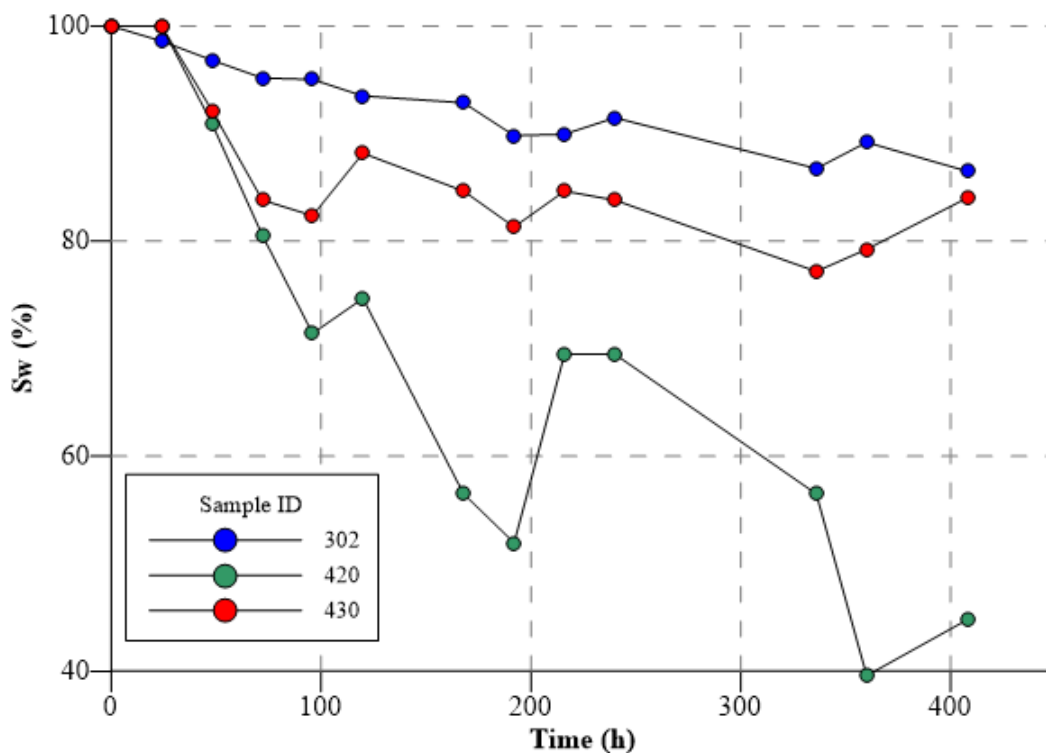


Figure 79: Change in the H<sub>2</sub>O saturation during diffusion.

The results of the study show that the minimum value of the recorded fluid for all three samples was reached 14 days after the start of the experiment. After completion of the experiment, for two cylindrical samples (#302 and #430), one-dimensional saturation profiles were built along the axis (sample height) (Figure 80). In the case of Sample #430, the depth of deuterium oxide penetration during the experiment is clearly illustrated. The maximum saturation peak with a coordinate of 0.5 cm corresponds to the center of the sample, while the profile shape demonstrates a relatively uniform fluid distribution and displacement in regards to plug ends. The small peak on the right side of the graph can be explained by the possible presence of heterogeneity in the structure of the sample under study.

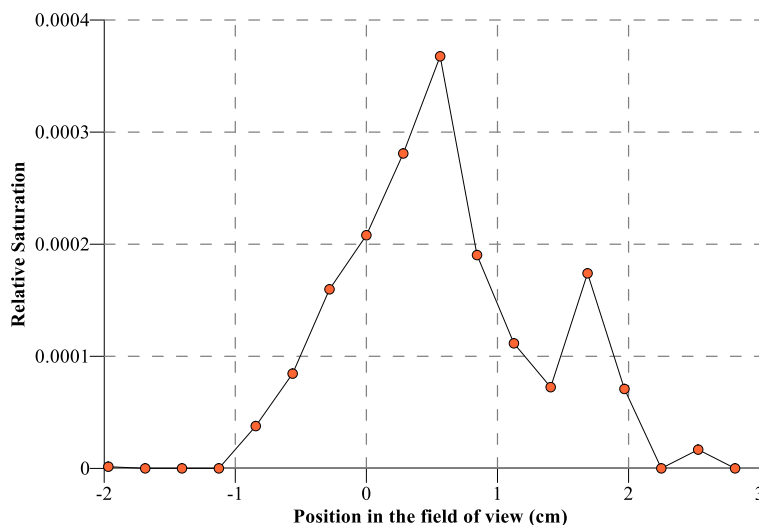


Figure 80: The saturation profile of Sample #430 after two weeks of diffusion.

Additionally, for each of the studied samples, the pore size distributions were plotted based on results of the  $T_2$  relaxation curve before and after the experiment (Figure 81–Figure 83). For samples with low porosity (#302 and #420), fluid displacement ( $H_2O$ ) is mainly observed in the pore range from 0.001 to 0.03 microns. Figure 83 shows that in Sample #430, the diffusion process takes place in the zone of pores of medium size (from 0.02 to 1 micron), and the zone of low  $T_2$  relaxation times remains unchanged.

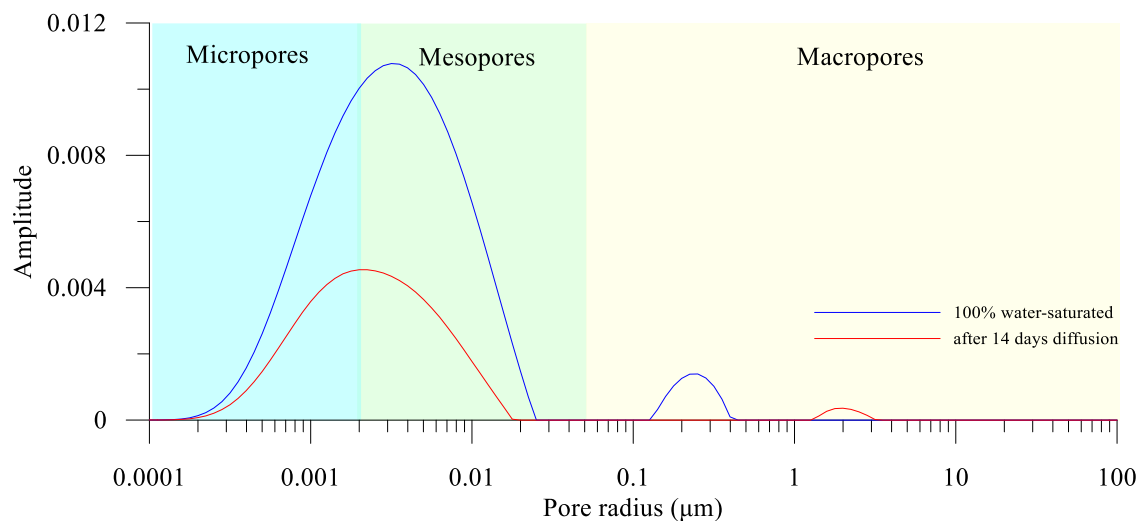


Figure 81: Pore size distribution before and after two weeks of the experiment, Sample #302.

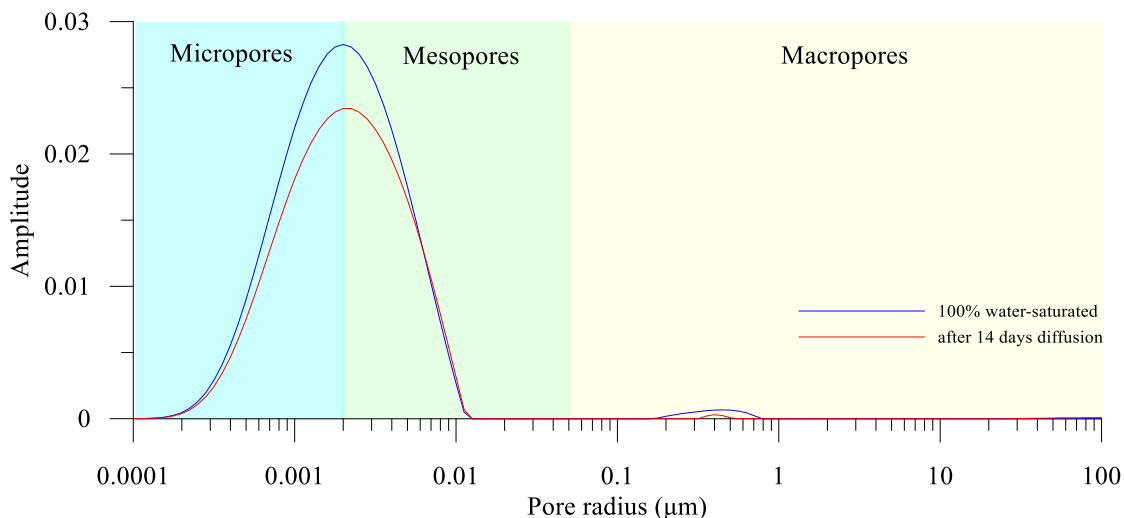


Figure 82: Pore size distribution before and after two weeks of the experiment, Sample #420.

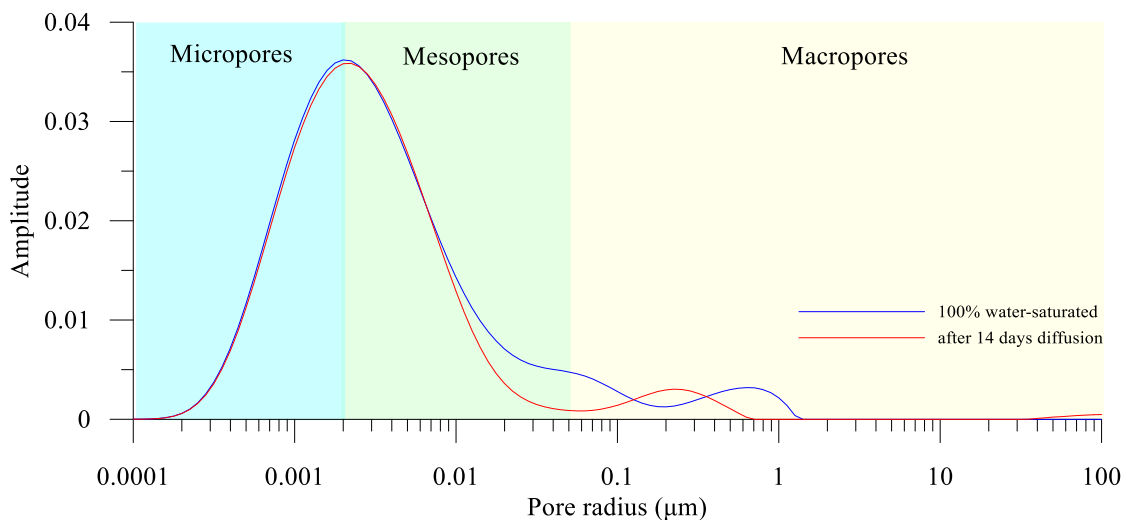


Figure 83: Pore size distribution before and after two weeks of the experiment, Sample #430.

### 5.4.2 Core Saturation

The low-permeability shale samples have very low porosity and pores filled with highly-viscous components and, therefore, cannot be saturated by the conventional procedure (by means of vacuum or automated saturator). To ensure the full saturation of the shale rock sample, the saturation was performed under constant NMR monitoring inside the high-pressure cell. The procedure of core saturation consisted of the following steps:

- 1) A pre-dried (in a vacuum oven) sample is placed in a Teflon shrink sleeve

and then placed inside the HPHT cell. Confining pressure of 150 atm is applied.

2) During 4 hours, the sample is vacuumed, and then the initial saturation profile of the sample is recorded.

3) After the sample is saturated with oil, oil is injected into the system from two sides of the core holder under the pressure of 150 atm with a stepwise rise for 5 hours while confining pressure is increased from 150 to 300 atm in order to keep effective confining stress at a constant level. Oil should be injected at the formation pressure.

4) At regular intervals of 30 min, saturation profiles are recorded until the level of oil saturation is stabilized (Figure 84a).

5) After saturation, the sample is removed from the Teflon sleeve and weighed.

Saturation profiling is used for online NMR monitoring (Green et al. 2008). Figure 84 shows the change in sample profile at different times of saturation. As seen from the graph, the saturation profile is steadily rising during the first 24 hours. The sample was held for more than 72 hours. The saturation profile stabilized after 72 hours. Therefore, one can conclude that the maximum saturation was reached (at the pressure of 150 atm) within 72 hours.

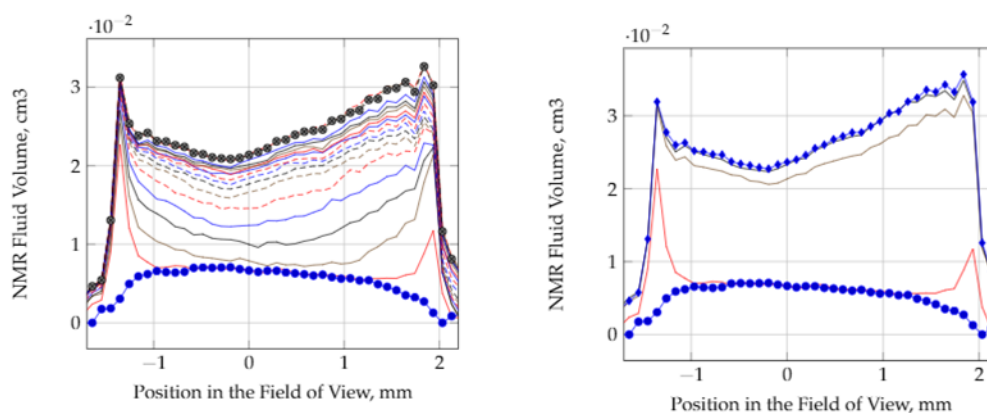


Figure 84: Saturation profiles for Sample B1 recorded by NMR first 24 h with a 30 min leg (left); in 72 h period with 24 h leg (right).

The first sample's (B1) saturation was performed in the NMR high-pressure cell. After establishing the saturation conditions (duration and pressure), we have repeated the saturation for the second object under study — heavy-oil carbonate rock. The procedure of

saturation for carbonate samples was conducted in a high-pressure vessel under pressure for 72 h. In both cases, the actual-field oil samples were used as a saturating fluid.

### 5.4.3 Organic-Rich Source Rock

In this chapter, we have attempted to experimentally model the CO<sub>2</sub> injection into the oil-saturated shale sample (B2).

The CO<sub>2</sub> phase diagram is shown in Figure 85 below. The determination of the diffusion coefficient can be carried out for CO<sub>2</sub> in the liquid or supercritical state (at pressures above 74 atm and temperatures above 30°C). CO<sub>2</sub>-based EOR for the rock of Bazhenov Formation is planned to be conducted at supercritical state of CO<sub>2</sub> due to multiple factors (low porosity of the rock, formation conditions). Therefore, in our experimental modeling, we had to maintain the required conditions for supercritical CO<sub>2</sub>. In the current research, it was decided to experiment with a maintained injection pressure of CO<sub>2</sub> at 150 atm and heating the sample at 28°C. In the case of Sample B2, the weight of the sample measured before and after oil injection was 31.42 g and 32.07 g, respectively. The volume of injected oil was 0.828 ml, which accounted for 6.1% of the total sample volume. The experiment was conducted according to the scheme introduces in Section 5.3.2.

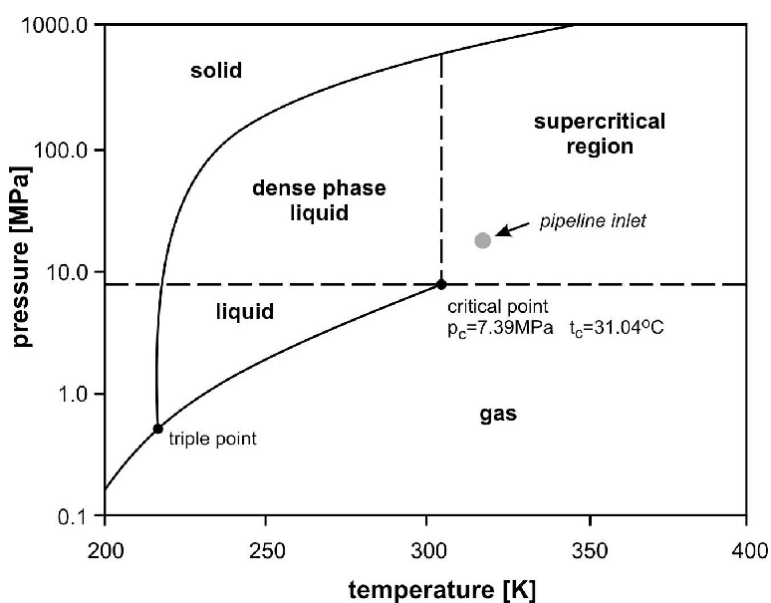


Figure 85: CO<sub>2</sub> phase diagram.

Figure 86 demonstrates the oil saturation distribution for the sample at different times during the injection of supercritical CO<sub>2</sub>. When the CO<sub>2</sub>-induced oil front was propagating, the profile change of the sample during the diffusion of CO<sub>2</sub> into the sample was constantly recorded. Thus, two phases (oil and gas) were present in the sample, wherein only oil was visible for NMR. Based on the results of the Saturation Profile test, gas propagation distances at each point of the sample axis at each moment of the time were recorded. In addition, the  $T_2$  test constantly recorded the change of total fluid volume, which was simultaneously affected by oil viscosity change and gas dissolution. In this connection, it is important to note that the process of diffusion registered by NMR doesn't separate gas dissolution, diffusion, and other physical interactions. However, we assume that there is no mechanical displacement of the oil by gas since the pressure on both outlets of the samples is maintained. Thus, Figure 86 shows the depth of front propagation in the sample obtained from the two profiles with the pronounced front was 15 mm and 25 mm for the 1.5 and 3 hours, respectively.

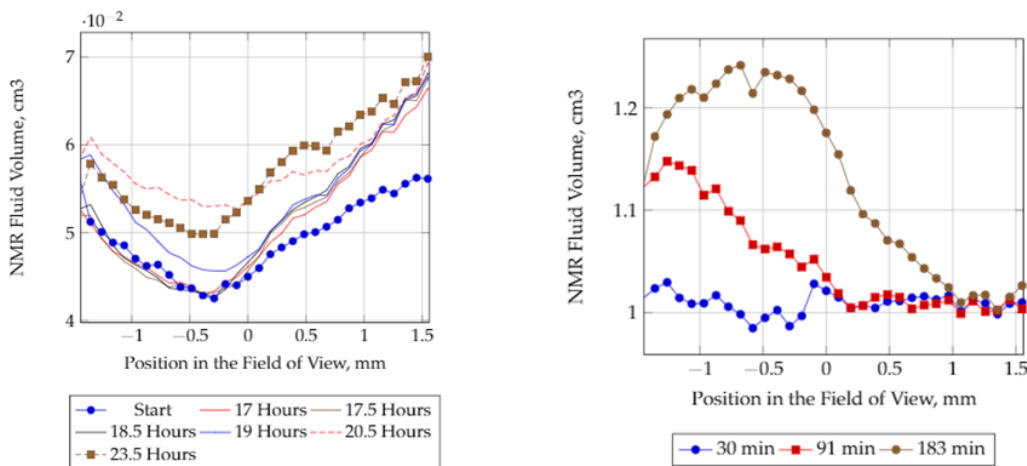


Figure 86: Change of NMR saturation profiles for Sample B1 (left) first 24 h of profiling; (right) first 3 h (normalized to initial saturation profile).

As a first approximation, the diffusion coefficient was calculated based on the Einstein relation for the time of diffusion ( $t$ ) and the depth of spreading ( $L$ ):

$$K_{dif} = \frac{L^2}{t_{dif}} \quad (1)$$

The average value of the diffusion coefficient of CO<sub>2</sub> in oil-saturated shale rock, determined experimentally, is  $4.91 \cdot 10^{-8}$  m<sup>2</sup>/s. It should be noted that the experiment did not observe changes of profiles at CO<sub>2</sub> saturation at a pressure of 150 atm for the first 18 hours. When the pressure was built up to 250 atm in 3 hours, a sharp change of profile saturation was observed. That may be attributed to the transition into the miscibility mode of displacement, as MMP was defined for the system in the range of 180–190 atm (Popov et al. 2016).

#### 5.4.4 Heavy-Oil Carbonate Rock

In the continuation of the first part of the research, the attempt to perform a similar experiment on heavy-oil carbonate reservoir rock with a complex void space structure was made. The workflow included sample saturation in a high-pressure setup and CO<sub>2</sub> injection under HPHT conditions. The main differences were the viscosity of the oil, which caused several complications in the technical preparation of the experiment, and the relatively high porosity/permeability of the rock, which, in turn, shortened the duration of the experiment. Also, CO<sub>2</sub> was injected at a liquid state.

The main injection experiment was carried out according to the earlier proposed procedure. In the first 12 hours, the saturation profiles of the sample were recorded at intervals of 30 minutes. For the next 60 hours, the test was repeated in order to register changes in the sample profile as CO<sub>2</sub> penetrated and diffused into the heavy-oil. Throughout the experiment, the confining pressure and pressure of CO<sub>2</sub> injection (as well as oil injection) were maintained at a constant level. The result of studies in the form of superimposed profiles characterizes the change in the saturation of the sample at intervals of several hours.

The change of profiles describes the main stage of the experiment— injection of CO<sub>2</sub> into the oil-saturated sample (Figure 87). The supply of CO<sub>2</sub> to the sample was carried out step by step; the pressure of CO<sub>2</sub> and oil was increased to 14 MPa (formation pressure). After 9 hours of continuous supply of CO<sub>2</sub> and NMR profiling, a decrease in overall sample oil saturation is observed (from 4.3 ml to 19.2 ml), which indicates the beginning of oil displacement from the sample. Due to the high porosity and permeability of Sample C2, it was proposed to

calculate the diffusion coefficient for the first time interval — 9 hours since the start of the experiment. The change of profiles in this period is shown in Figure 87.

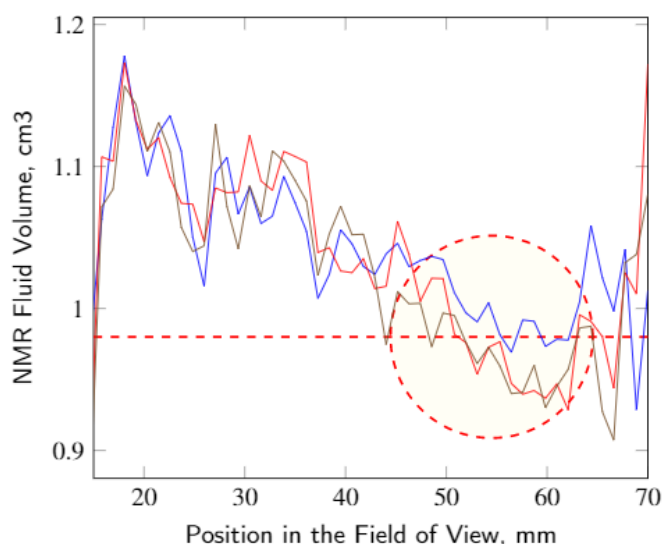


Figure 87: Normalized saturation profiles for Sample C2.

As can be seen from the change in profiles, due to the diffusion of CO<sub>2</sub> in oil, a change in the viscosity of the oil was observed, which led to an increase in oil saturation and expansion of the front as the CO<sub>2</sub> diffused and moved along the sample. The diffusion coefficient was calculated, taking into account the Einstein equation for the diffusion time obtained and the depth of CO<sub>2</sub> propagation. The diffusion coefficient equaled to  $5.5 \cdot 10^{-7} \text{ m}^2/\text{s}$ .

### **5.5 Summary**

The goal of this research was to develop a methodology and an experimental determination of the fluid diffusion coefficient in porous media at atmospheric and reservoir conditions under the control of NMR. The first part of the work consisted of water-water diffusion in low-permeable rock. The second part described the design of the NMR HPHT system and its application for diffusion coefficient calculation of CO<sub>2</sub> into oil-saturated rock samples. Our findings can be summarized in the following points:

- The applicability of the NMR technique was demonstrated on the example of the water-water diffusion in ultra-low permeable rock samples of dolerite; diffusion process completed

in 14 days and demonstrated the change in registered fluid volume by NMR both by 1D and 2D NMR tests.

- The methodology of determination of the CO<sub>2</sub> diffusion coefficient using NMR profiling in reservoir conditions was developed and tested on two different rock types.
- In the framework of HPHT experiments, an investigation of the tight rock saturation was performed. It was established that low-porous rock reaches its highest saturation within constant oil injection for no less than 72 h under pressure up to 15 MPa.
- According to the results of the experiment, it was found that the diffusion of CO<sub>2</sub> in the process of gas injection leads to a shift in the front of the oil saturation profile and can be used as initial data for further mathematical calculation of the CO<sub>2</sub> diffusion coefficient in the porous medium. Monitoring of saturation profiles by NMR for 72 hours confirmed that after a certain period of time, the diffusion of CO<sub>2</sub> is followed by the process of oil displacement, whereas the constant pressure is maintained.
- An experimental determination of the CO<sub>2</sub> diffusion coefficient under reservoir temperature and pressure conditions has been carried out for two different objects. The experimental diffusion coefficient was equal to  $4.91 \cdot 10^{-8} \text{ m}^2/\text{s}$  for the shale sample and  $5.5 \cdot 10^{-7} \text{ m}^2/\text{s}$  for the carbonate sample.

## CHAPTER 6

### NMR APPLICATIONS IN THERMAL EOR STUDIES

#### **6.1 Introduction**

Recently, thermal enhanced oil recovery methods have attracted a high level of interest because of their possible application to unconventional reservoirs (Alvarado and Manrique 2010, Sheng 2017). One of the effective techniques is high-pressure air injection (HPAI) or *in-situ* combustion (ISC), which involves the initiation of an oxidation front in the formation which does not only displace the oil by combustion gases, heated fluids, and steam but also causes an increase of reservoir pressure and temperature (Sarathi 1999, Moore et al. 2002). The necessary critical conditions in the formation can be achieved artificially in the laboratory by an external impact on the rock, for example, by thermal exposure. The most critical experiment for evaluating the effect of technology and obtaining technological parameters is a combustion tube test (Sarathi 1999, Gutierrez et al. 2012). The combustion tube (CT) test is the physical modeling of thermal exposure on porous media in formation conditions. It is conducted to assess the ISC/HPAI potential for a particular reservoir type as well as to obtain parameters for further upscaling of the technology in the field.

High-temperature exposure results in a significant evolution of the shale porosity and permeability due to kerogen transformation. This affects the reservoir properties and leads to a change in the rock's porous structure and the expansion of the stimulated reservoir area. The change in petrophysical properties during thermal conversion is often evaluated by defining the porosity and permeability alteration (Kibodeaux 2014). Multiple studies are devoted to the study of the pore evolution during the controlled pyrolysis of the shales (Sun et al. 2015, Bai et al. 2017, Geng et al. 2017). According to the published studies, heating (pyrolysis) of organic-rich shales generally leads to an increase in porosity and pore connectivity (Kobchenko et al. 2011, Panahi et al. 2013, Saif et al. 2016). Tiwari et al. (2013) investigates the oil shale before and after the pyrolysis and demonstrates changes in the pore structure of raw and pyrolyzed shale using X-ray micro CT. They showed a porosity increase at 20–25% as a result of heating to a temperature of 500°C. Kobchenko et al. (2011)

demonstrated the first micro-fractures nucleation at the temperature of 350°C using advanced real-time 3D X-ray tomography. Also, in the latter study (Panahi et al. 2013), they stated that the reason for this fracturing is the expansion of organic matter. Using a similar approach of 3D X-ray tomography, Saif et al. (2016) noticed that a significant increase of porosity occurs at the temperature of 390°C (up to 20-25%); further heating mainly causes growth of pore connectivity. To assess the changes in shale pore structure, a number of advanced laboratory techniques can be applied. For instance, Liu et al. presented results on the evolution of oil shale pore structure from 23 to 650°C by simulating in-situ pyrolysis using a TGA, MIP, and LPNA (Liu et al. 2018). To estimate the organic matter transformation, pyrolytic chromatography of rock samples by the Rock-Eval method is required before and after the combustion. The parameters may serve as engineering guidelines for in-situ combustion or other HPHT processes (Tisot 1967).

To get a full picture of the changes before and after the thermal exposure during the combustion test, it is necessary to provide a detailed laboratory analysis of the core samples (Deng et al. 2011, Kibodeaux 2014). In physical modeling of the combustion process, the tube is typically filled with unconsolidated core or core chips. However, the use of the crushed core pack is beside the purpose as the shale is characterized by low porosity and permeability, whereas the carbonates are characterized by caverns and cracks. It is complicated to evaluate the saturation of the rock in the crushed samples caused by physical and chemical changes. First, one of the tasks of the current study was to study and analyze the petrophysical and geochemical rock properties caused by front propagation and oil displacement in organic-rich shale and carbonate consolidated core samples (standard cylinders). The second was to select and check the viability of advanced laboratory techniques to control and evaluate these changes.

One of the conventional methods for determining reservoir properties is the standard pressure pulse-decay permeametry (Sander et al. 2017). Investigation of reservoir properties of tight samples requires new and different methodologies in comparison with ones adopted for the study of conventional reservoir rocks (Guidry et al. 1996, Simpson and Fishman 2015). The reason is the low porosity and permeability values, high content of organic matter (mainly

solid) insoluble in organic solvents phase (kerogen) in shales, high-viscosity oil, and the complex void structure in carbonates.

Among the recent technologies used in studies of unconventional reservoirs, attention is paid to fluids identification based on NMR relaxometry. Low-field NMR is often used as a non-disruptive tool for determining the saturation and pore space structure of the complex rock (Straley et al. 1997, Fleury 2014, Liu et al. 2020). In addition to the reservoir properties and liquid saturation, it is important to characterize the OM properties by Rock-Eval pyrolysis. The integration of the set of experimental techniques (gas permeametry, NMR, Rock-Eval pyrolysis, and SEM) allowed us to investigate the dynamics of changes in the physicochemical state of rock samples before and after exposure

In this research direction, we analyze the influence of thermal and oxidation exposure on petrophysical (porosity, permeability, saturation) and geochemical properties (OM quality) on the case of local Bazhenov Formation rock samples and heavy-oil carbonate formation.

The same reasoning applies for heavy-oil formations where due to multiple technical reasons, the EOR methods such as *in-situ* combustion (ISC) show high interest. The integration of the set of experimental techniques (gas permeametry, NMR, and Rock-Eval pyrolysis) enables investigating the dynamics of changes in the physicochemical state of rock samples before and after exposure. Therefore, the best practices to trace the total saturation and change in rock void structure during thermal EOR are the methods of NMR and Rock-Eval pyrolysis. In the current chapter, we demonstrate the results of NMR applications on the investigation of the fluid displacement, porous structure, and pore size change in target oilfields.

## **6.2 HPAI in the Shale Formation**

### **6.2.1 Introduction**

Bazhenov Formation is one of the most prominent shale formations in the world, and it is characterized by complex lithological structure, high amount of viscous components, and heterogeneity of the rock (Prishchepa et al. 2014). That is why thermal enhanced oil recovery techniques should be developed to unlock the oil shale potential (Tiwari et al. 2013, Zhirong Zhang 2014). The results of laboratory modeling of various thermal recovery methods for

the Bazhenov Formation are presented in many publications (Bondarenko et al. 2017, Popov et al. 2017, Bondarenko 2018). This work was designed to investigate the change in reservoir rock properties and kerogen conversion induced by the temperature of exposure in the combustion tube experiment, the results of which are detailed in separate work (Bondarenko et al. 2017).

The core pack consists of oil-saturated rock samples from several fields of the Bazhenov Formation. As a result of the exothermic combustion, the maximum temperature achieved was 463°C, and the pressure reached 27 MPa. HPAI was physically simulated on BF core samples—from Oilfield #2, Oilfield #5, and Oilfield #3 (Section 2.1) (Figure 88). Core plugs were evenly distributed along the combustion tube along with the sand and crushed core pack. The entire tube can be divided into six zones exposed to different maximum temperatures.

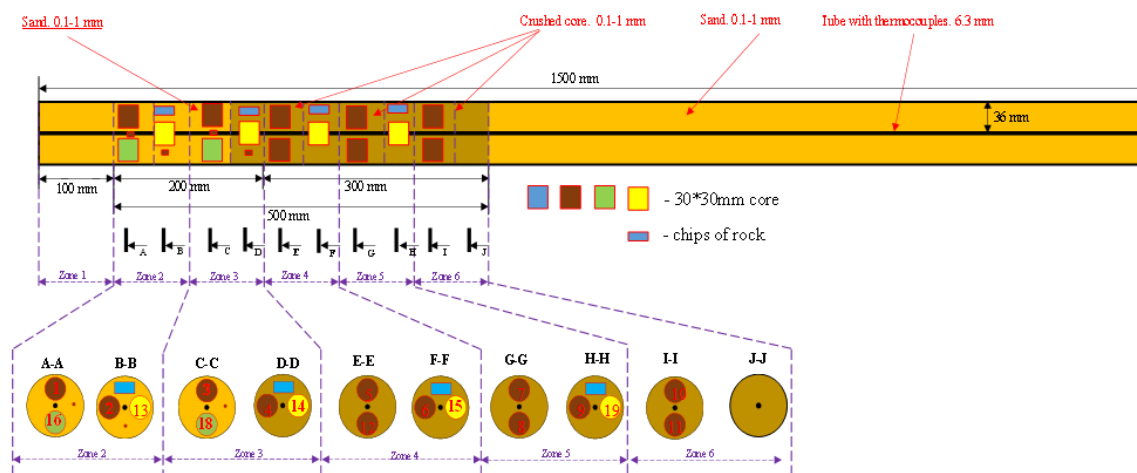


Figure 88: Location of the analyzed samples in the combustion tube (Modified after Bondarenko 2018). Zone numeration corresponds to the CT section numbers.

## 6.2.2 Experimental Methodology

Diversity in the sample's origin (different oil fields) and their properties led to the difference in their after-combustion state. To test the effectiveness of HPAI in consolidated samples, we analyzed rock properties before and after the combustion. In the current study, this was performed by the NMR, Rock-Eval pyrolysis, SEM, and gas permeameter.

The main requirement for core analysis was a non-disruptive testing method to characterize the thermal exposure effect on consolidated core samples. The set of core plugs was analyzed in their initial saturation or as-received state (before combustion) and after the exposure. Air injection was stopped after the temperature of the fourth zone reached its peak temperature. The last two zones, packed with core chips, were exposed only to moderate temperatures; in other words, the combustion front did not pass through these (5.1–6.1) zones. The test goal was to reveal differences in the rock properties in the zones behind and in front of the combustion front; for this purpose, we analyzed the core from each temperature zone. In this study, Bazhenov Formation cylindrical (30×30 mm) rock samples from four oil fields of interest were selected for the investigation. Table 21 contains information about the samples selected for investigation.

Table 21. List of the investigated samples

Sample ID	Oilfield	Lithology	CT zone	Exposed Temperature (°C)
1	Oilfield #2	Siliceous mudstone	2.1	301
2			2.2	369
3			3.1	430
10			6.1	207
12			4.1	463
13	Oilfield #5	Mixed argillaceous-siliceous mudstone	2.2	368
14			3.4	461
15			4.2	422
16	Oilfield #3	Siliceous mudstone	2.1	300
18			3.1	430
n1, n2, n3, n4, n5	Oilfield #4	Mixed argillaceous-siliceous mudstone	n/a	n/a

## 6.2.3 Results

### 6.2.3.1 Gas Porosity and Permeability after Thermal Exposure

Each section in the combustion tube contained up to four core plugs. At least one representative sample from each CT section was selected for the analysis, including NMR,

Rock-Eval pyrolysis, and gas porosimetry. We attempted to obtain the maximum knowledge on the reservoir and geochemical properties of the rock. Gas porosimetry evaluated the porosity and permeability evolution of the rock. NMR relaxometry examined the saturation and porous space changes induced by combustion; pyrolysis analyzed the kerogen conversion in exposed rock species.

Before and after the combustion tube test, the entire set of core samples underwent testing on a standard gas permeameter used for determining the reservoir properties such as porosity and permeability. In addition, all core plugs were photographed after the combustion in order to record the visual changes (Figure 89).

The photographs of samples subject to thermal exposure illustrate the visible changes in the rock matrix. Images show how rock samples have changed color: two samples (#2 and #3) of Oilfield #2 changed color to coral-red, which may be caused by the increased pyrite content in the samples. In Samples #16 and #18 of Oilfield #3, bitumen is observed. In Sample #14 of Oilfield #5, we can notice a newly formed fracture.

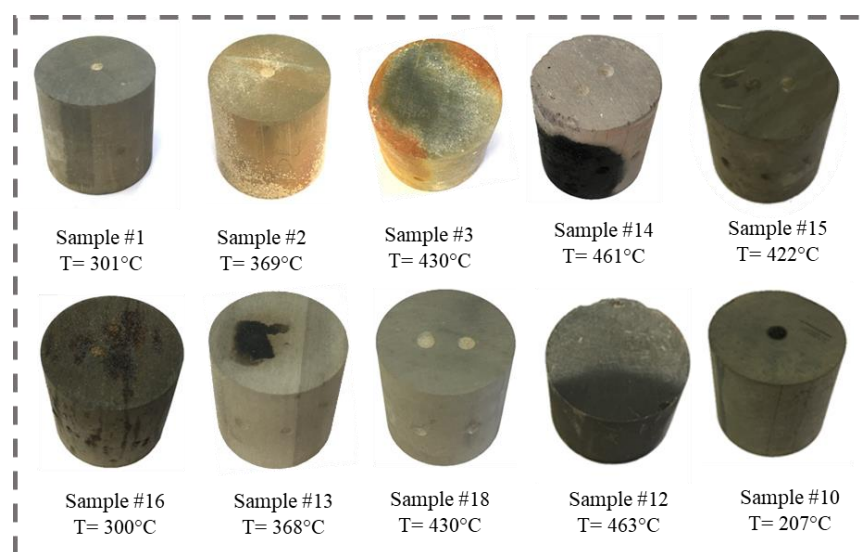


Figure 89: Photographs of cylindrical samples after the combustion tube experiment (upper left corner — sample id; lower right corner — tube section) (modified after [Bondarenko 2018](#)).

The first non-contact method used was porosity determination by nitrogen flow and pressure decay. For standard measurement with nitrogen, a significant increase in porosity values was obtained; it was caused by increased void space in the core cylinders (Figure 90).

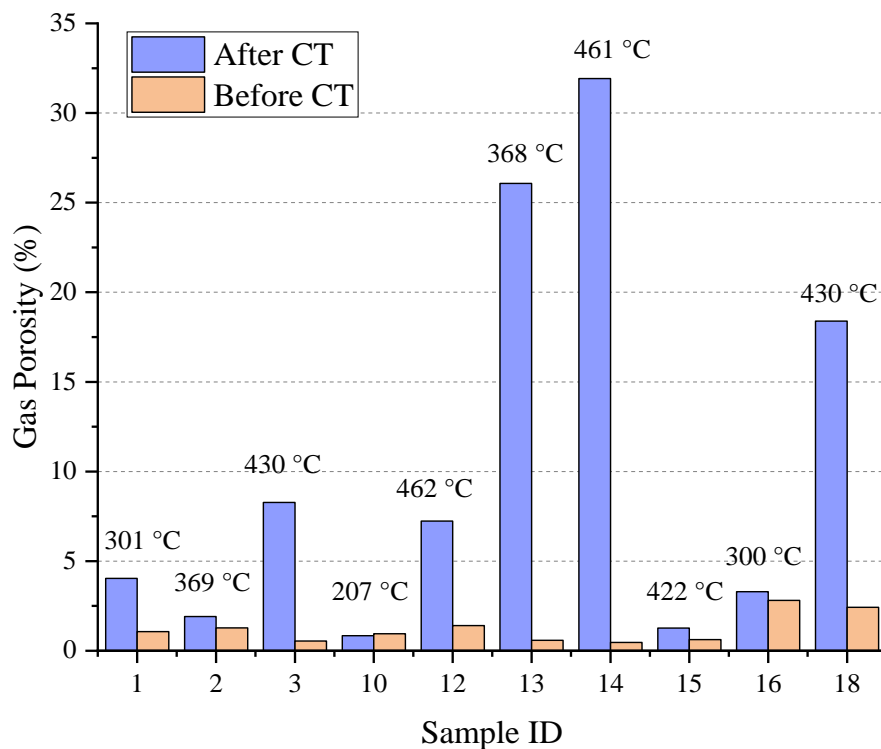


Figure 90: Change in gas porosity before and after the combustion (Mukhametdinova et al. 2020).

The full data of porosity and permeability are summarized in Table 22. The tendency of a significant increase in both parameters at high exposure temperatures was noted. This confirms the front propagation and reflects the importance of reached temperature on porosity and pore connectivity evolution.

Table 22. Gas porosity and permeability before and after the combustion

Sample ID	Section	Temperature (°C)	Porosity	Permeability	Porosity	Permeability
			before CT (%)	before CT (mD)	after CT (%)	after CT (mD)
1	2.1	301	1.07	0.004	4.04	0.062
2	2.2	368	1.28	0.003	1.91	0.034
3	3.1	430	0.54	0.033	8.27	0.769
10	6.1	207	0.95	0.003	0.84	0.014
12	4.1	462	1.41	0.003	7.24	0.030
13	2.2	368	0.58	0.024	-	-
14	3.4	461	0.47	0.012	31.92	4.277

Sample ID	Section	Temperature (°C)	Porosity	Permeability	Porosity	Permeability
			before CT (%)	before CT (mD)	after CT (%)	after CT (mD)
15	4.2	422	0.62	0.007	1.27	0.085
16	2.1	300	2.81	0.053	3.30	1.591
18	3.1	429	2.43	0.065	18.39	0.577

### **6.2.3.2 Development of $T_1$ - $T_2$ Interpretation Scheme**

In the framework of rock analysis before and after the thermal exposure, the multistage NMR analysis of the rock at different states of saturation was conducted on a collection of the same BF rocks. A detailed NMR analysis of 5 core plugs (n1–n5) in order to develop the  $T_1$ - $T_2$  interpretation scheme for target collection prior to the main experimental section was performed. The selected shale samples had similar petrophysical, geochemical properties, and lithotype.

The core plugs underwent a 4-step routine core analysis, including drying and saturation of the rock with water and decane. For each of the samples studied, an individual interpretation of  $T_1$ - $T_2$  maps was carried out, and the values of water and oil saturation were calculated. An example of the  $T_1$ - $T_2$  maps for representative Sample n5 is illustrated in Figure 91. The change of fluid signal of the rock at different stages of saturation was observed. This enabled fluid separation in the sample based on the information obtained.

An increase in the fluid viscosity is accompanied not only by changes in the  $T_1$  and  $T_2$  relaxation times but also, most importantly, by the ratio of longitudinal relaxation time to transverse relaxation time  $T_1/T_2$ . Recently, many scholars have presented their own interpretation schemes of  $T_1$ - $T_2$  maps for shale rock (Khatibi et al. 2018, Liu et al. 2018, Li et al. 2020, Zhang et al. 2020). In the current work, we utilized the modified interpretation scheme, which was introduced in Section 3.5.

In the as-received or primary saturation state, there is an insignificant signal region of reduced  $T_1/T_2$  (2–10 ms/ms) and low  $T_2$  (less than 1 ms) area, which is responsible for water-bound by clay minerals (Figure 91a)—drying the sample results in a significant change in the NMR signal in the clay and bound water region of the porous medium (Figure 91b).  $T_1$ -

$T_2$  maps (Figure 91d) show that decane resaturation is predominantly indicated by an increase in NMR signal due to the  $T_1$ - $T_2$  distribution region with low  $T_1/T_2 \sim 1$  and long  $T_2$  (40–300 ms), which indicates the filling of large pores of the inorganic matrix (IP — inorganic porosity). This proportion in the structure of the void space of the sample is dominant. With a small number of large pores, the NMR signal in the region of long  $T_2$  is usually leveled. The volume of pore space in the region of large pores is equal to more than 60% of the total volume of pore space recorded after the sample is saturated with the decane.

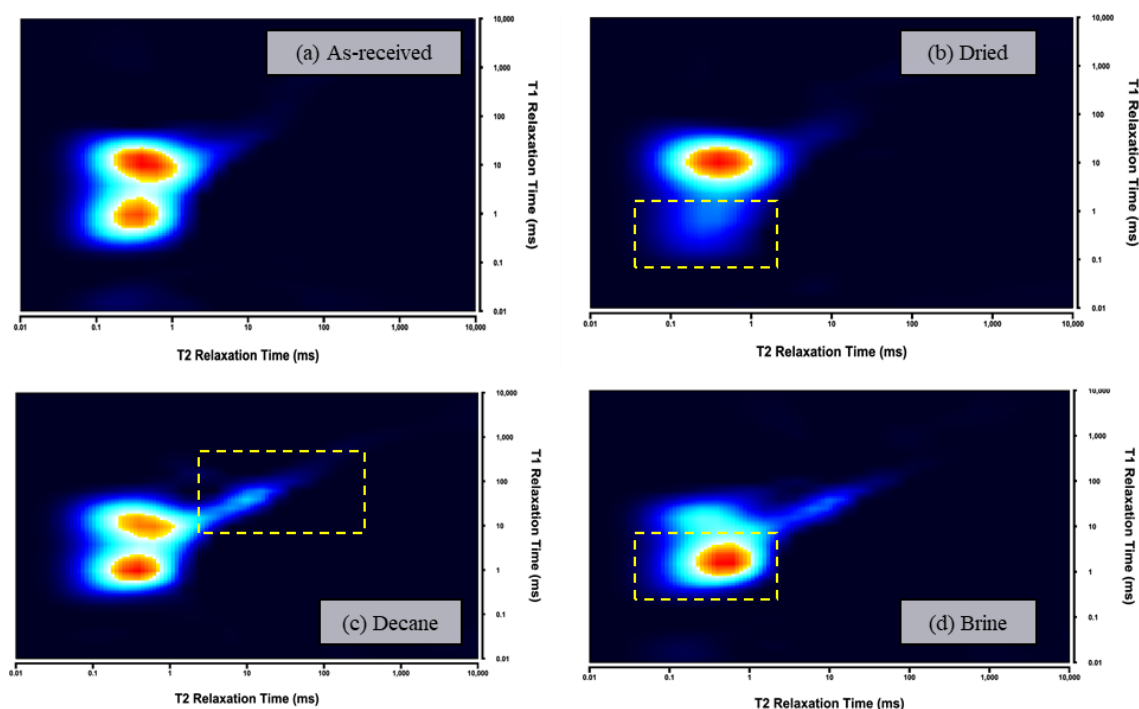


Figure 91:  $T_1$ - $T_2$  map studies, Sample n5 in (a) as-received state; (b) dried state; (c) decane-saturated state; (d) brine-resaturated state. (Mukhametdinova et al. 2020)

Based on the results for the remaining samples and literature review, we have analyzed and proposed the  $T_1$ - $T_2$  map interpretation scheme for target rock samples. The presented collection of samples of the BF shows different reservoir properties (porosity and pore size), which is caused by a high degree of heterogeneity in composition, structured pore space, and surface properties. Therefore, we have simplified the  $T_1$ - $T_2$  scheme focusing on hydrogen populations corresponding to bitumen and adsorbed oil, structural and adsorbed water, and mobile oil in IP. The development of this interpretation scheme enabled the ready framework to be set for further analyses of the core saturation and oil displacement for  $T_1$ - $T_2$  maps of

rock before and after the air injection in CT.

### **6.2.3.3 NMR Analysis of the Core before and after Thermal Exposure**

NMR enables tracking of the change in porous space occupied by fluids and provides this value both in volume (ml) and in porosity (%) units. We utilized the NMR for registering the fluid saturation by a number of selected tests: CPMG  $T_2$  relaxation, 1D saturation profile, and  $T_1$ - $T_2$  map for fluid separation. Samples before and after the combustion tube were analyzed according to the proposed methodology; at each stage, the series of above-mentioned test types were repeated with the same parameters (Figure 92).

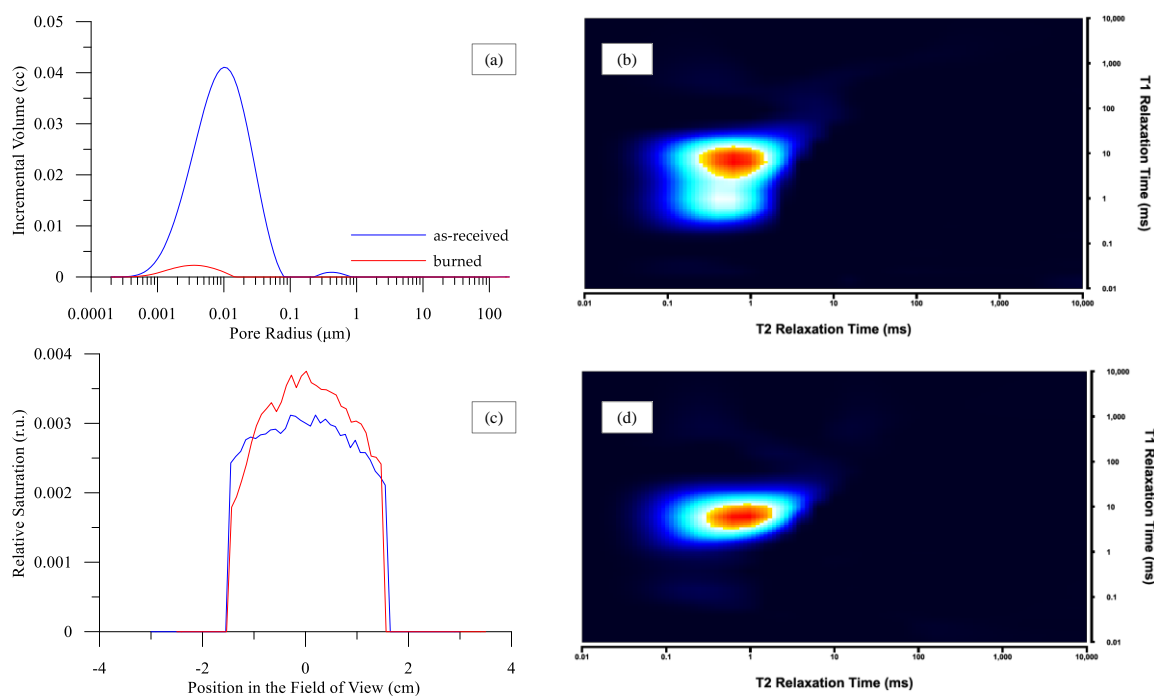


Figure 92: NMR analysis of Sample #16: (a)  $T_2$  relaxation before (blue) and after CT (red); (b)  $T_1$ - $T_2$  map for as-received sample; (c) saturation profiles before (blue) and after CT (red); (d)  $T_1$ - $T_2$  map for the burnt sample. (Mukhametdinova et al. 2020)

After the combustion, there was a near-zero volume of fluids left in the samples (Figure 93). At first approximation, the residual fluid saturation for target rocks depends on their initial saturation, the temperature of the zone, and the combustion tube section. We clearly observe an apparent decrease in total fluid volume for samples that were exposed to 300–369°C, whereas in sections with higher temperatures, the fluid is almost completely removed. Exceptions can be explained by the example of Sample #15, where a certain amount of fluid

remains after exposure to 422°C. This sample was located in Section 4.2, which is near the end of the propagation front. We explain the remaining fluid by generated oil, which was not removed. Thus, the results of measurement mainly indicate the displacement and burning of hydrocarbons from cylindrical samples along the combustion front, but this difference is controlled by several factors. These factors primarily include the petrophysical background of the rock samples (rock lithology, OM properties) and experiment conditions (temperature in the CT zone, location in CT, and duration of exposure).

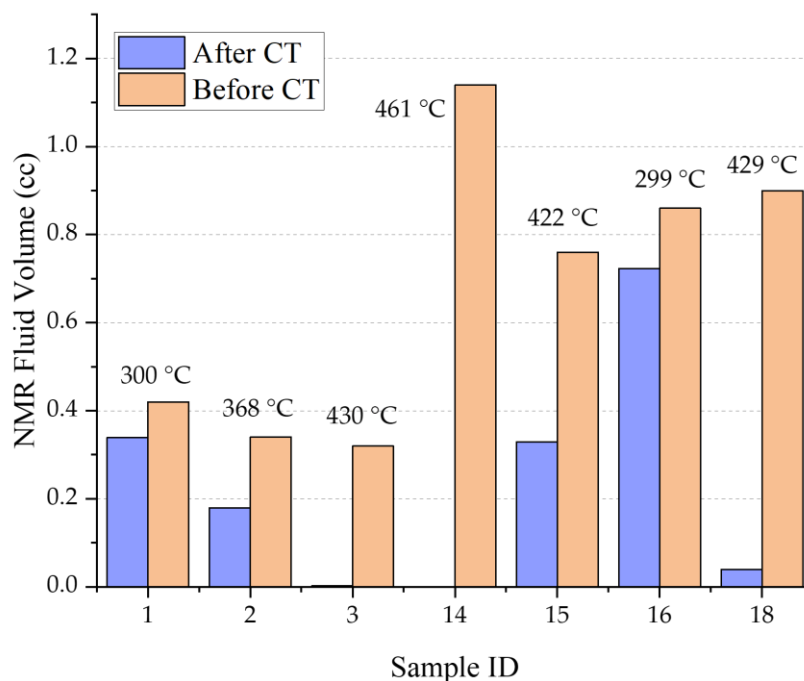


Figure 93: Change in the fluid saturation by NMR before and after the combustion. (Mukhametdinova et al. 2020)

NMR measured the change in total fluid volume of the sample and the spatial saturation using 1D NMR profiling. We used  $T_2$  relaxation curves for illustrating the distribution of fluid-occupied pores inside the rock (Figure 94 a,b). Images illustrate how the liquid phase was redistributed in the samples exposed at different temperatures. Sample #2 (located in Section 2.2) shows a decrease in the number of pores filled with the heavy components, and residual fluid relocation to larger pores, after the combustion. In the case of Sample #12 (Section 4.1 — where the temperature reaches the maximum value), we observe the entire removal of mobile fluids and a small amount of heavy components in the microporous region.

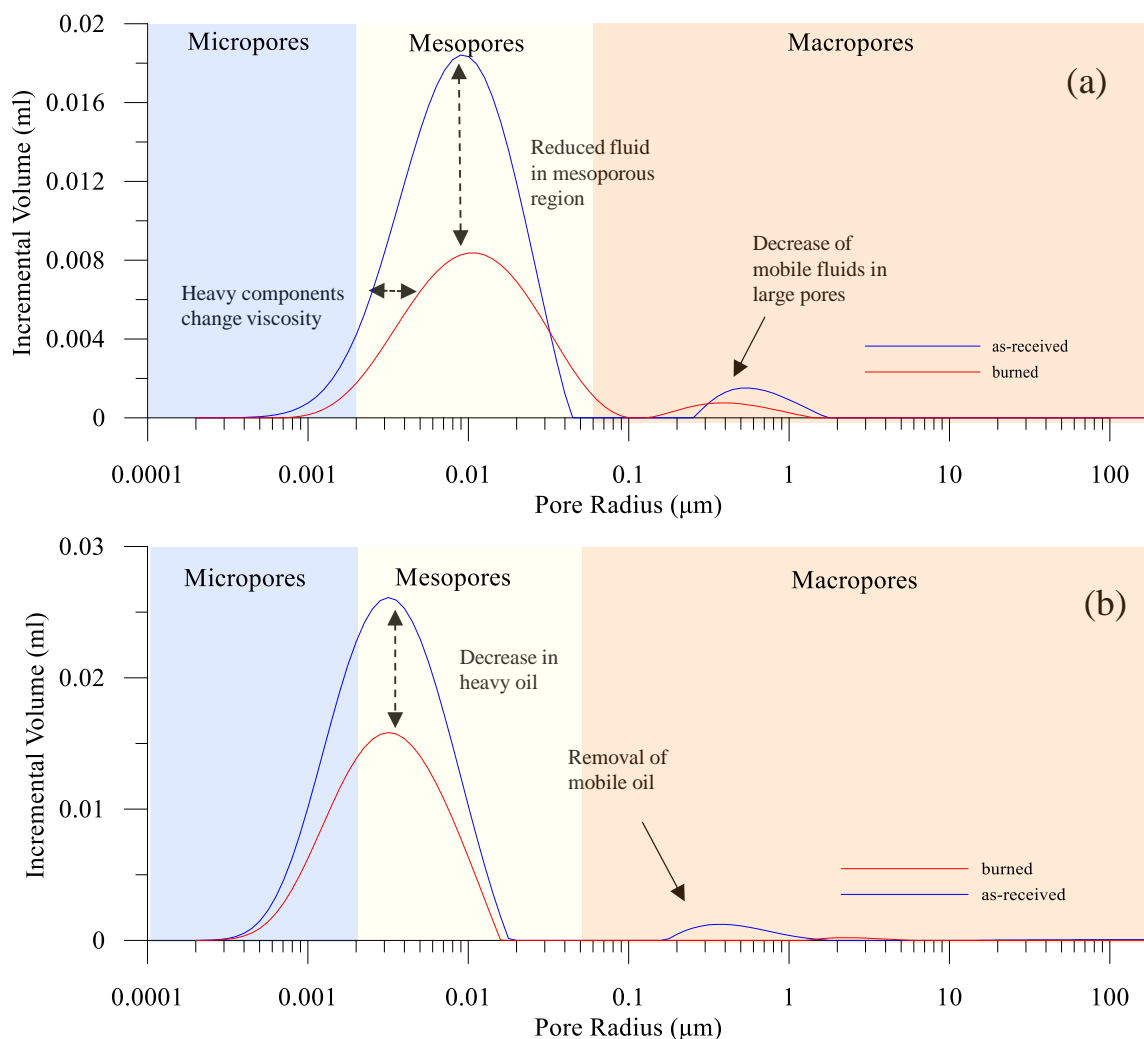


Figure 94: Pore size distribution for Samples (a) #2 (b) #12. (Mukhametdinova et al. 2020)

Additionally, we have utilized the developed NMR  $T_1$ - $T_2$  interpretation scheme for registering the change in saturation and residual fluid types in the rock samples. In general, the total fluid volume is applicable for estimating the common saturation level change in rock and evaluate the influence of thermal exposure in the tube. Therefore, the disintegration of HC populations (fluid types) might be useful for modeling the thermal EOR processes and validation with experimental data. As explained earlier, we have developed a simplified  $T_1$ - $T_2$  interpretation map by reducing the number of fluid categories to bitumen & adsorbed oil, structural & adsorbed water, and mobile oil in IP. The summary of the samples investigated before and after CT is provided in Table 23.

Table 23. Results of NMR analysis of samples before and after CT

Sample ID	Before CT				After CT			
	Total Fluid Volume (cc)	Bitumen & Adsorbed Oil (%)	Structural & Adsorbed Water (%)	Mobile Oil in IP (%)	Total Fluid Volume (cc)	Bitumen & Adsorbed Oil (%)	Structural & Adsorbed Water (%)	Mobile Oil in IP (%)
1	0.42	84.22	8.40	5.34	0.33	86.45	8.13	5.96
2	0.34	86.29	6.45	6.72	0.17	68.86	26.75	5.26
3	0.32	82.14	7.65	8.16	0.002	31.72	13.10	18.62
10	-	-	-	-	0.49	28.78	64.39	7.19
12	-	-	-	-	0.28	44.74	41.67	10.53
14	1.14	93.83	2.53	2.02	8*10 <sup>-8</sup>	n/a	n/a	n/a
15	0.76	77.68	16.19	11.23	0.32	81.20	2.87	14.36
16	0.86	59.98	42.18	4.54	0.03	85.84	7.77	5.18
18	0.90	59.25	41.09	5.12	0.72	0	20.83	0

#### **6.2.3.4 Organic Matter Characterization by Rock-Eval Pyrolysis**

The OM properties of the target samples (rock specimen was taken from the same depth within a well section) are characterized by the Rock-Eval technique (Table 24). According to S2 values, Samples #1/2 and #13/15 show extremely high generation potential. Tmax demonstrates relatively the same maturity for all samples investigated. TOC content varies in the range of 5.39–16.98 wt.%. According to the pyrolytic parameters, the maturity of Oilfield #2 and Oilfield #5 is at the beginning of the oil window. Oilfield #3 parameters correspond to the peak of oil generation. All specimens of the initial samples were prepared using a single-point drilling scheme. The same applied to most samples after combustion resulted in core fragility.

Table 24. Pyrolytic properties of samples before CT

Sample ID	S1	S2	S3	TOC	Tmax
	<i>mg HC/g rocks</i>	<i>mg HC/g rocks</i>	<i>mg CO2/g rocks</i>	<i>wt%</i>	<i>°C</i>
1/2	3.96	100.2	0.34	14.01	424
10	1.41	36.65	0.39	6.01	429
12	0.63	38.36	0.24	5.39	428

	<b>S1</b>	<b>S2</b>	<b>S3</b>	<b>TOC</b>	<b>Tmax</b>
<b>Sample ID</b>	<i>mg HC/g rocks</i>	<i>mg HC/g rocks</i>	<i>mg CO2/g rocks</i>	<i>wt%</i>	<i>°C</i>
13/15	6.30	107.6	0.2	16.98	433
16/18	6.95	31.26	0.31	7.98	446

Results of 2D pyrolysis and SEM imaging of selected samples before and after the exposure are presented in [Mukhametdinova et al. \(2020\)](#). The study of fragile Samples # 1–3, 13, 15, 18 was carried according to the standard procedure where the sample for pyrolysis was taken in the center of the core, as the most characteristic point according to 2D studies. The obtained data are listed in Table 25.

Table 25. Pyrolytic properties of samples after CT

	<b>S0</b>	<b>S1</b>	<b>S2</b>	<b>S3</b>	<b>TOC</b>	<b>Tmax</b>
<b>Sample ID</b>	<i>mg HC/g rocks</i>	<i>mg HC/g rocks</i>	<i>mg HC/g rocks</i>	<i>mg CO2/g rocks</i>	<i>wt%</i>	<i>°C</i>
1	0.05	0.13	4.56	0.7	1.55	425
2	0.3	0.55	3.25	0.49	1.43	430
3	0.04	0.1	0.44	0.38	1.41	457
13	4.2	17.14	22.99	0.17	10.88	439
15	2.2	2.69	26.42	0.24	5.3	434
18	0.19	0.69	1.33	0.16	4.86	586

In this work, we have attempted to define the correlations between parameters obtained, such as gas porosity and permeability, residual saturation by NMR, S2 value, and exposed temperature (Figure 95). Notably, for all samples, we observe an increase in porosity and permeability. Crossplot for gas porosity relative change (Figure 14a) shows that there is a good correlation between porosity and the section temperature. In the case of NMR saturation of the rock (Figure 95b), we observe a direct relation of change in NMR fluid volume and CT zone temperature. At higher temperatures in CT, more HC fluid in the rock is displaced, resulting in lower residual saturation by NMR. When plotted for gas permeability (Figure 95c), it is less pronounced and can be applied for mainly 3–4 samples (in the 400–470°C range). Similar applies to the S2 value change (Figure 95d), which directly indicates the

kerogen transformation in rock. Decreased S<sub>2</sub> values prove the generation of synthetic oil during the combustion process. In turn, NMR and Rock-Eval results demonstrate the presence of liquid oil, which remains in rock samples and, therefore, not collected at the tube fluid samplers. For this reason, the TOC content should not be considered as an OM indicator within the combustion experiment.

However, samples exposed to the same temperature demonstrate different behavior. This confirms the presence of multiple factors influencing the change in rock properties. Besides the CT section temperature, other important factors include the rock lithology, OM content, and maturity. Thus, the exposure temperature, location in the combustion tube (section), and initial properties of the rock might significantly affect the combustion results. In our case, we investigated samples from three oilfields with different rock lithology and OM maturation. Oilfields #2 and #3 are of similar rock lithology – siliceous organic-rich shales. Oilfield 5# is represented by mixed argillaceous-siliceous shale mudstone (shale). In turn, all oil fields have various OM maturity — Oilfields #2 and #5 are at the beginning of the oil window but with higher generation potential for oilfield 2. Rocks from Oilfield #3 have OM at the peak of oil generation, and, therefore, they demonstrate distinct behavior (Samples #16 and #18 Figure 95a,c,d). At the same time, Samples #12 and #14 were exposed to the same temperature (463°C and 461°C, accordingly) and had the relatively same order of porosity and permeability before the experiment. However, their final values of porosity and permeability are drastically different (Figure 95). Samples #13 and #14 from Oilfield #5 shows very high gas porosity (26% and 32%) and permeability (5.7 mD and 4.2 mD). It can be explained by specifics of mineral composition (as for argillaceous-siliceous mudstone), higher OM maturity (than that for Oilfield #2), a higher amount of transformed kerogen (proved by S<sub>2</sub> values), or other technical reasons such as the occurrence of large fractures and voids. In other words, it is crucial to account for the rock heterogeneity in original reservoir properties and technical specifics of the experiment when modeling the HPAI for target oilfields.

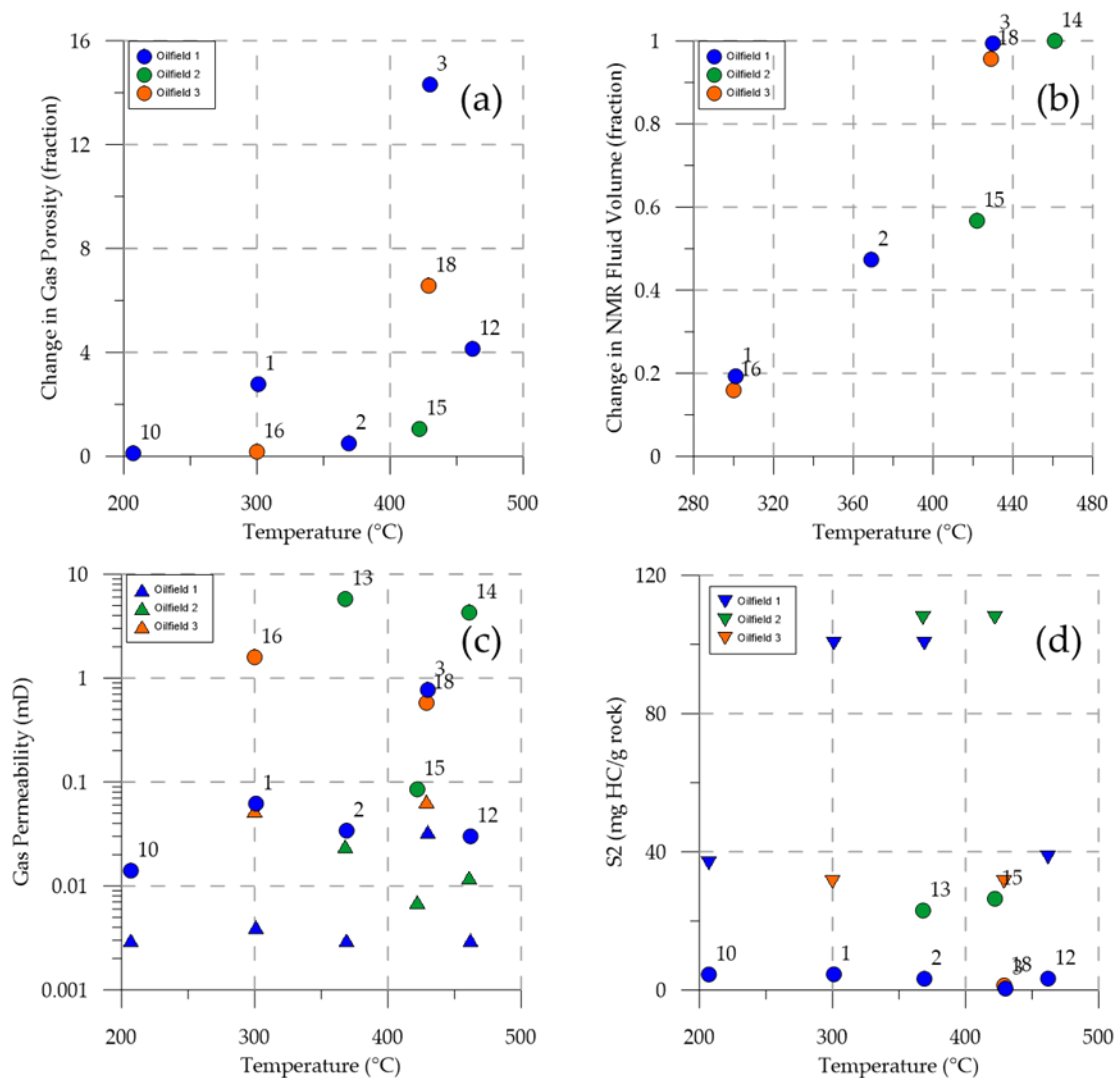


Figure 95: Crossplot of (a) porosity by gas; (b) residual saturation by NMR; and (c) residual TOC vs. temperature. Triangle-shaped symbols indicate the measured parameter before CT. (Mukhametdinova et al. 2020)

The standard practice of laboratory HPAI, experimental data interpretation, includes recording the change in temperature profiles during the test. The reservoir and geochemical properties of rock before and after the thermal exposure can be upscaled from the laboratory level to the combustion tube characterization. Hence, it is recommended to enhance the standard laboratory HPAI combustion tube protocol and to include a comprehensive analysis of core plugs using available non-invasive techniques. Known parameters of the tube (section length) and size for each particular sample make it possible to correlate the saturation level and other parameters with the location of the rock inside. Thus, complementary analysis of

standard rock samples enables the maximum knowledge to be obtained on the physical and chemical processes within the laboratory thermal EOR tests.

### **6.3 In-Situ Combustion in Heavy-Oil Carbonate Formation**

#### **6.3.1 Introduction**

This section summarizes the work conducted within combustion tube experiments on rock samples from carbonate fields located in the southern part of Russia (Oilfield #7, Section 2.1).

As described earlier, the laboratory ISC experiment is an important tool for estimating the potential application of air injection technology in the selected field. At the initial stage of the research, the main goal of laboratory research is updating and defining the petrophysical rock properties. Particularly, it is crucial when investigating the carbonate rock with complex void space structure. An object of our investigation is the carbonate formation from Tournaisian deposits, which are represented by viscous oil-saturated light-gray dolomites with a beige shade, fine-grained intercalations, with inclusions of anhydrite and kaolinite. Rocks are characterized by a medium density and strength, cavernous-pore, and fissure-cavernous-pore structure.

Results consist of data on sample poroperm properties obtained by different methods. Porosity, permeability, fluid saturation, pore size distribution are the critical characteristics defined during each combustion tube test. Rock samples were measured in as-received, dried, hydrocarbon (oil), and water-saturated states. Pore size distribution enabled visualizing the changes in the porous structure at nano- and micro levels.

#### **6.3.2 Experimental Methodology**

This study focuses on the post-analysis of consolidated and non-consolidated rock samples before and after the combustion tube experiment and analysis of changes due to the thermal and oxidation exposure. Table 26 lists the rock samples used in the study.

Table 26. List of rock samples

Sample ID	Oilfield	Porosity by NMR (%)
7	Oilfield #7	6.3
10		9.8
14		4.6
22		6.4
23		3.3
25		2.8
26		6.7
27		4.8
30		2.9
33		2.8
32		3.2
35		2.0

Results of gas porosity and permeability measurements using the PDP technique for the entire collection are presented in Figure 96. The figure illustrates that the gas porosity of the whole core collection varies from 0.5–16%, while the average permeability is around 0.6 mD with a maximum of 4.5 mD.

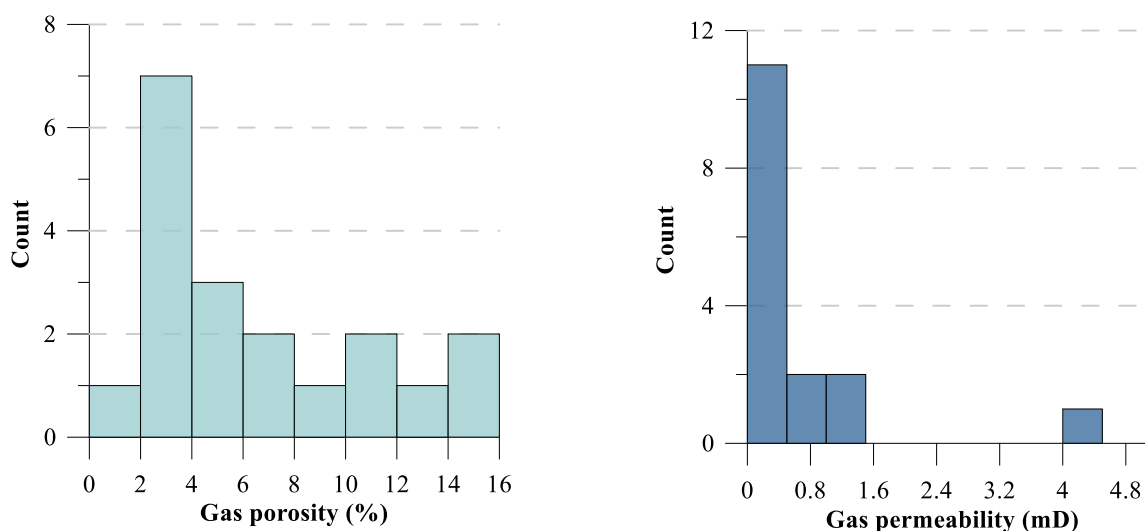


Figure 96: Porosity (left) and permeability (right) of target collection.

Three major experiments on a unique installation of medium-pressure combustion tube (MPCT) (up to 21 MPa) (Figure 97) were carried out on a bulk core model of the formation

under reservoir temperature and pressure. The experiments were carried out with different initial oil saturation of the model, which caused different velocity rates of the combustion front in the model. The temperature at the combustion front in the core model varied in the range of 500–650°C.

After the experiment, core extraction, fluid collection from the lines, analysis of the selected oil, water, and core samples was carried out. In our study, we focus on analyzing the main petrophysical properties change caused by the combustion process and accompanying chemical reactions.

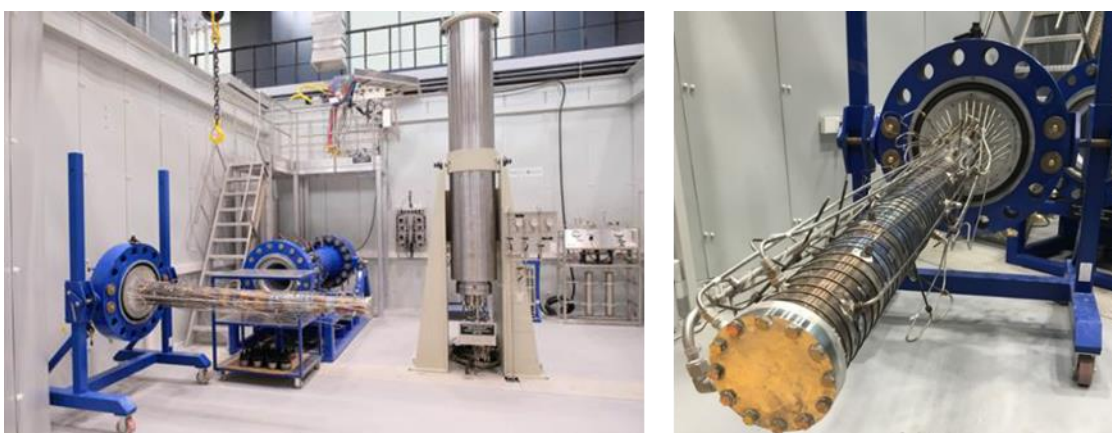


Figure 97: Photograph of the MPCT setup (*photo credentials: archive of Skoltech photo collection*).

To study the properties change due to the combustion process before each test, a collection of 4–5 cylindrical samples was selected for analyzing the porous structure by X-Ray CT and NMR. The tube was filled with a bulk crushed core model. However, the consolidated rock samples were located inside the tube for an extensive study of the rock properties change after the combustion. More than ten small core plugs and chips were packed in the tube to study changes in the reservoir and geochemical properties (Figure 98).

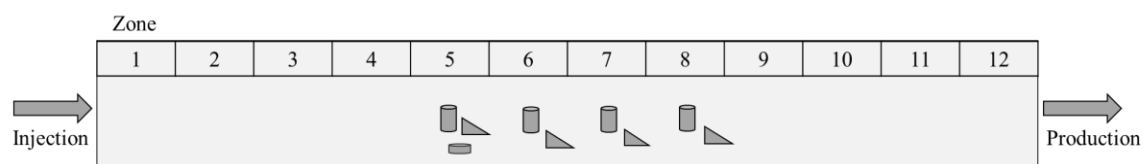


Figure 98: Scheme of combustion tube packing.

Two series of cylindrical samples were selected for NMR rock analysis: part of the collection was saturated with oil and the other one with a brine model. Core preparation, cleaning, and saturation were carried out in accordance with procedures presented in Section 2.2.7.

### 6.3.3 Results

First, we analyzed the change in petrophysical properties by conventional gas porosimetry (Figure 99). Due to core fragility and the presence of large voids and cracks in the rock after the combustion, the number of investigated samples was limited. Similar to shale samples, we observed a significant increase in void space, which led to boosted porosity values and increased permeability (including the contribution of cracks development). Gas porosity for samples has increased up to 3 times, while the permeability has increased by 2-3 orders of magnitude.

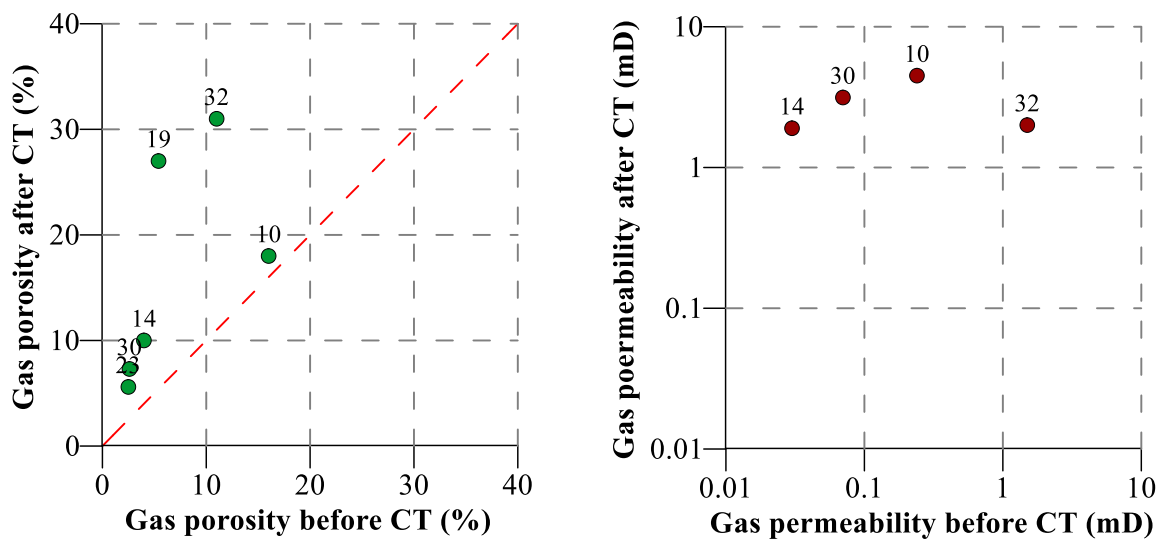


Figure 99: Porosity (left) and permeability of samples (right) before and after CT.

Second, as for the visual analysis of the rock, Figure 100 shows how the combustion process affected the matrix of some of the samples.

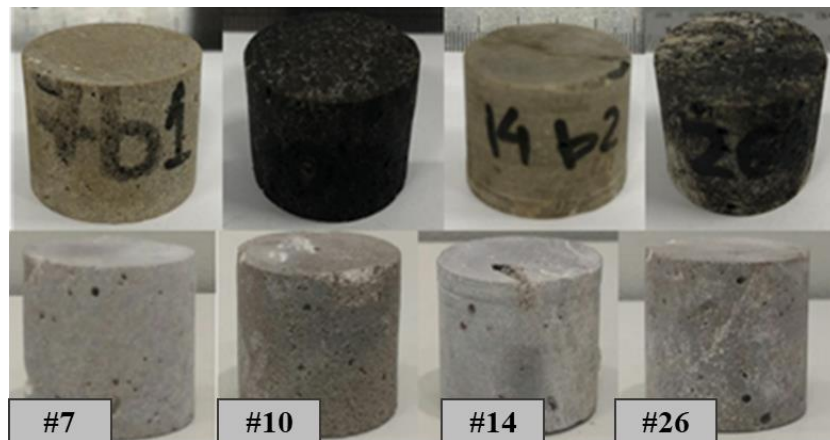


Figure 100: Photographs of the rock samples before and after CT.

Visualization of open and closed pores by X-ray CT is presented in Figure 101 for Sample #14. The presence of a noticeable amount of closed pores may be confirmed since closed pores show coherence on a smaller scale. The current resolution ( $5\ \mu\text{m}$ ) was limited and, respectively, restricted by technical conditions of the computed tomography. Overall, after experiments in the X-ray CT unit, no noticeable changes in the structure of the void space were found either. This shows the limitation of this technique in recording the changes in porous space structure within the task.

In addition to X-Ray CT, SEM was utilized. Results of imaging showed that the dolomite crystals before the combustion had an idiomorphic structure and relatively smooth surface. After the heating, the surface obtained crystals of irregular shape due to the destruction of dolomite under heating, which led to an increase in the specific surface, and at the same time, to an increase in porosity.

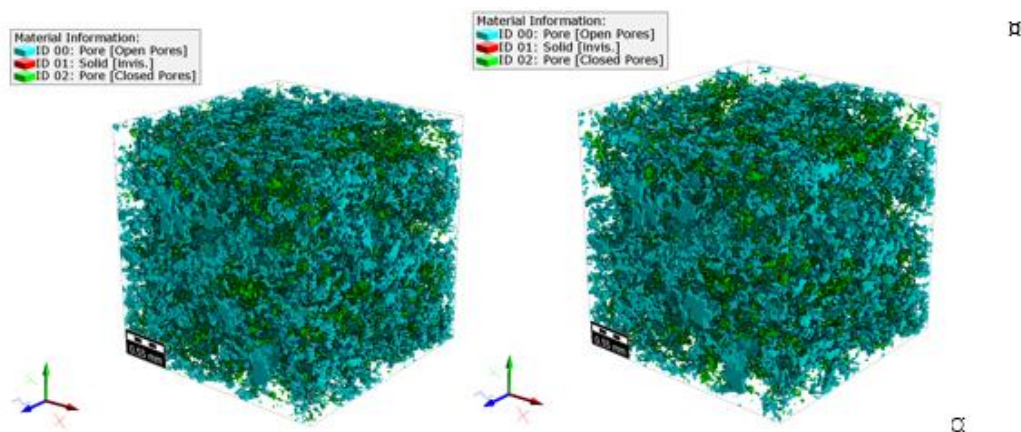


Figure 101: 3D X-Ray CT visualization of the rock porous space before (left) and after the combustion test (right).

For the first series of samples (#10 and #26),  $T_2$  relaxation spectra and two-dimensional  $T_1$ - $T_2$  maps were plotted in order to assess changes in the initial oil saturation and porosity by NMR. Two samples were placed in the combustion tube during the first ISC experiment (Test #1). The values of porosity after combustion, according to NMR, are close to zero caused by near-zero saturation of the rock. The pore size distribution was recalculated from the results of the  $T_2$  relaxation. The fraction of fluids remaining in the rock is in the pores of 1–10 nm size (Figure 102); the specific range is close to the range of visible pores for LF-NMR.

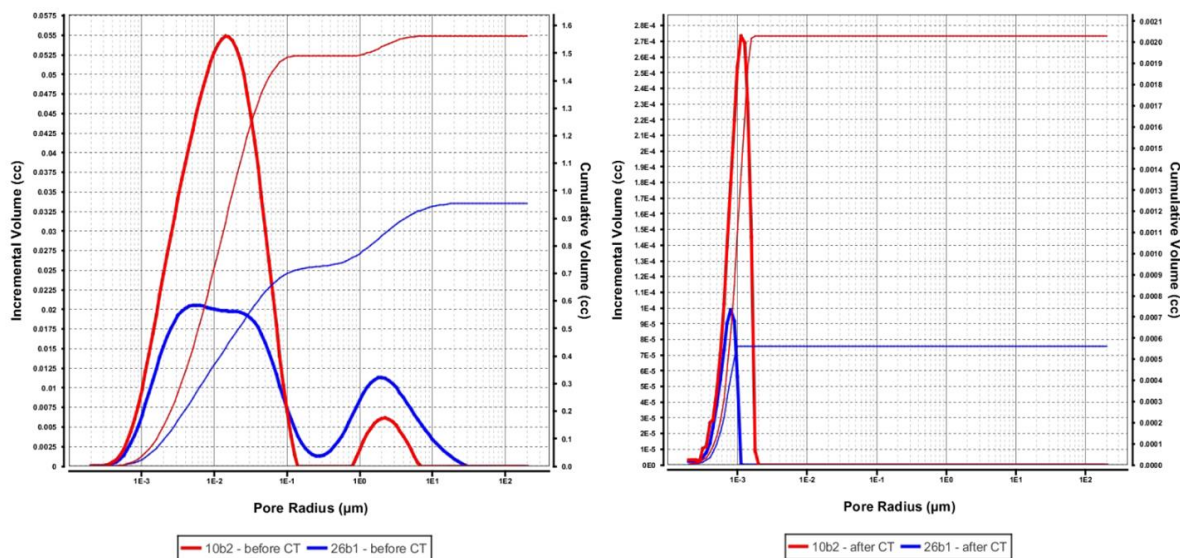


Figure 102: Pore size distribution by NMR.

A series of samples consisting of 5 standard core cylinders underwent a multistage procedure, which consisted of solvent cleaning, saturation with oil, and thermal exposure. The porosity values at all stages of the study are shown in

Table 27. Unlike the first group of samples (#10 and #26), two samples (#7, #14) were saturated with the actual-field oil sample before the ISC Test #1.  $T_2$  tests, as expected, showed a decrease in porosity to 1.3% and 1.4% of porosity.

Table 27. Porosity change of oil-saturated samples

Sample ID	Porosity by NMR before cleaning (%)	Porosity by NMR after cleaning (%)	Porosity by NMR after saturation with oil (%)	Porosity by NMR after CT (%)
7	6.3	1.5	12.2	1.4
14	4.6	1.5	8.4	1.3

The distribution of  $T_2$  relaxation-based pore size indicated a residual fluid in these samples in the range up to 1 ms (corresponds to pores with a radius of  $10E-2 \mu\text{m}$ , which is typical of heavy hydrocarbons in bound pores), as well as a significant amount of free fluids in the range from 10 to 100 ms (pores with a radius of  $0.1-10 \mu\text{m}$ ) (Figure 103). Thus, it is important to register the change of the fluid volume in the rock after thermal exposure. This information can be used in the material balance calculation for the estimation of the oil recovered. Neglecting the residual fluid in rock may lead to underestimating the amount of oil and, in turn, distort the test results.

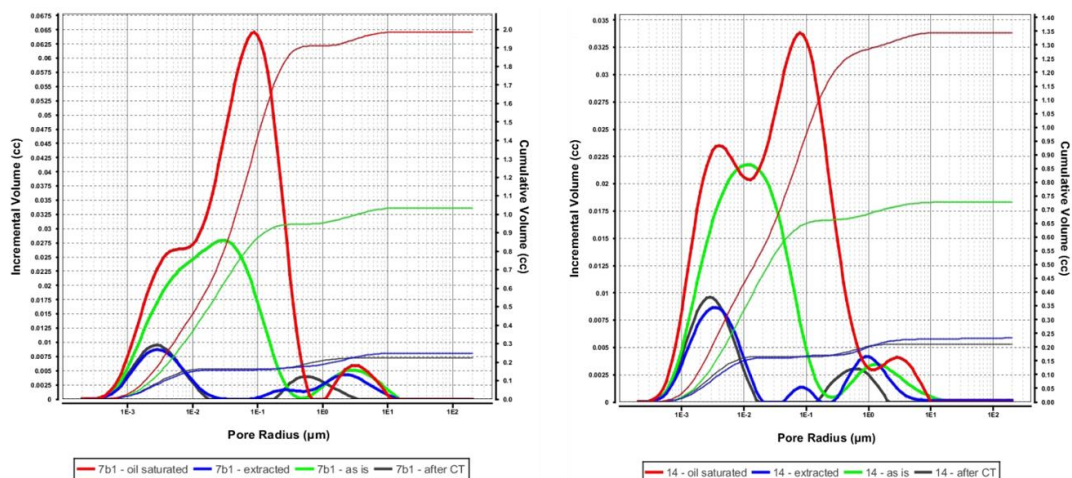


Figure 103:  $T_2$  relaxation curves, Sample #7 (left); (b) Sample #14 (right).

Two-dimensional maps  $T_1$ - $T_2$  demonstrate the presence of residual oil in the zone of 0.1–30 ms in samples before the combustion (Figure 104). After the ISC test, the registration of fluids is complicated due to the low amount of fluid left inside the samples. However, plotted maps demonstrate the two hydrogen populations remaining in the rock after the combustion (Zone #1 and Zone #2). Fluid in Zone #1 corresponds to the highly-viscous components or mobile oil, which may reside after the front propagation. Fluid in Zone #2 has a  $T_1/T_2$  ratio  $\sim 1$ , which indicates that water is more likely to be contained in these pores. This statement requires further research with the re-construction of  $T_1$ - $T_2$  maps after the samples are saturated with a reservoir water model.

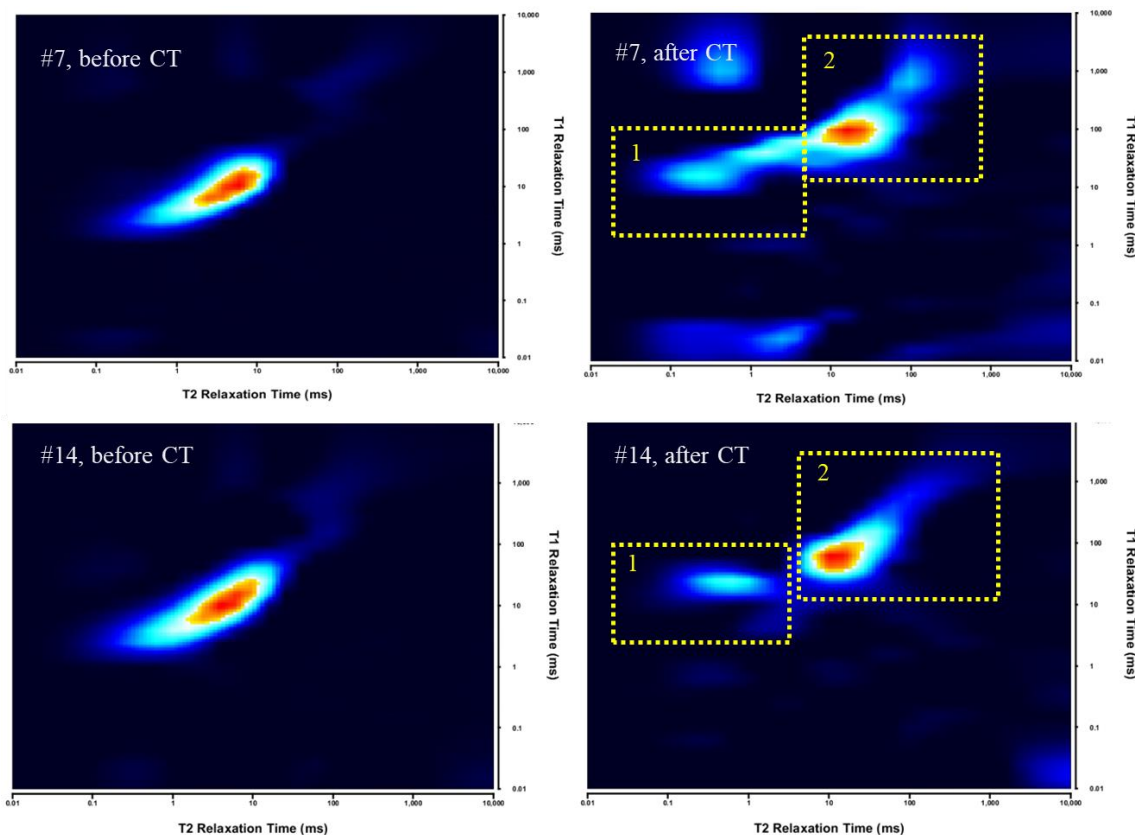


Figure 104: Two-dimensional maps  $T_1$ - $T_2$  (a) before and (b) after the experiment in the CT, Sample #7. The color scale for samples after CT is adjusted to detailize the fluid categories.

## 6.4 Summary

In this chapter, we demonstrate the workflows where we investigate the change in properties of unconventional reservoir rock (shale and heavy-oil carbonate) during the thermal EOR studies.

1. For shale samples, the gas pressure-decay technique revealed a significant increase of porosity (on average, for 9 abs. % of porosity) and permeability (on average, for 1 mD) of core samples after the CT experiment. Samples located in high-temperature zones showed a direct correlation between the measured parameter and the combustion temperature. However, the changes were also conditioned by the initial properties of the core plugs, such as rock lithology and OM properties.

2. The NMR  $T_1$ - $T_2$  fluid identification scheme was proposed by the results of preliminary research conducted on five core samples with a similar lithological type and reservoir properties. We applied the proposed scheme in the analysis of the  $T_1$ - $T_2$  maps obtained for samples before and after combustion. Interpretation of the maps allowed us to categorize the total fluid saturation into several fluid types (bitumen and adsorbed oil, structural and adsorbed water, and mobile oil in inorganic porosity) and estimate the changes induced by thermal exposure.

3. NMR  $T_2$  results included the determination of fluid saturation of the sample, as well as the pore size distribution before and after the combustion experiment. For low-permeability samples, NMR and Rock-Eval pyrolysis proved to be useful and reliable tools in determining the saturation of fragile core plugs and types of hydrocarbons in the rock, which can be applied in the assessment of the amount of displaced oil. In turn, conventional porosimetry also demonstrated satisfactory results in the estimation of open porosity and permeability of the rock.

4. For heavy-oil carbonate fields, NMR studies of the samples were mainly carried out to assess the porosity of the samples and change in pore size distribution before and after the experiment in the combustion tube. At the first stage of research, samples (#10, #26) were studied in an unextracted state to assess the change in the residual (initial) oil saturation. NMR studies of these samples after the first ISC showed near-complete removal of fluids and revealed the pore size which hosts the fluid.

5. For the second combustion test on carbonate samples, the samples were extracted and saturated with oil and further analyzed by an NMR relaxometer. The porosity by NMR for each sample was defined at the stage of 100% oil saturation and after the ISC test. Unlike the first group of samples, samples from the main collection also showed a decrease in porosity, but at the same time, revealed a certain amount of residual fluids in small and medium pores. A specific part of bound fluids (0.1–1 ms, pores with a radius of 0.001–0.01 microns) corresponds to the fraction of unremoved hydrocarbons. There is a fraction of free liquid in the region of 10–100 ms (0.1–10  $\mu\text{m}$ ). The  $T_1/T_2$  ratio, according to two-dimensional  $T_1$ - $T_2$  maps, was close to 1, and it proved the presence of water in rock samples. In comparison

with X-Ray CT results, NMR proved to be an extensive and more sensitive tool for registering the changes in carbonate porous structure.

## CHAPTER 7

### CONCLUSION

#### **7.1 Summary**

The importance of the detailed research of unconventional formations (shales, tight oil, heavy oil carbonates) is proven by many economic and scientific reports. In Russia, there are three main unconventional shale formations — Bazhenov, Domanik, and Khadym and a number of carbonate fields classified as hard-to-recover reserves. Recently, the intensive research and development of Bazhenov and Domanik oil fields have begun by local petroleum companies. Prior to pilot field development and recovery potential determination, analysis of the core material and fluid properties is required. Due to constraints caused by the chemical and physical properties of the studied objects (low reservoir properties, presence of highly-viscous components, heavy oil, or kerogen), it hampers the application of conventional laboratory methods for investigation of the reservoir properties of unconventional rocks.

In this work, the characterization of the porosity, porous structure, and saturation of low-permeability organic-rich carbonates, organic-rich shales, heavy-oil carbonates, and permafrost soils are investigated. As the main experimental method, the low-field NMR relaxometer was chosen. The literature review has revealed the potential of the NMR method for identifying the liquid saturation in complex rocks on the example of the many unconventional reservoirs located worldwide. In addition to NMR, a number of advanced experimental techniques were used, including X-Ray computed tomography, SEM, gas porosimetry, MICP, etc. Work consists of different research applications of NMR applied to targeted objects.

#### **7.2 Conclusions**

1. The NMR core analysis recommendations and methodologies for determining fluid saturation and porosity of samples of Bazhenov and Domanik deposits were developed. A series of tests on the target collection revealed an excellent sensitivity of the method to low

values of porosity and permeability, as well as the repeatability of the results of one-dimensional and two-dimensional tests. The results of the  $T_2$  analysis showed that the most saturation of the hydrocarbons in the as-received samples is concentrated in the region of low relaxation times (up to 10 ms), which corresponds to highly-viscous components, including kerogen, bitumen, and adsorbed oil. The porosity was defined for shale rock at each stage of the saturation. Modification of the core analysis workflow (related to core cleaning, saturation) was proposed based on results of the Bazhenov and Domanik Formation studies. The porosity of rock samples and fluid saturation depends on the shale rock lithotype and mineral composition. The workflow of fluid identification by  $T_1$ - $T_2$  maps was demonstrated for rocks of the Bazhenov Formation.

2. For Domanik Formation, several methods were used to determine  $T_2$  cut-off: drying at a constant temperature with mass control, centrifugation, and membrane method.  $T_2$  cut-off values ranged from 0.4 to 30 ms. For the set of core plugs and chips, the NMR method was used in conjunction with the liquid saturation and the volumetric gas method. The porosity of the shale rock by NMR varied in the range from 0.94% to 10.8%. Also, as a part of core analysis and fluid identification, the existing fluid identification schemes by  $T_1$ - $T_2$  maps were modified and adapted for the target rock.

3. The interpretation results for 6 existing  $T_1$ - $T_2$  map fluid interpretation schemes on three types of organic-rich rock samples were compared, and significant variations in final fluid typing results were noticed. The data analysis showed that no single published interpretation scheme could be applied to fluid identification in target rock without modification and adaptation. The most accurate scheme (by Li et al, 2020) was selected, and the original, sophisticated way to modify it for target samples based on our experimental results and petrophysical was proposed.

4. Wettability determination for shale samples by NMR and other methods was illustrated. All methods provided an initial assessment of the shale rock wettability. The results showed mainly a water-wet and neutral wettability of the section. For target rock samples, the surface wettability turned out to be significantly sensitive to the rock lithology and OM morphology in the rock. NMR obtained index provides the integral wettability characteristic for the entire

core plug. This technique showed low sensitivity for clusters of rock lithotypes and OM categories and mostly characterized the rock as a medium to strong water-wet.

5. The novel methodology for the evaluation of the unfrozen water content in permafrost samples in ambient and formation conditions was presented. The object of the study was soil samples with different particle size distributions (quartz sand, sandy loam, and polymineral clay). As a result of methodological research, optimal NMR scanning modes (total scanning time, number of scans acquired, and signal-to-noise ratio) were selected for frozen soil investigations, with a guaranteed absence of temperature changes in the sample and ensure the necessary accuracy of unfrozen water content determination. This allowed one to study the sediment samples in the temperature range of  $-3...-6^{\circ}\text{C}$  and to obtain good consistency of the NMR data with results of other methods for determining the phase composition of frozen sediments. So, the difference of unfrozen water values obtained by NMR and results of calculation by the activity of pore water or the contact method was averaged 0.2%, which is comparable with the accuracy of the methods used. New coreholders for high-pressure tests were designed and manufactured, and the influence of pressure on soil saturation was demonstrated.

6. The developed NMR methodologies were implemented in the EOR studies. Within thermal EOR research, oil displacement estimation by  $T_1$ - $T_2$  maps was carried out by NMR. The results of this interpretation included the number of hydrocarbons in the sample before and after combustion, which is directly applied for the calculation of the oil displaced during *in-situ* combustion and high-pressure air injection. Moreover, pore size and porosity changes in shales and carbonates were registered after the thermal exposure. NMR enabled to construct of the saturation profiling along the combustion tube, which was used for analyzing the propagation of the combustion front during the high-pressure air injection process.

7. Novel HPHT NMR installation was utilized for complex multiphase diffusion experiments such as  $\text{CO}_2$  injection in shale and carbonate samples. The average value of the  $\text{CO}_2$  diffusion coefficient, determined experimentally, was  $4.91 \cdot 10^{-8} \text{ m}^2/\text{s}$  for shales and  $5.5 \cdot 10^{-7} \text{ m}^2/\text{s}$  for heavy-oil carbonates. HPHT experiments enabled to set of the required

conditions for saturation of the shale core samples and control the saturation profile change in formation conditions.

8. In the framework of this work, workflows for characterization of different rock types by NMR in conjunction with other experimental techniques (gas porosimetry, Rock-Eval pyrolysis, thin-section analysis, X-Ray computed tomography, MICP) were developed. Results of NMR were compared with other experimental methods (conventional and advanced). The advantages of using NMR were demonstrated; therefore, the non-invasiveness of the method, the speed of analysis, and the repeatability of the results proved an LF-NMR as one of the most effective methods for the analysis of unconventional reservoirs.

### **7.3 Recommendations**

The following questions and research directions are subject to further investigation. Core analysis by NMR:

- Extended studies on cross-validation of low-permeability rock saturation with other advanced methods such as MICP and SEM should enhance the assessment of methods comparison;
- The research of NMR signal response and OM and lithological properties of the rocks must be demonstrated on a large set of samples;
- Developed workflows and fluid interpretation techniques based on  $T_2$  and  $T_1-T_2$  NMR analysis should be verified and tested on a large number of core samples;
- The research on  $T_1-T_2$  maps interpretation automation should be continued using ML-based algorithms for further optimization of the unconventional reserves assessment using the NMR technique
- Comparison between low-field (2 MHz) and relatively higher-field NMR (10–20 MHz) must be demonstrated on the example of shale samples; that must raise the basement height in understanding the NMR visibility limits as well as the saturation of shale work with solid kerogen and viscous bitumen.

#### Unfrozen Water Content:

- One further direction include the study of the methane hydrate investigations in the HPHT NMR cell under constant profiling and study of limiting pressure and temperature conditions;
- The number of measurement points under pressure must be increased to enable the further use of obtained data in processes modeling and numerical simulation.

#### NMR Applications in Diffusion Studies:

- There are several methods of NMR utilization in diffusion studies. In the current work, we demonstrated the procedures involving the  $T_2$  measurement and saturation profile change. In further works, other analytical models of diffusion calculation should be implemented.
- Results received by NMR relaxometry should be further verified by other methods such as X-Ray microtomography or pressure-decay method on the rock of the same origin and with the same properties.
- The NMR HPHT-based technique should be applied for performing complex core flooding tests using NMR cell, particularly in obtaining the relative permeability curves for multiphase systems on low-permeability and shale rock samples.

#### NMR Applications in EOR Studies:

- A comprehensive study on the influence of thermal exposure conditions should be performed; numerical analysis of such effect will be done to evaluate the processes at the micro and macro level by an extended set of laboratory methods.
- Information obtained from NMR, Rock-Eval pyrolysis, and SEM must be accounted for in the final evaluation of the laboratory-scale combustion experiments, including the material balance and simulation of the combustion.

## REFERENCES

- Abdallah, W., J. S. Buckley, J. Carnegie, J. Edwards, B. H. E. Fordham, A. Graue, T. Habashy, N. Seleznev, C. Signe, H. Hussain, B. Montaron and M. Ziauddin (2007). "Fundamentals of wettability." Oilfield review 2007: 44-61.
- Abragam, A. (1961). The principles of nuclear magnetism. Oxford,, Clarendon Press.
- Abrams, M. A., A. M. Apanel, O. M. Timoshenko and N. N. Kosenkova (1999). "Oil Families and Their Potential Sources in the Northeastern Timan Pechora Basin, Russia." AAPG Bulletin 83(4): 553-577.
- Ahmed, U. and M. Nathan (2016). Unconventional Oil and Gas Resources. Boca Raton, CRC Press. 894.
- Ahr, W. M. (2008). Geology of Carbonate Reservoirs : The Identification, Description, and Characterization of Hydrocarbon Reservoirs in Carbonate Rocks. Hoboken, N.J., Wiley.
- Ali, M. R., V. Anand, A. Abubakar, R. Grover, I. Pirie and O. Neto (2016). Characterizing Light versus Bound Hydrocarbon in a Shale Reservoir by Integrating New Two-Dimensional NMR and Advanced Spectroscopy Measurements. SPE/AAPG/SEG Unconventional Resources Technology Conference. San Antonio, Texas, USA, Unconventional Resources Technology Conference: 16.
- Alvarado, V. and E. Manrique (2010). "Enhanced Oil Recovery: An Update Review." Energies 3(9).
- Amott, E. (1959). "Observations Relating to the Wettability of Porous Media." AIME(216): 156–162.
- Andersland, O. B. and B. Ladanyi (1994). An Introduction to Frozen Ground Engineering. Boston, MA, Springer.
- Anderson, D. M. and A. R. Tice (1972). "Predicting Unfrozen Water Contents in Frozen Soils from Surface Area Measurements." Highw Res Rec(39): 12-18.
- Andrianov, P. I. (1936). The freezing temperature of soils. Moscow, Publishing House AS USSR.
- API (1998). Recommended Practices for Core Analysis. Recommended Practice 40. Washington, D.C., USA, American Petroleum Institute (API).
- Are, F. E. (2014). "Thermal aspects of Tsytoich principle of water and ice equilibrium state in frozen ground." Earth's Cryosphere XVIII(1): 47-56.
- Astarkin, S., O. Goncharenko, Y. Pisarenko and V. Morozov (2016). "Typical sections of the terrigenous Lower Visean oil and gas basin of the Middle Volga region." Oil Industry Journal(07): 66-68.
- Astarkin, S., V. Kolpakov, O. Goncharenko, Y. Pisarenko and V. Morozov (2017). "Lithological and paleogeographic characteristics of the Bobrikovsky sedimentation stage in the Orenburg region." Oil Industry Journal 10.
- Bai, F., Y. Sun, Y. Liu and M. Guo (2017). "Evaluation of the porous structure of Huadian oil shale during pyrolysis using multiple approaches." Fuel 187: 1-8.

- Balushkina, N. S., G. A. Kalmykov, V. S. Belokhin, R. A. Khamidullin and D. V. Korost (2014). "Siliceous reservoirs of the Bazhenov formation, the Sredny Nazym Oil Field, and the structure of their pore space." Moscow University Geology Bulletin 69(2): 91-100.
- Bloembergen, N., E. M. Purcell and R. V. Pound (1948). "Relaxation effects in nuclear magnetic resonance absorption." Phys Rev 73.
- Bogdanovich, N. N., S. A. Borisenko, E. V. Kozlova, M. Y. Spasennykh and S. Y. Rudakovskaya (2017). Mosaic Hydrophobization of the Surface of Organic-Mineral Matrix from Rocks of Bazhenov Formation (Russian). SPE Russian Petroleum Technology Conference. Moscow, Russia, Society of Petroleum Engineers: 18.
- Bondarenko, T. (2018). Evaluation of High-Pressure Air Injection Potential for In-Situ Synthetic Oil Generation from Oil Shale: Bazhenov Formation. PhD, Skolkovo Institute of Science and Technology.
- Bondarenko, T., E. Popov, A. Cheremisin, E. Kozlova, I. Karpov and N. Morozov (2017). "Laboratory Modeling of High-Pressure Air injection in Oil Fields of Bazhenov formation." Oil Industry 03(03): 34-39.
- Borisenko, S., N. N. Bogdanovich, E. Kozlova, M. Spasennykh and D. E. Zagranovskaya (2017). "Estimating lyophilic properties of the Bazhenov formation rocks by adsorption and NMR methods." Neftyanoe khozyaystvo - Oil Industry: 12-16.
- Bryan, J., F. Hum, A. Kantzas, R. MacPherson and T. Hancsicsak (2005). In-situ viscosity using low field NMR: a field case study. International symposium of the society of core analysts held in Toronto, Canada.
- Burchette, T. (2012). "Carbonate Rocks and Petroleum Reservoirs: A Geological Perspective From the Industry." Geological Society of London Special Publications 370: 17-37.
- Burrows, L. C., F. Haeri, P. Cvetic, S. Sanguinito, F. Shi, D. Tapriyal, A. Goodman and R. M. Enick (2020). "A Literature Review of CO<sub>2</sub>, Natural Gas, and Water-Based Fluids for Enhanced Oil Recovery in Unconventional Reservoirs." Energy & Fuels 34(5): 5331-5380.
- Bushnev, D. A. and N. S. Burdel'naya (2013). "Modeling of Oil Generation by Domanik Carbonaceous Shale." Petroleum Chemistry 53(3): 145-151.
- Callaghan, P. (1991). Principles of Nuclear Magnetic Resonance Microscopy. Oxford, Clarendon Press.
- Chen, T., Z. Yang, Y. Luo, W. Lin, J. Xu, Y. Ding and J. Niu (2018). "Evaluation of Displacement Effects of Different Injection Media in Tight Oil Sandstone by Online Nuclear Magnetic Resonance." Energies 11(10).
- Cnudde, V. and M. N. Boone (2013). "High-resolution X-ray computed tomography in geosciences: A review of the current technology and applications." Earth-Science Reviews 123: 1-17.
- Coates, G. R., L. Xiao and M. G. Prammer (1999). NMR Logging Principles and Applications, Elsevier Science.

- Deng, S., Z. Wang, Q. Gu, F. Meng, J. Li and H. Wang (2011). "Extracting hydrocarbons from Huadian oil shale by sub-critical water." Fuel Processing Technology 92: 1062-1067.
- Donaldson, E. C., R. D. Thomas and P. B. Lorenz (1969). "Wettability Determination and Its Effect on Recovery Efficiency." Society of Petroleum Engineers Journal 9(01): 13-20.
- Du, F. and B. Nojabaei (2019). "A Review of Gas Injection in Shale Reservoirs: Enhanced Oil/Gas Recovery Approaches and Greenhouse Gas Control." Energies 12(12).
- EIA (2013). Technically Recoverable Shale Oil and Shale Gas Resources: An Assessment of 137 Shale Formations in 41 Countries Outside the United States
- Eide, F., M. A. Fernø, Z. Karpyn, A. Haugen and A. Graue (2013). CO<sub>2</sub> Injections for Enhanced Oil Recovery Visualized with an Industrial CT-scanner. 17th European Symposium on Improved Oil Recovery. St. Petersburg, Russia.
- Eide, Ø., M. A. Fernø, Z. Alcorn and A. Graue (2016). "Visualization of Carbon Dioxide Enhanced Oil Recovery by Diffusion in Fractured Chalk." SPE Journal 21(01): 112-120.
- Erdman, N. and N. Drenzek (2013). Integrated preparation and imaging techniques for the microstructural and geochemical characterization of shale by scanning electron microscopy. Electron microscopy of shale hydrocarbon reservoirs. W. Camp, E. Diaz and B. Wawak, AAPG Memoir. 102: 7-14.
- Espitalie, J. and M. Bordenave (1993). Rock-Eval Pyrolysis: 237-261.
- Fadeeva, N. P., E. V. Kozlova, E. N. Poludetkina, T. A. Shardanova, N. V. Pronina, A. V. Stupakova, G. A. Kalmykov and A. N. Khomyak (2016). "The Hydrocarbon-Generation Potential of the Domanik Rocks in the Volga-Ural Petroliferous Basin." Moscow University Geology Bulletin 71(1): 41-49.
- Fanchi, J. R. (2002). Chapter 7 - Measures of Rock-Fluid Interactions. Shared Earth Modeling. J. R. Fanchi. Woburn, Butterworth-Heinemann: 108-132.
- Fernø, M. A., L. P. Hauge, A. Uno Rognmo, J. Gauteplass and A. Graue (2015). "Flow visualization of CO<sub>2</sub> in tight shale formations at reservoir conditions." Geophysical Research Letters 42(18): 7414-7419.
- Fleury, M. (2014) "Characterization of shales with low field NMR."
- Fleury, M. and M.-F. Romero-Sarmiento (2015). "Characterization of shales using T1-T2 NMR maps." Journal of Petroleum Science and Engineering 137.
- Foley, I., S. A. Farooqui and R. L. Kleinberg (1996). "Effect of Paramagnetic Ions on NMR Relaxation of Fluids at Solid Surfaces." Journal of Magnetic Resonance, Series A 123(1): 95-104.
- Gabnasyrov, A. V., N. A. Lyadova, I. S. Putilov and S. I. Solovyev (2016). Domanik Shale Oil: Unlocking Potential. SPE Russian Petroleum Technology Conference and Exhibition. Moscow, Russia, Society of Petroleum Engineers.
- Geng, Y., W. Liang, J. Liu, M. Cao and Z. Kang (2017). "Evolution of Pore and Fracture Structure of Oil Shale under High Temperature and High Pressure." Energy & Fuels 31(10): 10404-10413.

Geologika (2016). Manual for PIK-PP Automated Unit for Measuring Porosity and Permeability of Rock Samples. Novosibirsk, Geologika.

GIT (2014). GIT Systems and Lithometrix User Manual R7.0.

Goral, J., I. Walton, M. Andrew and M. Deo (2019). "Pore System Characterization of Organic-Rich Shales using Nanoscale-Resolution 3D Imaging." Fuel 258.

Green, D. P. (2009). Extracting Pore Throat size and relative permeability from MRI-based capillary pressure curves. The International Symposium of the Society of Core Analysts held in Noordwijk, The Netherlands.

Green, D. P., J. R. Dick, M. McAloon, P. F. d. J. Cano-Barrita, J. Burger and B. Balcom (2008). Oil/Water Imbibition and Drainage Capillary pressure Determined by MRI on a Wide Sampling of Rocks. International Symposium of the Society of Core Analysts. Abu Dhabi, UAE.

Green, D. P. and D. Veselinovic (2010). "Analysis of unconventional reservoirs using new and existing NMR Methods." GeoCanada, Calgary, Canada.

Gudok, N. S. and N. N. Bogdanovich (2007a). Experimental methods of reservoir physics. Moscow, Sputnik.

Guidry, K., D. Luffel and J. Curtis (1996). Development of Laboratory and Petrophysical Techniques for Evaluating Shale Reservoirs. Final Reports 1995. Des Plaines, Illinois, Gas Technology Institute. GRI-95/0496: 304.

Gultinan, E. J., M. B. Cardenas, P. C. Bennett, T. Zhang and D. N. Espinoza (2017). "The effect of organic matter and thermal maturity on the wettability of supercritical CO<sub>2</sub> on organic shales." International Journal of Greenhouse Gas Control 65: 15-22.

Gutierrez, D., R. G. Moore, M. G. Ursenbach and S. A. Mehta (2012). "The ABCs of in-situ-combustion simulations: from laboratory experiments to field scale." Journal of Canadian Petroleum Technology 51(04): 256-267.

Habina, I., N. Radzik, T. Topór and A. T. Krzyżak (2017). "Insight into oil and gas-shales compounds signatures in low field 1H NMR and its application in porosity evaluation." Microporous and Mesoporous Materials 252: 37-49.

Handa, Y. P., M. Zakrzewski and C. Fairbridge (1992). "Effect of restricted geometries on the structure and thermodynamic properties of ice." The Journal of Physical Chemistry 96(21): 8594-8599.

Iglauer, S. (2017). "CO<sub>2</sub>-Water-Rock Wettability: Variability, Influencing Factors, and Implications for CO<sub>2</sub> Geostorage." Accounts of Chemical Research 50(5): 1134-1142.

Ishizaki, T., M. Maruyama, Y. Furukawa and J. G. Dash (1996). "Premelting of ice in porous silica glass." Journal of Crystal Growth 163(4): 455-460.

Istomin, V., E. Chuvilin and B. Bukhanov (2017). "Fast estimation of unfrozen water content in frozen soils." Earth's Cryosphere 21: 116-120.

Istomin, V., E. Chuvilin and B. Bukhanov (2017). "Fast Estimation Of Unfrozen Water Content In Frozen Soils." Earth's Cryosphere XXI: 134-139.

- Istomin, V., E. Chuvilin, B. Bukhanov and T. Uchida (2017). "Pore water content in equilibrium with ice or gas hydrate in sediments." Cold Regions Science and Technology 137: 60-67.
- Ivanova, A. A., N. A. Miturev, S. N. Shilobreeva and A. N. Cheremisin (2019). "A review of experimental methods for studying the wetting properties of oil reservoir rocks." Earth Physics(3): 135-149.
- Jagadisan, A. and Z. Heidari (2019). "Experimental Quantification of the Effect of Thermal Maturity of Kerogen on Its Wettability." SPE Reservoir Evaluation & Engineering 22(04): 1323-1333.
- Jian-Ping, Y. A. N., W. E. N. Dan-Ni, L. I. Zun-Zhi, G. Bin, C. A. I. Jin-Gong, L. Qiang and Y. A. N. Yu (2016). "A Quantitative Evaluation Method Of Low Permeable Sandstone Pore Structure Based On Nuclear Magnetic Resonance (Nmr) Logging: A Case Study Of Es4 Formation In The South Slope Of Dongying Sag." Chinese Journal of Geophysics 59(3): 313-322.
- Jiang, H., H. Daigle, X. Tian, M. J. Pyrcz, C. Griffith and B. Zhang (2019). "A comparison of clustering algorithms applied to fluid characterization using NMR T1-T2 maps of shale." Computers & Geosciences 126: 52-61.
- Jiang, T., E. Rylander, P. M. Singer, R. E. Lewis and S. M. Sinclair (2013). Integrated petrophysical interpretation of Eagle Ford Shale with 1-D and 2-D nuclear magnetic resonance (NMR). SPWLA 54th annual logging symposium, Society of Petrophysicists and Well-Log Analysts.
- Kadyrov, R., B. Galiullin and E. Statsenko (2018). The Porous Space Structure of Domanik Shales in the East of Russian Plate.
- Kausik, R., K. Fellah, E. Rylander, P. M. Singer, R. E. Lewis and S. M. Sinclair (2016). "NMR Relaxometry in Shale and Implications for Logging." Petrophysics 57(04): 339-350.
- Kausik, R. e. a. (2015). NMR Relaxometry in Shale and Implications for Logging. SPWLA 56th Annual Logging Symposium.
- Kazak, A., S. Chugunov and A. Chashkov (2018). "Integration of Large-Area Scanning-Electron-Microscopy Imaging and Automated Mineralogy/Petrography Data for Selection of Nanoscale Pore-Space Characterization Sites." SPE Reservoir Evaluation & Engineering 21(04): 821-836.
- Kazak, E. S. and A. V. Kazak (2019). "A Novel Laboratory Method for Reliable Water Content Determination of Shale Reservoir Rocks." Journal of Petroleum Science and Engineering 183: 106301.
- Kazak, E. S. and A. V. Kazak (2020). "Experimental Features of Cation Exchange Capacity Determination in Organic-Rich Mudstones." Journal of Natural Gas Science and Engineering 83: 103456.
- Kenyon, W. E. (1997). "Petrophysical Principles of Applications of NMR Logging." The Log Analyst 38(02): 23.

- Khamidullin, R. R., G. A. Kalmykov, D. V. Korost, N. S. Balushkina and A. I. Bakay (2012). Reservoir properties of the Bazhenov formation. SPE Russian Oil and Gas Exploration and Production Technical Conference and Exhibition. Moscow, Russia, Society of Petroleum Engineers: 11.
- Khatibi, S., M. Ostadhassan, H. Xie, T. Gentzis, B. Bubach, Z. Gan and H. Carvajal-Ortiz (2018). "NMR relaxometry a new approach to detect geochemical properties of organic matter in tight shales." Fuel 235.
- Kibodeaux, K. R. (2014). Evolution of Porosity, Permeability, and Fluid Saturations During Thermal Conversion of Oil Shale. SPE Annual Technical Conference and Exhibition. Amsterdam, The Netherlands, Society of Petroleum Engineers: 22.
- Kleinberg, R. and D. Griffin (2005). "NMR measurements of permafrost: Unfrozen water assay, pore-scale distribution of ice, and hydraulic permeability of sediments." Cold Regions Science and Technology 42: 63-77.
- Kobchenko, M., H. Panahi, F. Renard, D. K. Dysthe, A. Malthes-Sørensen, A. Mazzini, J. Scheibert, B. Jamtveit and P. Meakin (2011). "4D imaging of fracturing in organic-rich shales during heating." Journal of Geophysical Research: Solid Earth 116(B12).
- Kondakov, V., O. Kondakova and G. Nikolayeva (1989). "Dependence of the phase composition of water in freezing and frozen soils on external pressure." Engineering Geology 5: 21-27.
- Kontorovich, A. E., V. I. Moskvina, O. I. Bostrikov, V. P. Danilova, A. N. Fomin, A. S. Fomichev, E. A. Kostyreva and V. N. Melenevsky (1997). "Main oil source formations of the West Siberian Basin." Petroleum Geoscience 3(4): 343-358.
- Kozłowski, T. and E. Nartowska (2013). "Unfrozen Water Content in Representative Bentonites of Different Origin Subjected to Cyclic Freezing and Thawing." Vadose Zone Journal 12(1): vzj2012.0057.
- Krzyżak, A. T., I. Habina-Skrzyniarz, G. Machowski and W. Mazur (2020). "Overcoming the barriers to the exploration of nanoporous shales porosity." Microporous and Mesoporous Materials 298: 110003.
- Labani, M. and R. Rezaee (2015). Petrophysical Evaluation of Gas Shale Reservoirs. Fundamentals of Gas Shale Reservoirs, Wiley & Sons: 117-137.
- Lazar, O. R., K. M. Bohacs, J. Schieber, J. H. Macquaker and T. M. Demko (2015). Mudstone Primer: Lithofacies variations, diagnostic criteria, and sedimentologic-stratigraphic implications at lamina to bedset scales, SEPM (Society for Sedimentary Geology).
- Li, J., W. Huang, S. Lu, M. Wang, G. Chen, W. Tian and Z. Guo (2018). "Nuclear Magnetic Resonance T1-T2 Map Division Method for Hydrogen-Bearing Components in Continental Shale." Energy & Fuels 32.
- Li, J., C. Jiang, M. Wang, S. Lu, Z. Chen, G. Chen, L. Jijun, Z. Li and S. Lu (2020). "Adsorbed and free hydrocarbons in unconventional shale reservoir: A new insight from NMR T1-T2 maps." Marine and Petroleum Geology 116: 104311.

- Liu, F., H. Yang, T. Chen, S. Zhang, D. Yu, Y. Chen and Q. Xie (2020). "Direct Evidence of Salinity and pH Effects on the Interfacial Interactions of Asphaltene-Brine-Silica Systems." Molecules 25(5).
- Liu, X., J. Zhang, Y. Liu, H. Huang and Z. Liu (2018). "Main factors controlling the wettability of gas shales: A case study of over-mature marine shale in the Longmaxi Formation." Journal of Natural Gas Science and Engineering 56: 18-28.
- Liu, Z., D. Liu, Y. Cai, Y. Yao, Z. Pan and Y. Zhou (2020). "Application of nuclear magnetic resonance (NMR) in coalbed methane and shale reservoirs: A review." International Journal of Coal Geology 218: 103261.
- Liu, Z., D. Yang, Y. Hu, J. Zhang, J. Shao, S. Song and Z. Kang (2018). "Influence of In Situ Pyrolysis on the Evolution of Pore Structure of Oil Shale." Energies 11(4).
- Lopatin, N. V., S. L. Zubairae, I. M. Kos, T. P. Emets, E. A. Romanov and O. V. Malchikhina (2003). "Unconventional Oil Accumulations in the Upper Jurassic Bazhenov Black Shale Formation, West Siberian Basin: a Self-Sourced Reservoir System." Journal of Petroleum Geology 26(2): 225-244.
- Lyu, C., Z. Ning, Q. Wang and M. Chen (2018). "Application of NMR T2 to Pore Size Distribution and Movable Fluid Distribution in Tight Sandstones." Energy & Fuels 32(2): 1395-1405.
- Mai, A. and A. Kantzas (2002). An evaluation of the application of low field NMR in the characterization of carbonate reservoirs. SPE Annual Technical Conference and Exhibition, Society of Petroleum Engineers.
- Marschall, D., J. Gardner, D. Mardon and G. Coates (1995). Method for correlating NMR relaxometry and mercury injection data. 1995 SCA Conference, paper.
- McPhee, C., J. Reed and I. Zubizarreta (2015). Core Analysis : A Best Practice Guide. Amsterdam, Netherlands, Elsevier.
- Mehana, M. and I. El-monier (2016). "Shale Characteristics Impact on Nuclear Magnetic Resonance (NMR) Fluid Typing Methods and Correlations." Petroleum 2.
- Mitchell, J., T. C. Chandrasekera, D. J. Holland, L. F. Gladden and E. J. Fordham (2013). "Magnetic resonance imaging in laboratory petrophysical core analysis." Physics Reports 526(3): 165-225.
- Moghadam, A. A. and R. Chalaturnyk (2015). Laboratory Investigation of Shale Permeability. SPE/CSUR Unconventional Resources Conference. Calgary, Alberta, Canada, Society of Petroleum Engineers: 27.
- Moore, R. G., S. A. Mehta and M. G. Ursenbach (2002). A Guide to High Pressure Air Injection (HPAI) Based Oil Recovery. SPE/DOE Improved Oil Recovery Symposium. Tulsa, Oklahoma, Society of Petroleum Engineers: 7.
- Morrow, N. R. (1990). "Wettability and Its Effect on Oil Recovery." Journal of Petroleum Technology 42(12): 1476-1484.

Mukhametdinova, A., T. Karamov, N. Bogdanovich, S. Borisenko, S. Rudakovskaya and A. Cheremisin (2020). "Wettability of organic-rich source rocks: case study on Bazhenov Formation (Abalak-Bazhenov group)." Adv. Geosci. 54: 195-204.

Mukhametdinova, A., T. Karamov, N. Bogdanovich, A. Cheremisin and V. Plotnikov (2019). "Complex Characterization of Organic - Rich Carbonate Shales Saturation." International Multidisciplinary Scientific GeoConference-SGEM 19(1.2): 719-726.

Mukhametdinova, A., A. Kazak, T. Karamov, N. Bogdanovich, M. Serkin, S. Melekhin and A. Cheremisin (2020). "Reservoir Properties of Low-Permeable Carbonate Rocks: Experimental Features." Energies 13(9).

Mukhametdinova, A., P. Mikhailova, E. Kozlova, T. Karamov, A. Baluev and A. Cheremisin (2020). "Effect of Thermal Exposure on Oil Shale Saturation and Reservoir Properties." Applied Sciences 10(24).

Musu, J. T. and B. Widarsono (2007). "Determination of NMR T2 cut off for ductile, low permeability shaly sandstone." ASEG Extended Abstracts 2007(1): 1-10.

Nelson, P. H. (2009). "Pore-Throat Sizes in Sandstones, Tight Sandstones, and Shales. Geologic Note." AAPG Bulletin 93(3): 329–340.

Nes, O.-M., P. Horsrud and T. Skjetne (1993). Shale porosities as determined by NMR. SEG Technical Program Expanded Abstracts 1993, Society of Exploration Geophysicists: 88-91.

Nicot, B., N. Vorapalawut, B. Rousseau, L. F. Madariaga, G. Hamon and J.-P. Korb (2015). "Estimating saturations in organic shales using 2D NMR." Petrophysics 57(01): 19-29.

Nikolaev, M. Y. and A. Kazak (2019). "Liquid saturation evaluation in organic-rich unconventional reservoirs: A comprehensive review." Earth-Science Reviews 194.

Odusina, E. O., C. H. Sondergeld and C. S. Rai (2011). NMR Study of Shale Wettability. SPE Unconventional Resources Conference. Calgary, Alberta, Canada, Society of Petroleum Engineers.

Ogunberu, A. L. and M. Ayub (2005). "The Role of Wettability in Petroleum Recovery." Petroleum Science and Technology 23(2): 169-188.

Pan, B., Y. Li, M. Zhang, X. Wang and S. Iglauer (2020). "Effect of total organic carbon (TOC) content on shale wettability at high pressure and high temperature conditions." Journal of Petroleum Science and Engineering 193: 107374.

Panahi, H., M. Kobchenko, F. Renard, A. Mazzini, J. Scheibert, D. Dysthe, B. Jamtveit, A. Malthé-Sørenssen and P. Meakin (2013). "A 4D Synchrotron X-Ray-Tomography Study of the Formation of Hydrocarbon-Migration Pathways in Heated Organic-Rich Shale." SPE Journal 18: 366-377.

Patterson, D. E. and M. W. Smith (1981). "The measurement of unfrozen water content by time domain reflectometry: results from laboratory tests." Canadian Geotechnical Journal 18(1): 131-144.

PerGeos (2018). PerGeos Software. Thermo Fisher Scientific Web site.

- Peters, K. E. (1986). "Guidelines for Evaluating Petroleum Source Rock using Programmed Pyrolysis." American Association of Petroleum Geologists Bulletin 70(3): 318-329.
- Popov, E., T. Bondarenko, S. Dobrovolskaya, A. Kalmykov, N. Morozov and A. Erofeev (2017). "The Potential of Tertiary Methods Application for Unconventional Hydrocarbon Systems Exposure on the Example of Bazhenov Formation." Oil Industry(3): 54-57.
- Popov, E., A. Myasnikov, A. Cheremisin, R. Miftakov, V. Stukachev and A. Mukhametdinova (2016). Experimental and Computational Complex for Determination of the Effectiveness of Cyclic Carbon Dioxide Injection for Tight Oil Reservoirs. SPE Russian Petroleum Technology Conference and Exhibition. Moscow, Russia, Society of Petroleum Engineers: 20.
- Prishchepa, O. M., O. Y. Averianova, A. A. Ilyinskiy and D. Morariu (2014). "Tight oil and gas formations - Russia's hydrocarbons future resources." 323.
- Profice, S., G. Hamon and B. Nicot (2016). "Low-Permeability Measurements: Insights." Petrophysics 57(01): 30-40.
- Razavifar, M., A. Mukhametdinova, E. Nikoee, A. Burukhin, A. Rezaei, A. Cheremisin and M. Riazi (2021). "Rock Porous Structure Characterization: A Critical Assessment of Various State-of-the-Art Techniques." Transport in Porous Media.
- Remeysen, K. and R. Swennen (2008). "Application of Microfocus Computed Tomography in Carbonate Reservoir Characterization: Possibilities and Limitations." Marine and Petroleum Geology 25(6): 486-499.
- Requejo, A. G., R. Sassen, M. C. Kennicutt, I. Kvedchuk, T. McDonald, G. Denoux, P. Comet and J. M. Brooks (1995). "Geochemistry of Oils from The Northern Timan-Pechora Basin, Russia." Organic Geochemistry 23(3): 205-222.
- Roehl, P. O. and P. W. Choquette (1985). Carbonate Petroleum Reservoirs. New York, Springer-Verlag.
- Rylander, E., et al. (2013) "NMR 2D Distributions in the Eagle Ford Shale : Reflections on Pore Size."
- Ryzhkova, S. V., L. M. Burshtein, S. V. Ershov, V. A. Kazanenkov, A. E. Kontorovich, V. A. Kontorovich, A. Y. Nekhaev, B. L. Nikitenko, M. A. Fomin, B. N. Shurygin, A. L. Beizel, E. V. Borisov, O. V. Zolotova, L. M. Kalinina and E. V. Ponomareva (2018). "The Bazhenov Horizon of West Siberia: structure, correlation, and thickness." Russian Geology and Geophysics 59(7): 846-863.
- Safari, M., A. Rahimi, R. Gholami, A. Permana and W. Siaw Khur (2020). "Underlying mechanisms of shale wettability alteration by low salinity water injection (LSWI)." Journal of Dispersion Science and Technology: 1-9.
- Saidian, M., U. Kuila, L. Godinez, S. Rivera and M. Prasad (2014). A Comparative Study of Porosity Measurement in MudRocks.

- Saif, T., Q. Lin, K. Singh, B. Bijeljic and M. J. Blunt (2016). "Dynamic imaging of oil shale pyrolysis using synchrotron X-ray microtomography." Geophysical Research Letters 43(13): 6799-6807.
- Sander, R., Z. Pan and L. D. Connell (2017). "Laboratory Measurement of Low Permeability Unconventional Gas Reservoir Rocks: A Review of Experimental Methods." Journal of Natural Gas Science and Engineering 37: 248-279.
- Sarathi, P. S. (1999). In-situ combustion handbook - Principles and practices. Tulsa, Oklahoma, National Petroleum Technology Office. U.S. Department of Energy.
- Sayers, C. M. (2013). "The effect of kerogen on the elastic anisotropy of organic-rich shales." GEOPHYSICS 78(2): D65-D74.
- Sheng, J. J. (2017). "Critical Review of Field EOR Projects in Shale and Tight Reservoirs." Journal of Petroleum Science and Engineering 159: 654-665.
- Sheng, J. J. (2018). "Discussion of shale rock wettability and the methods to determine it." Asia-Pacific Journal of Chemical Engineering 13(6): e2263.
- Simpson, G. A. and N. S. Fishman (2015). Unconventional Tight Oil Reservoirs: A Call For New Standardized Core Analysis Workflows And Research International Symposium of the Society of Core Analysts St. John's, Newfoundland and Labrador, Canada.
- Singer, P. (2013). NMR T2 Distributions in the Eagle Ford Shale: Reflections on Pore Size.
- Song, X., Y. Qin, H. Ma, M. Wu and L. Ma (2018). "The effect of sedimentary microfacies on wettability of tight sandstone in coal-bearing strata: a case from Ordos Basin, China." Petroleum Science and Technology 36(23): 1958-1967.
- Straley, C., D. Rossini, H. J. Vinegar, P. Tutunjan and C. E. Morriss (1997). "Core Analysis by Low-Field NMR." The Log Analyst 38: 84-94.
- Stupakova, A. V., G. A. Kalmikov, N. I. Korobova, N. P. Fadeeva and Y. A. Gotovskiy (2017). "The Domanic Formation of the Volga-Ural Basin — Types of the Section, Formation Conditions and Hydrocarbon Potential." Georesursy 1: 112-124.
- Sulucarnain, I. D., C. H. Sondergeld and C. S. Rai (2012). An NMR study of shale wettability and effective surface relaxivity. SPE Canadian Unconventional Resources Conference, Society of Petroleum Engineers.
- Sumgin, M. I., S. P. Kachurin, N. I. Tolstikhin and V. F. Tumel (1940). General permafrost. Moscow, Publishing House AS USSR.
- Sun, L., J. Tuo, M. Zhang, C. Wu, Z. Wang and Y. Zheng (2015). "Formation and development of the pore structure in Chang 7 member oil-shale from Ordos Basin during organic matter evolution induced by hydrous pyrolysis." Fuel 158: 549-557.
- Thyne, G. (2015). A review of the measurement of wettability.
- Tice, A., P. Black and R. Berg (1988). "Unfrozen Water Contents of Undisturbed and Remolded Alaskan Silt as Determined by Nuclear Magnetic Resonance." 23.

Tice, A. R., J. L. Oliphant, Y. Nakano and T. F. Jenkins (1982). Relationship between the Ice and Unfrozen Water Phases in Frozen Soil as Determined by Pulsed Nuclear Magnetic Resonance and Physical Desorption Data.

Tisot, P. R. (1967). "Alterations in structure and physical properties of Green River oil shale by thermal treatment." Journal of Chemical & Engineering Data 12(3): 405-411.

Tiwari, P., M. Deo, C. L. Lin and J. D. Miller (2013). "Characterization of oil shale pore structure before and after pyrolysis by using X-ray micro CT." Fuel 107: 547-554.

Trevisan, O. V., S. V. Araujo, R. G. D. Santos and J. A. Vargas (2013). Diffusion Coefficient of CO<sub>2</sub> in Light Oil Under Reservoir Conditions Using X-Ray Computed Tomography. OTC Brasil. Rio de Janeiro, Brazil, Offshore Technology Conference: 13.

Valori, A. and B. Nicot (2019). "A Review of 60 Years of NMR Wettability." Petrophysics 60(02): 255-263.

Venkataramanan, L., N. Evirgen, D. F. Allen, A. Mutina, Q. Cai, A. C. Johnson, A. Y. Green and T. Jiang (2018). "An Unsupervised Learning Algorithm to Compute Fluid Volumes From NMR T1-T2 Logs in Unconventional Reservoirs." Petrophysics 59(05): 617-632.

Vugmeyster, L., B. Hagedorn, M. Clark and R. Sletten (2017). "Evaluating the effect of grain size and salts on liquid water content in frozen soils of Antarctica by combining NMR, chemical equilibrium modeling, and scattered diffraction analysis." Geoderma 299: 25-31.

Washburn, K. E. and J. E. Birdwell (2013). "Updated methodology for nuclear magnetic resonance characterization of shales." Journal of Magnetic Resonance 233.

Washburn, K. E., C. D. Eccles and P. T. Callaghan (2008). "The dependence on magnetic field strength of correlated internal gradient relaxation time distributions in heterogeneous materials." Journal of Magnetic Resonance 194(1): 33-40.

Watanabe, K. and M. Mizoguchi (2002). "Amount of unfrozen water in frozen porous media saturated with solution." Cold Regions Science and Technology 34: 103-110.

Watanabe, K. and T. Wake (2009). "Measurement of unfrozen water content and relative permittivity of frozen unsaturated soil using NMR and TDR." Cold Regions Science and Technology - COLD REG SCI TECHNOL 59: 34-41.

Wen, Y., J. Bryan and A. Kantzas (2005). "Estimation of Diffusion Coefficients in Bitumen Solvent Mixtures as Derived From Low Field NMR Spectra." Journal of Canadian Petroleum Technology 44(04): 7.

Westphal, H., I. Hinze, C. Kiesel, H. Thern and T. Kruspe (2005). "NMR Measurements in Carbonate Rocks: Problems and an Approach to a Solution." Pure and Applied Geophysics 162: 549-570.

Yan, F. and D.-h. Han (2013). Measurement of elastic properties of kerogen. SEG Technical Program Expanded Abstracts 2013, Society of Exploration Geophysicists: 2778-2782.

- Yang, R., S. He, Q. Hu, G. Zhai, J. Yi and L. Zhang (2018). "Comparative Investigations on Wettability of Typical Marine, Continental, and Transitional Shales in the Middle Yangtze Platform (China)." Energy & Fuels 32(12): 12187-12197.
- Yao, Y. and D. Liu (2012). "Comparison of low-field NMR and mercury intrusion porosimetry in characterizing pore size distributions of coals." Fuel 95: 152-158.
- Yoshikawa, K. and P. Overduin (2005). "Comparing unfrozen water content measurements of frozen soil using recently developed commercial sensors." Cold Regions Science and Technology 42: 250-256.
- Yuan, Y. and R. Rezaee (2019). "Comparative Porosity and Pore Structure Assessment in Shales: Measurement Techniques, Influencing Factors and Implications for Reservoir Characterization." Energies 12(11): 2094.
- Zhang, B., A. M. Gomaa, H. Sun, Q. Qu and J.-H. Chen (2014). A study of shale wettability using NMR measurements. SCA-A089, presented at the International Symposium of the Society of Core Analysts held in Aignon, France.
- Zhang, K., K. Sebakhy, K. Wu, G. Jing, N. Chen, Z. Chen, A. Hong and O. Torsæter (2015). Future Trends for Tight Oil Exploitation. SPE North Africa Technical Conference and Exhibition. Cairo, Egypt, Society of Petroleum Engineers: 14.
- Zhang, P., S. Lu, J. Li and X. Chang (2020). "1D and 2D Nuclear magnetic resonance (NMR) relaxation behaviors of protons in clay, kerogen and oil-bearing shale rocks." Marine and Petroleum Geology 114: 104210.
- Zhirong Zhang, J. K. V., Paul F. Greenwood, Wenxuan Hu, Jianzhong Qin, Tenger Borjigin, Changbo Zhai, Weixin Liu (2014). "Flash pyrolysis of kerogens from algal rich oil shales from the Eocene Huadian Formation, NE China." Organic Geochemistry 76: 167-172.